Synthesis and Post-synthesis Transformations of Colloidal Semiconductor Nanocrystals

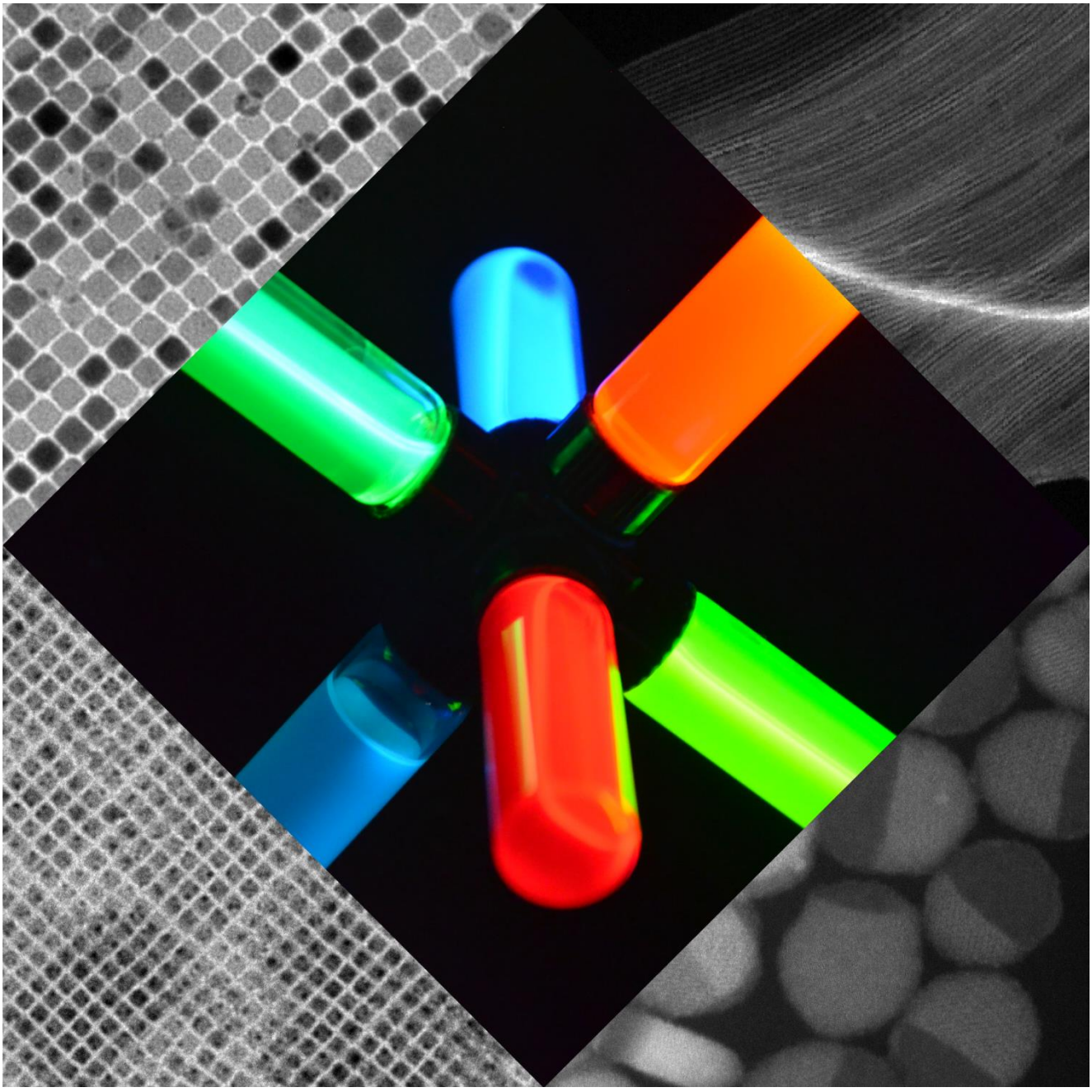

Muhammad Imran

Università degli Studi di Genova

Istituto Italiano di Tecnologia

Sciences and Technologies of Chemistry and Materials

Doctoral Curriculum: Nanochemistry

Cycle: XXX

Synthesis and Post-synthesis Transformations of Colloidal Semiconductor Nanocrystals

Doctoral dissertation presented by

Muhammad Imran

Supervisors:

Prof. Liberato Manna (Istituto Italiano di Tecnologia)

Prof. Maurizio Ferretti (Università degli Studi di Genova)

Dr. Rosaria Brescia (Istituto Italiano di Tecnologia)

Dedicated to my son Muhammad Ahmad Imran who passed away during this journey,

Acknowledgement:

I would like to start with my gratitude to Prof. Liberato manna for giving me the opportunity to work in his prestigious group. I deeply admire his tremendous support in my educational and personal affairs over the years.

I gratefully acknowledge funding from the European Union under grant agreement n. 614897 (ERC Grant TRANS-NANO).

I am thankful to my scientific advisors Prof. Liberato manna, Dr. Rosaria Brescia and Prof. Maurizio Ferretti for their constant support, patience and magnificent guidance throughout this journey. I admired the way they trust me and gave me freedom to explore on my own.

I am thankful to Dr. Francesco Di Stasio, Dr. Vincenzo Caligiuri and Palvasha Ijaz for spectroscopy related measurements. My sincere thanks to, Dr. Luca Goldoni for NMR measurements, Dr. Mirko Prato for XPS measurements, Dr. Rosaria Brescia and Dr. Zhiya Dang for HRTEM experiments, Dr. Ivan Infante and Dr. Urko Petralanda for theoretical calculations, Dr. Paolo Bianchini for confocal microscopy measurements and Simone Lauciello for HRSEM measurements.

I would like to thank all the technician of Nanochemistry and Electron Microscope facility for always being available and supportive.

I would like to thank Prof. Roman Krahne, Dr. Ivan Infante, Dr. Mirko Prato, Dr. Luca de Trizio, Dr. Ahmed L. Abdelhady, Dr. Dmitry Baranov Quinten A. Akkerman and all other group members for their productive discussions and help on various projects.

I am thankful to Prof. Adriana Saccone and Iulia Manolache Orlatan for their support in all administrative matters.

I would like to offer my sincere thanks to the referees and examination committee for their efforts and time.

I will be always thankful to my entire family especially my father Malik Khadim Hussain, mother Zuhran Bibi, daughter Minal Fatima, wife Palvasha Ijaz, mother in law Saeeda Bano, father in law M. Ijaz Khan brothers M. Irfan and M. Behram and all sisters for their endless love and support.

Muhammad Imran

Table of content

Summary:

The present PhD thesis focuses on two main classes of semiconductor colloidal nanocrystals, i.e. lead halide perovskite and copper chalcogenides. The former class of semiconductor NCs are promising materials for many high performance optoelectronics applications, as they exhibit a tunable band gap in the range of 1.4 to 2.9 eV and an efficient photoluminescence characterized by narrow emission linewidths and have been explored the most in the last years. Following the standard hot injection based synthesis and selecting a combination of short chain acid (octanoic acid or hexanoic acid) together with alkyl amines (octylamine and oleylamine) we prepared strongly fluorescent $CsPbBr_3$ perovskite nanowires with tuneable width, in the range from 20 nm (exhibiting no quantum confinement, hence emitting in the green) to 3 nm (in the strong quantum-confinement regime, emitting in the blue) for the first time. However the main limitation of the colloidal synthesis protocols that was followed in aforementioned case including the ligand assisted reprecipitation routes which is the second most frequently used method for preparation of LHPs, is that they employ PbX_2 (X= Cl, Br, or I) salts as both lead and halide precursors which consequently limit the precise tunability of the amount of reaction species such as metals or halides precursors and are not applicable to entire family of $APbX_3$ (A=FA, MA and Cs; X=Cl, Br, I). To overcome this issue we developed benzoyl halide based colloidal synthesis route i.e broadly applicable to the entire family of LHP NCs and not only ensures the independent tunability of reaction precursors but also maintain the overall integrity of the NCs such as phase purity and high PLQY. Despite the significant advances in synthesis procedures, the control over size monodispersity, shape and phase purity remains another long standing challenge. This is in fact due to the tendency of primary alkyl amine in the form of alkylammonium ions that could compete with Cs^+ ions and leads to the anisotropic growth such as NPLs or their use in excess permotes the Pb-depleted Cs_4PbX_6 phases. We develop here a strategy to achieve size, shape and phase pure $CsPbBr_3$ nanocubes by substituting primary alkyl amines with secondary alkyl amines. We attributed this excellent control over the shape and phase purity to the inability of secondary amines to find the right steric conditions at the surface of the nanocrystals which consequently limits the formation of low dimensional structures. The shape purity and narrow size distribution leads to their ease of self-assembly in superlattices reaching up to 50 microns in lateral dimensions, which are the largest dimensions reported to date for superlattices of LHP NCs. The second class of materials studied here, i.e. copper chalcogenides, are mainly attractive due to their tunable composition via post synthesis chemical transformations, plasmonic properties, low toxicity and environmental friendliness. Taking the advantage of colloidal

synthesis and using Cu_2S as a template we develop a strategy to obtain novel AuCuS-Cu_2S heterostructure through cation exchange, which cannot be realized through conventional synthesis approaches. We further investigated the stability of Cu_2S NCs with different dimensionalities and their thermal evolution subsequent to the metal decoration. Interestingly the presence of additional metallic NCs, such as Au and Pt not only improves their thermal stability but also leads to the formation of bi-metallic alloys semiconductor heterostructure.

Chapter 1

1.1 Introduction to Semiconductor NCs

The term "nanocrystal" (NC) is generally referred to a material having at least one dimension smaller than 100 nm and is composed of hundreds to thousands atoms. The quantum mechanical coupling between these atoms plays a fundamental role in the formation of band structure. The term “colloidal” NCs refers to the liquid-phase methods for synthesizing the corresponding material or to the fact that these NCs are handled in the form of stable colloidal dispersion in solvents. Historically, colloidal NCs have deep roots in the mid of 18th century when Faraday demonstrated for the first time demonstrated “colloidal sols of gold”.[1] However a major innovation in the field of NCs took place in second last decade of 20th century with the discovery of quantum-size effects in the optical spectra of nanometer sized semiconductors NCs,[2,3] often referred to as quantum dots (QDs). Briefly, these QDs are semiconducting NCs whose excitons are spatially confined in all three dimensions giving rise to the remarkable optical properties. Interestingly, the bandgap of the semiconductor strongly becomes size dependent in nanoscale regime. For instance, the profound impact of size variation on the bandgap of the semiconductor NCs is illustrated in Figure 1.[4] Basically individual atomic orbitals in materials are coupled to form molecular orbitals and accumulation of these molecular band leads to the formation of a “band”. The band formed by the coupling of Highest Occupied Molecular Orbitals (HOMO) is called valence band (VB) and the band formed by the coupling of Lowest Unoccupied Molecular Orbitals (LUMO) is called the conduction band (CB). The separation between valence band and conduction band is called Band gap (Eg). More precisely the dimensionality dependence of semiconductor band gap can be further explained by considering exciton Bohr radius, i.e a dimension illustrating the degree of spatial extension of exciton in solids. When the size of NCs approaches exciton Bohr radius the quantum confinement effect begins to decouple the molecular orbitals. Further decrease in the size of NCs, less atomic orbital would take part in the formation of the band structure and hence more discrete energy levels will appear at the edges of valance band and conduction band (see Figure 1). Consequently, the optoelectronic properties of the semiconductor NCs become strongly size and shape dependent and further making it possible to tune the photoluminescence by precisely varying the size of NCs. These features have turned colloidal semiconductor NCs as a versatile photonic source with emission broadly tunable across the entire visible spectrum. However achieving bright photoluminescence (PL) with conventional semiconductor NCs strictly depends on the electronic passivation with the layers of wide-gap semiconductors (for example CdSe/CdS and CdSe/ ZnS core−shell NCs).[5-7] In context of

these limitations a semiconducting material with the surface defects that are not detrimental to their electronic structure would be highly desired especially for light emission and photonic applications.

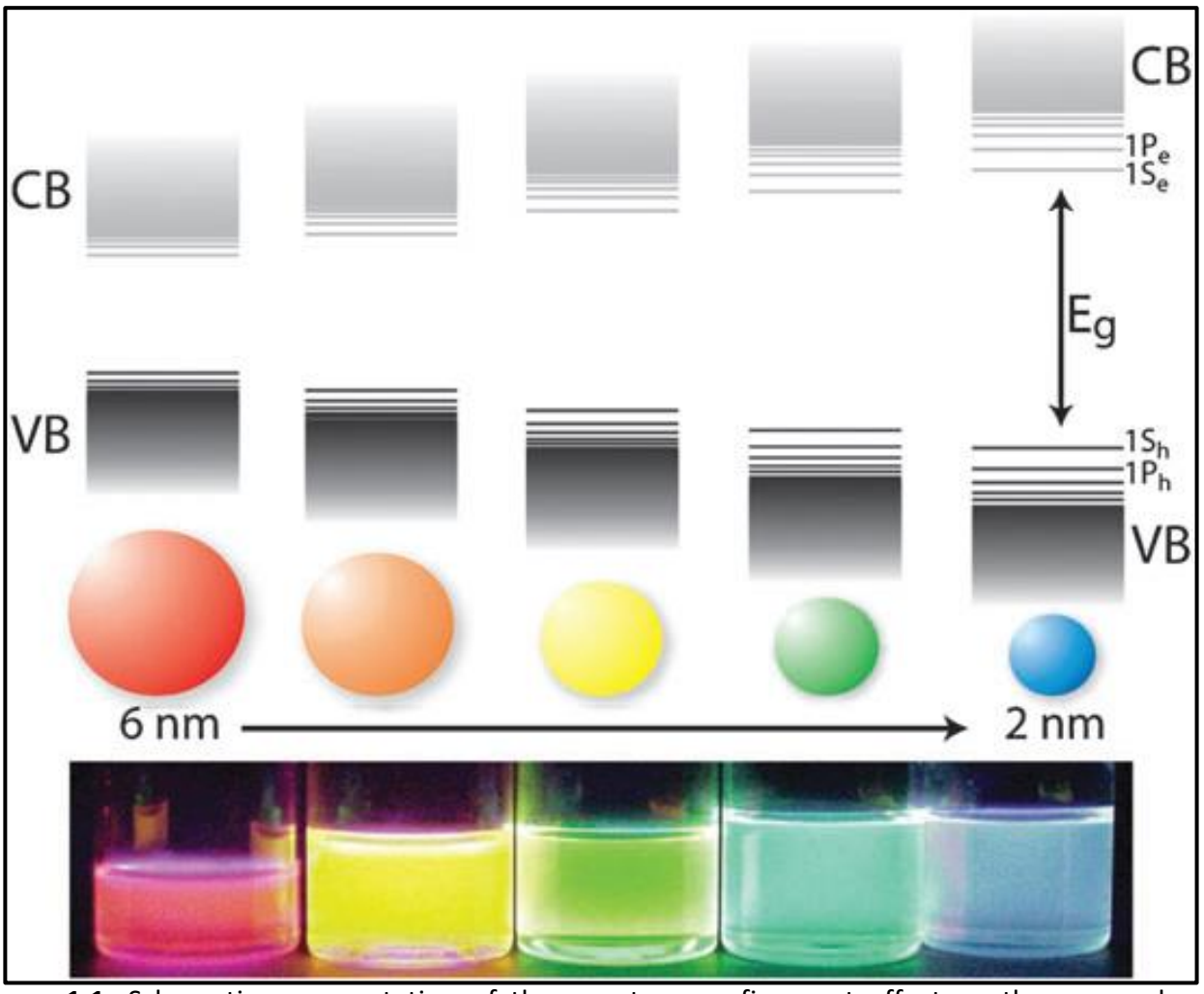

Figure 1.1: Schematic representation of the quantum confinement effect on the energy level structure of a semiconductor material. The lower panel shows colloidal suspensions of CdSe NCs of different sizes under UV excitation.

The present PhD thesis can be subdivided into two main sections, as it deals with two main classes of semiconductor colloidal nanocrystals, i.e. lead halide perovskite and copper chalcogenide NCs. The former class of NCs is one of the most studied topics in the last few years due to their excellent optical properties, defect tolerance, tunable emission line widths across entire visible spectrum and promising for many applications. The present thesis gives a contribution to the advancement of colloidal synthesis methods, size and shape control of lead halide perovskite NCs. The second class of materials studied here are copper chalcogenides NCs which are mainly attractive due to their plasmonic properties, low toxicity and environmental friendliness. Taking the advantage of colloidal synthesis which is indeed a wonderful platform to prepare the NCs with desired size, shape, crystal

structure and exploiting the post synthesis chemical/thermal transformation on copper chalcogenides NCs, we developed novel metal semiconductor heterostructures.

Section I

1.2. Lead halide Perovskite NCs

In parallel to work on classical semiconductor materials, a significant discovery of methyl ammonium lead iodide ($MAPbI_3$) as a promising PV material in 2012 has attracted the attention of scientific community and since then have been the subject of intense research.[8] This perovskite semiconductor material initially shows very modest efficiencies but surprisingly within few years it reaches a certified power conversion efficiency of more than 20% which is remarkable improvement in the history of any material in such a time frame. This unprecedented photovoltaic performance is fortunately due to the long electron–hole diffusion lengths, low recombination rates and low-temperature solution processability and on top of all these, unusual defect tolerant photophysics of these semiconductors.[9-12] LHP are generally referred to ABX_3 compound (analogous to oxide perovskites, $CaTiO_3$) where A is monovalent cation (such as methylammonium (MA, $CH_3NH_3^+$), formamidinium (FA, $CH(NH_2)_2^+$) or caesium (Cs^+)), B is divalent cation (Pb^{2+}) and X is one or more halides (Cl^- , Br^- or I^-) Figure 2.[13]

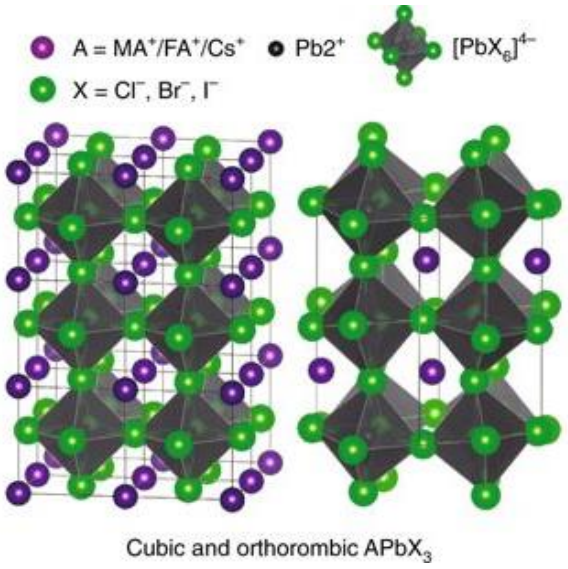

Figure 1.2: The $APbX_3$ perovskite structure with 3D-corner-sharing octahedra. Two typical structures are shown: cubic ($MAPbX_3$, $FAPbX_3$; two unit cells shown) on the left and orthorhombic (CsPbX3) on the right.

A site monovalent cation occupy the lattice corners and B site divalent cation occupy the center of the cell while the halides (Cl^-, Br^-, I^-) are arranged on the lattice faces coordinating in a BX_6 octahedra. Goldschmidt tolerance factor, *t*,[14] has been used extensively used to predict the formation of 3D-

perovskite for various A and B site cations. Stability of perovskite structures is basically assessed based on the chemical formula ABX_3 and the ionic radii, r_i, of each ion (*A*, *B*, *X*):

$$t = rA + rX/\sqrt{2(rB + rX)}.$$

In general, stable perovskite structures are formed if the tolerance factor is within the range 0.76 and 1.13 and beyond this range non-emissive orthorhombic or 2D perovskites structures are stabilized[15]. For such reason, in the case of LHP perovskites only a limited number of A site cations such as Cs, MA, and FA, can give rise to stable structures while other possible candidates are either too small (Na, K, Rb) or too large (for example guanidinium)[16]. Another factor to gauge the stability of 3D Perovskite structures is the octahedral factor μ, defined as,

$$\mu = rB/rX$$

Which describes the stability of the BX_6^{2-} octahedra, and depends on the sizes of B and X ions radii. The stability limit of μ is between 0.442 and 0.895 for 3D perovskite phase.[17] Inspired by the striking performance of lead halide perovskites (LHP) in thin films in solar cells[18-20], remarkable efforts have been devoted by various groups to develop synthetic approaches to high quality LHP NCs (e.g. $CsPbX_3$, $MAPbX_3$, $FAPbX_3$; MA = methylammonium, FA = formamidinium, and X = Cl^-, Br^-, I^-). the first solution-based colloidal approach for $MAPbBr_3$ NCs was reported by Schmidt et al. in 2014 with the photoluminescence quantum yield (PLQY) of 20%.[21] Soon after, Protesescu et al. developed colloidal synthesis tragedy to synthesize monodisperse $CsPbX_3$ NCs by the adaption of classical hot-injection method in 2015.[22] The latter work manifested three remarkable properties of LHP NCs: i) high PLQY (up to 90%), ii) narrow full width at half maximum (FWHM) of < 100 meV and iii) PL tunability across the entire visible spectral range through compositional modulations and quantum size-effects.[22] Such interesting properties have indeed attracted scientist from different fields to LHP NCs and triggered the vast exploration into these ternary metal halide compounds. Massive effort from the scientific community led to the development of serval approaches for high quality LHP NCs in terms of control over size, shape and their optical integrity and can be generally classified into top-down and bottom-up approaches. The top-down cases comprise fragmentation and structuring of macroscopic solids by mechanical or chemical means, whereas the bottom-up approaches starts with molecules and ions and proceeds via gas- or liquid-phase chemical reactions. Later approach has been proven as an efficient method to fabricate well-defined colloidal LHP NCs.[23,24] The liquid phase strategy can be further classified into serval routes as illustrated in figure 1.3. Among them the hot injection (HI) and the ligand assisted reprecipitation (LARP) methods, which are by far the most developed ones are broadly applicable to the entire family of LHP NCs.

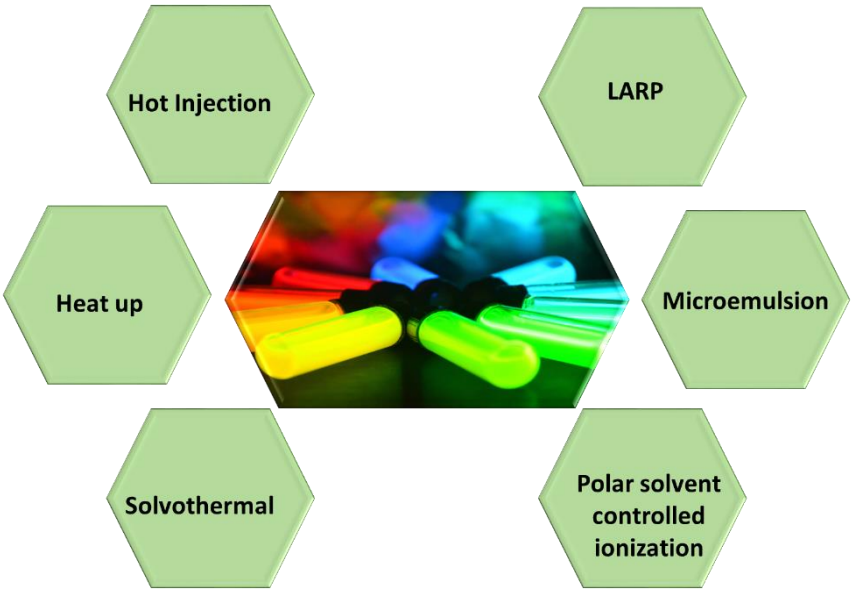

Figure 1.3. Schematic illustration of the different synthesis procedures used for colloidal synthesis of Lead halide perovskite NCs.

Briefly in case of LARP, synthesis is mostly performed at room temperature and it is based on the reprecipitation of halide salts in the presence of ligands, metal halides salts (or organic halide salts in case of hybrid materials) are solubilized in one or more polar solvents, like DMF in presence of ligands (Carboxylic acid and amines), subsequently added dropwise to a solution of a non-polar medium like toluene. The low solubility of halide salts in the new medium triggers their precipitation with the consequent recrystallization of perovskite NCs. This procedure is limited not only by the intrinsic solubility of the halide salts in polar solvents (i.e. the solubility of chorides in DMSO, common polar solvent used in this approach, but also, these solvents may be detrimental for the stability of the product halide NCs. Hot injection method would discussed in detail here onwards.

1.3. Hot Injection Method for LHP NCs

The first HI method was developed two and half decades ago for the synthesis of cadmium chalcogenide NCs[25]. This approach is based on the rapid injection of a precursor into a hot solution of the remaining precursors, ligands and a high boiling solvent."[26-28] The HI method enables, in general, the synthesis of small NCs with a narrow size distribution by attaining a separation between the nucleation and growth stages.[29] More in detail, immediately after the injection, a rapid nucleation burst takes place with the simultaneous formation of small nuclei. A rapid depletion of monomers terminates the nucleation stage, after which the nuclei continue growing (with basically no new nuclei forming), leading, over time, to the evolution of a NCs population characterized by a narrow size distribution. This is true if the reaction is stopped when the reaction is still in the in the size focusing regime, *i.e.* when there are still plenty of monomers in the growth environment.[30] Key

parameters, which allow to control the size, size-distribution and shape of colloidal NCs synthesized by the HI method are: (i) ratios of the surfactants to the precursors; (ii) the injection temperature of the cations or anions precursor; (iii) the reaction time; and (iv) the concentration of precursors. In 2015, Protesescu *et al.* extended the HI approach to the colloidal synthesis of cesium LHP NCs ($CsPbX_3$, X=Cl, Br and I)[22]. $CsPbX_3$ NCs were obtained by injecting Cs-oleate into a hot solution (140-200°C) of PbX_2 (X= Cl, Br, I) salts, which served both as the Pb^{2+} and X^- source, dissolved in octadecene (ODE), carboxylic acids and primary amines (See Figure 1.4). Equal ratios of amines and acids were observed to result in the formation of monodisperse NCs whose size could be adjusted by varying the reaction temperature. Mixed-halide perovskite NCs could also be conveniently produced by simply adjusting the ratios of lead halide salts ($PbCl_2$/$PbBr_2$ or $PbBr_2$/PbI_2). The PL emission of the resulting NCs could be finely modulated across the entire visible spectrum (410-700nm) by varying the halide composition or by tuning the size of NCs. The HI method was further extended to $MAPbX_3$ (X=Br, I) NC systems by replacing Cs-oleate with a methylamine solution.[31] $MAPbBr_3$ and $MAPbI_3$ NCs were successfully obtained by varying the relative amount of oleylamine (OLA) and oleic acid (OA) capping ligands. The HI method was further extended to the colloidal synthesis of $MAPbX_3$ (X=Br, I) by replacing Cs-oleate with a methylamine solution[31]. $MAPbBr_3$ and $MAPbI_3$ NCs were successfully obtained by varying the relative amount of surfactants (that is by varying the OAm/OA ratio).

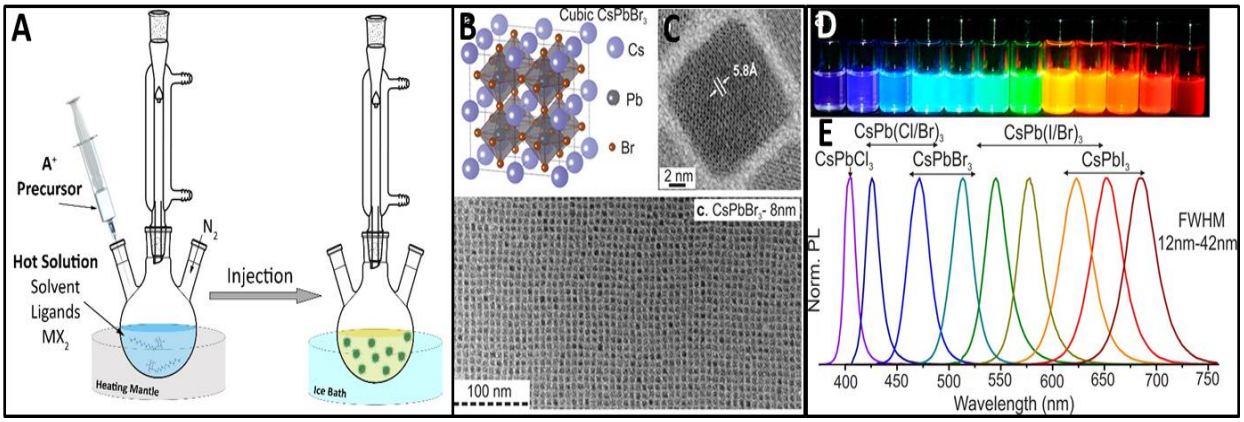

Figure 1.4. Schematic illustration of HI method A, Schematic of the cubic perovskite lattice B, TEM image of $CsPbBr_3$ NCs C. Colloidal solutions of various composition of $CsPbX_3$ NCs under UV lamp D and their PL spectra E.

In order to get insights into the growth kinetics of $CsPbX_3$ NCs produced *via* the HI approach, Lignos et al. employed a droplet-based microfluidic platform.[32,33] Following the *in-situ* absorption and photoluminescence of $CsPbX_3$ NCs, they revealed that the entire nucleation and growth took place in the first 1-5 seconds of reaction, highlighting the extremely fast reaction kinetics. Slightly different

results were reported by Koolyk *et al.* who investigated the growth kinetics of $CsPbBr_3$ and $CsPbI_3$ NCs by taking aliquots at different stages of the reaction and analyzing them by transmission electron microscopy (TEM)[34]. What they observed is that in $CsPbI_3$ NCs the size focusing regime lasted the first 20 s, followed by a subsequent size de-focusing regime. On the contrary, $CsPbBr_3$ NCs did not exhibit any size focusing regime, being characterized, from the very beginning, by broadening of the size distribution that persisted during the whole reaction time of 40s[34]. Udayabhaskararao *et al.*, later on, monitored the growth of $CsPbX_3$ NCs at different stages by electron microscopy, eventually proposing a two-step growth mechanism:[35] during the first step, Pb° NCs forms, subsequently acting as seeds onto which $CsPbX_3$ NCs nucleate. In the second stage, the growth of NCs occurs through self-assembly and oriented attachment. However, the authors did not provide any evidence of the initial formation of Pb° NCs. Also, it is now well established that the observed Pb° clusters on the surface of NCs, are formed by the electron beam irradiation.[36,37] Overall, all these studies revealed that, in contrast to classical colloidal heat-up or hot-injection techniques, used to produce II−VI (e.g., CdTe, CdSe, CdS and HgS), IV−VI (e.g., PbSe), III−V (e.g., InP and InAs) or ternary I−III−VI (e.g. $CuInS_2$) QDs, the nucleation and growth of MHPs NCs are not separable in time, most likely due to their highly ionic bonding. An important shortcoming of MHP colloidal NCs is their instability under ambient atmospheric conditions (with variable humidity, heat, and/or light) that leads to a rapid drop of their PLQY[38]. An example in this direction is represented by the work of Yuan *et al.*[39] They have shown that perovskite NCs are particularly sensitive to anti-solvents used in their cleaning. Starting from $CsPbBr_{1-x}I_x$ NCs, they found that different anti-solvents, like isopropanol, n-butanol or acetone, can change the NCs' halide composition, and, thus their overall optical properties.[39] In an effort to overcome the issue related to solvent cleaning, Woo et al. found that the stability of $CsPbX_3$ NCs can be considerably enhanced without drastic drop of PLQY by inorganic surface passivation.[40] In that work, $ZnBr_2$ was used as an extra source of Br ions in addition to $PbBr_2$ precursor. The resulting NCs had halide rich compositions (Cs:Pb:Br = 1.0:1.2:3.4) compared to the one synthesized in absence of metal bromide (Cs:Pb:Br = 1.0:1.0:2.8). This approach was considered by the authors as the first universal *in situ* stabilization of $CsPbX_3$ NCs (where X is Br or I) by inorganic passivation.[40]

One important drawback of the HI methods described so far is that they rely on the use of metal halide salts as both cation and anion precursors, limiting, thus, the possibility of working with the desired ions stoichiometry.[22,41] In order to overcome such restrictions Liu *et al.* developed the so called "three-precursor" HI approach for the synthesis of $CsPbX_3$ (X = Cl, Br, or I) NCs[42]. The novelty consisted on using NH_4X (X = Cl, Br, or I) and PbO as sources of halide and lead ions separately, instead of conventional PbX_2 (X = Cl, Br, or I) salts.[42] Also in that case, as already observed by Woo *et al.*, [40]

the $CsPbBr_3$ NCs synthesized under Br-rich conditions (that is, by employing an excess of NH_4Br) had superior optical properties and remarkable stability, as they endured the purification step.[42] Yassitepe *et al.* further extended the three precursor HI approach to synthesize OA-capped $CsPbX_3$ NCs by eliminating alkylamines from the synthesis.[43] In their approach, Cs-acetate and Pb-acetate were reacted with quaternary alkylammonium halides, such as tetraoctylammonium halides (TOA-X), which cannot form, even in the presence of protons, ammonium species. It was observed that the absence of OLA considerably speeded up the growth kinetics and $CsPbX_3$ NCs could be synthesized at lower temperature (i.e. 75°C). $CsPbBr_3$ NCs obtained by this approach exhibited PLQY up to 70%, and enhanced colloidal stability. The method however failed to produce $CsPbI_3$ NCs of similar quality and stability.[43] The three precursor HI approach was later adopted and modified by Protesescu *et al.* for the colloidal synthesis of $FAPbX_3$ NCs.[44-46] Briefly $FAPbBr_3$ NCs were prepared by reacting FA and Pb acetates with oleic acid in ODE and, subsequently, injecting oleylammonium bromide. It was further observed that the final product contained a 5-10% of $NH_4Pb_2Br_5$ byproduct that might have formed upon the thermal decomposition of FA^+ to NH^{4+} during the synthesis.[44] Phase pure $FAPbI_3$ NCs with better optical quality were uccessfully synthesized in 2017 by the two precursor HI method by reacting FA-oleate with PbI_2 complex in presence of oleic acid and oleylamine in ODE with excess FA (FA:Pb = 2.7) at 80 °C[45].

1.4. Limitation of the Conventional HI Synthesis

Although the "three precursors" HI approach overcomes the issue of two precursor HI method and allows to work with the desired stoichiometry of ions (as the halide and the metal cations sources are not linked anymore) but its potential versatility is severely limited by a series of disadvantages. First, the fact that the synthesis of $CsPbI_3$, $CsPbCl_3$, and $MAPbX_3$ (X=Br, I) NCs has not been reported using this strategy suggests a poor reactivity of the halide precursors in the reaction conditions of that approach.[44,45,47] Second major issue is phase impurity especially in case of $FAPbX_3$ NCs and is ascribed to the decomposition of the alkylammonium halide in the synthesis.[44] In order to overcome these issues a generalized synthesis approach i.e broadly applicable to the entire family of LHP NCs is inevitable which not only ensures the independent tunability of reaction precursors but also maintain the overall integrity of the NCs such as phase purity and high PL QY.

1.5. Influence of Ligands on Size and Shape of LHPs NCs

Size and shape control was demonstrated in the HI strategy mainly by varying the ligands combination, their ratios and the reaction temperature. As a general trend, it was observed that working with OLA and OA at low reaction temperatures, in the 90-130 °C range, tended to strongly favor anisotropic growth of NCs, producing quasi 2D geometries, usually referred to as

"nanoplatelets" (NPLs).[48] On the other hand, high reaction temperatures (i.e. 170-200°C) and long reaction times lead to nanowires (NWs).[49] In order to investigate the role of ligands on the morphology of $CsPbBr_3$ NCs, Pan *et al.* carried out a comprehensive study by systematically varying the chain length of alkyl amines and carboxylic acids used in the reaction.[50] In one series of experiments, while keeping fixed the amount of OLA, they employed different carboxylic acids (at 170°C). An increase in average edge length of $CsPbBr_3$ nanocubes from 9.5 to 13 nm was observed by decreasing the chain length of the carboxylic acids. Also, working with OA and lowering the reaction temperature to 140°C, NPLs with a thickness of 2.5nm and 20 nm wide were formed see figure 1.5. In a second series of experiments, while fixing the amount of oleic acid, different alkylamines were tested at 170°C: in all the experiments, the authors observed the formation of NPLs except when using OLA, which led to the formation of NPLs, although only at lower reaction temperatures (140°C).

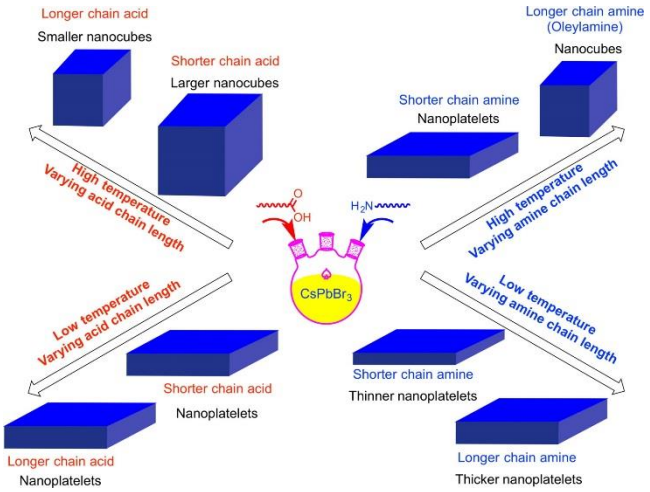

Figure 1.5. Summary of the shape and size dependence of $CsPbBr_3$ NCs on the chain length of carboxylic acids and amines. Reproduced with permission of Reference,[51] Copyright 2016 American Chemical society.

While many works have aimed to control the lateral size of lead halide based nanocubes, efforts were also made to synthesize anisotropic nanostructures, such as NPLs and NWs with control over their dimensions. Song *et al.* reported the HI synthesis of atomically thin $CsPbBr_3$ NSs with thickness of 3.3 nm and edge length of about 1 µm using dodecylamine and oleic acid and prolonging the reaction time up to 3 hours (Figure 1.6 a).[52] The same year (2016) our group reported the synthesis of $CsPbBr_3$ NSs with tunable lateral dimensions from 200 nm up to few micrometers while keeping their thickness to few unit cells.[53] This was achieved by employing short chain ligands, namely octylamine and octanoic acid, in addition to the conventional OA and OLA (Figure 1.6 b). In parallel, in another work we demonstrated the synthesis of $CsPbBr_3$ NWs with width tunable down to few unit cells via

the HI approach.[54] Green emitting $CsPbBr_3$ NWs with 10–20 nm width (hence non-confined) were prepared by employing octylamine and OLA only (no carboxylic acid was used)[55]. The width of the NWs could be decreased from 10 nm to 3.4 nm by introducing short chain carboxylic acid (octanoic acid, or hexanoic acid) (Figure 1.6 c, this work).[54] Zhang *et al.* later reported a synthesis strategy to prepare ultrathin $CsPbBr_3$ nanowires (width 2.2 ± 0.2 nm and length up to several microns). The NWs were prepared by using OLA, OA and dodecyl amine as a ligands via HI approach and stepwise purification was carried out to enhance the yield.[56]

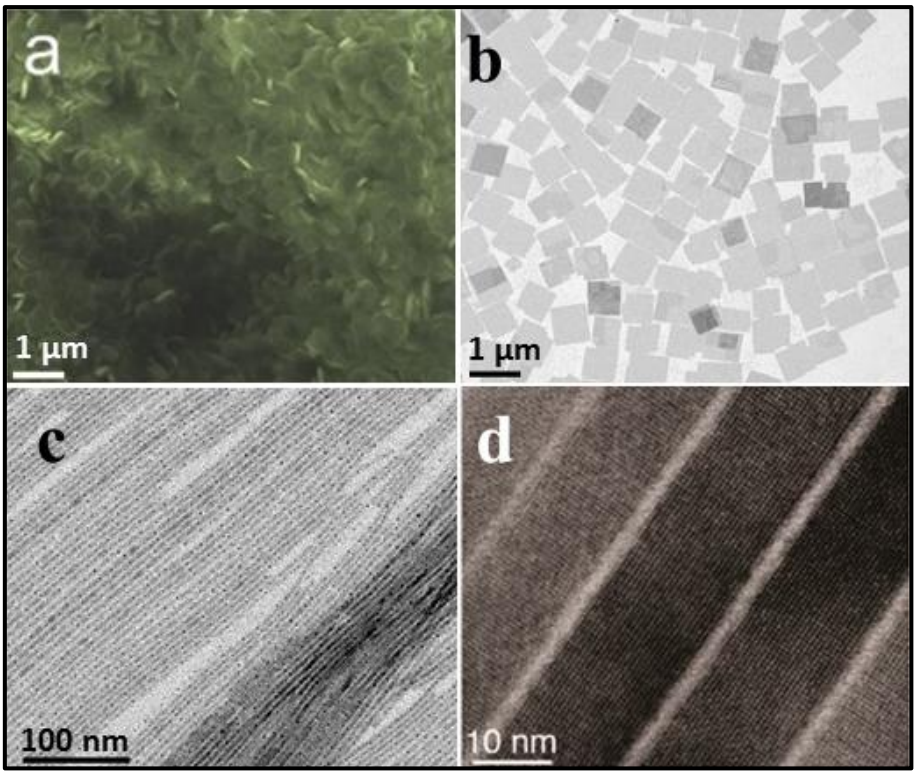

Figure 1.6. $CsPbBr_3$ NSs and NWs synthesized by colloidal Approaches**.**

To better elucidate the way alkylamines and carboxylic acids interact with each other before and during the HI synthesis, our group performed an in depth investigation on the interplay between oleylamine and oleic acid and how their relative concentration was affecting the size, size distribution and shape of $CsPbX_3$ NCs[57]. It was found that by increasing the concentration of ligands the precipitation temperature of PbX_2 could be significantly enhanced from 195 to 290°C, allowing to conduct syntheses of $CsPbX_3$ NCs at higher temperatures. It was also elucidated how the protonation of oleylamine, conducted by the oleic acid, occur in a non-polar medium. Interestingly it was revealed by NMR analysis that concentration of oleylammonium species could be increased not only by raising the concentration of oleic acid, but also by lowering the reaction temperature. The concentration of oleylammonium species was found to determine the shape of the final NCs: a high concentration of oleylammonium species favors anisotropic growth of the NCs, whereas a low concentration leads to

the formation of nanocubes. It was observed that Ostwald ripening could be suppressed by reducing the concentration of ligands (to the minimum amount needed to solubilize $PbBr_2$ at a given temperature), and, as a result, $CsPbBr_3$ nanocubes from 4.0 nm to 16.4 nm with narrow size distribution (8 to 15%) could be prepared (Figure 1.7).

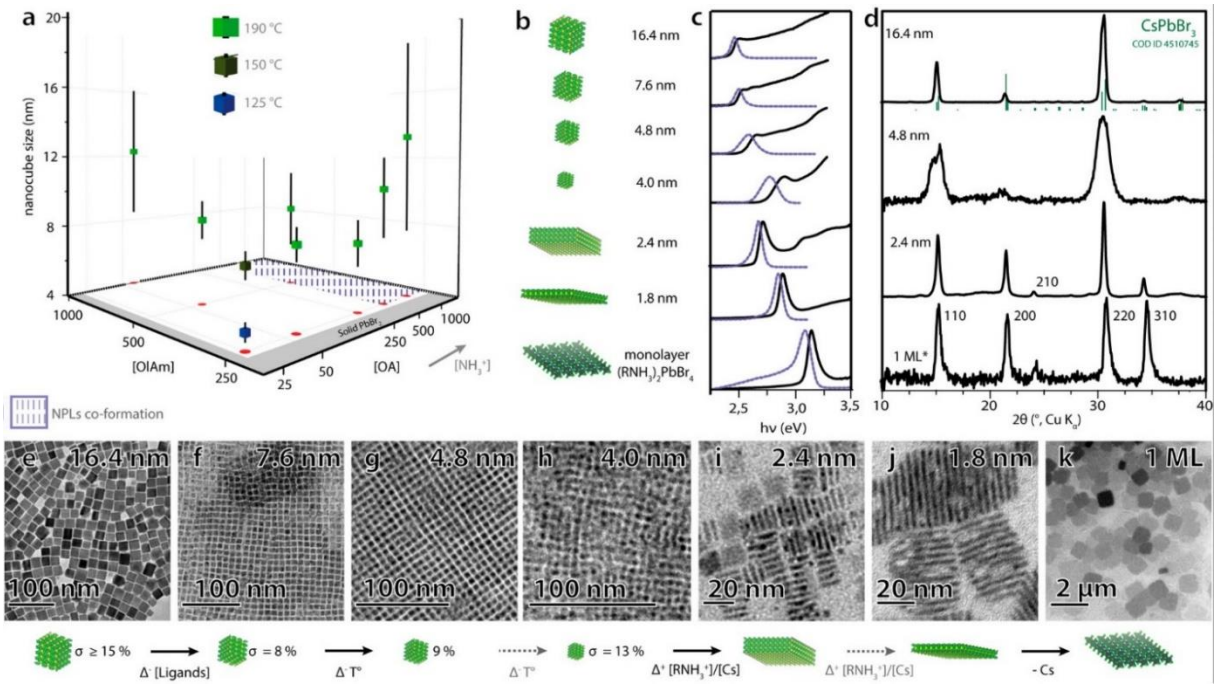

Figure 1.7. (a) Sizes of $CsPbBr_3$ nanocubes synthesized using various concentrations of oleylamine and oleic acid and different reaction temperatures (size distributions are represented as vertical bars across each symbol). (b) Image illustrating the range of monodisperse $CsPbBr_3$ nanocubes, nanoplatelets and nanosheets synthesized in this work using only oleylamine and oleic acid as ligands. (c) Absorbance (black solid line) and photoluminescence (blue dashed line) spectra, (d) XRD patterns and (e-k) TEM images of the depicted samples. Reproduced from reference[57] Copyright 2018 American chemical society.

Apart from varying the length of ligands and the amine/acid ratio, the control over the size of $CsPbBr_3$ NCs was also demonstrated employing extra halide sources such as alkylammonium bromide or $ZnBr_2$ salts.[58,59] In the first case, the size of $CsPbBr_3$ nanocubes could be finely tuned from 17.5nm to 3.8nm by varying the amount of OLA-HBr, while keeping the reaction temperature and the ligand concentration fixed.[58] In the second case, Dong et al. demonstrated a very good control over the size and size distribution of $CsPbX_3$ NCs by adjusting the reaction temperature and the ZnX_2/PbX_2 ratio in the reaction mixture.[59] Of particular interest here is that an excess of ZnX_2 was found to strongly enhance the surface passivation of the resulting NCs, leaving, eventually to high PLQY. A disadvantage of the HI method is that it is, in fact, a two-step approach as it requires, in the first step, the

preparation of the organo-metallic complex (e.g. the Cs-oleate) and, in the second step, the actual reaction. Another disadvantage is that the Cs/FA-oleate precursors are solid at room temperature, and often require a pre-heating step (up to 100 ^{0}C) prior to their injection. It is also known that this strategy is hardly up-scalable, preventing its use for a large scale production[22]. To overcome these limitations, different groups have developed alternative routes which rely on the same precursors, ligands and solvents used for the HI route, with the difference that all the chemicals are mixed together in one-pot and reacted by means of heat (heat-up or solvothermal approaches), ultrasonication or microwave irradiation. Chen *et al.* reported the solvothermal synthesis of both $CsPbX_3$ nanocubes and NWs.[60] Briefly, $CsPbX_3$ nanocubes were synthesized by directly mixing precursors (such as cesium carbonate and lead halides salts) together with ligands, and the resulting mixture was heated up in an autoclave at the desired temperature for a certain amount of time. Ultrathin $CsPbBr_3$ NWs were instead obtained when pre-dissolved precursors (such as Cs-oleate and lead halide dissolved in ODE by using OA and OLA) were used. In 2016, Tong et al. first reported a single step ultra-sonication assisted synthesis to produce $CsPbX_3$ NCs with tunable halide composition, thickness and morphology.[61] The same authors, later on, further extended such procedure, prolonging the reaction time to produce $CsPbX_3$ NWs.[62] Similarly, $CsPb(Br/I)_3$ nanorods were also prepared by adjusting the ratios of ligands (OLA/OA) and reaction temperature.[63]

1.6. Lack of Control on Shape Purity

Lead halide perovskite nanocrystals (NCs) are top contenders in the semiconductor NCs family due to their high photoluminescence quantum yield (PLQY) and composition dependent broadly tunable band gap, covering the entire visible spectrum. Significant progress has been made in the synthesis especially with regard to control over shape of $CsPbX_3$ NCs, by choosing the appropriate combination of primary amines and aprotic acids (in terms of chain length and molar ratio) and/or by adjusting the reaction temperature. This ease of shape tuneability can also be detrimental as it is not always easy to obtain homogeneous samples in terms of shape purity. For instance, the synthesis methods for nanocubes represent an emblematic case: attempts to vary their size (by reducing the reaction temperature or increasing the concentration of the acid) often lead to the contamination of the sample with NPLs. This is attributed to an increased concentration of oleylammonium species which start competing with Cs^+ ions in the addition to the surface of the growing NCs.[64,65] Shortening the hydrocarbon chain length of the primary amine also leads to the formation of NPLs, irrespective of the syntheses temperature. Finally, the use of excess amines promotes the formation of Cs-rich (Pb-depleted) phases, such as Cs_4PbX_6,[66,67] which can also be an undesired product. In short a synthesis

method which is completely in sensitive to all these reaction parameters but still produces nanocubes with no contamination of NCs with other shapes and undesired phases is highly needed.

Section II

1.7. Metal chalcogenide NCs and their post-synthesis transformations

Metal chalcogenide nanocrystals have been extensively investigated during the past three decades due to their extreme versatility.[68] Interesting development in this field was the ability to combine several materials in the same nano-object through direct synthesis or post synthesis transformation, with topological control, which has contributed to expand the functionality of NCs and the range of their applications considerably.[69] Remarkably post synthesis transformation such as the "cation exchange reaction" on preformed NCs led to several new nanomaterials especially the one which are inaccessible so far by direct chemical synthesis or by other means of fabrication[70]. This is in fact the evidence that during transformation cations sublattices of a parent nanocrystal can be partially or completely replaced by new guest cations while anion sublattices remain in place with preservation of its size, shape, and in some cases crystal structure (See figure 1.8).[71] Preservation of anion sublattice during exchange of guest and host cations is due to much larger size of the anions that lower their mobility in the lattice.

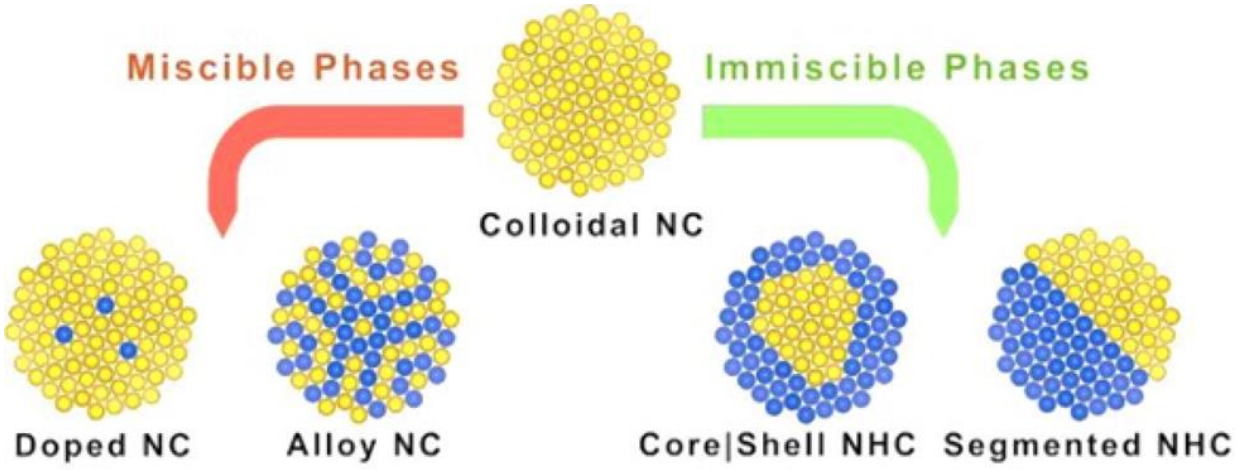

Figure 1.8. Schematic Representation of Nanostructures Accessible via Cation Exchange Transformations of a Preformed Colloidal NC. The original cations (yellow spheres) are replaced with new guest cations (blue spheres) with minimal distortion (or no distortion at all) of the anion framework. Reproduced from reference[70], Copyright 2018 American chemical society.

In particular, considerable attention has been paid to the colloidal Cu chalcogenide NCs due to the ease of synthesis with control over the size and shape.[72] In addition to this, engineering of cation-vacancy in copper chalcogenides NCs gives rise to distinct crystal phases that have similar crystal

structures but different material properties as well as the ease of guest cation diffusion into/out of the lattice. For example, low chalcocite, djurleite, and roxbyite are $Cu_{2-x}S$ phases having similar hexagonal close packing sulfur sublattices but significantly different material properties.

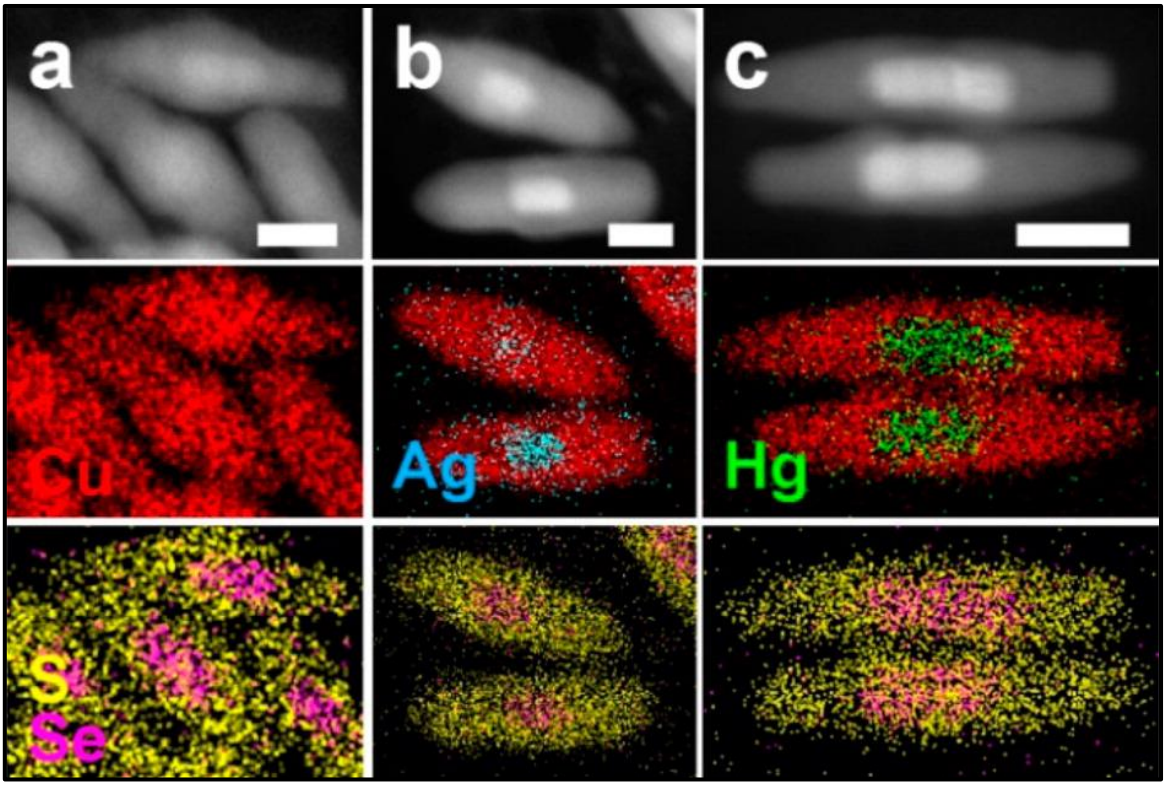

Figure 1.9. CE in $Cu_{2-x}Se/Cu_{2-x}S$ NRs with Ag^{+} and Hg^{2+} ions. HAADF-STEM images of groups of (a) pristine, (b) Ag^{+}, and (c) Hg^{2+} partially exchanged $Cu_{2-x}Se/Cu_{2-x}S$ NRs with the corresponding STEM-EDS elemental maps.

Since the material properties can significantly be affected by crystal phase and composition, post synthesis transformations (induced by thermal, chemical and electrochemical stimuli) of nanocrystals also lead to new nanomaterials with unique properties which are inaccessible by conventional synthesis methods. In this regard our group systematically investigated cation exchange reactivity in close-to-stoichiometric (that is, Cu_2Se) with that of sub-stoichiometric ($Cu_{2-x}Se$) copper selenide NCs. It was observed that cation exchange reaction in Cu_2Se NCs proceeds much slower than in the corresponding $Cu_{2-x}Se$ NCs under identical reaction.[73] Hence, it is evident from the finding of this report that Cu vacancies plays an important role in cation exchange reaction most likely by providing several alternative pathways for ions diffusion, even at low temperature. Another fascinating area in such transformation is partial replacement of the original cations and has been successfully exploited to create segmented or even striped nanostructures.[74] These transformation can even yield NC phases characterized by a crystal structure that is metastable in

the bulk or does not exist at all in their bulk counterpart.[75] For example selective cation exchange in core of $Cu_{2-x}Se/Cu_{2-x}S$ core/shell nanocrystals (reported by our group) open up a new avenue to further manipulate the entire properties of nanocrystals (Figure 1.8).[76] The peculiarity of the cation exchange reaction in later case is that the guest cation rapidly probe the whole nanocrystal and start exchanging the host cations in more energetically favorable regions. In general cation exchange reactions have emerged as a new strategy for the fabrication of more complex structures which cannot be accessed through direct synthesis routes and presence of Cu vacancies in Cu chalcogenides NCs makes them ideal template for exploring new materials.

Additionally Cu selenides and sulfides are promising materials due to their localized surface plasmon resonance (LSPR) exhibited in their Cu-deficient versions, with energy tunable with their composition and crystal structure.[77] An increasing number of studies, moreover, addressed the combination of Cu chalcogenide nanomaterials with noble metals, with the aim of tuning their optical properties.[78-82] These materials indeed allow to combine the low cost and compositional tunability of Cu chalcogenides with the intense LSPR characteristic noble metals. These materials indeed allow to combine the low cost and compositional tunability of Cu chalcogenides with the intense LSPR characteristic noble metals. Moreover, the stability of Cu chalcogenide nanocrystals in an ideal phase for attaining the desired properties is extremely important prior to their integration in device fabrication. In particular, the thermal stability in a certain range is desirable for some applications and it can simply be investigated by the study of phase transformation and stability of copper chalcogenides nanocrystals. Within the context of post synthesis transformation by using cation-exchange mediated synthesis and taking advantage of Cu chalcogenide-based nanomaterials, in this section we will focus on the search for finding new possible materials and their in depth phase stability related investigation by using advanced electron microscopy related techniques.

1.8. References

(1) Faraday, M. Philosophical Transactions of the Royal Society of London 1857, 147, 145.

(2) Brus, L. The Journal of Physical Chemistry 1986, 90, 2555.

(3) Rossetti, R.; Nakahara, S.; Brus, L. E. The Journal of Chemical Physics 1983, 79, 1086.

(4) de Mello Donegá, C. Chemical Society Reviews 2011, 40, 1512.

(5) Hines, M. A.; Guyot-Sionnest, P. The Journal of Physical Chemistry 1996, 100, 468.

(6) Cao, Y. W.; Banin, U. Angewandte Chemie International Edition 1999, 38, 3692.

(7) Mićić, O. I.; Smith, B. B.; Nozik, A. J. The Journal of Physical Chemistry B 2000, 104, 12149.

(8) Lee, M. M.; Teuscher, J.; Miyasaka, T.; Murakami, T. N.; Snaith, H. J. Science 2012, 1228604.

(9) Egger, D. A.; Rappe, A. M.; Kronik, L. Accounts of chemical research 2016, 49, 573.

(10) Li, W.; Wang, Z.; Deschler, F.; Gao, S.; Friend, R. H.; Cheetham, A. K. Nature Reviews Materials 2017, 2, 16099.

(11) Saparov, B.; Mitzi, D. B. Chemical reviews 2016, 116, 4558.

(12) Manser, J. S.; Christians, J. A.; Kamat, P. V. Chemical reviews 2016, 116, 12956.

(13) Akkerman, Q. A.; Rainò, G.; Kovalenko, M. V.; Manna, L. Nature materials 2018, 1.

(14) Manser, J. S.; Christians, J. A.; Kamat, P. V. Chemical reviews 2016, 116, 12956.

(15) Li, W.; Wang, Z.; Deschler, F.; Gao, S.; Friend, R. H.; Cheetham, A. K. Nature Reviews Materials 2017, 2, 16099.

(16) Correa-Baena, J. P.; Saliba, M.; Buonassisi, T.; Gratzel, M.; Abate, A.; Tress, W.; Hagfeldt, A. Science 2017, 358, 739.

(17) Travis, W.; Glover, E. N. K.; Bronstein, H.; Scanlon, D. O.; Palgrave, R. G. Chemical Science 2016, 7, 4548.

(18) Park, N.-G.; Grätzel, M.; Miyasaka, T.; Zhu, K.; Emery, K. Nature Energy 2016, 1, 16152.

(19) Yang, W. S.; Park, B.-W.; Jung, E. H.; Jeon, N. J.; Kim, Y. C.; Lee, D. U.; Shin, S. S.; Seo, J.; Kim, E. K.; Noh, J. H. Science 2017, 356, 1376.

(20) Etgar, L.; Gao, P.; Xue, Z.; Peng, Q.; Chandiran, A. K.; Liu, B.; Nazeeruddin, M. K.; Grätzel, M. Journal of the American Chemical Society 2012, 134, 17396.

(21) Schmidt, L. C.; Pertegas, A.; Gonzalez-Carrero, S.; Malinkiewicz, O.; Agouram, S.; Minguez Espallargas, G.; Bolink, H. J.; Galian, R. E.; Perez-Prieto, J. Journal of the American Chemical Society 2014, 136, 850.

(22) Protesescu, L.; Yakunin, S.; Bodnarchuk, M. I.; Krieg, F.; Caputo, R.; Hendon, C. H.; Yang, R. X.; Walsh, A.; Kovalenko, M. V. Nano letters 2015, 15, 3692.

(23) de Weerd, C.; Gregorkiewicz, T.; Gomez, L. Advanced Optical Materials 2018.

(24) Wang, N.; Liu, W.; Zhang, Q. Small Methods 2018, 2.

(25) Murray, C. B.; Norris, D. J.; Bawendi, M. G. Journal of the American Chemical Society 1993, 115, 8706.

(26) Yu, W. W.; Peng, X. Angewandte Chemie International Edition 2002, 41, 2368.

(27) Bullen, C. R.; Mulvaney, P. Nano letters 2004, 4, 2303.

(28) Deka, S.; Genovese, A.; Zhang, Y.; Miszta, K.; Bertoni, G.; Krahne, R.; Giannini, C.; Manna, L. Journal of the American Chemical Society 2010, 132, 8912.

(29) Li, X.; Zhang, K.; Li, J.; Chen, J.; Wu, Y.; Liu, K.; Song, J.; Zeng, H. Advanced Materials Interfaces 2018, 5, 1800010.

(30) Manna, L.; Milliron, D. J.; Meisel, A.; Scher, E. C.; Alivisatos, A. P. Nat Mater 2003, 2, 382.

(31) Vybornyi, O.; Yakunin, S.; Kovalenko, M. V. Nanoscale 2016, 8, 6278.

(32) Lignos, I.; Stavrakis, S.; Nedelcu, G.; Protesescu, L.; deMello, A. J.; Kovalenko, M. V. Nano letters 2016, 16, 1869.

(33) Maceiczyk, R. M.; Dümbgen, K.; Lignos, I.; Protesescu, L.; Kovalenko, M. V.; deMello, A. J. Chemistry of Materials 2017, 29, 8433.

(34) Koolyk, M.; Amgar, D.; Aharon, S.; Etgar, L. Nanoscale 2016, 8, 6403.

(35) Udayabhaskararao, T.; Kazes, M.; Houben, L.; Lin, H.; Oron, D. Chemistry of Materials 2017, 29, 1302.

(36) Dang, Z.; Shamsi, J.; Palazon, F.; Imran, M.; Akkerman, Q. A.; Park, S.; Bertoni, G.; Prato, M.; Brescia, R.; Manna, L. ACS nano 2017, 11, 2124.

(37) Dang, Z.; Shamsi, J.; Akkerman, Q. A.; Imran, M.; Bertoni, G.; Brescia, R.; Manna, L. ACS Omega 2017, 2, 5660.

(38) Li, X.; Cao, F.; Yu, D.; Chen, J.; Sun, Z.; Shen, Y.; Zhu, Y.; Wang, L.; Wei, Y.; Wu, Y.; Zeng, H. Small 2017, 13.

(39) Yuan, L.; Patterson, R.; Wen, X.; Zhang, Z.; Conibeer, G.; Huang, S. Journal of colloid and interface science 2017, 504, 586.

(40) Woo, J. Y.; Kim, Y.; Bae, J.; Kim, T. G.; Kim, J. W.; Lee, D. C.; Jeong, S. Chemistry of Materials 2017, 29, 7088.

(41) Su, Y.; Chen, X.; Ji, W.; Zeng, Q.; Ren, Z.; Su, Z.; Liu, L. ACS applied materials & interfaces 2017, 9, 33020.

(42) Liu, P.; Chen, W.; Wang, W.; Xu, B.; Wu, D.; Hao, J.; Cao, W.; Fang, F.; Li, Y.; Zeng, Y.; Pan, R.; Chen, S.; Cao, W.; Sun, X. W.; Wang, K. Chemistry of Materials 2017, 29, 5168.

(43) Yassitepe, E.; Yang, Z.; Voznyy, O.; Kim, Y.; Walters, G.; Castañeda, J. A.; Kanjanaboos, P.; Yuan, M.; Gong, X.; Fan, F.; Pan, J.; Hoogland, S.; Comin, R.; Bakr, O. M.; Padilha, L. A.; Nogueira, A. F.; Sargent, E. H. Advanced Functional Materials 2016, 26, 8757.

(44) Protesescu, L.; Yakunin, S.; Bodnarchuk, M. I.; Bertolotti, F.; Masciocchi, N.; Guagliardi, A.; Kovalenko, M. V. Journal of the American Chemical Society 2016, 138, 14202.

(45) Protesescu, L.; Yakunin, S.; Kumar, S.; Bar, J.; Bertolotti, F.; Masciocchi, N.; Guagliardi, A.; Grotevent, M.; Shorubalko, I.; Bodnarchuk, M. I.; Shih, C. J.; Kovalenko, M. V. ACS nano 2017, 11, 3119.

(46) Lignos, I.; Protesescu, L.; Emiroglu, D. B.; Maceiczyk, R.; Schneider, S.; Kovalenko, M. V.; deMello, A. J. Nano letters 2018, 18, 1246.

(47) Li, Q.; Li, H.; Shen, H.; Wang, F.; Zhao, F.; Li, F.; Zhang, X.; Li, D.; Jin, X.; Sun, W. ACS Photonics 2017, 4, 2504.

(48) Bekenstein, Y.; Koscher, B. A.; Eaton, S. W.; Yang, P.; Alivisatos, A. P. Journal of the American Chemical Society 2015, 137, 16008.

(49) Zhang, D.; Eaton, S. W.; Yu, Y.; Dou, L.; Yang, P. Journal of the American Chemical Society 2015, 137, 9230.

(50) Pan, A.; He, B.; Fan, X.; Liu, Z.; Urban, J. J.; Alivisatos, A. P.; He, L.; Liu, Y. ACS nano 2016, 10, 7943.

(51) Pan, A.; He, B.; Fan, X.; Liu, Z.; Urban, J. J.; Alivisatos, A. P.; He, L.; Liu, Y. ACS nano 2016, 10, 7943.

(52) Song, J.; Xu, L.; Li, J.; Xue, J.; Dong, Y.; Li, X.; Zeng, H. Advanced materials 2016, 28, 4861.

(53) Shamsi, J.; Dang, Z.; Bianchini, P.; Canale, C.; Stasio, F. D.; Brescia, R.; Prato, M.; Manna, L. Journal of the American Chemical Society 2016, 138, 7240.

(54) Imran, M.; Di Stasio, F.; Dang, Z.; Canale, C.; Khan, A. H.; Shamsi, J.; Brescia, R.; Prato, M.; Manna, L. Chemistry of materials : a publication of the American Chemical Society 2016, 28, 6450.

(55) Zhang, D.; Yang, Y.; Bekenstein, Y.; Yu, Y.; Gibson, N. A.; Wong, A. B.; Eaton, S. W.; Kornienko, N.; Kong, Q.; Lai, M.; Alivisatos, A. P.; Leone, S. R.; Yang, P. Journal of the American Chemical Society 2016, 138, 7236.

(56) Zhang, D.; Yu, Y.; Bekenstein, Y.; Wong, A. B.; Alivisatos, A. P.; Yang, P. Journal of the American Chemical Society 2016, 138, 13155.

(57) Almeida, G.; Goldoni, L.; Akkerman, Q.; Dang, Z.; Khan, A. H.; Marras, S.; Moreels, I.; Manna, L. ACS nano 2018, 12, 1704.

(58) Dutta, A.; Dutta, S. K.; Das Adhikari, S.; Pradhan, N. Acs Energy Letters 2018, 3, 329.

(59) Dong, Y.; Qiao, T.; Kim, D.; Parobek, D.; Rossi, D.; Son, D. H. Nano letters 2018.

(60) Chen, M.; Zou, Y.; Wu, L.; Pan, Q.; Yang, D.; Hu, H.; Tan, Y.; Zhong, Q.; Xu, Y.; Liu, H.; Sun, B.; Zhang, Q. Advanced Functional Materials 2017, 27, 1701121.

(61) Tong, Y.; Bladt, E.; Ayguler, M. F.; Manzi, A.; Milowska, K. Z.; Hintermayr, V. A.; Docampo, P.; Bals, S.; Urban, A. S.; Polavarapu, L.; Feldmann, J. Angewandte Chemie 2016, 55, 13887.

(62) Tong, Y.; Bohn, B. J.; Bladt, E.; Wang, K.; Muller-Buschbaum, P.; Bals, S.; Urban, A. S.; Polavarapu, L.; Feldmann, J. Angewandte Chemie 2017, 56, 13887.

(63) Tang, X.; Zu, Z.; Shao, H.; Hu, W.; Zhou, M.; Deng, M.; Chen, W.; Zang, Z.; Zhu, T.; Xue, J. Nanoscale 2016, 8, 15158.

(64) Ravi, V. K.; Santra, P. K.; Joshi, N.; Chugh, J.; Singh, S. K.; Rensmo, H.; Ghosh, P.; Nag, A. The journal of physical chemistry letters 2017, 8, 4988.

(65) Almeida, G.; Goldoni, L.; Akkerman, Q.; Dang, Z.; Khan, A. H.; Marras, S.; Moreels, I.; Manna, L. ACS nano 2018, 12, 1704.

(66) Akkerman, Q. A.; Park, S.; Radicchi, E.; Nunzi, F.; Mosconi, E.; De Angelis, F.; Brescia, R.; Rastogi, P.; Prato, M.; Manna, L. Nano Lett 2017, 17, 1924.

(67) Saidaminov, M. I.; Almutlaq, J.; Sarmah, S.; Dursun, I.; Zhumekenov, A. A.; Begum, R.; Pan, J.; Cho, N.; Mohammed, O. F.; Bakr, O. M. ACS Energy Letters 2016, 1, 840.

(68) Talapin, D. V.; Lee, J. S.; Kovalenko, M. V.; Shevchenko, E. V. Chem. Rev. 2010, 110, 389.

(69) Carbone, L.; Cozzoli, P. D. Nano Today 2010, 5, 449.

(70) De Trizio, L.; Manna, L. Chemical reviews 2016, 116, 10852.

(71) Jain, P. K.; Amirav, L.; Aloni, S.; Alivisatos, A. P. J. Am. Chem. Soc. 2010, 132, 9997.

(72) Coughlan, C.; Ibanez, M.; Dobrozhan, O.; Singh, A.; Cabot, A.; Ryan, K. M. Chemical reviews 2017, 117, 5865.

(73) Lesnyak, V.; Brescia, R.; Messina, G. C.; Manna, L. Journal of the American Chemical Society 2015, 137, 9315.

(74) Robinson, R. D.; Sadtler, B.; Demchenko, D. O.; Erdonmez, C. K.; Wang, L.-W.; Alivisatos, A. P. Science 2007, 317, 355.

(75) Li, H. B.; Zanella, M.; Genovese, A.; Povia, M.; Falqui, A.; Giannini, C.; Manna, L. Nano Lett. 2011, 11, 4964.

(76) Miszta, K.; Gariano, G.; Brescia, R.; Marras, S.; De Donato, F.; Ghosh, S.; De Trizio, L.; Manna, L. Journal of the American Chemical Society 2015, 137, 12195.

(77) Liu, Y.; Liu, M.; Swihart, M. T. The Journal of Physical Chemistry C 2017, 121, 13435.

(78) Deng, X.; Li, K.; Cai, X.; Liu, B.; Wei, Y.; Deng, K.; Xie, Z.; Wu, Z.; Ma, P. a.; Hou, Z.; Cheng, Z.; Lin, J. Advanced Materials 2017, 29, 1701266.

(79) Hu, C.; Chen, W.; Xie, Y.; Verma, S. K.; Destro, P.; Zhan, G.; Chen, X.; Zhao, X.; Schuck, P. J.; Kriegel, I.; Manna, L. Nanoscale 2018, 10, 2781.

(80) Wang, X.; Liu, X.; Zhu, D.; Swihart, M. T. Nanoscale 2014, 6, 8852.

(81) Wolf, A.; Kodanek, T.; Dorfs, D. Nanoscale 2015, 7, 19519.

(82) Dalmases, M.; Ibáñez, M.; Torruella, P.; Fernàndez-Altable, V.; López-Conesa, L.; Cadavid, D.; Piveteau, L.; Nachtegaal, M.; Llorca, J.; Ruiz-González, M. L.; Estradé, S.; Peiró, F.; Kovalenko, M. V.; Cabot, A.; Figuerola, A. Chemistry of Materials 2016, 28, 7017.

(83) Wu, P. S. C.; Otting, G. Journal of Magnetic Resonance 2005, 176, 115.

(84) Wagner, R.; Berger, S. Journal of Magnetic Resonance, Series A 1996, 123, 119.

(85) Boyer, R. D.; Johnson, R.; Krishnamurthy, K. Journal of Magnetic Resonance 2003, 165, 253.

(86) Schneider, C. A.; Rasband, W. S.; Eliceiri, K. W. Nature methods 2012, 9, 671.

Chapter 2. Methods and Techniques

All the characterization tool used to investigate the materials reported in the thesis are listed here.

2.1. X-ray diffraction (XRD) characterization

The XRD analysis was performed on a PANanalytical Empyrean X-ray diffractometer, equipped with a 1.8 kW Cu Kα ceramic X-ray detector, operating at 45 kV and 40 mA. Samples for the measurements were prepared by drop casting concentrated solution of NCs on zero diffraction silicon substrate. All the diffraction patterns reported here were collected at room temperature under ambient conditions using parallel beam geometry and symmetric reflection mode. Post-acquisition XRD data analysis was carried out by using the HighScore 4.1 software from PANalytical.

2.2. Transmission Electron Microscopy (TEM) characterization

The samples were prepared by dropping dilute solutions of NCs onto carbon coated copper grids. Low-resolution bright-field TEM (BF-TEM analyses were performed on a JEOL JEM-1011 TEM (thermionic source: W filament) operating at an acceleration voltage of 100 kV.

High-resolution (HRTEM), selected area electron diffraction (SAED) and high-angle annular dark field-scanning TEM (HAADF-STEM) analyses were performed on a JEOL JEM-2200FS microscope equipped with a Schottky emitter operated at 200 kV, a CEOS spherical aberration (Cs) corrector for the objective lens, and an in-column energy filter (Omega-type). If not otherwise specified, HRTEM images and SAED patterns were acquired using a conventional CCD camera (Gatan, Ultrascan 894 US1000).

2.3. High resolution scanning electron microscopy (HRSEM) characterization

High-resolution SEM imaging was carried out using a JEOL JSM 7500FA (Jeol, Tokyo, Japan) equipped with a cold field emission gun (FEG), operating at 5 kV acceleration voltage. The electrons used for imaging are backscattered electrons.

2.4. Atomic force microscopy (AFM)

Atomic force microscopy (AFM) was employed to obtain a detailed three-dimensional representation of the NW topography. AFM images were acquired with a Nanowizard III AFM setup (JPK Instruments, Germany), working in tapping mode in ambient conditions. Single beam silicon cantilevers (NCHV, Bruker, USA) with a nominal spring constant of 42 N/m and resonance frequency of 320 kHz were used. The typical radius of curvature of the tip was 10 nm. 3 µl aliquots of solution

containing NWs were spread on freshly cleaved graphite substrates and subsequently dried under a mild nitrogen flow.

2.5. UV-VIS absorption and PL measurements

The UV-Visible absorption spectra were recorded using a Varian Cary 300 UV-VIS absorption spectrophotometer. The PL spectra were measured on a Varian Cary Eclipse spectrophotometer using an excitation wavelength (λ_{ex}) of 350nm for all the chloride and the bromide samples, and 450nm for all the iodide compounds. Samples were prepared by diluting NC solutions in toluene, in quartz cuvettes with a path length of 1 cm.

2.6. PL Quantum Yields and time-resolved PL measurements

The samples were measured with an Edinburgh FLS900 fluorescence spectrometer equipped with a Xenon lamp, a monochromator for steady-state PL excitation, and a time-correlated single photon counting unit coupled with a pulsed laser diode (λ_{ex} = 375 & 405 nm, pulse width = 50 ps) for time-resolved PL. The PLQY was measured using a calibrated integrating sphere (λ_{ex} = 350nm for all the chloride and the bromide samples, and λ_{ex} = 450nm for all the iodide samples). All solutions were diluted to an optical density of 0.1 or lower (at the corresponding excitation wavelength) in order to minimize the re-absorbance of the fluorophore.

2.7. Amplified Spontaneous Emission (ASE) measurements

All the $APbBr_3$ ($A=Cs^+$, MA^+, or FA^+) NC samples that were used for ASE dynamics were cleaned twice by precipitation using ethyl acetate (the volume ratio of toluene to ethyl acetate was 5:1) and re-dispersion in toluene. Eventually, thick NC films were produced on glass substrates by drop-casting the colloidal solutions. The NC films were optically excited by a pulsed laser source at λ = 405nm, with a pulse width of 50fs, and a repetition rate of 1kHz at normal incidence. The pump beam was focused on the sample by a cylindrical lens, producing an excitation stripe of about 0.6cm in length. The emission spectra were recorded using a collection lens and a fiber coupled Ocean Optics HR4000 spectrometer at an angle close to 90° with respect to that of the excitation beam.

2.8. X-ray Photoelectron Spectroscopy (XPS) characterization

Measurements were performed on a Kratos Axix Ultra DLD spectrometer, using a monochromatic Al Kα source (15kV, 20mA). The photoelectrons were detected at a take-off angle of φ = 0° with respect to the surface normal. The pressure in the analysis chamber was maintained below 7×10^{-9} Torr for data acquisition. The data was converted to VAMAS format and processed using CasaXPS software, version 2.3.17. The binding energy (BE) scale was internally referenced to C1s peak (BE for C-C = 284.8 eV).

2.9. Nuclear magnetic resonance experimental details

All NMR spectra were acquired on a Bruker Avance III 400 MHz spectrometer, equipped with a Broad Band Inverse probe (BBI) at 300K. In the *quantitative* ^{1}H-NMR (*q*-NMR) experiment, after the ^{1}H 90° pulse was optimized, by an automatic pulse calculation routine,[1] 16 transients were acquired, using 64k data points, 30s of inter-pulses delay and no steady state scans, over a spectral width of 20.55 ppm (offset at 6.175 ppm), at a fixed receiver gain (64). ^{1}H-NMR spectra for the titration curves were performed using identical acquisition parameters except the receiver gain (1). *2D ^{1}H-^{1}H NOESY (Nuclear Overhauser Effect SpectroscopY)* experiment (*noesygpphpp*, Bruker library)[2] was performed using a mixing time of 300 ms, with 32 transients, 2048 data points and 256 increments. 2D ^{1}H-^{13}C HSQC (multiplicity edited Heteronuclear Single Quantum Coherence, hsqcedetgpsp.3, Bruker library)[3] spectrum was acquired using 12 transients, 2048 data points and 400 increments, with an automatic spectral width and transmitter frequency offset optimization for ^{1}H. A line broadening of 0.3 Hz was applied to FIDs (Free Induction Decay) before Fourier Transform. The NMR chemicals shifts were referenced to the peak of residual non-deuterated toluene at 7.09 ppm (^{1}H) and 129.2 ppm (^{13}C).

2.10. Confocal photoluminescence microscopy of superlattices

The photoluminescence imaging of $CsPbBr_3$ NC superlattices grown on Si wafer was performed using a Nikon confocal microscope system A1-plus-s [Nikon Instruments, Yokohama, Japan; equipped with the A1-DUS Spectral Detector Unit that allows the parallel acquisition of 32 channel spectral image at a maximum wavelength resolution of 2.5nm]. Depending on the level of details desired, we used a 10X air (Nikon CFI Plan Apo Lambda 10x 0.45NA) and a 60x oil (Nikon CFI Plan Apo Lambda 60X Oil 1.4NA) objective lens, the selected excitation wavelength was 488 nm. The spectrally-resolved images were recorded with the emission detection bandwidth of 2.5 nm over 498-578 nm wavelength range. The resulting stacks (32 spectral slices per stack) were processed using open source Fiji distribution of ImageJ ver. 1.52e.[4] The spectral profiles of individual superlattices were obtained by drawing polygonal regions of interest (ROIs) around selected superlattices and performing "Plot Z-stack Profile" operation in Fiji, that yields a plot of the brightness of ROI (mean grey value, proportional to the number of emitted photons) as a function of the slice number (emission wavelength bin with the width of the spectral resolution). The overall spectrum-colored images shown below were obtained by using "Temporal Color Code" hyperstacks function in Fiji with LUT setting "Spectrum."

2.11. References

(1) Wu, P. S. C.; Otting, G. *Journal of Magnetic Resonance* **2005**, *176*, 115.

(2) Wagner, R.; Berger, S. *Journal of Magnetic Resonance, Series A* **1996**, *123*, 119.

(3) Boyer, R. D.; Johnson, R.; Krishnamurthy, K. *Journal of Magnetic Resonance* **2003**, *165*, 253.

(4) Schneider, C. A.; Rasband, W. S.; Eliceiri, K. W. *Nature methods* **2012**, *9*, 671.

Chapter 3. Colloidal Synthesis of Strongly Fluorescent $CsPbBr_3$ Nanowires with Width Tunable down to the Quantum-Confined Regime

ABSTRACT: We report here the colloidal synthesis of strongly fluorescent $CsPbBr_3$ perovskite nanowires (NWs) with tuneable size, in the range from 20 nm (exhibiting no quantum confinement, hence emitting in the green) to 3 nm (in the strong quantum-confinement regime, emitting in the blue), by introducing in the synthesis a short acid (octanoic acid or hexanoic acid) together with alkyl amines (octylamine and oleylamine). A relatively low reaction temperature promoted the formation of monodisperse, few unit cell thick NWs that were free from byproducts. The photoluminescence quantum yield of the NWs samples went from 12% for non-confined NWs emitting at 524 nm to a maximum of 77% for the 5 nm diameter NWs emitting at 497 nm, down to 30% for the thinnest NWs (diameter ~ 3nm), in the latter sample most likely due to aggregation occurring in solution.

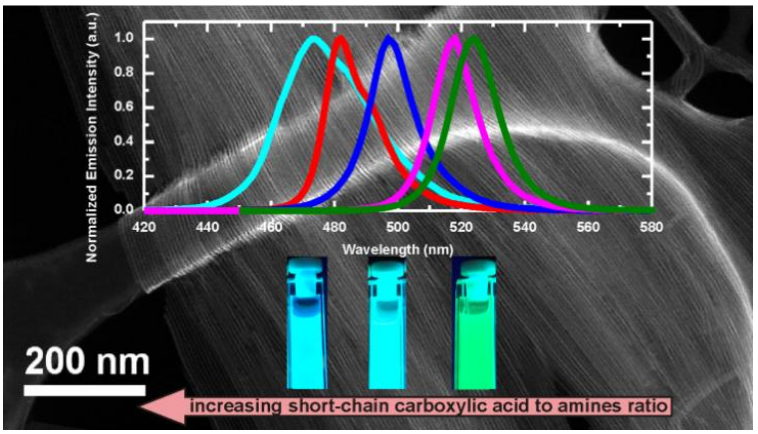

Most of the results dicussed in this chapter have been published in "Imran M, et al. Colloidal synthesis of strongly fluorescent $CsPbBr_3$ nanowires with width tunable down to the quantum confinement regime. *Chemistry of Materials*. 2016, *28* (18), 6450–6454."

3.1. Introduction

Anisotropic growth of the nanostructures are of both fundamental and technological interest. It is generally believed that nanostructures with a well-defined morphology could serve as an ideal platform for the investigation of fundamental properties and the development of future applications in nanoscale devices. In particular one dimensional nanostructures (1-D) have continuously drawn significant research attention due to their unique capability to combine the few unit cell thin radial dimension with the micron scale lengths. The combination of the confinement effect in nanoscaled dimensions along with bulk like properties in another dimension that makes them ideal candidate to investigate the dimensionality dependent structural properties. Semiconductor nanowires[1] (NWs) have received considerable attention as potential candidates in a wide variety of applications, such as in optoelectronics,[2,3,4] photovoltaics,[5] thermoelectrics,[6] and sensing.[7] Several studies have also addressed the fabrication of strongly quantum confined NWs, for example made of SnO_2[8] or cadmium chalcogenides.[9] A major issue of NWs that are only few unit cells thick is that they suffer from low photoluminescence quantum yield (PLQY), most likely due to their high surface-to-volume ratio leading to a high density of surface traps. In some cases, the PLQY could be increased by growing a shell around the NW core, as for traditional quantum dots.[10] The rapid emergence of lead halide perovskites as promising materials in photovoltaics and optoelectronics[11,12] has recently placed NWs under the spotlight again. For example, NWs based on methyl ammonium lead halide perovskites ($CH_3NH_3PbX_3$), prepared by a surface-initiated solution growth,[13] were reported to have low lasing thresholds accompanied by high quality factors, PLQYs close to 100% and broad tunability through the whole visible range. Similar results have been obtained also with fully inorganic $CsPbX_3$ NWs.[14] Colloidal approaches have been proposed for both hybrid[15] and fully inorganic[16,17] perovskite NWs. For hybrid lead halide perovskites, $CH_3NH_3PbBr_3$ NWs could be grown up to 900 nm in length and their width could be tuned by varying the reaction time, such that blue emitting NWs (hence strongly confined) were formed at short reaction times, and green emitting ones (not-confined) at longer times. Fully inorganic Cs-based perovskites are less susceptible to hydrolysis from moisture than their hybrid counterparts,[18] and therefore are preferable for applications. However, protocols developed to date could deliver wires of up to 5 microns length, but not with width in the strong quantum confinement regime.

3.2. Experimental details

Materials: Lead(II) bromide ($PbBr_2$, 99.999% trace metals basis), cesium carbonate (Cs_2CO_3, reagentPlus, 99%), 1-octadecene (ODE, technical grade, 90%), oleylamine (OlAm, 70%), oleic acid (OlAc, 90%), Hexanoic acid (HexAc, ≥99.5%), Octanoic acid (OctAc, 99%), Octylamine (OctAm 99,5%),

Toluene (anhydrous), Hexane (anhydrous, 95%) were purchased from Sigma-Aldrich. All chemicals were used without any further purification.

Preparation of Cesium-oleate solution: The Cs-oleate solution was prepared following the approach developed by Protesescu *et al*[1]. Briefly, 0.4 g Cs_2CO_3 and 1.2 mL OA were loaded into a 3-neck flask along with 15 mL ODE, degassed and dried under vacuum at 120 °C for 60min, and then heated under N_2 to 150 °C until all Cs_2CO_3 reacted with OA.

Synthesis of $CsPbBr_3$ NWs with widths of 10 nm or above. In order to grow NWs with widths of 10 nm and above, the following procedure was followed: 8 mL ODE, 0.069g $PbBr_2$, and proper amounts of OlAm and OctAm (see table S1 for details) were loaded into a 25 mL 3-neck flask and dried under vacuum for 45 minutes at 95ºC, leading to a *cloudy* solution. *Note that in these syntheses no short chain acid was added*. Subsequently, the temperature was raised to 120ºC under N_2. After 10 min at 120 °C, 0.6mL of Cs-oleate solution (prepared as described above) were swiftly injected in the flask. The NWs were then allowed to grow for 50 minutes at 120 °C, after which the reaction mixture was slowly cooled down to room temperature using a water bath. The NWs were isolated by centrifugation at 3000 rpm for 10 mins and re-dispersed in hexane/toluene for further use. A sketch of the temperature ramp for the 10 nm width NW synthesis is reported in Figure 1 A.

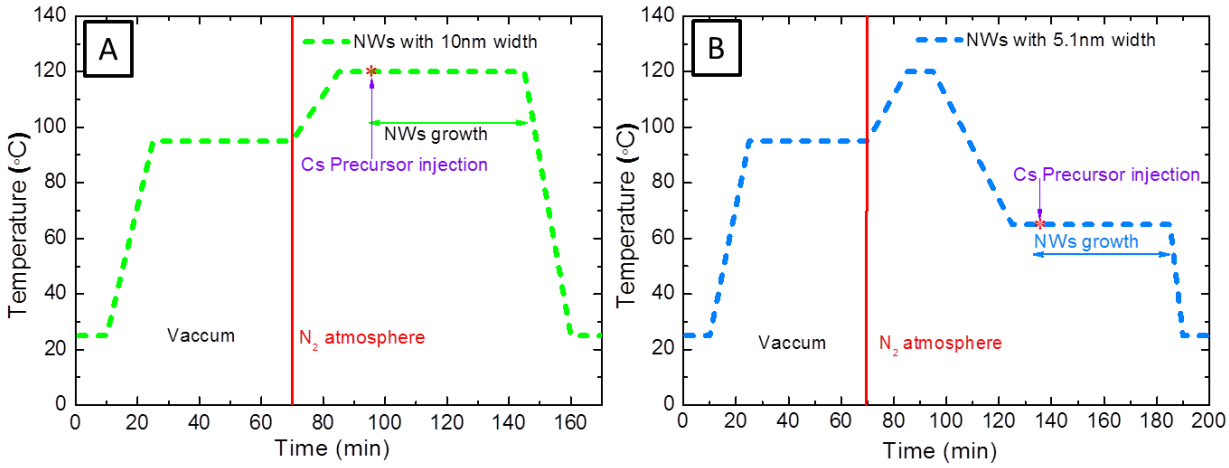

Figure 1. Examples of temperature ramps for the syntheses of NWs with (a) 10 nm width, and (b) 5.1 nm width. Reaction conditions for (a) and (b) were: 0.069g $PbBr_2$, 8mL ODE, 500µL OctAm, 500µL OlAm, with an additional 50 µL of HexAc in (B).

NWs with widths below 10 nm. In order to grow NWs with widths below 10 nm, the following procedure was followed: 8 mL ODE, 0.069g $PbBr_2$, 500 µL OlAm, 500 µL OctAm and a proper volume of a hexanoic acid (see table S1 for details) were loaded into a 25 mL 3-neck flask and dried under vacuum for 45 minutes at 95ºC, leading to a *clear* solution. Subsequently, the temperature was

increased to 120ºC under N_2 and kept at 120°C for 10 mins. The temperature was then lowered to 65ºC and 0.6mL of Cs-oleate solution (prepared as described above) were swiftly injected in the flask. The NWs were then allowed to grow for 50 minutes at 65 °C, after which the reaction mixture was slowly cooled down to room temperature using a water bath. The NWs were isolated by centrifugation at 3000 rpm for 10 mins and re-dispersed in hexane/toluene for further use. A sketch of the temperature ramp for the 5.1 nm width NW synthesis is reported in Figure 1B.

Table 1: Synthetic conditions for the various $CsPbBr_3$ NWs. All syntheses had in common the following parameters: ODE: 8mL; $PbBr_2$: 0.069g; Cs-oleate: 0.6ml; Reaction time: 50min.

NWs width (nm)	OlAm (µl)	OctAm (µl)	HexAc (µl)	Reaction Temp (°C)
20	1000	100	0	120
10	500	500	0	120
5.1	500	500	50	65
4.4	500	500	100	65
3.4	500	500	150	65
2.8	500	500	250	65

3.3. Results and discussion

Here, we report a colloidal synthesis of $CsPbBr_3$ NWs with width that is tunable down to the quantum-confined regime (few-unit-cell thick), using a mixture of alkyl amines and a short alkyl carboxylic acid as growth medium, following standard air-free techniques (for details see Figure 1 and Table 1). In our initial scheme (similar to that of Zhang *et al.*[17]), we could synthesize NWs with 10-20 nm width (hence non-confined) by regulating the ratio of octylamine (OctAm) to oleylamine (OlAm) and by varying the reaction time (from 30 to 50 min), see Figure 2. $CsPbBr_3$ NWs with width that is tunable down to the quantum-confined regime (few-unit-cell thick) were synthesized by using a mixture of alkyl amines and a short alkyl carboxylic acid as growth medium, following standard air-free techniques (see experimental details Figure 1 and Table 1). In our initial scheme (similar to that of Zhang *et al.*[16]), we could synthesize NWs with 10-20 nm width (hence non-confined) by regulating the ratio of octylamine (OctAm) to oleylamine (OlAm) and by varying the reaction time (from 30 to 50 min). The addition of an acid with a long alkyl chain oleic acid (OA) combined with short and long

chain amines led instead to the formation of nanosheets, as recently shown by us.[18] If, in *lieu* of oleic acid, a shorter alkyl chain carboxylic acid (octanoic acid–OctAc, or hexanoic acid–HexAc) was used, thinner NWs could be prepared see Figure 2.

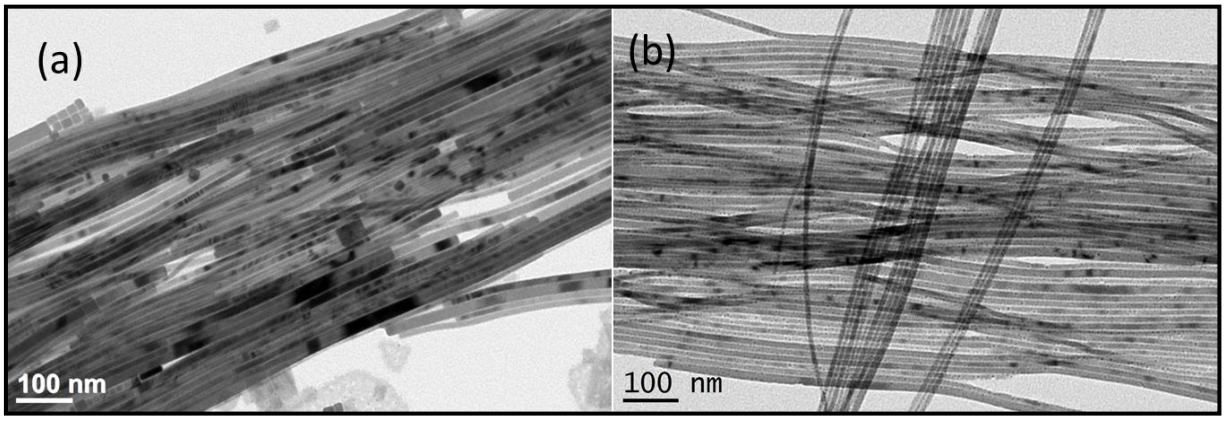

Figure 2. BF-TEM images of NWs prepared without any acid (neither oleic acid nor hexanoic acid). Reaction conditions: 0.069g $PbBr_2$, 8mL ODE, (a) 200µL OctAm, 800µL OlAm, (b) 500µL OctAm, 500µL OlAm. Reaction temperature: 120°C, Reaction time: 50 min.

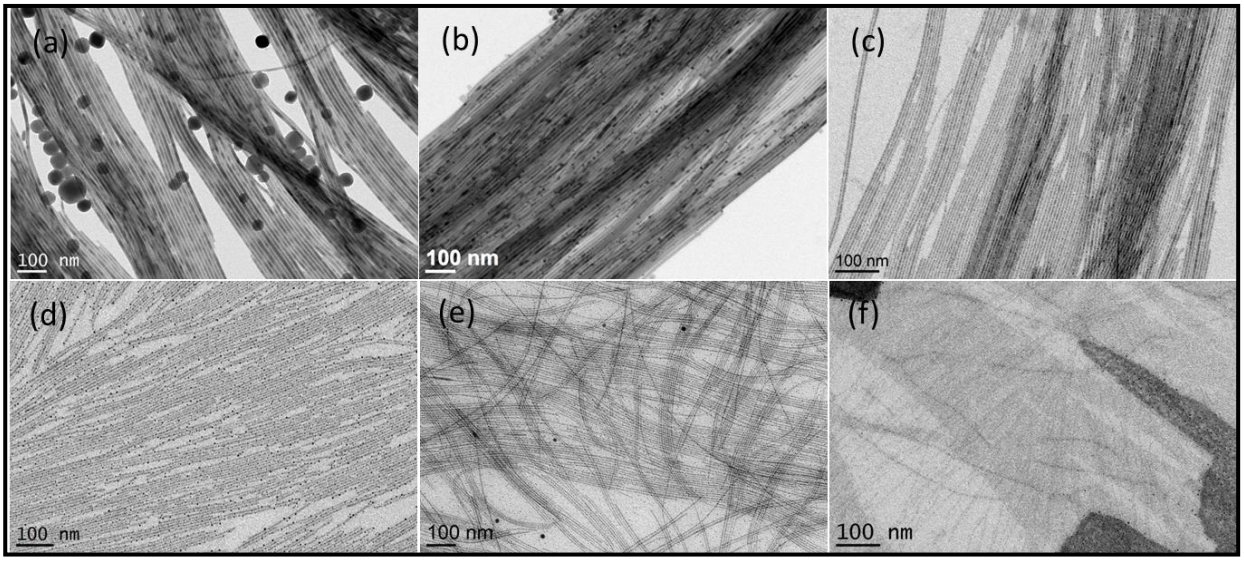

Figure 3. BF-TEM images of NWs prepared using hexanoic acid instead of Oleic acid: Reaction conditions: 0.069g $PbBr_2$, 8 mL ODE, 500µL OlAm, 500µL OctAm, and 50µL of HexAc. Reaction temperature: 65°C, Reaction: time 50mint. If, in *lieu* of oleic acid, a shorter alkyl chain carboxylic acid (octanoic acid–OctAc, or hexanoic acid–HexAc) was used, thinner NWs could be prepared (Figure 3).

The addition of an acid with a long alkyl chain (oleic acid) combined with short and long chain amines led instead to the formation of nanosheets as recently shown by us.[19] By increasing the concentration of the short acid over that of the amine ligands (OctAm and OlAm), the width of nanowires could be systematically tuned from 10±1 to 3.4±0.5 nm, that is, down to the strong

quantum confinement regime Figure 4. Other parameters that were found critical to control the width of the NWs were the temperature and the reaction time. For non-confined nanowires (width≥10nm) 120-130°C was the optimal temperature range for growth. For the growth of confined NWs (width ≤10nm) the same temperature range (or higher temperature) yielded various by-products (including cubes) in addition to wires, whereas below 70°C the NWs growth was much slower, which helped to improve the size mono dispersity and led essentially to NWs free of

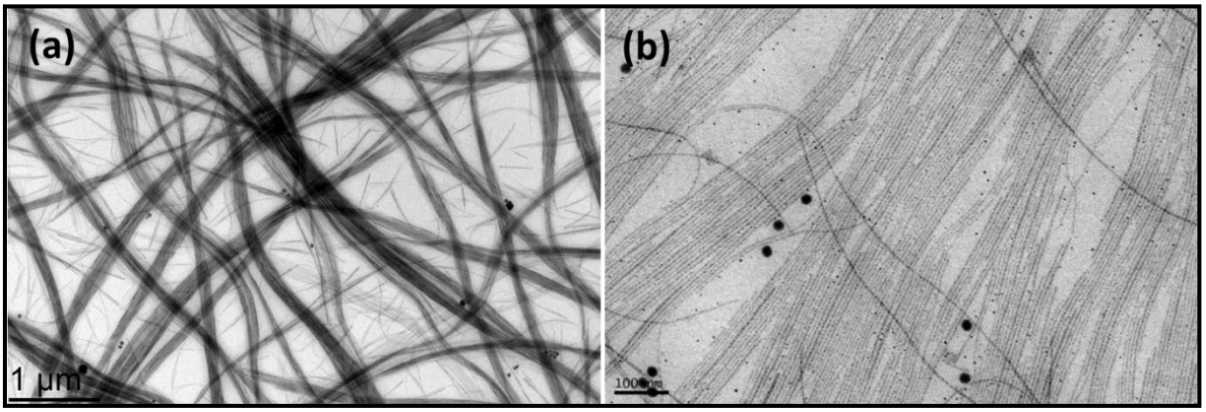

byproducts. The optimal time of growth was 50 minutes for both non-confined and confined NWs. Increasing the reaction time resulted in aggregation of the NWs.

Figure 4. BF-TEM images of NWs prepared with different ratios of short acids to amine ligands. The widths of the wires are: (A) 20 nm, (B) 10 nm, (c) 5.1 nm, (d) 4.1 nm, (e) 3.4 nm, (f) 2.8 nm (the latter NWs were not stable over time). See Table S1 for synthesis details.

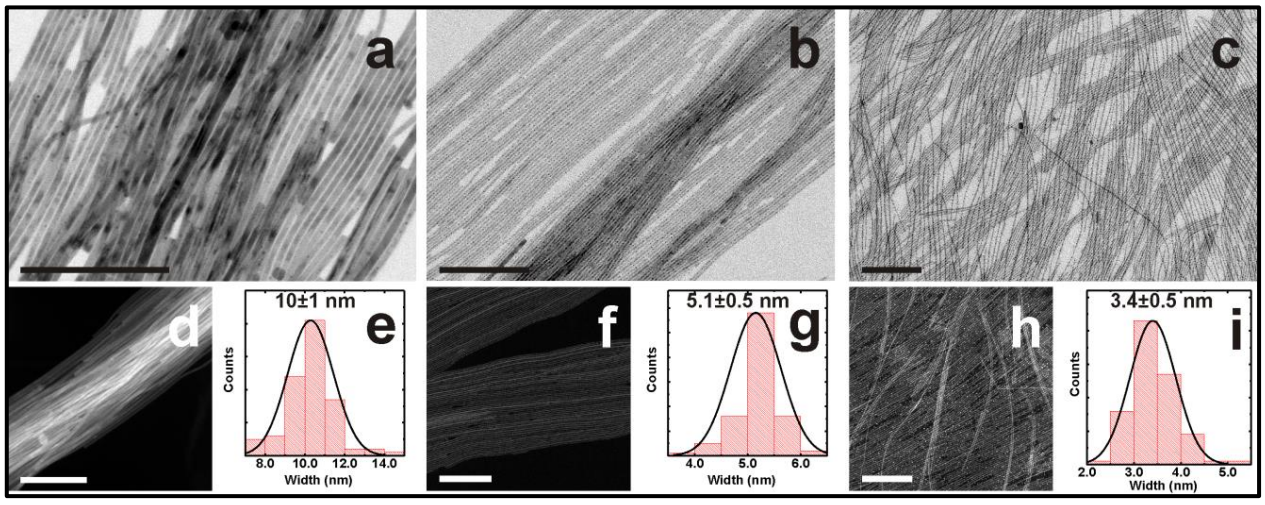

Figure 5. Effect of increasing the ratio of short chain carboxylic acid to amine ligands on controlling the width of the $CsPbBr_3$ NWs. Representative BF-TEM and HAADF-STEM images for 10 nm (a,d), 5.1 nm (b,e) and 3.4 nm (c,f) width NWs and (e,g,i) their respective size distributions. Short chain carboxylic acid to alkyl amines volume ratios respectively: 0 (a), 0.1 (b), 0.3 (c) (see Table 1). Scale bars are 200 nm in all images.

Bright field transmission electron microscopy (BF-TEM) images are reported in Figure 5 (a-c), along with high-angle angular dark field scanning TEM (HAADF-STEM) images (d, f, g) and histograms of widths distributions (e, g, i), for NW samples prepared under different conditions (see Figure 4 and Table 1 for details). High resolution TEM (HRTEM) analyses revealed the single-crystal nature of the NWs, compatible with the orthorhombic structure (ICSD #97851) already reported by us for $CsPbBr_3$ nanosheets[19] and by Zhang *et al.*[16] for NWs.

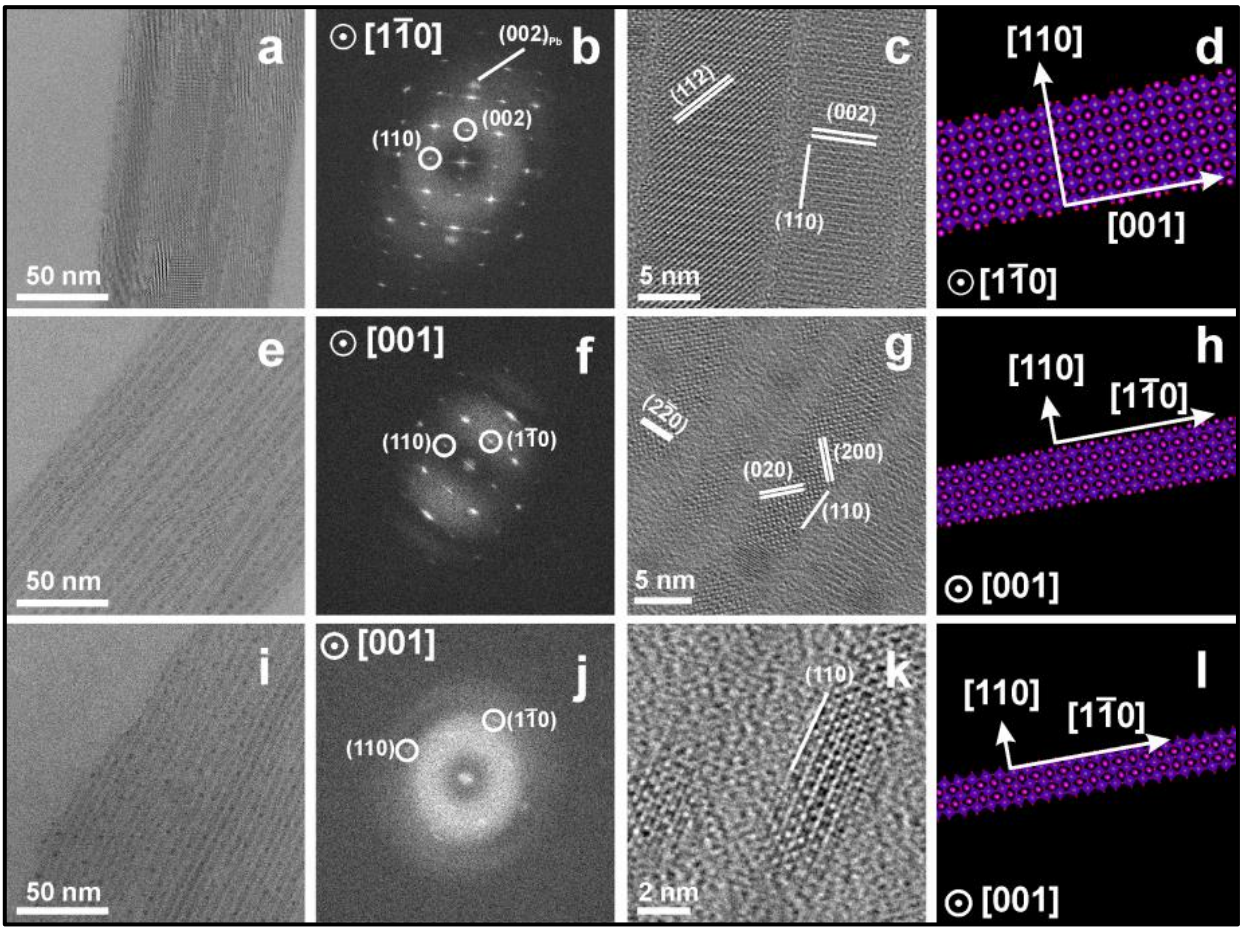

Figure 6. Structural analyses of (a-d) 10 nm, (e-h) 5.1 nm and (i-l) 3.4 nm-wide NWs: (a,e,i) wide FOV HRTEM images of the NWs, (b,f,j) corresponding FFTs and (c,g,k) magnified view of respective portions; (d,h,l) schematic crystallographic models of the NWs, showing the orientation of the observed facet and the elongation direction for the NWs.

Due to the well-known electron-beam-irradiation sensitivity of lead halide perovskite NCs in general (both the hybrid[20] and the fully inorganic[21] ones), and to the extremely small size of the most confined NWs reported here, HRTEM analyses of these few-nm wide nanocrystals were challenging. For this reason, HRTEM images shown in the current work were collected using a direct-electron detection camera instead of the more conventional CCD camera, by which we could obtain, while using short acquisition times, high resolution images at relatively low electron dose and wide field of

view (FOV). A careful look at these results revealed that the NWs do not have a circular but rather a rectangular section, as each sample was made of bundles of NWs exhibiting identical orientation (*i.e.*, zone axis), as can be seen in the wide FOV HRTEM images in Figure 6 (a,e,i) and their respective FFTs (panels b,f,j). In particular, all the NWs were enclosed by {110}, {1-10} and {001} facets and all of them were confined along the <110> direction. However, the 10 nm thick NWs on the carbon support film were <1-10>-oriented and elongated along the <001> direction, while thinner ones (both 5.1 nm and 3.4 nm) were <001>-oriented and elongated along the <1-10> direction.

This difference can be ascribed to the addition of short chain acids in the synthesis, which clearly favor the growth along <1-10> while inhibiting the growth along the <001> direction.[16,17] An additional indication of the rectangular section of the NWs, in the particular case of the 10 nm wide NW sample, comes from the two different values measured for the size along the transverse direction, hinting at width and thickness of the NWs (see Figure 8). The 10 nm NW image in Figure 5(a) shows additional information, which is investigated in Figure 7. As noticed from Figure 7(a), the spacing between 10 nm NWs is only few nm, and some of the neighboring NWs (Figure 7 (b, c)) merge into one single wire. The sizes of the individual NWs in (a) are all labelled, and there are two sets of sizes, clearly indicating the rectangular cross section of this NW sample, with width of 9.5 nm, and thickness 7.7 nm.

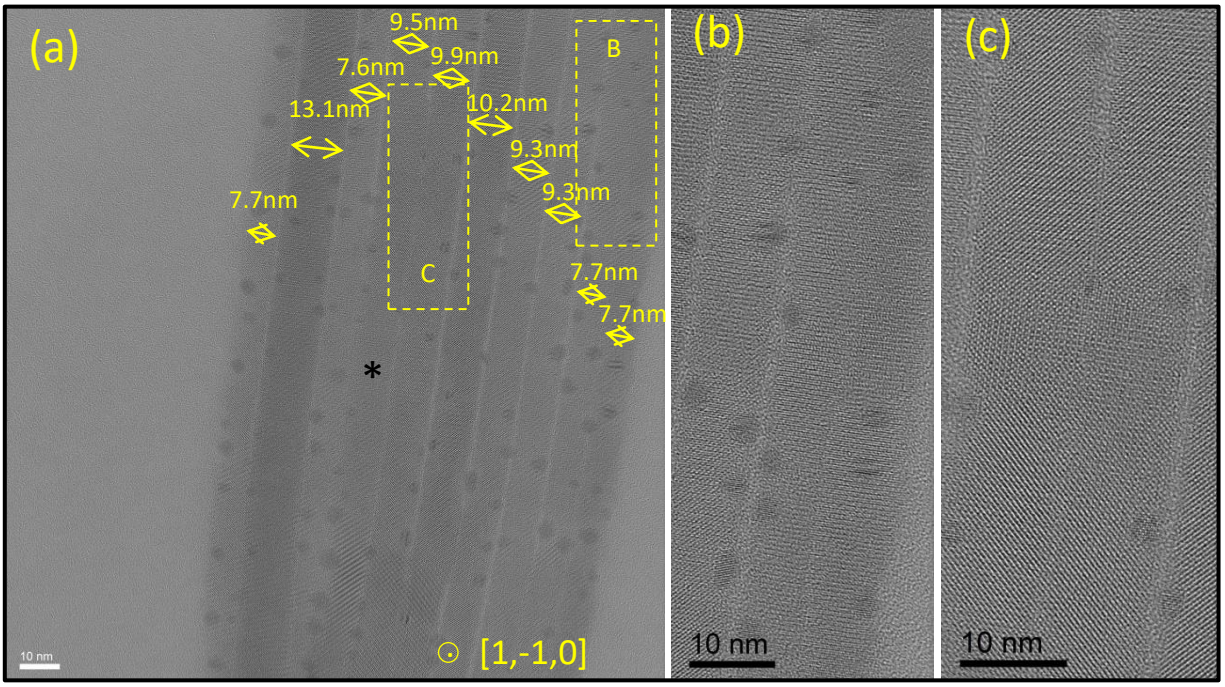

Figure 7. HRTEM image of 10 nm NWs. (b, c) are the magnified view of region B and C labelled in (a), showing merging of the 10 nm NWs at some of the locations.

We conclude therefore that the synthesis conditions inhibited the growth of some crystallographic facets, while enhancing three sets of them, namely the {110}, {1-10} and {001} ones, and the relative stability of the facets was likely related to the concentration of the short chain acids used. In addition to this, epitaxially oriented Pb nanocrystals were found along the NWs (see Figure 6(a,b,e,f,i)). Their formation was due to electron-beam irradiation (despite the low dose), as previously reported for cesium lead halide nanocrystals.[19,21] In accordance with what observed in the HRTEM analyses, SAED patterns and their azimuthally integrated profiles (Figure 8) for the thick NWs exhibited sharper Bragg peaks, due to larger size of the coherently scattering domain. While 10 nm and 5.1 nm-thick NWs featured the distinctive peaks for the orthorhombic phase, labelled by arrows, the phase of 3.4 nm NWs could not be undoubtedly stated based on SAED pattern taken from a bundle of them, due to their smaller width.

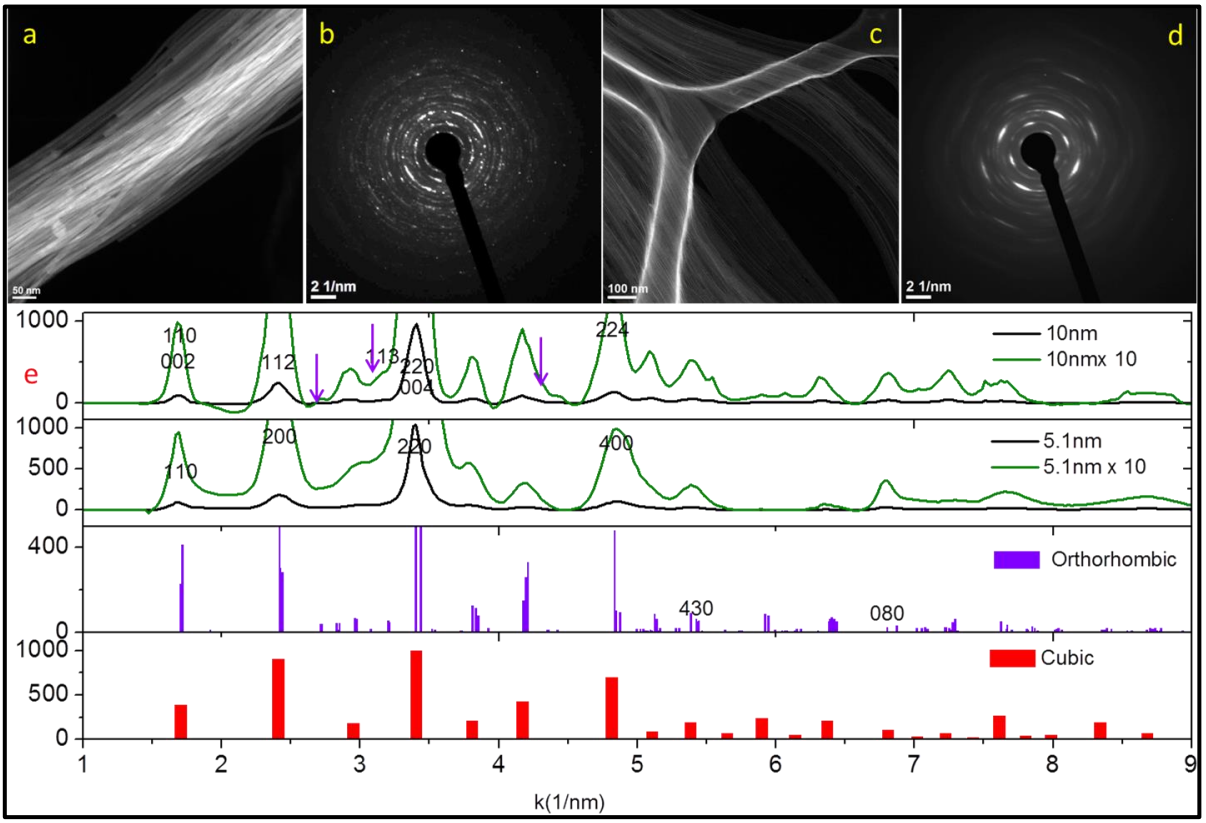

Figure 8. HAADF-STEM images and the SAED patterns of the 10 nm (a, b) and 5.1 nm (c, d) NWs respectively. The SAED pattern in (b) was taken without tilting the sample for 10 nm NWs, while the patterns in (d) was acquired after tilting the 5.1 nm NWs samples by 20°. (e) Azimuthal integration of the corresponding SAED patterns, and their comparison with the powder XRD data for reference orthorhombic (ICSD 97851) and cubic phases (ICSD 29073) of $CsPbBr_3$.

Note: The SAED pattern in Figure 8 (b) was taken for 10 nm NWs without tilting the sample, while the patterns (d, f) were taken for 5.1 nm NWs, and 3.4 nm NWs by tilting the sample 20° around the

sample holder axis, in order to enhance the contribution of planes parallel to the support film. The camera length was 30 cm for all three diffraction patterns. The azimuthal integration of the SAED patterns in Figure 8 (b, d, f) is compared with the powder XRD data for reference orthorhombic (ICSD 97851) and cubic phases (ICSD 29073) of $CsPbBr_3$. The 10 nm wires show distinctive peaks for orthorhombic phase, labelled by purple arrows in the panel. One weak peak unique for orthorhombic phase is shown for 5.1 nm wires, which indicates the orthorhombic phase is maintained despite the addition of acid in the synthesis. The peaks for the 3.4 nm wires are broad due to their low thickness, thus distinctive features for the orthorhombic phase cannot be appreciated. However, the phase of the 3.4 nm wires is likely to remain orthorhombic since the synthesis protocol is the same as 5.1 nm NWs, with the only difference being the amount of short chain acid added.

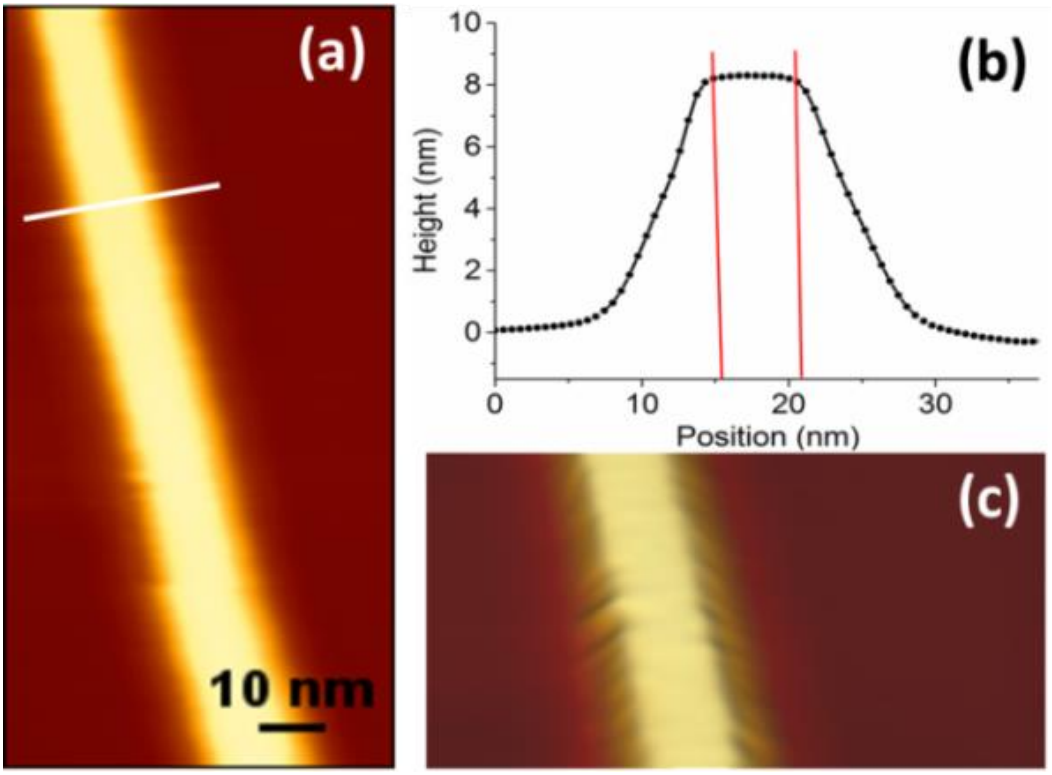

Figure 9. (a) Tapping mode AFM height image of a single NW. (b) cross-section along the profile defined by the white line reported in (a). The flat upper part of a NW is clearly visible in the three-dimensional reconstruction of the NW topography reported in panel (c).

The shape of the NWs was also verified by atomic force microscopy (AFM). Figure 9a shows the typical aspect of a single NW, in the case of 5.1 nm thick NWs. A profile along the white line traced in Figure 9a is shown in Figure 9b. The AFM data show that the shape of the NW is not cylindrical, thus corroborating what found by HRTEM. Indeed, the cross section indicated that the single wires presented a planar structure. The 3D representation of the NWs (Figure 9c) evidences that the upper

surface of the NWs is flat. The average thickness of the NWs, derived from the analysis of single line profiles obtained from 10 NWs from 3 different samples, was 8.1±0.4 nm (n=36), while the lateral size of the upper face of the NWs was 5.5±0.6 nm (n=36), in agreement with the lateral size determined by size statistics based on BF-TEM images. Note that, except for the flat upper surface, the lateral size and shape of the NWs is affected by tip enlargement effect.[22] Considering the nominal size of the AFM tip used in the experiments, we estimated the size of the lower surface through the formula reported in ref. [23], and obtained the same value as measured for the upper facet. Hence the NWs had rectangular section.

Table 2. Comparison of the absorption and photoluminescence peak position, PL FWHM, PLQY and PL lifetime for $CsPbBr_3$ NWs with different widths.

Width (nm)	Abs. max (nm)	PL max (nm)	PL FWHM (nm)	PLQY (%)	Average PL lifetime (ns)
20±3	511	524	18	12 ± 2	20.6
10±1	504	517	16	38 ± 4	16.4
5.1±0.5	484	496	16	77 ± 8	4.9
4.1±0.7	472	481, 491	18	40 ± 4	2.8
3.4±0.5	455, 467	473, 483	33	30 ± 3	2.5

We recorded UV−visible absorption and PL spectra and measured PLQY and PL lifetime of the various NW samples. The relevant parameters are summarized in Table 2. The presence of strong quantum confinement in the NWs is demonstrated by the optical absorption and PL spectra of Figure a (note that the exciton Bohr diameter for $CsPbBr_3$ is around 7 nm[24]): by shrinking the NWs width, the main excitonic absorption peak shifted from 511 nm (for a width *W* of 10 nm) to 455 nm (*W* = 3.4 nm), accompanied by a PL peak blue shift from 524 to 473 nm (see Table 2, the full width at half maximum, FWHM, ranged from 16 to 33 nm). Such tunability in the PL peak position is similar to what observed for $CsPbBr_3$ quantum dots,[25] nanoplatelets[21] and hybrid organolead halide NWs[15] exhibiting different degrees of quantum confinement. Here, both NW samples with 4.1±0.7 and

3.4±0.5 nm width evidenced a secondary PL peak (at around 483 and 491 nm, respectively), and a second absorption peak at 467 nm was seen for the *W* = 3.4 nm sample. These additional spectral features are not seen during the synthesis. In Figure S10 we report for example the PL spectrum from the 4.1±0.7nm NWs directly after the final washing step and immediately after resuspension in toluene. This was characterized by a single emission peak at 473 nm (FWHM 33 nm). However, less than 15 min later, a second PL peak was observed at longer wavelengths. This additional PL peaks is likely due to aggregation of the NWs, which reduces the quantum confinement by allowing delocalization of the holes/electrons on neighbouring NWs. Hence the thinnest NWs had limited stability over time.

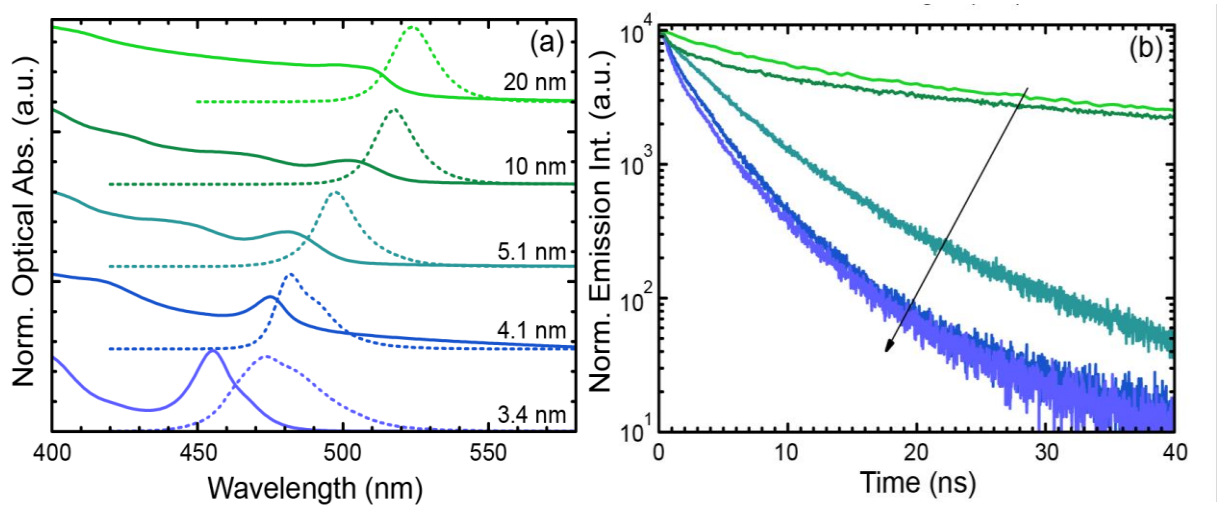

Figure 10. (a) Optical absorption (solid line) and PL spectra (dashed line, λ_{exc}=400 nm) of the NWs in toluene solutions. (b) Time-resolved PL ,(λ_{exc}=405 nm) measured at the PL peak for the $CsPbBr_3$ NWs in toluene solution. Color coding is the same in panels (a) and (b).

The PLQY measured in solution (Table 1) increased from 12% to 77% when the width was reduced from 20±3 to 5.1±0.5 nm. By further reducing the NW width, the PLQY dropped to 30%. The reduction in PLQY was accompanied by the appearance of a second PL peak in the thinnest NWs. This suggests that the red-shifted secondary PL peak has a detrimental effect on the PLQY. Time-resolved PL measurements (Figure 4b) evidenced on the other hand a continuous decrease in PL lifetime, from the green to blue emitting NW samples, from 20.6 ns for 20 nm width to 2.5 ns for 3.4 nm width (Table 1). The NWs with 5.1 nm width, which had the highest PLQY (77%), exhibited a substantially short PL lifetime of 4.9 ns that is in line with that of other CsPbBr3 NCs of different shapes.[21,26,27] The increase in PLQY from the thickest (20 nm) to the 5.1 nm NWs, accompanied by a shortening of the PL lifetime, indicates a continuous increase in the radiative rate. Considering that the various samples here reported were prepared under different syntheses conditions, we cannot ascribe the variation in PLQY only to the effect of quantum confinement. It is indeed possible that each sample was

characterized by a different number of trap states (hence overall material quality). For the NW samples with width smaller than 5.1 nm (last two rows of Table 1) the decrease in PLQY and the further shortening of the PL lifetime indicate an increase in non-radiative decay rate that can again be tentatively ascribed to the appearance of the secondary PL arising from either NWs aggregation or trap-emission.

3.4. Conclusion

In conclusion, we have reported the colloidal synthesis of $CsPbBr_3$ perovskite NWs with tunable width, from the non-confined regime to strong quantum-confinement regime, by introducing carboxylic acids with short aliphatic chains (octanoic acid or hexanoic acid). The NWs had photoluminescence quantum yield that could be as high as 77%, with PL spectral position that could be varied from green to blue. NWs with a width below ~5 nm show a reduced stability with the appearance of additional PL and absorption peaks and a reduction in PLQY. Future progress in this direction will require the stabilization of the thinnest wires. Another challenge will reside in understanding and modeling the growth kinetics and thermodynamics of these nanostructures. Also, as syntheses protocols to $CsPbBr_3$ perovskite nanostructures of various shapes have reached maturity, interesting developments can be the study of the effect of shape/dimensionality on quantum confinement and on the rate and extent of anion exchange.

3.5. References

1. Dasgupta, N. P.; Sun, J.; Liu, C.; Brittman, S.; Andrews, S. C.; Lim, J.; Gao, H.; Yan, R.; Yang, P.25th Anniversary Article: Semiconductor Nanowires – Synthesis, Characterization, and Applications, *Adv. Mater.* **2014**, *26*, 2137-2184.

2. Cui, Y.; Lieber, C. M.Functional Nanoscale Electronic Devices Assembled Using Silicon Nanowire Building Blocks, *Science* **2001**, *291*, 851-853.

3. Gudiksen, M. S.; Lauhon, L. J.; Wang, J.; Smith, D. C.; Lieber, C. M.Growth of Nanowire Superlattice Structures for Nanoscale Photonics and Electronics, *Nature* **2002**, *415*, 617-620.

4. Huang, M. H.; Mao, S.; Feick, H.; Yan, H.; Wu, Y.; Kind, H.; Weber, E.; Russo, R.; Yang, P.Room-Temperature Ultraviolet Nanowire Nanolasers, *Science* **2001**, *292*, 1897-1899.

5. Wallentin, J.; Anttu, N.; Asoli, D.; Huffman, M.; Åberg, I.; Magnusson, M. H.; Siefer, G.; Fuss-Kailuweit, P.; Dimroth, F.; Witzigmann, B.; Xu, H. Q.; Samuelson, L.; Deppert, K.; Borgström, M. T.Inp Nanowire Array Solar Cells Achieving 13.8% Efficiency by Exceeding the Ray Optics Limit, *Science* **2013**, *339*, 1057-1060.

6. Hochbaum, A. I.; Chen, R.; Delgado, R. D.; Liang, W.; Garnett, E. C.; Najarian, M.; Majumdar, A.; Yang, P.Enhanced Thermoelectric Performance of Rough Silicon Nanowires, *Nature* **2008**, *451*, 163-167.

7. Cui, Y.; Wei, Q.; Park, H.; Lieber, C. M.Nanowire Nanosensors for Highly Sensitive and Selective Detection of Biological and Chemical Species, *Science* **2001**, *293*, 1289-1292.

8. Xu, X.; Zhuang, J.; Wang, X.Sno2 Quantum Dots and Quantum Wires: Controllable Synthesis, Self-Assembled 2d Architectures, and Gas-Sensing Properties, *J. Am. Chem. Soc.* **2008**, *130*, 12527-12535.

9. Yu, H.; Li, J.; Loomis, R. A.; Gibbons, P. C.; Wang; Buhro, W. E.Cadmium Selenide Quantum Wires and the Transition from 3d to 2d Confinement, *J. Am. Chem. Soc.* **2003**, *125*, 16168-16169.

10. Groeneveld, E.; van Berkum, S.; van Schooneveld, M. M.; Gloter, A.; Meeldijk, J. D.; van den Heuvel, D. J.; Gerritsen, H. C.; de Mello Donega, C.Highly Luminescent (Zn,Cd)Te/CdSe Colloidal Heteronanowires with Tunable Electron–Hole Overlap, *Nano Lett.* **2012**, *12*, 749-757.

11. Zhao, Y.; Zhu, K.Organic-Inorganic Hybrid Lead Halide Perovskites for Optoelectronic and Electronic Applications, *Chem. Soc. Rev.* **2016**, *45*, 655-689.

12. Zhang, W.; Eperon, G. E.; Snaith, H. J.Metal Halide Perovskites for Energy Applications, *Nat. Energy* **2016**, *1*, 16048.

13. Zhu, H.; Fu, Y.; Meng, F.; Wu, X.; Gong, Z.; Ding, Q.; Gustafsson, M. V.; Trinh, M. T.; Jin, S.; Zhu, X. Y.Lead Halide Perovskite Nanowire Lasers with Low Lasing Thresholds and High Quality Factors, *Nat. Mater.* **2015**, *14*, 636-642.

14. Eaton, S. W.; Lai, M.; Gibson, N. A.; Wong, A. B.; Dou, L.; Ma, J.; Wang, L.-W.; Leone, S. R.; Yang, P.Lasing in Robust Cesium Lead Halide Perovskite Nanowires, *Proc. Nat. Acad. Sci.* **2016**, *113*, 1993-1998.

15. Teunis, M. B.; Jana, A.; Dutta, P.; Johnson, M. A.; Mandal, M.; Muhoberac, B. B.; Sardar, R.Mesoscale Growth and Assembly of Bright Luminescent Organolead Halide Perovskite Quantum Wires, *Chem. Mater. 2016, 28, 5043-5054*.

16. Zhang, D.; Eaton, S. W.; Yu, Y.; Dou, L.; Yang, P.Solution-Phase Synthesis of Cesium Lead Halide Perovskite Nanowires, *J. Am. Chem. Soc.* **2015**, *137*, 9230-9233.

17. Zhang, D.; Yang, Y.; Bekenstein, Y.; Yu, Y.; Gibson, N. A.; Wong, A. B.; Eaton, S. W.; Kornienko, N.; Kong, Q.; Lai, M.; Alivisatos, A. P.; Leone, S. R.; Yang, P.Synthesis of Composition Tunable and Highly Luminescent Cesium Lead Halide Nanowires through Anion-Exchange Reactions, *J. Am. Chem. Soc.* **2016**, *138*, 7236-7239.

18. Service, R. F.Cesium Fortifies Next-Generation Solar Cells, *Science* **2016**, *351*, 113-114.

19. Shamsi, J.; Dang, Z.; Bianchini, P.; Canale, C.; Stasio, F. D.; Brescia, R.; Prato, M.; Manna, L.Colloidal Synthesis of Quantum Confined Single Crystal CsPbBr3 Nanosheets with Lateral Size Control up to the Micrometer Range, *J. Am. Chem. Soc.* **2016**, *138*, 7240-7243.

20. Sichert, J. A.; Tong, Y.; Mutz, N.; Vollmer, M.; Fischer, S.; Milowska, K. Z.; García Cortadella, R.; Nickel, B.; Cardenas-Daw, C.; Stolarczyk, J. K.; Urban, A. S.; Feldmann, J.Quantum Size Effect in Organometal Halide Perovskite Nanoplatelets, *Nano Lett.* **2015**, *15*, 6521-6527.

21. Akkerman, Q. A.; Motti, S. G.; Srimath Kandada, A. R.; Mosconi, E.; D'Innocenzo, V.; Bertoni, G.; Marras, S.; Kamino, B. A.; Miranda, L.; De Angelis, F.; Petrozza, A.; Prato, M.; Manna, L.Solution Synthesis Approach to Colloidal Cesium Lead Halide Perovskite Nanoplatelets with Monolayer-Level Thickness Control, *J. Am. Chem. Soc.* **2016**, *138*, 1010-1016.

22. Canale, C.; Torre, B.; Ricci, D.; Braga, P. C. In *Atomic Force Microscopy in Biomedical Research: Methods and Protocols*; Braga, C. P., Ricci, D., Eds.; Humana Press: Totowa, NJ, 2011, p 31-43.

23. Josep, C.-F.; Eugenio, C.; Alicia, F.-A.; Elena, P.-C.Correction of the Tip Convolution Effects in the Imaging of Nanostructures Studied through Scanning Force Microscopy, *Nanotechnology* **2014**, *25*, 395703.

24. Protesescu, L.; Yakunin, S.; Bodnarchuk, M. I.; Krieg, F.; Caputo, R.; Hendon, C. H.; Yang, R. X.; Walsh, A.; Kovalenko, M. V.Nanocrystals of Cesium Lead Halide Perovskites (CsPbX3, X = Cl, Br, and I): Novel Optoelectronic Materials Showing Bright Emission with Wide Color Gamut, *Nano Lett.* **2015**, *15*, 3692-3696.

25. Sun, S.; Yuan, D.; Xu, Y.; Wang, A.; Deng, Z.Ligand-Mediated Synthesis of Shape-Controlled Cesium Lead Halide Perovskite Nanocrystals Via Reprecipitation Process at Room Temperature, *ACS Nano* **2016**, *10*, 3648-3657.

26. Dou, L.; Wong, A. B.; Yu, Y.; Lai, M.; Kornienko, N.; Eaton, S. W.; Fu, A.; Bischak, C. G.; Ma, J.; Ding, T.; Ginsberg, N. S.; Wang, L.-W.; Alivisatos, A. P.; Yang, P.Atomically Thin Two-Dimensional Organic-Inorganic Hybrid Perovskites, *Science* **2015**, *349*, 1518-1521.

27. Yakunin, S.; Protesescu, L.; Krieg, F.; Bodnarchuk, M. I.; Nedelcu, G.; Humer, M.; De Luca, G.; Fiebig, M.; Heiss, W.; Kovalenko, M. V.Low-Threshold Amplified Spontaneous Emission and Lasing from Colloidal Nanocrystals of Caesium Lead Halide Perovskites, *Nat. Commun.* **2015**, *6*, 8056.

Chapter 4. Benzoyl Halides as Alternative Precursors for the Colloidal Synthesis of Lead Based Halide Perovskite Nanocrystals

ABSTRACT: We propose here a new colloidal approach for the synthesis of both all-inorganic and hybrid organic-inorganic lead halide perovskite nanocrystals (NCs). The main limitation the protocols that are currently in use, such as the hot-injection and the ligand assisted reprecipitation routes, is that they employ PbX_2 (X= Cl, Br, or I) salts as both lead and halide precursors. This imposes restrictions on being able to precisely tune the amount of reaction species and, consequently, on being able to regulate the composition of the final NCs. In order to overcome this issue, we show here that benzoyl halides can be efficiently used as halide sources to be injected in a solution of metal cations (mainly in the form of metal carboxylates) for the synthesis of $APbX_3$ NCs (in which A= Cs^+, $CH_3NH_3^+$ or $CH(NH_2)_2^+$). In this way, it is possible to independently tune the amount of both cations and halide precursors in the synthesis. The $APbX_3$ NCs that were prepared with our protocol show excellent optical properties, such as high photoluminescence quantum yields, low amplified spontaneous emission thresholds, and enhanced stability in air. It is noteworthy that $CsPbI_3$ NCs, which crystallize in the cubic α phase, are stable in air for weeks without any post-synthesis treatment. The improved properties of our $CsPbX_3$ perovskite NCs can be ascribed to the formation of lead halide terminated surfaces, in which Cs cations are replaced by alkylammonium ions.

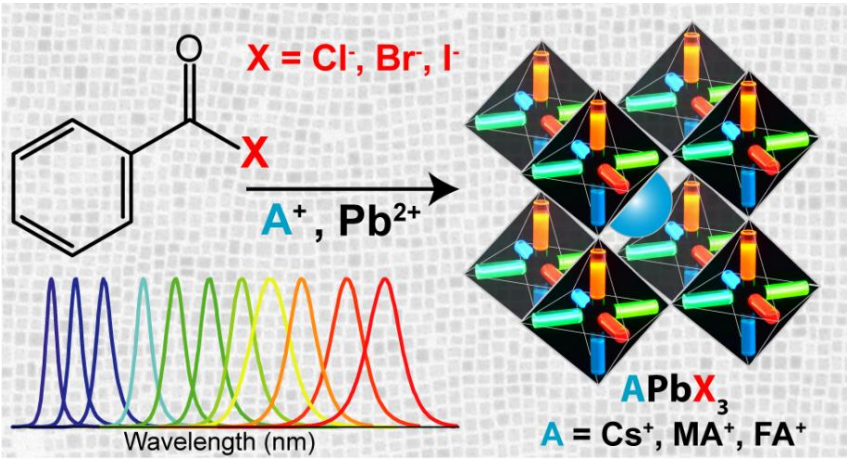

Most of the results dicussed in this chapter have been published in "Imran M, et al. Benzoyl Halides as Alternative Precursors for the Colloidal Synthesis of Lead-Based Halide Perovskite Nanocrystals. *Journal of the American Chemical Society*. 2018, 29 (140), 2656-64."

4.1. Introduction

Over the last few years, semiconductor metal halide nanocrystals (NCs) with a perovskite crystal structure have emerged as one of the most interesting materials for optoelectronic applications.[1-11] In particular, lead based halide perovskite NCs with formula $APbX_3$, in which A can be Cs^+, $CH_3NH_3^+$ (MA) or $CH(NH_2)_2^+$ (FA) and X is Cl, Br or I, have been recently shown to have outstanding optical properties.[12] Such compounds are characterized by a broad tunable photoluminescence (PL) that ranges from the ultraviolet (UV) to the near infrared region of the electromagnetic spectrum, a narrow full width at half-maximum (FWHM), and high PL quantum yields (PLQY).[7-11,13-19] Interestingly, the PL emission of such perovskite NCs can be easily adjusted not only through size control, and subsequently through quantum confinement, as is the case for standard quantum dots, but also through compositional mixing, for example via simple anion exchange reactions.[20-27] Such properties have inspired researchers to exploit this class of materials for use in efficient solar cells, sensitive photodetectors, low threshold lasers, and light emitting diodes (LEDs).[3,4,7,9-13]

To date, various approaches have been proposed for the direct synthesis of all-inorganic and organic-inorganic metal halide perovskite colloidal NCs, with the hot-injection and the ligand-assisted reprecipitation (LARP) ones being the most used and most developed methods.[7,9-11] The former, which was initially devised for all-inorganic perovskite NCs, is based on the hot-injection (up to 200°C) of the A cation (in the form of Cs-oleate for Cs or methylamine for MA) to a solution containing a metal halide salt (*e.g.* PbX_2, X= Cl, Br, I) and surfactants (*e.g.* oleylamine and oleic acid).[19,28-33] Immediately after the injection, a rapid salt metathesis reaction occurs, forming ternary halide NC materials. Conversely, the LARP strategy, which was originally proposed for the synthesis of organic-inorganic $MAPbX_3$ NCs but was later extended to the synthesis of all-inorganic $CsPbX_3$ systems, is performed at low temperatures (typically from room temperature, RT, to 60°C). This method is based on the reprecipitation of halide salts in the presence of ligands: metal halide salts (or organic halide salts in the case of hybrid perovskites) are solubilized in one or more polar solvents, like DMF, and are subsequently added dropwise to a solution of a non-polar medium, like toluene, in the presence of ligands.[2,15,18,34-40] The low solubility of halide salts in the non-polar solvent triggers their precipitation with the recrystallization of halide NCs. Both procedures have various limitations, the main one of which is the use of inorganic salts (*i.e.* PbX_2) as both cation and anion precursors for the metathesis reaction. Indeed, since the ratio of cations to anions employed in the synthesis is linked to that of the chosen inorganic salts, it is not possible to precisely tune the composition of the final NCs. Furthermore, a notable disadvantage is that it is difficult to work with an excess of halide ions,

which is an experimental condition that has been shown to favor the formation of lead halide perovskite NCs with improved stability and optical properties.[2,29,41]

The obstacles imposed by these two techniques were partially overcome by Wei *et al.*, who proposed an alternative colloidal route for the preparation of $CsPbX_3$ NCs, that was later called the "three-precursors approach".[42] Such a synthesis is based on the dissolution of Cs^+ and Pb^{2+} cations in fatty acids followed by the injection of an alkylammonium halide salt (as the halide precursor). This procedure was then adopted and revised by Yassitepe *et al.* for the preparation of amine-free $CsPbX_3$ NCs for LEDs,[43] and by Protesescu *et al.* and Li *et al.* for the synthesis of $FAPbX_3$ (X=Br, I) NCs.[44-46] This approach allows one to work with the desired stoichiometry of the ions, since the halide ions and the metal cation sources are not delivered together, *i.e.* they are not delivered with the same chemical precursor. On the other hand, its potential versatility is limited by the poor reactivity of the alkylammonium halide salts (*i.e.* $CsPbI_3$, $CsPbCl_3$, $MAPbX_3$ and $FAPbCl_3$ NCs have not been reported by using this strategy), which can also lead to the formation of undesired secondary phases.

In order to overcome the restrictions associated with the aforementioned synthetic procedures, we propose here a new colloidal synthesis approach which independently ensure the tenability of reaction precursors. This synthetic strategy basically was inspired by the one employed for the non-aqueous synthesis of metal oxide NCs.[47] In a typical synthesis of metal oxide NCs, the release of water, *i.e.* the oxygen precursor, can be achieved by reacting carboxylic acids with either amines or alcohols at relatively high temperatures (above 200°C), as is illustrated by Equations 1 and 2.

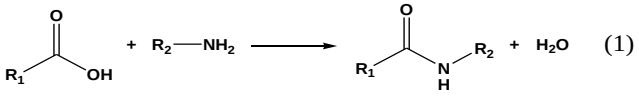

(1)

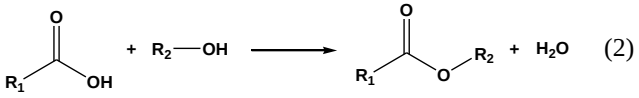

(2)

Similarly, acyl halides are well known for their strong reactivity toward nucleophilic compounds (*i.e.* amines, alcohols, carboxylic acids) which form carboxylic acid derivatives even at room temperature (*i.e.* amides, esters, anhydrides) and simultaneously release hydrohalic acids (see Equations 3-5).[48]

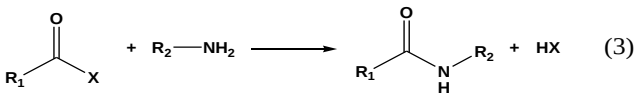

(3)

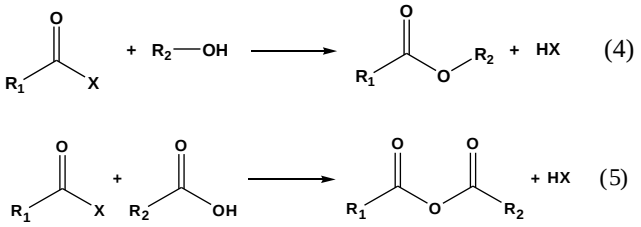

(4)

(5)

Thus, the idea behind our colloidal approach is to inject acyl halide molecules into a solution of metal cations that have been dissolved in nucleophilic molecules, namely amines and carboxylic acids, at a desired temperature, in order to trigger the release of halide ions and, consequently, the nucleation and growth of metal halide NCs. Among the possible acyl halide molecules, we selected benzoyl halides since they are low-cost and have a sufficiently high boiling point (~200°C) which allows for the synthesis of metal halide NCs even at relatively high temperatures. Furthermore, considering the strong reactivity of acyl halides toward nucleophilic species, another important aspect of benzoyl halides is that they are more stable than aliphatic acyl halides as a result of their stabilization by the π-overlap in the ground state.[49] Indeed, the more stable the anion precursor is, the more controlled the release of the halide ions should be, which, in turn, could lead to the fine tuning of the size distribution of the NC.[50] Our new approach relies on the use of benzoyl halides as halide precursors, which can be easily injected into a solution of metal cations (such as metal carboxylates) and desired ligands (oleylamine and oleic acid). This injection immediately triggers the nucleation and the growth of metal halide NCs (see Scheme 1). By simply tuning the relative amount of cation precursors, ligands, solvents, benzoyl halides and the injection temperature, it is possible to synthesize either all-inorganic or organic-inorganic $APbX_3$ (A= Cs, MA or FA and X= Cl, Br or I) NCs with tight control over the size distribution and with high phase purity. In addition, thanks to the strong reactivity of benzoyl halides even at RT, they can be used for anion exchange reactions using pre-synthesized $CsPbX_3$ NCs.

Scheme: Colloidal synthesis of lead based halide perovskite nanocrystals using benzoyl halides as halide precursors.

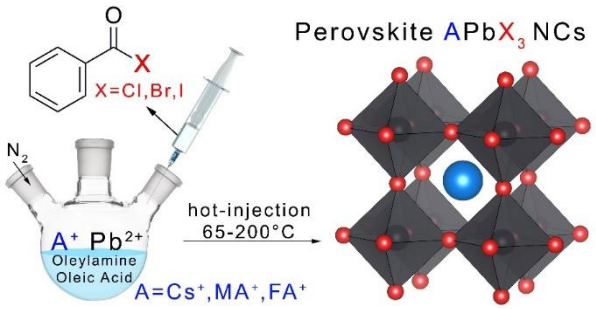

The $APbBr_3$ NCs that were prepared using our protocol are characterized by their PLQYs, which were as high as 92%, and by their very low amplified spontaneous emission (ASE) thresholds. Moreover, the $APbI_3$ NCs had PLQYs of around 55% and, finally, the $CsPbCl_3$ NCs exhibited a record PLQY value of 65%. Also, they exhibited a much higher phase stability than that which has been previously reported for NCs prepared with other synthesis methods. It is noteworthy that cubic $CsPbI_3$ NCs are stable in air for weeks without any post-synthetic treatment, which is different from those prepared using the classic hot-injection or LARP approaches.[28,44,51-54] The optimal properties of our $CsPbX_3$ perovskite NCs can be ascribed to the formation of lead halide terminated surfaces in which Cs cations are replaced by alkylammonium ions. Indeed, our X-Ray photoelectron spectroscopy analysis revealed that all our $CsPbX_3$ NCs are Cs poor and they contain a considerable amount of amines, most likely in the form of oleylammonium ions. Indeed, the formation of these surfaces is favored under our synthetic conditions: the use of benzoyl halides provides a halide rich environment and, at the same time, an efficient protonation of the oleylamine.

4.2. Experimental details

Chemicals. Lead acetate trihydrate ($Pb(CH_3COO)_2{\times}3H_2O$, 99.99%), lead(II) oxide (PbO, 99.999%), sodium iodide (NaI, 99.99%) cesium carbonate (Cs_2CO_3, reagent Plus, 99%), cesium acetate (CH_3COOCs, 99.9%), methylamine (CH_3NH_2, 2M solution in tetrahydrofuran, THF), formamidinium acetate salt ($HN{=}CHNH_2{\cdot}CH_3COOH$, 99%), benzoyl bromide (C_6H_5COBr, 97%), benzoyl chloride (C_6H_5COCl, 98%), toluene (anhydrous, 99.5%), octadecene (ODE, technical grade, 90%), oleylamine (OLAM, 70%) and oleic acid (OA, 90%) were purchased from Sigma-Aldrich. All chemicals were used without any further purification.

Preparation of Benzoyl Iodide. The reaction was performed in a N_2-filled glovebox following the procedure reported by Theobald and Smith.[55] In short, sodium iodide (3g) was mixed with benzoyl chloride (1.4mL) in a 20mL vial. The mixture was vigorously stirred at 75°C on a hot plate for five hours. The reaction mixture turned from colorless to an orange red color, indicating that the transformation of the benzoyl chloride into the benzoyl iodide was successful. Next, the reaction mixture was cooled down to RT and diluted using 3mL of anhydrous ODE. Finally, the solution was filtered, by using a polytetrafluorethylene membrane filter with a 0.45µm pore size, in order to collect the liquid precursor. The reaction yield, which was measured by a *quantitative* NMR (*q*NMR), is virtually complete (97.7%, with only 2.3% of residual benzoyl chloride). A small amount of benzoic acid (1.2%), which was unambiguously identified by using an authentic material (see Figure 1 A, B iii), likely derives from the traces of moisture in the reactants or is due to the cap of the NMR tube not

being sealed during the analysis. Indeed, over time, repeated analyses show an increase in the intensity of the benzoic acid signals, which are accompanied by a corresponding reduction in the intensity of the signals of the benzoyl iodide. The high reactivity with water is a further confirmation of the chlorine substitution with the iodine.

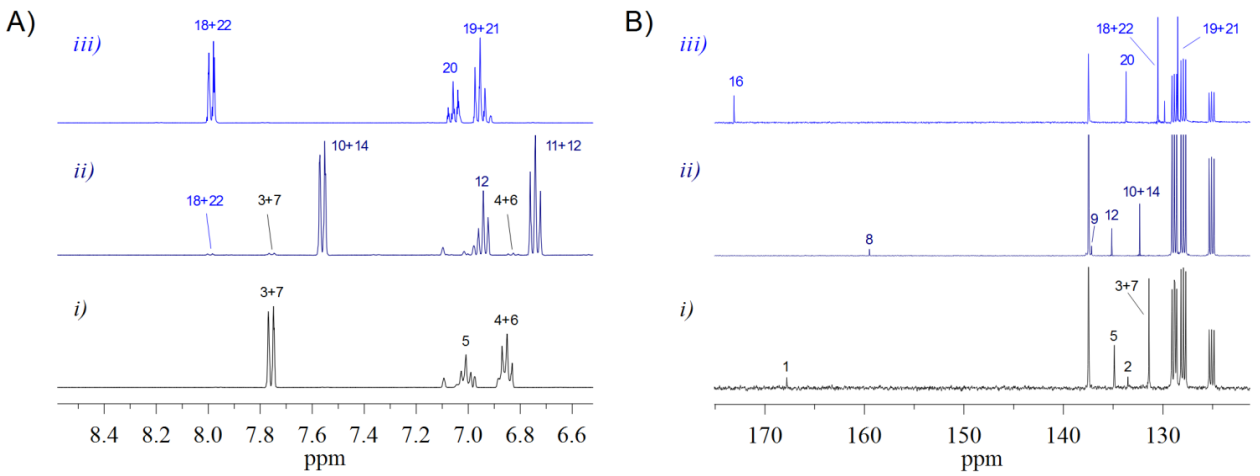

Figure 1. (A) 1H NMR spectra of i) benzoyl chloride, ii) benzoyl iodide, iii) benzoic acid; (B) 13C NMR spectra of i) benzoyl chloride, ii) benzoyl iodide, iii) benzoic acid, in toluene-d8.

Synthesis of $CsPbX_3$ NCs. In a typical synthesis, cesium carbonate (16mg), lead acetate trihydrate (76mg), 0.3ml of OA, 1ml of OLAM and 5ml of ODE were loaded into a 25ml 3-neck round bottom flask and dried under vacuum for 1h at 130°C. Subsequently, the temperature was increased to 165-200°C (See Table 1 for details) under N_2 and the desired amount of the benzoyl halide precursor was swiftly injected (0.6mmol in the case of benzoyl bromide and iodide, and 1.8mmol in the case of benzoyl chloride). The reaction mixture was immediately cooled down in an ice-water bath for $CsPbBr_3$ and $CsPbI_3$ NCs, while it was quenched after 20sec for $CsPbCl_3$ NCs. Finally, 5ml of toluene was added to the crude NC solutions and the resulting mixture was centrifuged for 10 min at 4 krpm. The supernatant was discarded and the precipitate was redispersed in 5 mL of toluene for further use.

Synthesis of mixed $CsPb(Br,Cl)_3$ and $CsPb(Br,I)_3$ NCs. Cesium carbonate (16mg), lead acetate trihydrate (76mg), 0.3ml of OA, 1ml of OLAM and 5ml of ODE were loaded into a 25ml 3-neck round bottom flask and dried under vacuum for 1h at 130°C. Subsequently, the temperature was increased to 170°C under N_2 and the 0.6mmol mixture of benzoyl chloride/bromide (a precursor ratio of 1:1 led to NCs emitting at 448nm) or benzoyl bromide/iodide (precursor ratios of 5:1 and 1:1 led to NCs emitting at 544nm and 594nm, respectively) was swiftly injected. The reaction mixture was immediately cooled down in an ice-water bath. The NCs were collected by adding 5ml of toluene to

the crude solution followed by centrifugation at 4 krpm for 10 min. The supernatant was discarded and the precipitate was redispersed in 5 mL of toluene.

Synthesis of $MAPbX_3$ NCs. Lead oxide (44mg), 2.5mL of OA, 0.025mL of OLAM and 5mL of ODE were mixed in a 25mL 3-neck round bottom flask and dried under vacuum for 1h at 125°C. Subsequently, the temperature was lowered to 65°C under N_2. Methylamine (0.170mL) was injected, followed by the injection of 0.6mmol of the benzoyl halide precursor (see Table 1 for details). The reaction was quenched by the addition of 5mL of toluene after 30 seconds in the case of $MAPbBr_3$ and $MAPbI_3$ NCs, and after 10 seconds in the case of $MAPbCl_3$ NCs. The NCs were collected by centrifuging the crude solution at 4 krpm for 10 min.

Synthesis of $FAPbX_3$ NCs. Lead acetate trihydrate (76mg), formamidinium acetate (40mg), 2.5mL of OA, 0.025mL of OLAM and 5mL of ODE were mixed in a 25mL 3-neck round bottom flask and dried under vacuum for 1h at 125°C. Subsequently, the temperature was lowered to 75-95°C (See table S1) under N_2 and 0.6mmol of the benzoyl halide precursor was rapidly injected. After 30 seconds, the reaction mixture was cooled down in an ice-water bath. 5ml of toluene was added to the crude solution and the resulting mixture was centrifuged for 10 min at 4 krpm. $FAPbI_3$ NCs were washed once with ethyl acetate (using a toluene/ethyl acetate ratio of 5/1) and were eventually redispersed in toluene.

Table 1. Synthetic parameters used for the synthesis of $APbX_3$ NCs

Sample	OLAM (mL)	OA (mL)	Temperature (°C)
$CsPbCl_3$	1	0.3	200
$CsPbBr_3$	1	0.3	170
$CsPbI_3$	1	0.3	165
$MAPbCl_3$	0.1	2.5	65
$MAPbBr_3$	0.025	2.5	65
$MAPbI_3$	0.150	2.5	65
$FAPbCl_3$	0.025	2.5	95
$FAPbBr_3$	0.025	2.5	75
$FAPbI_3$	0.200	2.5	95

Anion Exchange Reactions. In short, 0.500 mL of the $CsPbX_3$ NC dispersion was diluted with 2 mL of anhydrous toluene, and different amounts of a 0.12M solution of benzoyl halide in toluene (ranging from 30µl to 500µl) were swiftly injected under vigorous stirring at RT. Finally, the NCs were collected by centrifugation at 4krpm for 10 min.

4.3. Results and discussion

In order to understand the efficacy of our synthetic protocol, we tested the synthesis of lead-based halide perovskites NCs, paying particular attention to the optimization of their phase purity, size distribution and optical properties. To this end, we chose to synthesize the benzoyl iodide precursor due to the commercial availability of only the benzoyl chloride and bromide compounds. This precursor can be easily prepared by reacting benzoyl chloride with anhydrous sodium iodide at 75°C in an inert atmosphere (see Experimental Details).[55,56] First, we will illustrate the results obtained for $CsPbX_3$ NCs. In a typical synthesis, cesium carbonate and lead acetate were dissolved and degassed in oleylamine, oleic acid and octadecene at 130°C in a three neck flask. Subsequently, the solution was heated up to the desired temperature (170-200°C) and the benzoyl halide precursor was swiftly injected into the reaction flask, triggering the immediate nucleation and growth of the NCs (see Experimental Details and Table 1).

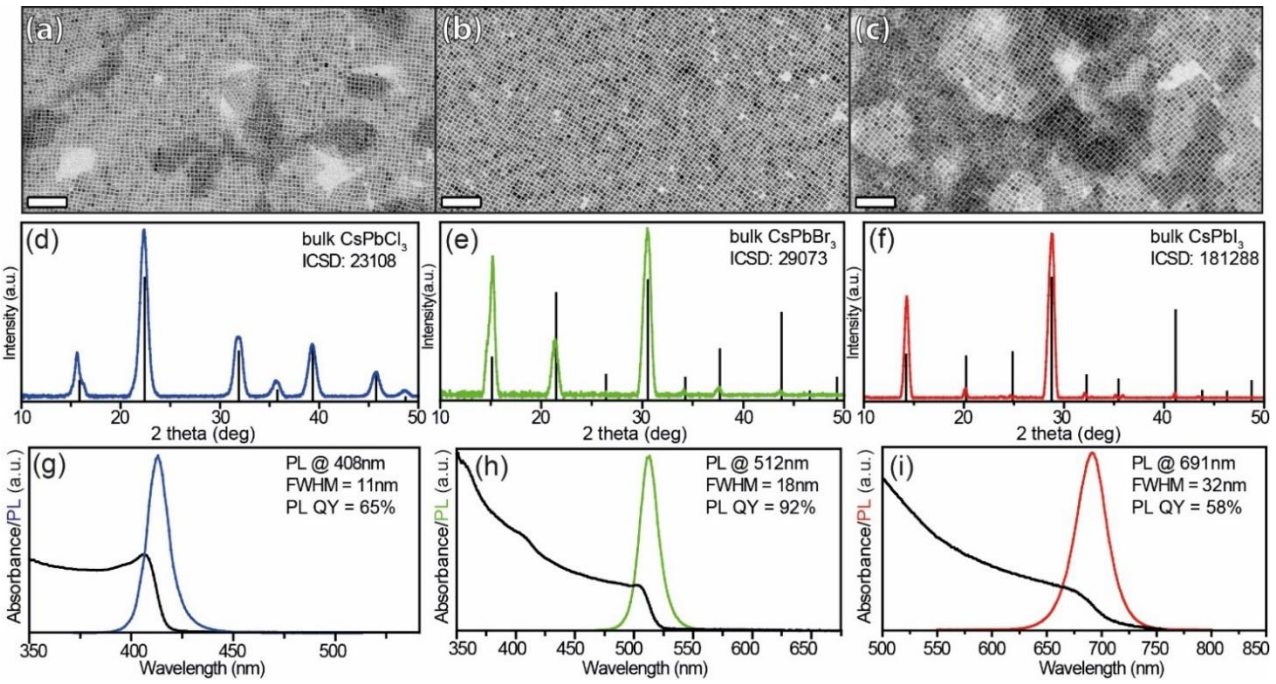

Figure 2. Bright field TEM images of (a) $CsPbCl_3$, (b) $CsPbBr_3$, and (c) $CsPbI_3$ NCs. Scale bars are 100 nm in all images. XRD patterns of (d) $CsPbCl_3$, (e) $CsPbBr_3$, and (f) $CsPbI_3$ NCs along with the corresponding bulk cubic reference patterns. Absorption and PL spectra of (g) $CsPbCl_3$, (h) $CsPbBr_3$, and (i) $CsPbI_3$ NCs dispersed in toluene.

Bright field TEM images of $CsPbX_3$ NCs show that the crystals had a cubic shape and a narrow size distribution (see Figure 1a-c). The average size of the $CsPbCl_3$ NCs was 8.6±1.0nm, while it was 7.8±1.3nm for the $CsPbBr_3$ ones and 10.1±1.6nm for the $CsPbI_3$ ones. The XRD patterns of $CsPbX_3$ NCs nicely match the cubic perovskite structure ($CsPbBr_3$ ICSD code 29073, $CsPbCl_3$ ICSD code 23108, $CsPbI_3$ ICSD code 181288) in all three cases, and no secondary phases were present (see Figure 2d-f). Remarkably, the $CsPbX_3$ NCs exhibited a narrow PL emission linewidth, ranging from 11nm ($CsPbCl_3$), to 18nm ($CsPbBr_3$) to 32nm ($CsPbI_3$), and had PLQYs as high as 92% (see Figure 2g-i). $CsPbCl_3$ NCs were of particular interest: while cesium lead chloride perovskite NCs are typically characterized by a significant non-radiative decay, the PLQY of $CsPbCl_3$ NCs was measured to be as high as 65%, which is a record value.[16,57] It is important to highlight that such a high PLQY was observed only when employing a large excess of the Cl precursor, *i.e.* 1.8mmol of benzoyl chloride and 0.2mmol of the Pb precursor (see the Experimental Details). On the other hand, $CsPbCl_3$ NCs were characterized by a weak PL emission when they were prepared using a lower amount of benzoyl chloride. For example, using 0.6mmol of benzoyl chloride and 0.2 mmol of the Pb precursor led to NCs with a PLQY of just a few percentage points. Time correlated single photon counting (TCSPC) measurements that were conducted on $APbX_3$ NCs revealed, as expected, that systems with higher bandgaps had faster PL decay rates (see Figure 3 and Table 2).[19] In particular, the calculated average lifetimes were 7.7ns for $CsPbCl_3$ NCs, 12.5ns for $CsPbBr_3$ NCs and 21ns for $CsPbI_3$ NCs. The average radiative and non-radiative decay rates that were estimated from the PLQYs and the average PL decay times are reported in Table S1 of the SI.

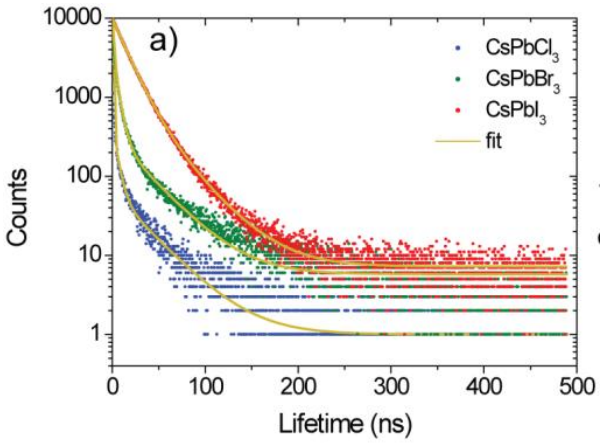

Figure 3. Decay lifetimes of $CsPbX_3$ together with their multi-exponential fittings.

Table 2. The table encloses all the photo-physical data of all the representative $APbX_3$ NCs.

Sample name	A_1	τ_1 (ns)	A_2	τ_2 (ns)	A_3	τ_3 (ns)	τ_{AVG} (ns)	QY %	Γ_{RAD} (1/µs)	$\Gamma_{NON-RAD}$ (1/µs)
$CsPbCl_3$	14471	0.53	418	4.97	60.85	35.44	7.63	65	85.19	45.87
$CsPbBr_3$	6401	1.32	3666	5.05	315.81	34.14	12.52	92	73.45	6.38
$CsPbI_3$	8411	14.43	1686	30.7	16.83	143.31	20.99	58	27.62	20.01

While, in general, lead-halide-based perovskite NCs exhibit excellent optical properties, some of these materials are known for their poor structural stability. In particular, red emitting $CsPbI_3$ NCs, the most interesting materials for photovoltaics applications, suffer from a delayed phase transformation from the metastable cubic (α) phase into the non-luminescent orthorhombic (δ) phase, also known as the "yellow phase".[58]

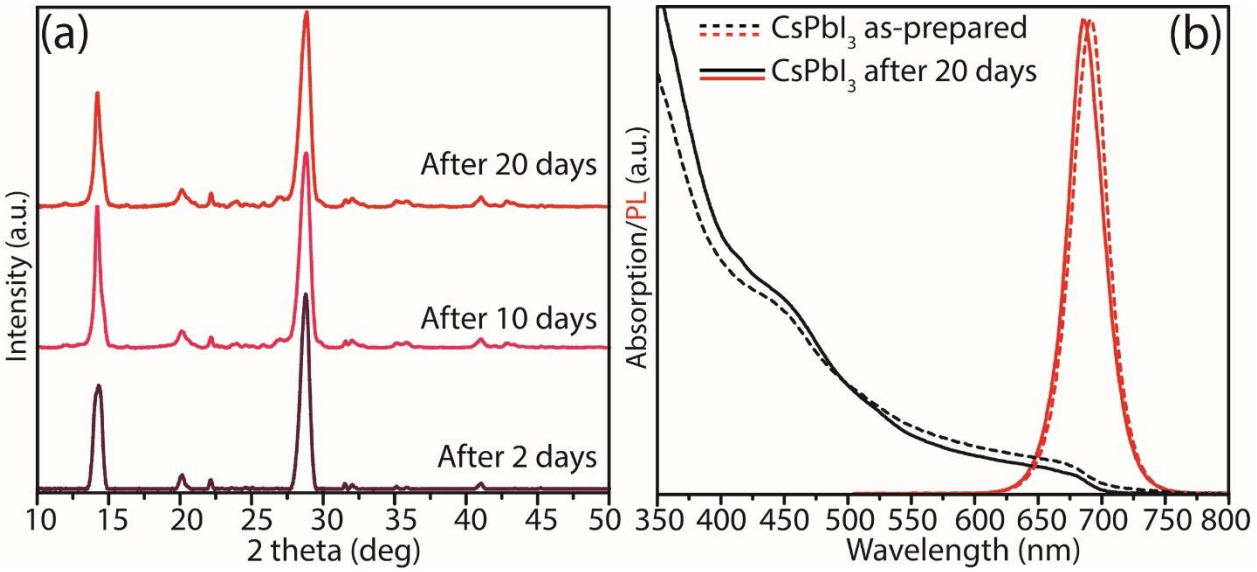

Figure 4. (a) XRD patterns, (b) UV-VIS and PL curves of $CsPbI_3$ NCs exposed to air up to 20 days.

Furthermore, our optical characterizations of the NCs after air exposure confirmed the absence of the $CsPbI_3$ yellow phase, since no absorption features appeared at ~440nm, which can be ascribed to the orthorhombic $CsPbI_3$ band-edge absoption,[59] and the NCs retained their PL emission (see Figure 4b).For this reason, different approaches have been reported for the stabilization of the cubic phase, such as: the use of alkyl phosphonic acids or phosphines in the synthesis of $CsPbI_3$ NCs;[51,52] washing procedures employing ethyl acetate;[28] replacing part of Cs^+ cations with bigger cations;[44] and replacing Pb^{2+} ions with Mn^{2+} cations.[53,54] In this regard, we observed that the cubic $CsPbI_3$ NCs that were synthesized with our procedure had a high phase stability, without any post-synthesis

treatment. The XRD patterns of $CsPbI_3$ NC films exposed to air indicated that no phase transition occurred after 20 days (see Figure 4a). In order to understand the reason behind the phase stability of $CsPbI_3$ NCs, and possibly also the PL properties of our $CsPbX_3$ NCs, we performed XPS characterization to study their surface and composition. The surface chemistry of lead halide based perovskite NCs has been shown to play a fundamental role in determining not only their stability in air or under annealing, but also their optical performances.[17,28,60-64] The analysis of the Cs 3d, Pb 4f and X peaks (Cl 2p, Br 3d and I 3d) revealed that our $CsPbX_3$ NCs were sub-stoichiometric in Cs, while the Pb:X ratio was always close to 3 (see Figure 5). In more detail, the Cs:Pb:X ratios found in our NCs were: 0.9:1:3.1 in the case of chlorides, 0.8:1:2.8 in the case of bromides and 0.8:1:2.7 in the case of iodides. We also roughly estimated the amount of oleylammonium ions bound to $CsPbX_3$ NCs by analyzing the N 1s peak (see Figure 4).

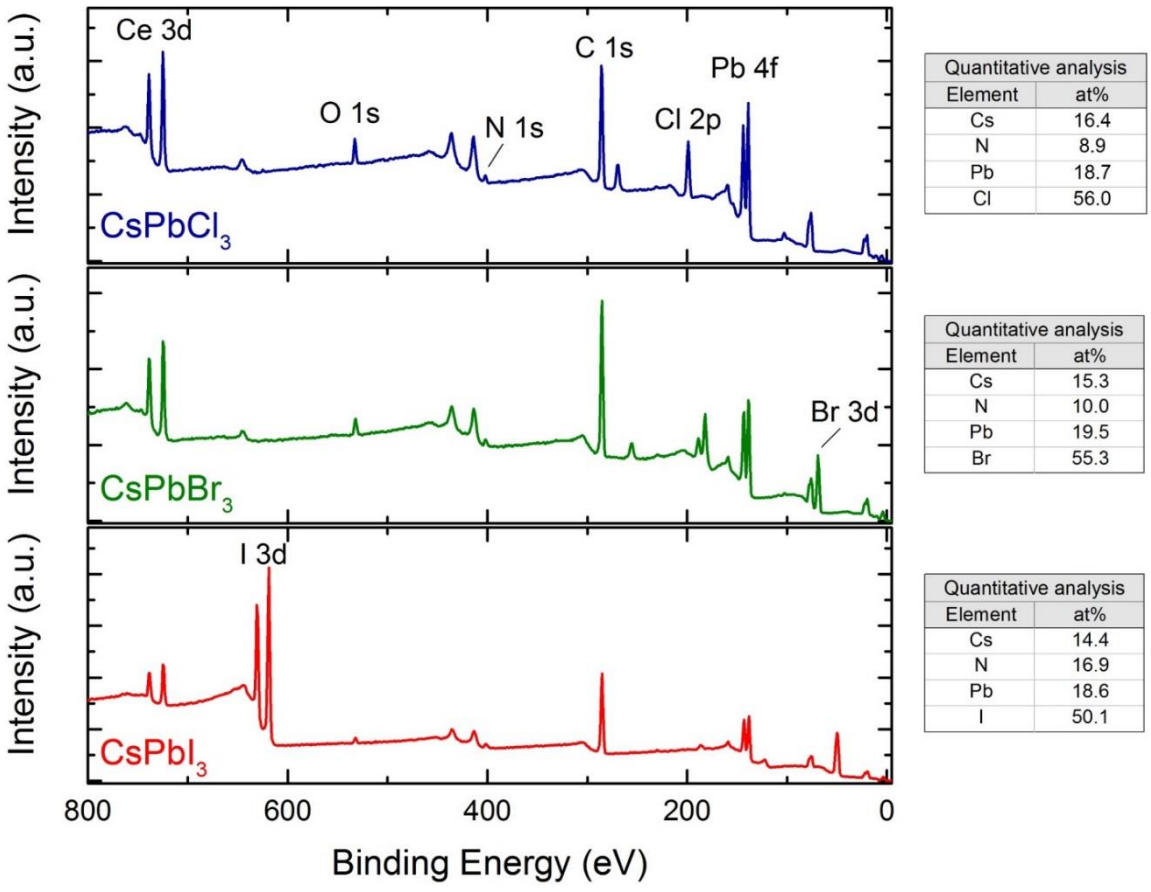

Figure 5. XPS spectra for (A) $CsPbBr_3$, (B) $CsPbCl_3$ and (C) $CsPbI_3$ NCs.

While, the chloride and bromide NCs had a ratio of Cs:N close to 1:0.5, the iodide ones had a ratio of 1:1.2. These results suggest that the surface of our $CsPbX_3$ NCs is lead halide terminated, i.e. the surface Cs ions are replaced by oleylammonium ions. Lead halide perovskite NCs with this type of surface have been reported to have improved stability and enhanced optical properties.[29,63] Indeed, Woo *et al.* ascribed the improved stability of their $CsPbBr_3$ NCs (which were obtained with the hot-

injection method, adding $ZnBr_2$ as an extra bromide source) to their lead bromide rich surfaces.[29] In addition, Ravi *et al.* demonstrated that alkylmmonium ions have the ability to substitute Cs ions on the surface of $CsPbX_3$ NCs, which consequently improves their stability and optical properties.[63] We believe that our new synthetic procedure is favorable with regards to the formation of oleylammonium-lead-halide surfaces thanks to the halide rich conditions that are used (see the Experimental Details). Moreover, the release of X^- ions from the acyl halides is accompanied by the concomitant release of H^+ ions which can drive the protonation of the oleylamine in solution (see Equations 3-5).

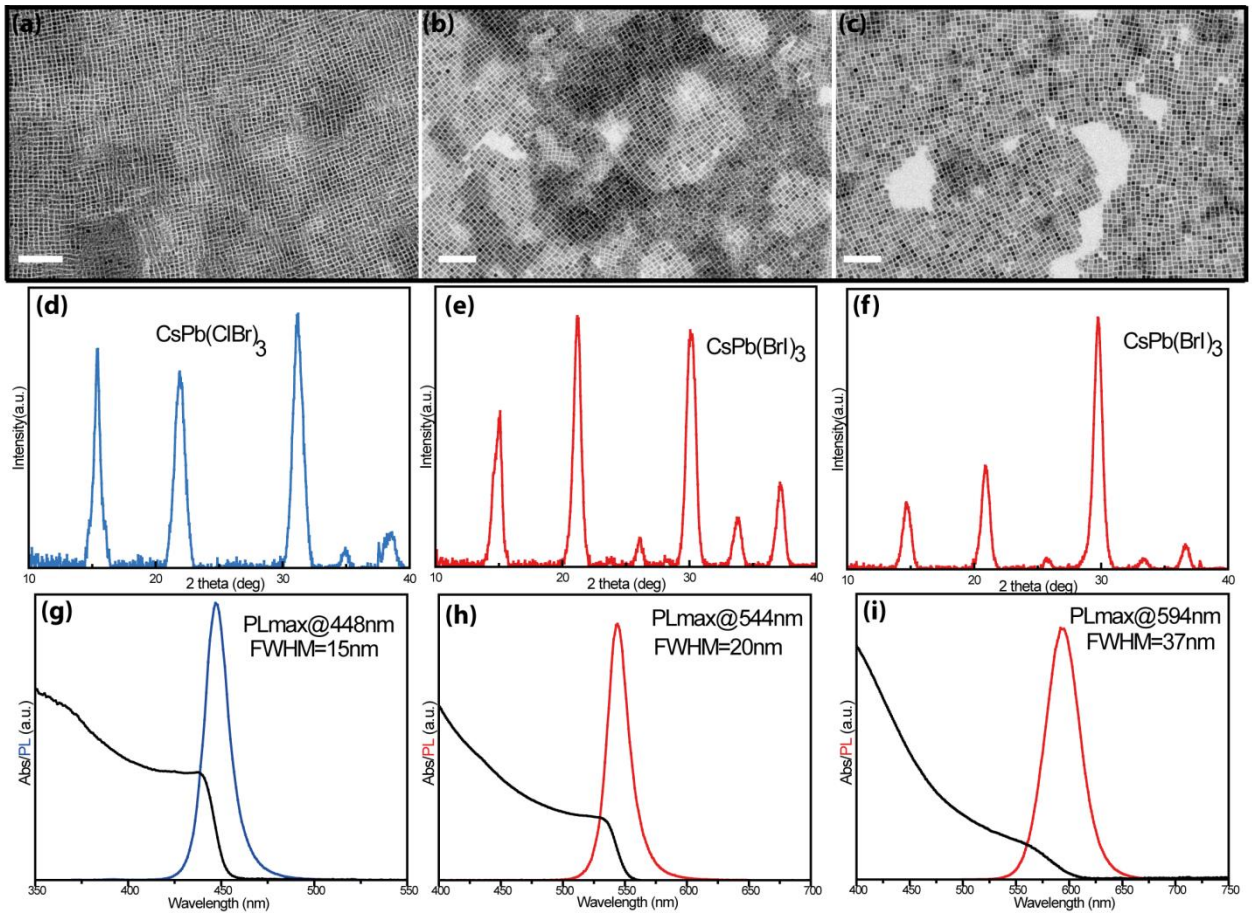

Figure 6. Bright field TEM images of (a) $CsPb(ClBr)_3$ and (b,c) $CsPb(BrI)_3$, NCs. Scale bars are 100 nm in all images. XRD patterns of (d) $CsPb(ClBr)_3$ and (e,f) $CsPb(BrI)_3$ along with their absorption and PL spectra (g-f) respectively.

As benzoyl halides can be easily mixed together, we also tested our procedure to synthesize mixed halide NCs, namely $CsPb(Cl/Br)_3$ and $CsPb(Br/I)_3$. These compounds, as well as the starting $CsPbX_3$ NCs, could be successfully synthetized with a narrow size distribution, phase purity and good optical properties, simply by injecting mixtures of benzoyl halides in appropriate ratios (see Experimental Details and Figure 6). Also, given the strong reactivity of benzoyl halides even at room temperature,

we tested the $CsPbX_3$ NCs for post-synthesis transformations, namely for anion-exchange reactions. So far, the most commonly used precursors for anion exchange reactions have been metal halide salts (*i.e.* MX_2 where M = Pb, Zn, Mg, Cu, Ca and X = Cl, Br, I) and oleylammonium or tetrabutylammonium halides.[20-25] However, a disadvantage of these halide sources is that they either suffer from poor solubility in non-polar solvents or their reactivity is limited at room temperature. On the contrary, benzoyl halides were observed to be efficient precursors for anion exchange reactions: the addition of benzoyl chloride or benzoyl iodide to pre-synthesized $CsPbBr_3$ NCs led to a fast blue shift or red shift, respectively, of both the PL and the absorption spectra of the NCs. In both cases, the XRD patterns of the resulting NCs confirmed the retention of the parent cubic perovskite structure, and there was a systematic shift of the peaks induced by the variation of the lattice parameters (see Figure 6b of the SI). Interestingly, the back exchange reactions, $CsPbCl_3 \rightarrow CsPbBr_3$ and $CsPbI_3 \rightarrow CsPbBr_3$, also worked efficiently when benzoyl bromide was added to the $CsPbCl_3$ and $CsPBI_3$ NCs, respectively (see Figure 7-9).

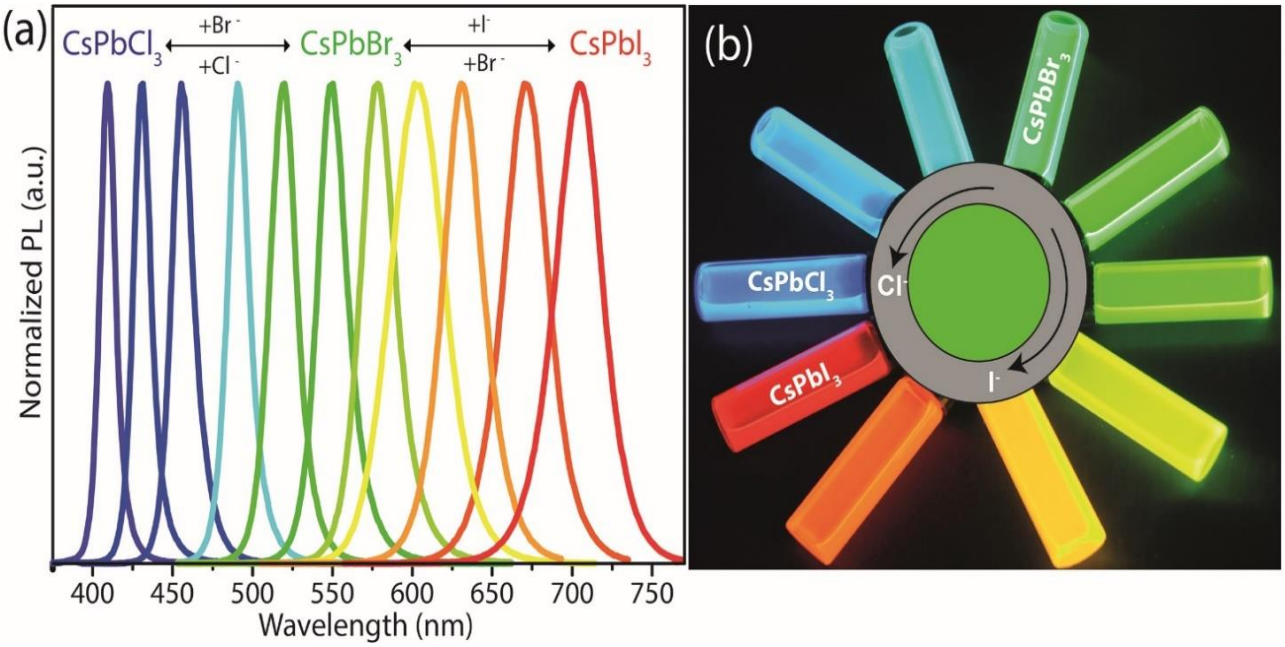

Figure 7. (a) Evolution of the PL spectra of $CsPbBr_3$ NCs by the addition of benzoyl chloride or benzoyl iodide. (b) Picture of the different $CsPbX_3$ NC solutions obtained by anion exchange under a UV lamp.

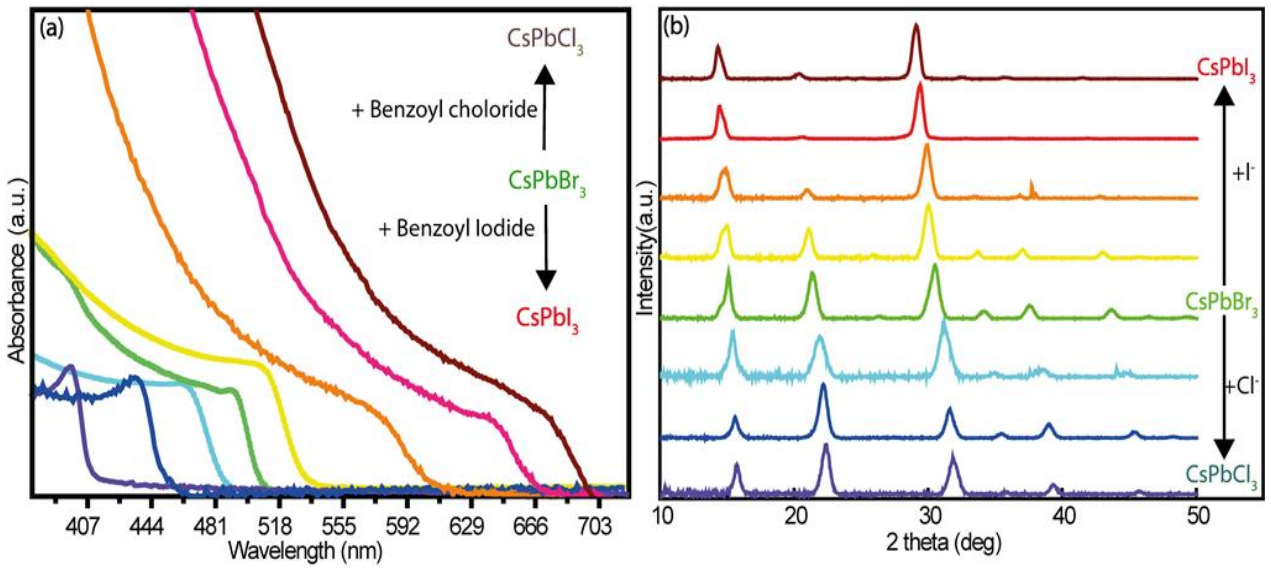

Figure 8. (a) Evolution of the absorbance spectra of representative anion-exchanged NCs, which were obtained from $CsPbBr_3$ NCs by adding benzoyl chloride or benzoyl iodide. (b) XRD patterns of the pristine $CsPbBr_3$ NCs and the anion-exchanged samples (using benzoyl chloride and benzoyl iodide), showing the retention of the cubic perovskite structure. The shift of the XRD reflections is linearly dependent on the composition, indicating the formation of uniform solid solutions.

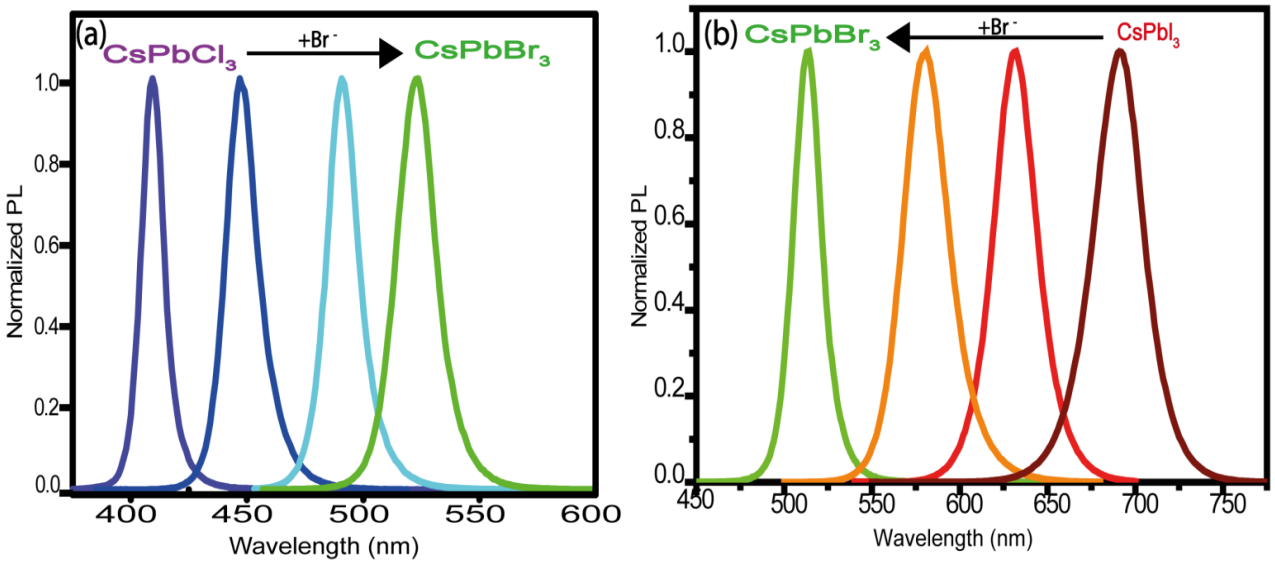

Figure 9. Evolution of the PL spectra of the exchanged NCs that were obtained from $CsPbCl_3$ NCs (upper panel) and $CsPbI_3$ NCs (lower panel) by adding benzoyl bromide.

We then extended our protocol to the colloidal synthesis of hybrid organic-inorganic $APbX_3$ (A=MA, FA) perovskite NCs. We first tested our hot-injection approach by preparing $MAPbX_3$ NCs which, to date, have been mainly produced using the LARP technique since standard hot-injection techniques

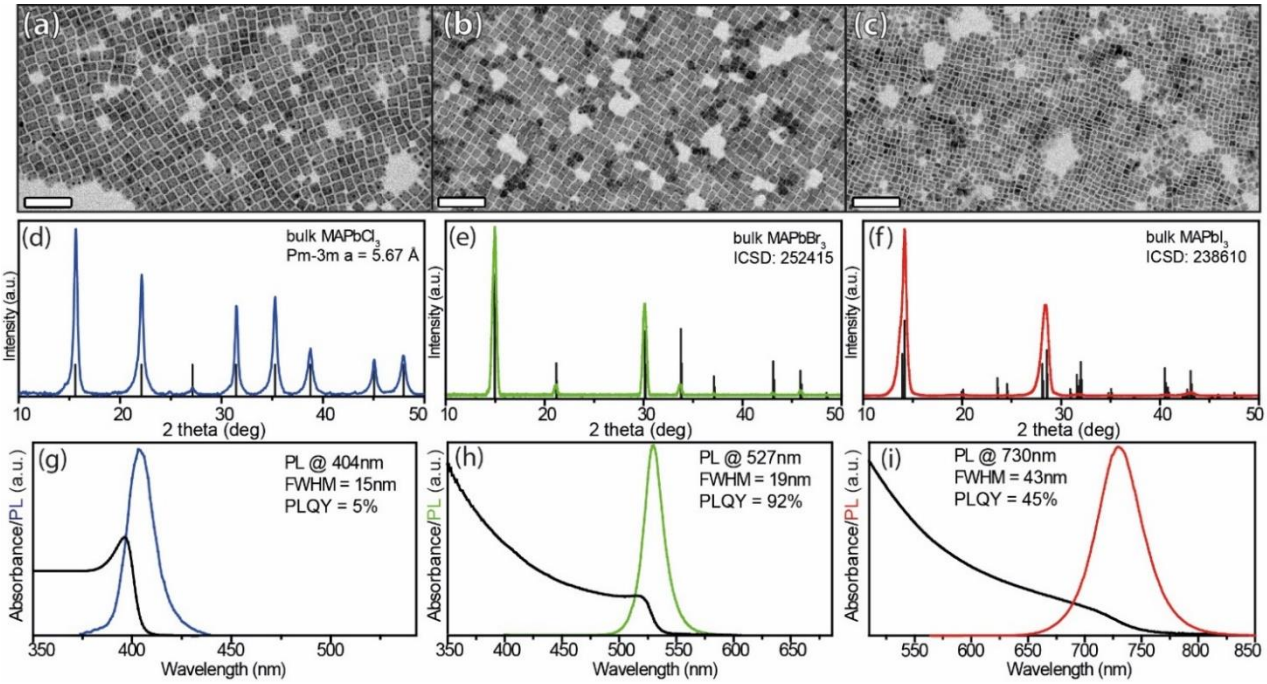

Figure 10. Bright-field TEM images of (a) MAPbCl3, (b) MAPbBr3, and (c) MAPbI3 NCs. Scale bars are 100 nm in all images. XRD patterns of (d) MAPbCl3, (e) MAPbBr3, and (f) MAPbI3 NCs along with their corresponding bulk cubic reference patterns. In the case of MAPbCl3, the bulk reflections were calculated using the crystal structure that was reported by Maculan et al.[65] Absorption and PL spectra of (g) MAPbCl3, (h) MAPbBr3, and (i) MAPbI3 NCs dispersed in toluene

result in NCs with poor optical properties.[32] These hybrid organic-inorganic NCs could be synthesized using the protocol we devised for $CsPbX_3$ NCs, with only minor modifications (see Experimental Details). Bright field TEM images of representative $MAPbX_3$ NCs are shown in Figure 10a-c. In all three cases, a nearly cubic morphology with a narrow size distribution was observed: the average length of the NCs was 20.1±2.9nm for $MAPbCl_3$, 15.5±1.8nm for $MAPbBr_3$ and 8.9±2.4nm for $MAPbI_3$. It is worth mentioning that PbO was used as the lead precursor for the synthesis of $MAPbX_3$ NCs instead of lead acetate as it enabled a greater control over the size distribution and shape of the final NCs (Figure 11). According to XRD analysis, the structure of the $MAPbBr_3$ NCs matched the cubic perovskite structure (ICSD code 252415), while that of $MAPbI_3$ NCs exhibited a tetragonal $CH_3NH_3PbI_3$ crystal phase (space group I4/mcm, ICSD code 238610). This is in agreement with a recent report by Zhang *et al.* on identical systems (Figure 10e-f).[38] Given the absence of any reference pattern for $MAPbCl_3$ in the ICSD database, we compared the XRD pattern of our $MAPbCl_3$ NCs with those of bulk crystals that are reported in literature, and we found a good match with that reported by Maculan *et al.,* which is a cubic perovskite structure (space group Pm-3m) with a = 5.67 Å (see Figure 9d).[65,66]

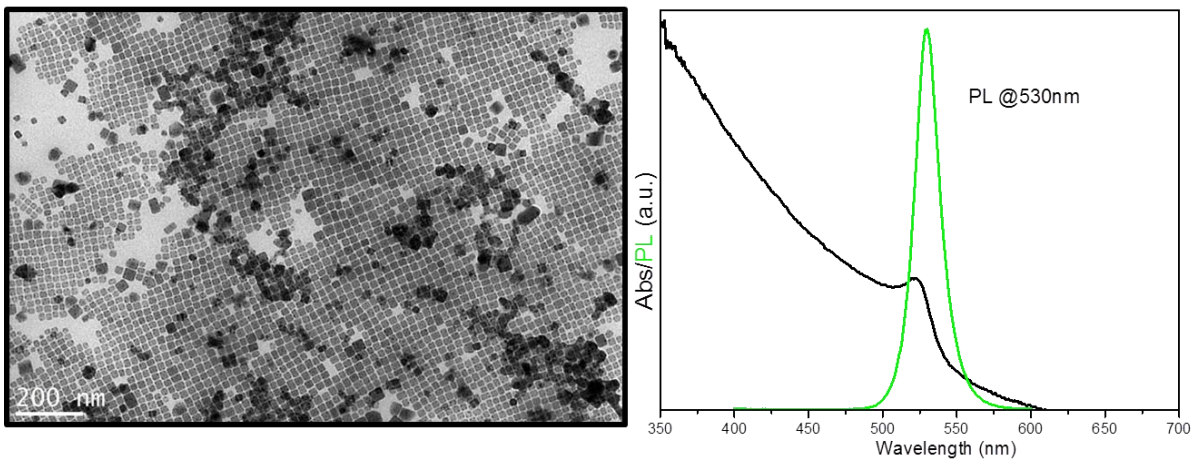

Figure 14. BF-TEM image along with absorption and PL spectra of $MAPbBr_3$ NCs, which were synthesized using lead acetate trihydrate.

The UV−visible absorption and PL spectra of $MAPbX_3$ NCs are shown in Figure 10g-i. Similar to what has been previously reported, all NC samples had a narrow PL emission with a FWHM of 15nm for $MAPbCl_3$, 19nm for $MAPbBr_3$ and 43nm for $MAPbI_3$.[15,32,66] Remarkably, the $MAPbBr_3$ and $MAPbI_3$ NCs had a PLQY as high as 92% and 45%, respectively, while $MAPbCl_3$ NCs the PLQY was around 5%. Similar to the case of $CsPbCl_3$ NCs, we did observe an enhancement of the PL emission of $MAPbCl_3$ NCs when increasing the amount of the Cl precursor to 1mmol. Such improvement occurred along with the formation of a secondary $PbCl_2$ undesired phase. These findings suggest that, as in the case of $CsPbX_3$ systems, a lead halide rich environment could enhance the PL emission of the resulting $MAPbCl_3$ NCs. Unfortunately, in this case such environment leads also to the formation of $PbCl_2$ which, thus, limits the effective amount of the Cl precursor that can be employed.

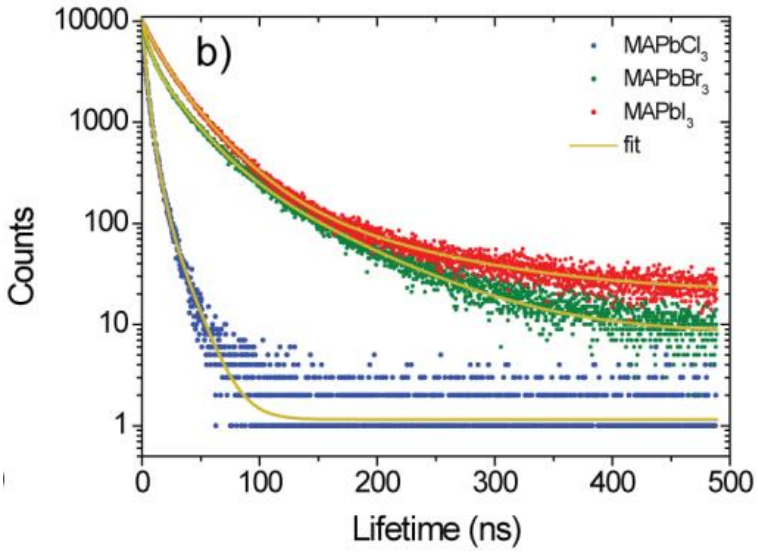

Figure 12. Decay lifetimes of $MAPbX_3$ NCs together with their multi-exponential fittings.

Table 3. The table encloses all the photo-physical data of all the representative $APbX_3$ NCs.

Sample name	A_1	τ_1 (ns)	A_2	τ_2 (ns)	A_3	τ_3 (ns)	τ_{AVG} (ns)	QY %	Γ_{RAD} (1/µs)	$\Gamma_{NON-RAD}$ (1/µs)
$MAPbCl_3$	4905	1.22	5444	4.24	608	12.39	5.42	5	9.21	175.15
$MAPbBr_3$	4771	5.6	4115	23.91	704	72.02	35	92	26.28	2.28
$MAPbI_3$	4798	12.85	4938	30.08	324	103.01	35.71	45	12.61	15.41

Decay lifetimes, which were acquired by means of TCSPC measurements, were 5.4ns for $MAPbCl_3$ NCs, 35ns for $MAPbBr_3$ NCs and 35.7ns for $MAPbI_3$ NCs (see Figure 12 and Table 3). Although the synthesis of $MAPbX_3$ NCs has been optimized over the last few years, $FAPbX_3$ NCs with optimal optical properties as well as a narrow size distribution and phase purity have not yet been prepared by either hot-injection techniques or by the LARP approach.[18,40,44-46] Lately, these compounds have received considerable interest since they have several advantages over their methylammonium counterparts, such as a higher stability due to a more symmetric and tightly packed crystal structure.[67-69] We could also synthetize $FAPbX_3$ NCs using our protocol (see Experimental Details). Typical TEM images of $FAPbCl_3$ and $FAPbBr_3$ NCs evidenced a narrow size distribution, which became slightly broader in the case of $FAPbI_3$ NCs (Figure 13a-c). The average size of the NCs was 11.2±1.4nm for $FAPbCl_3$, 12.4±1.6nm for $FAPbBr_3$ and 14.2±2.8nm for $FAPbI_3$. Regarding the structural analysis, given the absence of any $FAPbX_3$ reference patterns in the ICSD database, we had to compare the XRD pattern of our $FAPbX_3$ NCs with those of bulk crystals which have been recently published.In the case of $FAPbBr_3$ and $FAPbI_3$ NCs, a good match was found with the cubic structures reported by Zhumekenov *et al.*[70] (Figure 13d-f). On the other hand, no cubic bulk structure has been reported so far for $FAPbCl_3$ compounds. This can be explained by its calculated tolerance factor (1.150), which in principle is too large to allow a 3D phase formation.[71] Conversely, the refinement of the XRD pattern of our $FAPbCl_3$ NCs led to a cubic structure (space group Pm-3m) with a = 5.67 Å. This represents the first report of a cubic $FAPbCl_3$ structure. UV-vis and PL spectra of the $FAPbX_3$ NCs are shown in Figure 5g-i. Furthermore, Br and I based compounds exhibited excellent optical properties, and had a high PLQY (90% for $FAPbBr_3$ and 65% for $FAPbI_3$) and narrow PL emission (20nm for $FAPbBr_3$ and 48nm for $FAPbI_3$).

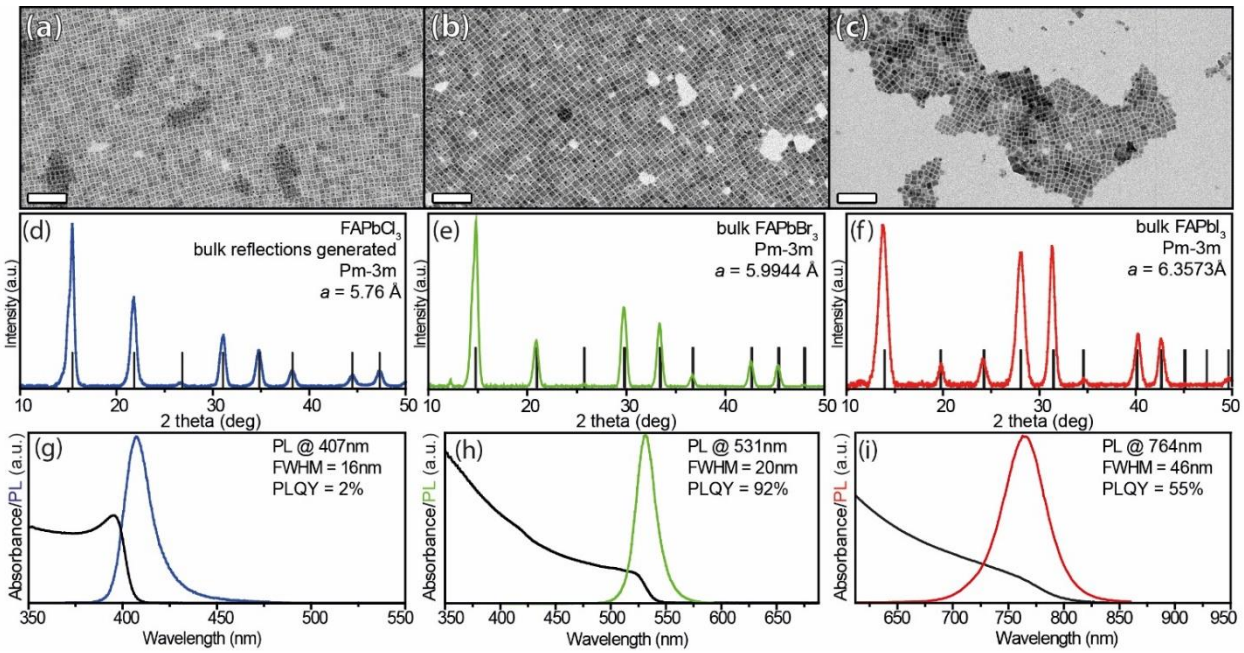

Figure 13. Bright field TEM images of (a) $FAPbCl_3$, (b) $FAPbBr_3$, and (c) $FAPbI_3$ NCs. Scale bars are 100 nm in all images. XRD patterns of (d) $FAPbCl_3$, (e) $FAPbBr_3$, and (f) $FAPbI_3$ NCs along with the corresponding bulk cubic reference patterns. For $FAPbBr_3$ and $FAPbI_3$ NCs, the bulk reflections were calculated using the crystal structure reported by Zhumekenov et al.,[70] while the reflections of the $FAPbCl_3$ NCs were generated using a cubic perovskite structure (Pm-3m) with a= 5.76 Å. Absorption and PL spectra of (g) $FAPbCl_3$, (h) $FAPbBr_3$, and (i) $FAPbI_3$ NCs dispersed in toluene.

The $FAPbCl_3$ NCs were characterized by having a narrow PL (FWHM = 16nm), but a low PLQY (about 2%). Decay lifetimes, which were acquired by means of TCSPC measurements, were 14.8ns for $FAPbCl_3$ NCs, 30.3 ns for $FAPbBr_3$ NCs and 75.2ns for $FAPbI_3$ NCs (Figure 14, Table 4).

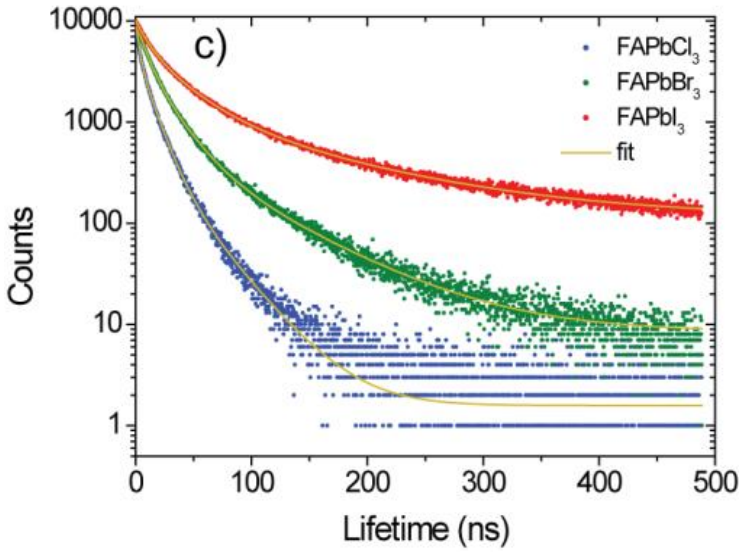

Figure 14. Decay lifetimes of $FAPbX_3$ NCs together with their multi-exponential fittings

Table 4. The table encloses all the photo-physical data of all the representative $FAPbX_3$ NCs.

Sample name	A_1	τ_1 (ns)	A_2	τ_2 (ns)	A_3	τ_3 (ns)	τ_{AVG} (ns)	QY %	Γ_{RAD} (1/μs)	$\Gamma_{NON-RAD}$ (1/μs)
$FAPbCl_3$	4752	2.63	4553	11.88	558	32.13	14.81	2	1.35	66.18
$FAPbBr_3$	4944	8.25	4305	21.06	643	69.37	30.33	92	30.33	2.63
$FAPbI_3$	4329	10.02	4501	36.13	1138	135.01	75.23	55	7.31	5.98

Finally, we investigated the amplified spontaneous emission (ASE) which occurred in the $APbBr_3$ NC films. These particular NCs had the highest PLQYs (more than 90% in all three of cases), much higher than those of their Cl and I counterparts ($APbCl_3$ and $APbI_3$). Figure 15 reports the emission spectra showing ASE of the three $APbBr_3$ NC samples together with the ASE thresholds that were calculated by the ratio of the ASE to the PL peaks. All three systems manifested very low ASE thresholds, ranging from 2.2 to 8.1 μJ/cm^2, which are either comparable to or lower than the lowest values that have een reported in the literature (see Table 5).[72] Moreover, all three of the systems had very narrow ASE FWHMs due to the very narrow gain in bandwidth (Figure 15).[73]

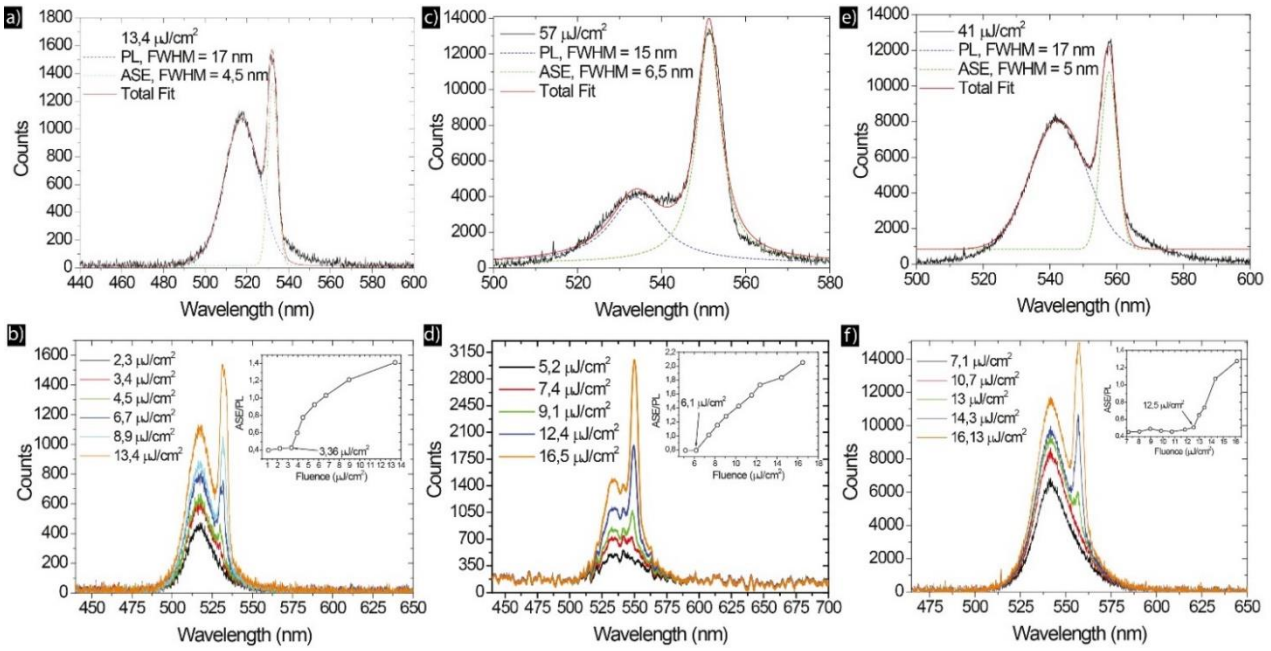

Figure 15: PL and ASE dynamics for a,b) $CsPbBr_3$, c,d) $MAPbBr_3$ and e, f) $FAPbBr_3$ together with the ASE threshold calculations (insets). The ASE FWHMs were calculated by Lorentzian fitting of the peaks.

Table 5. Overview of the amplified spontaneous emission thresholds of organic-inorganic and all-inorganic lead bromide perovskite NCs.

Material [morphology]	ASE threshold [μJ/cm^2]	Reference
$CsPbBr_3$ [NCs]	2.2	this work
$MAPbBr_3$ [NCs]	4.4	this work
$FAPbBr_3$ [NCs]	8.1	this work
$CsPbBr_3$ [NCs]	5	[73]
$CsPbBr_3$ [NCs]	22	[74]
$CsPbBr_3$ [NCs]	192	[62]
$CsPbBr_3$ [NCs]	2.1	[57]
$MAPbBr_3$ [NCs]	13.9	[72]
$MAPbBr_3$ [NCs]	350	[75]
$MAPbBr_3$ [NWs]	3.0	[32]
$FAPbBr_3$ [NCs]	14	[45]

4.4. Conclusion

In conclusion, we have demonstrated a new colloidal route for the preparation of both all-inorganic and hybrid organic-inorganic $APbX_3$ NCs (A= Cs, MA, FA and X= Cl, Br, I). Our approach is based on the injection of benzoyl halides (as halide precursors) into a solution of desired cations and proper ligands (oleylamine and oleic acid) at a desired temperature. After the injection, a fast release of halide ions occurs, which is followed by the nucleation and growth of metal halide NCs. In all the cases, the resulting $APbX_3$ NCs show a high phase stability, a very good size distribution and excellent optical properties. They exhibit a narrow PL emission and high PLQYs, which are around 90% in the case of $APbBr_3$ systems, 55% in the case of $APbI_3$ materials, and a record value of 65% in the case if $CsPbCl_3$ NCs. The optical quality of our materials was also reflected by the low values of their ASE thresholds. The origin of such improvements with regards to the stability and optical properties of $CsPbX_3$ NCs was tentatively ascribed to the formation of lead-halide terminated surfaces in which Cs ions are partially replaced by oleylammonium ions. Indeed, the formation of such surfaces is

promoted by our synthetic conditions. To conclude, we believe that the versatility of our synthetic approach could allow for the future development of inorganic and organic metal halide NC systems.

4.5. References

(1) Huang, H.; Bodnarchuk, M. I.; Kershaw, S. V.; Kovalenko, M. V.; Rogach, A. L. *ACS Energy Lett.* **2017**, *2*, 2071.

(2) Li, X.; Wu, Y.; Zhang, S.; Cai, B.; Gu, Y.; Song, J.; Zeng, H. *Adv. Funct. Mater.* **2016**, *26*, 2435.

(3) Liu, Z.; Bekenstein, Y.; Ye, X.; Nguyen, S. C.; Swabeck, J.; Zhang, D.; Lee, S.-T.; Yang, P.; Ma, W.; Alivisatos, A. P. *Journal of the American Chemical Society* **2017**, *139*, 5309.

(4) Ono, L. K.; Juarez-Perez, E. J.; Qi, Y. *ACS Appl. Mater. Interfaces* **2017**, *9*, 30197.

(5) Giustino, F.; Snaith, H. J. *ACS Energy Lett.* **2016**, *1*, 1233.

(6) Zhao, X.-G.; Yang, J.-H.; Fu, Y.; Yang, D.; Xu, Q.; Yu, L.; Wei, S.-H.; Zhang, L. *J. Am. Chem. Soc.* **2017**, *139*, 2630.

(7) Amgar, D.; Aharon, S.; Etgar, L. *Adv. Funct. Mater.* **2016**, *26*, 8576.

(8) Manser, J. S.; Christians, J. A.; Kamat, P. V. *Chem. Rev.* **2016**, *116*, 12956.

(9) Huang, H.; Polavarapu, L.; Sichert, J. A.; Susha, A. S.; Urban, A. S.; Rogach, A. L. *NPG Asia Mater.* **2016**, *8*, e328.

(10) Bai, S.; Yuan, Z.; Gao, F. *J. Mater. Chem. C* **2016**, *4*, 3898.

(11) Fu, P.; Shan, Q.; Shang, Y.; Song, J.; Zeng, H.; Ning, Z.; Gong, J. *Sci. Bull.* **2017**, *62*, 369.

(12) Kovalenko, M. V.; Protesescu, L.; Bodnarchuk, M. I. *Science* **2017**, *358*, 745.

(13) Adjokatse, S.; Fang, H.-H.; Loi, M. A. *Mater. Today* **2017**, *20*, 413.

(14) Hu, F.; Zhang, H.; Sun, C.; Yin, C.; Lv, B.; Zhang, C.; Yu, W. W.; Wang, X.; Zhang, Y.; Xiao, M. *ACS Nano* **2015**, *9*, 12410.

(15) Gonzalez-Carrero, S.; Francés-Soriano, L.; González-Béjar, M.; Agouram, S.; Galian, R. E.; Pérez-Prieto, J. *Small* **2016**, *12*, 5245.

(16) Kim, Y.; Yassitepe, E.; Voznyy, O.; Comin, R.; Walters, G.; Gong, X.; Kanjanaboos, P.; Nogueira, A. F.; Sargent, E. H. *ACS Appl. Mater. Interfaces* **2015**, *7*, 25007.

(17) Koscher, B. A.; Swabeck, J. K.; Bronstein, N. D.; Alivisatos, A. P. *J. Am. Chem. Soc.* **2017**, *139*, 6566.

(18) Levchuk, I.; Osvet, A.; Tang, X.; Brandl, M.; Perea, J. D.; Hoegl, F.; Matt, G. J.; Hock, R.; Batentschuk, M.; Brabec, C. J. *Nano Lett.* **2017**, *17*, 2765.

(19) Protesescu, L.; Yakunin, S.; Bodnarchuk, M. I.; Krieg, F.; Caputo, R.; Hendon, C. H.; Yang, R. X.; Walsh, A.; Kovalenko, M. V. *Nano Lett.* **2015**, *15*, 3692.

(20) Zhang, T.; Li, G.; Chang, Y.; Wang, X.; Zhang, B.; Mou, H.; Jiang, Y. *CrystEngComm* **2017**, *19*, 1165.

(21) Akkerman, Q. A.; D'Innocenzo, V.; Accornero, S.; Scarpellini, A.; Petrozza, A.; Prato, M.; Manna, L. *J. Am. Chem. Soc.* **2015**, *137*, 10276.

(22) Guhrenz, C.; Benad, A.; Ziegler, C.; Haubold, D.; Gaponik, N.; Eychmüller, A. *Chem. Mater.* **2016**, *28*, 9033.

(23) Nedelcu, G.; Protesescu, L.; Yakunin, S.; Bodnarchuk, M. I.; Grotevent, M. J.; Kovalenko, M. V. *Nano Lett.* **2015**, *15*, 5635.

(24) De Trizio, L.; Manna, L. *Chem. Rev.* **2016**, *116*, 10852.

(25) Parobek, D.; Dong, Y.; Qiao, T.; Rossi, D.; Son, D. H. *J. Am. Chem. Soc.* **2017**, *139*, 4358.

(26) Dou, L. *Journal of Materials Chemistry C* **2017**, *5*, 11165.

(27) Ning, C.-Z.; Dou, L.; Yang, P. *Nat. Rev. Mater.* **2017**, *2*, 17070.

(28) Swarnkar, A.; Marshall, A. R.; Sanehira, E. M.; Chernomordik, B. D.; Moore, D. T.; Christians, J. A.; Chakrabarti, T.; Luther, J. M. *Science* **2016**, *354*, 92.

(29) Woo, J. Y.; Kim, Y.; Bae, J.; Kim, T. G.; Kim, J. W.; Lee, D. C.; Jeong, S. *Chem. Mater.* **2017**, *29*, 7088.

(30) Koolyk, M.; Amgar, D.; Aharon, S.; Etgar, L. *Nanoscale* **2016**, *8*, 6403.

(31) Li, G.; Wang, H.; Zhang, T.; Mi, L.; Zhang, Y.; Zhang, Z.; Zhang, W.; Jiang, Y. *Adv. Funct. Mater.* **2016**, *26*, 8478.

(32) Vybornyi, O.; Yakunin, S.; Kovalenko, M. V. *Nanoscale* **2016**, *8*, 6278.

(33) Jellicoe, T. C.; Richter, J. M.; Glass, H. F. J.; Tabachnyk, M.; Brady, R.; Dutton, S. E.; Rao, A.; Friend, R. H.; Credgington, D.; Greenham, N. C.; Böhm, M. L. *J. Am. Chem. Soc.* **2016**, *138*, 2941.

(34) Sun, S.; Yuan, D.; Xu, Y.; Wang, A.; Deng, Z. *ACS nano* **2016**, *10*, 3648.

(35) Kumar, S.; Jagielski, J.; Yakunin, S.; Rice, P.; Chiu, Y.-C.; Wang, M.; Nedelcu, G.; Kim, Y.; Lin, S.; Santos, E. J. G.; Kovalenko, M. V.; Shih, C.-J. *ACS Nano* **2016**, *10*, 9720.

(36) Schmidt, L. C.; Pertegás, A.; González-Carrero, S.; Malinkiewicz, O.; Agouram, S.; Mínguez Espallargas, G.; Bolink, H. J.; Galian, R. E.; Pérez-Prieto, J. *J. Am. Chem. Soc.* **2014**, *136*, 850.

(37) Zhang, F.; Zhong, H.; Chen, C.; Wu, X.-g.; Hu, X.; Huang, H.; Han, J.; Zou, B.; Dong, Y. *ACS Nano* **2015**, *9*, 4533.

(38) Zhang, F.; Huang, S.; Wang, P.; Chen, X.; Zhao, S.; Dong, Y.; Zhong, H. *Chem. Mater.* **2017**, *29*, 3793.

(39) Levchuk, I.; Herre, P.; Brandl, M.; Osvet, A.; Hock, R.; Peukert, W.; Schweizer, P.; Spiecker, E.; Batentschuk, M.; Brabec, C. J. *Chem. Commun.* **2017**, *53*, 244.

(40) Minh, D. N.; Kim, J.; Hyon, J.; Sim, J. H.; Sowlih, H. H.; Seo, C.; Nam, J.; Eom, S.; Suk, S.; Lee, S.; Kim, E.; Kang, Y. *Chem. Mater.* **2017**, *29*, 5713.

(41) Kang, J.; Wang, L.-W. *J. Phys. Chem. Lett.* **2017**, *8*, 489.

(42) Wei, S.; Yang, Y.; Kang, X.; Wang, L.; Huang, L.; Pan, D. *Chem. Commun.* **2016**, *52*, 7265.

(43) Yassitepe, E.; Yang, Z.; Voznyy, O.; Kim, Y.; Walters, G.; Castañeda, J. A.; Kanjanaboos, P.; Yuan, M.; Gong, X.; Fan, F.; Pan, J.; Hoogland, S.; Comin, R.; Bakr, O. M.; Padilha, L. A.; Nogueira, A. F.; Sargent, E. H. *Adv. Funct. Mater.* **2016**, *26*, 8757.

(44) Protesescu, L.; Yakunin, S.; Kumar, S.; Bär, J.; Bertolotti, F.; Masciocchi, N.; Guagliardi, A.; Grotevent, M.; Shorubalko, I.; Bodnarchuk, M. I.; Shih, C.-J.; Kovalenko, M. V. *ACS Nano* **2017**, *11*, 3119.

(45) Protesescu, L.; Yakunin, S.; Bodnarchuk, M. I.; Bertolotti, F.; Masciocchi, N.; Guagliardi, A.; Kovalenko, M. V. *J. Am. Chem. Soc.* **2016**, *138*, 14202.

(46) Li, Q.; Li, H.; Shen, H.; Wang, F.; Zhao, F.; Li, F.; Zhang, X.; Li, D.; Jin, X.; Sun, W. *ACS Photonics* **2017**, *4*, 2504.

(47) Ito, D.; Yokoyama, S.; Zaikova, T.; Masuko, K.; Hutchison, J. E. *ACS Nano* **2014**, *8*, 64.

(48) Patai, S. *The chemistry of acyl halides*; John Wiley & Sons Ltd: UK, 1972.

(49) Hoffmann, H. M. R.; Haase, K. *Synthesis* **1981**, *9*, 715.

(50) Harris, D. K.; Bawendi, M. G. *J. Am. Chem. Soc.* **2012**, *134*, 20211.

(51) Wang, C.; Chesman, A. S. R.; Jasieniak, J. J. *Chem. Commun.* **2017**, *53*, 232.

(52) Liu, F.; Zhang, Y.; Ding, C.; Kobayashi, S.; Izuishi, T.; Nakazawa, N.; Toyoda, T.; Ohta, T.; Hayase, S.; Minemoto, T.; Yoshino, K.; Dai, S.; Shen, Q. *ACS Nano* **2017**, *11*, 10373.

(53) Zou, S.; Liu, Y.; Li, J.; Liu, C.; Feng, R.; Jiang, F.; Li, Y.; Song, J.; Zeng, H.; Hong, M.; Chen, X. *J. Am. Chem. Soc.* **2017**, *139*, 11443.

(54) Akkerman, Q. A.; Meggiolaro, D.; Dang, Z.; De Angelis, F.; Manna, L. *ACS Energy Lett.* **2017**, *2*, 2183.

(55) Theobald, D. W.; Smith, J. C. *Chem. Ind.* **1958**, *32*, 1007.

(56) Voronkov, M. G.; Tsyrendorzhieva, I. P.; Lis, A. V.; Grinberg, E. E.; Shatokhina, V. A.; Rakhlin, V. I. *Russ. J. Org. Chem.* **2013**, *49*, 147.

(57) Tong, Y.; Bladt, E.; Aygüler, M. F.; Manzi, A.; Milowska, K. Z.; Hintermayr, V. A.; Docampo, P.; Bals, S.; Urban, A. S.; Polavarapu, L.; Feldmann, J. *Angew. Chem., Int. Ed.* **2016**, *55*, 13887.

(58) Trots, D. M.; Myagkota, S. V. *J. Phys. Chem. Solids* **2008**, *69*, 2520.

(59) Kim, Y. G.; Kim, T.-Y.; Oh, J. H.; Choi, K. S.; Kim, Y.-J.; Kim, S. Y. *Phys. Chem. Chem. Phys.* **2017**, *19*, 6257.

(60) Pan, A.; He, B.; Fan, X.; Liu, Z.; Urban, J. J.; Alivisatos, A. P.; He, L.; Liu, Y. *ACS Nano* **2016**, *10*, 7943.

(61) Giansante, C.; Infante, I. *J. Phys. Chem. Lett.* **2017**, *8*, 5209.

(62) Pan, J.; Sarmah, S. P.; Murali, B.; Dursun, I.; Peng, W.; Parida, M. R.; Liu, J.; Sinatra, L.; Alyami, N.; Zhao, C.; Alarousu, E.; Ng, T. K.; Ooi, B. S.; Bakr, O. M.; Mohammed, O. F. *J. Phys. Chem. Lett.* **2015**, *6*, 5027.

(63) Ravi, V. K.; Santra, P. K.; Joshi, N.; Chugh, J.; Singh, S. K.; Rensmo, H.; Ghosh, P.; Nag, A. *J. Phys. Chem. Lett.* **2017**, *8*, 4988.

(64) De Roo, J.; Ibáñez, M.; Geiregat, P.; Nedelcu, G.; Walravens, W.; Maes, J.; Martins, J. C.; Van Driessche, I.; Kovalenko, M. V.; Hens, Z. *ACS Nano* **2016**, *10*, 2071.

(65) Maculan, G.; Sheikh, A. D.; Abdelhady, A. L.; Saidaminov, M. I.; Haque, M. A.; Murali, B.; Alarousu, E.; Mohammed, O. F.; Wu, T.; Bakr, O. M. *J. Phys. Chem. Lett.* **2015**, *6*, 3781.

(66) Shamsi, J.; Abdelhady, A. L.; Accornero, S.; Arciniegas, M.; Goldoni, L.; Kandada, A. R. S.; Petrozza, A.; Manna, L. *ACS Energy Lett.* **2016**, *1*, 1042.

(67) Pellet, N.; Gao, P.; Gregori, G.; Yang, T.-Y.; Nazeeruddin, M. K.; Maier, J.; Grätzel, M. *Angew. Chem., Int. Ed.* **2014**, *53*, 3151.

(68) Eperon, G. E.; Stranks, S. D.; Menelaou, C.; Johnston, M. B.; Herz, L. M.; Snaith, H. J. *Energy Environ. Sci.* **2014**, *7*, 982.

(69) Amat, A.; Mosconi, E.; Ronca, E.; Quarti, C.; Umari, P.; Nazeeruddin, M. K.; Grätzel, M.; De Angelis, F. *Nano Lett.* **2014**, *14*, 3608.

(70) Zhumekenov, A. A.; Saidaminov, M. I.; Haque, M. A.; Alarousu, E.; Sarmah, S. P.; Murali, B.; Dursun, I.; Miao, X.-H.; Abdelhady, A. L.; Wu, T.; Mohammed, O. F.; Bakr, O. M. *ACS Energy Lett.* **2016**, *1*, 32.

(71) Becker, M.; Kluner, T.; Wark, M. *Dalton Trans.* **2017**, *46*, 3500.

(72) Veldhuis, S. A.; Tay, Y. K. E.; Bruno, A.; Dintakurti, S. S. H.; Bhaumik, S.; Muduli, S. K.; Li, M.; Mathews, N.; Sum, T. C.; Mhaisalkar, S. G. *Nano Lett.* **2017**, 7424.

(73) Yakunin, S.; Protesescu, L.; Krieg, F.; Bodnarchuk, M. I.; Nedelcu, G.; Humer, M.; De Luca, G.; Fiebig, M.; Heiss, W.; Kovalenko, M. V. *Nat. Commun.* **2015**, *6*, 8056.

(74) Wang, Y.; Li, X.; Song, J.; Xiao, L.; Zeng, H.; Sun, H. *Adv. Mater.* **2015**, *27*, 7101.

(75) Priante, D.; Dursun, I.; Alias, M. S.; Shi, D.; Melnikov, V. A.; Ng, T. K.; Mohammed, O. F.; Bakr, O. M.; Ooi, B. S. *Appl. Phys. Lett.* **2015**, *106*, 081902.

Chapter 5. Shape Pure, Nearly Monodisperse $CsPbBr_3$ Nanocubes Prepared using Secondary Aliphatic Amine

ABSTRACT: Fully inorganic cesium lead halide perovskite ($CsPbX_3$) nanocrystals (NCs) have been intensively studied due to their excellent optical properties, especially their high photoluminescence quantum yield (PLQY), and ease of spectral tunability of the PL across the visible spectrum. Most strategies for synthesizing $CsPbX_3$ NCs so far are highly sensitive to the processing conditions and ligands combination. For example, in the synthesis of nanocubes of different sizes, it is not uncommon to have samples containing various other shapes, such as nanoplatelets and nanosheets. Here, we report a colloidal synthesis strategy for preparing shape pure and nearly monodisperse $CsPbBr_3$ nanocubes using secondary amines. Regardless of the length of the alkyl chains, the oleic acid concentration as well as the reaction temperature, only cube shape nanocrystals were obtained. . We attribute this excellent shape and phase purity to the inability of secondary amines to find the right steric conditions at the surface of the nanocrystals which consequently limits the formation of low dimensional structures. Also, no contamination from other phases, most notably Cs_4PbBr_6, was observed, presumably due to the poor ability of secondary aliphatic amines to coordinate $PbBr_2$, hence to provide a reaction environment that is depleted in Pb.

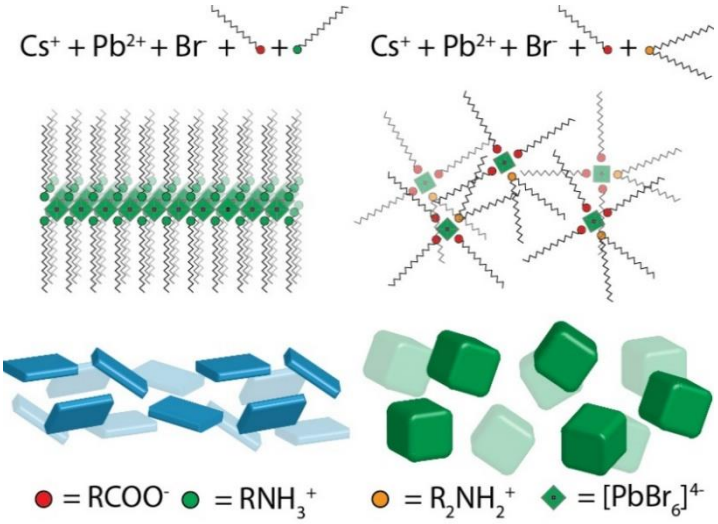

Most of the results dicussed in this chapter have been published in "Imran M, et al. Shape Pure, Nearly Monodisperse $CsPbBr_3$ Nanocubes Prepared using Secondary Aliphatic Amines. *Nano letters*. 2018 (DOI: 10.1021/acs.nanolett.8b03598)".

5.1. Introduction

Inspired by the striking performance of lead halide perovskites (LHPs) in thin films in solar cells[1-3] and starting from the works of Schmidt *et al.*[4] and Protesescu *et al.*[5], remarkable efforts have been devoted by various groups to develop synthetic approaches to high quality LHP nanocrystals (NCs) (e.g. $CsPbX_3$, $MAPbX_3$, $FAPbX_3$; MA = methylammonium, FA = formamidinium, and X = Cl^-, Br^-, I^-).[6-10] Among the various LHPs NCs, the $CsPbX_3$ ones have been particularly investigated owing to their high stability, narrow emission linewidths and high photoluminescence quantum yield (PLQY, 65-95%).[5,6] $CsPbX_3$ nanocubes were initially prepared by injecting Cs-oleate into a hot solution (140-200 °C) of PbX_2 (serving as a source of both the Pb^{2+} and X^- ions) dissolved in a mixture of oleic acid (OA) and oleylamine (OLAM). In the many works that have followed, it was shown that by choosing the appropriate combination of primary amines and protic acids (in terms of chain length and molar ratio) and/or by adjusting the reaction temperature, several groups have reported the synthesis of LHPs in different shapes: nanocubes, nanoplatelets (NPLs), nanorods (NRs), nanowires (NWs) and nanosheets (NSs).[11-18] Unfortunately, this shape variability can also be detrimental, as it is not always easy to obtain homogeneous samples in terms of shape purity. The synthesis methods for nanocubes represent an emblematic case: attempts to vary their size (by reducing the reaction temperature[11] or increasing the concentration of the acid[16,19]) often lead to the contamination of the sample with NPLs. This is attributed to an increased concentration of oleylammonium species which start competing with Cs^+ ions in the addition to the surface of the growing NCs.[19,20] Shortening the hydrocarbon chain length of the primary amine also leads to the formation of NPLs, irrespective of the syntheses temperature.[21] Finally, the use of excess amines promotes the formation of Cs-rich (Pb-depleted) phases, such as Cs_4PbX_6,[22,23] which can also be an undesired product. Ideally, one would need a robust synthesis scheme to nanocubes that is not limited by all these reaction parameters, so that cubes of various sizes can be reproducibly prepared by sampling a broad set of reaction conditions, with no contamination of NCs with other shapes and/or crystal phases. Here, we report a general synthesis procedure for nearly monodisperse, shape and phase pure $CsPbBr_3$ nanocubes. The key strategy to achieve shape and phase pure $CsPbBr_3$ nanocubes is by omitting oleylamine, a primary amine that promotes both the anisotropic growth and the formation of unwanted phases. The $CsPbBr_3$ NCs reported in this work can be synthesized by simplest possible synthesis scheme, which employs a protic acid such as OA as *the only* surfactant present in the reaction environment, delivering phase pure $CsPbBr_3$ NCs, capped only with oleate molecules. However, by using only OA the tunability of the NC size and size distribution is not optimal.

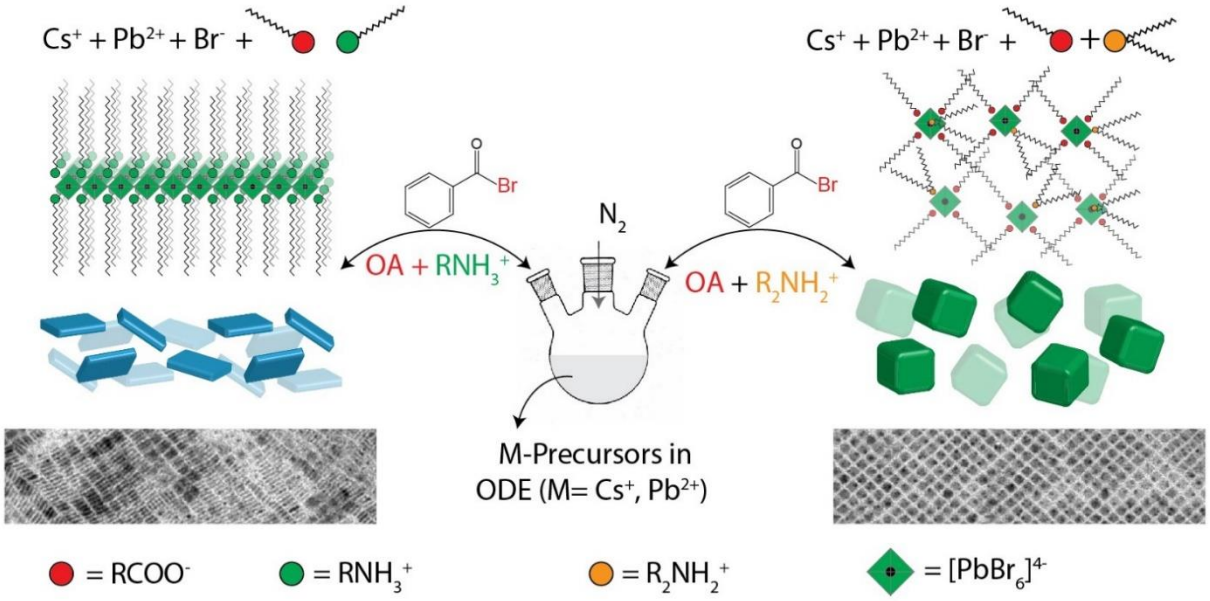

Scheme 1. Synthesis of $CsPbBr_3$ NCs in presence of protonated primary and secondary amines

To modulate the growth of the NCs, we instead introduce a secondary aliphatic amine in addition to OA. By varying either the chain length of the secondary amine or the reaction temperature (or both), we could tune the edge-length of the cubes from 5 nm to 25 nm (in the range of conditions explored). The size distributions of the NCs were also narrow, with PL emission line widths down to 68 meV. Remarkably, the secondary amines, in the form of protonated ammonium ions, are not able to bind to the surface of the $CsPbBr_3$ NCs nearly as effectively as oleylamine (or a primary amine in general), see Scheme 1. Hence they do not compete effectively with oleate molecules for binding to the surface of the NCs, and this inhibits the growth of NPLs under any of the conditions tested: different temperatures, ligand concentrations and lengths of the aliphatic chains of the amines. The much lower surface coverage (6-8%) by secondary ammonium ions compared to oleate molecules (92-94%) in our NCs is supported by nuclear magnetic resonance (NMR) measurements and X-ray photoelectron spectroscopy (XPS). Density Functional Theory (DFT) calculations further confirm that dialkylammonium molecules cannot stabilize lamellar 2D perovskites and thus they do not promote the anisotropic growth of NPLs. The homogeneity in size and shape of the $CsPbBr_3$ NCs translated in the ability of the nanocubes to spontaneously self-assemble into superlattices up to 50 microns lateral dimensions, which are the largest dimensions reported to date for superlattices (SLs) of LHP NCs. Notably this record size SLs were achieved without any size-selective precipitation and washings steps beyond the NCs isolation after synthesis.

5.2. Experimental details

Chemicals. Lead acetate trihydrate ($(PbAc_2 \cdot 3H_2O)$, 99.99%), cesium carbonate (Cs_2CO_3, reagent Plus, 99%), benzoyl bromide (C_6H_5COBr, 97%), Acetone (99.5%), ethyl acetate (98.8%), toluene (anhydrous,

99.5%), octadecene (ODE, technical grade, 90%), toluene-d8 (99 atom. % D) oleylamine (OLAM, 98%) dihexylamine (DHAm, 97%), dioctylamine (DOAm, 97%), didecylamine (DDAm, 98%), dioctdecylamine (DODAm, 99%), and oleic acid (OA, 90%), were purchased from Sigma-Aldrich. Didodecylamine (DDDAm, 97%), was purchased from TCI. Oleic acid and oleylamine were dried at 120 °C for an hour and stored in glove box whereas all other chemicals were used without any further purification.

Synthesis of $CsPbBr_3$ nanocubes.

76 mg of lead(II) acetate trihydrate, 16 mg of cesium carbonate and 10 ml of octadecene were combined in a 25 ml 3-neck flask. Reaction mixture was degassed for 5 minutes at room temperature and one hour at 115 °C. Then ligand mixture containing 1.5 mL of pre dried OA, 1.25 mmol of dialkyamine dissolved in 1 mL of anhydrous toluene was rapidly injected under nitrogen. After complete dissolution of metal precursors the temperature of reaction mixture was decreased to 80 °C followed by the injection of 50uL of benzoyl bromide precursor diluted in 500 µL of dried ODE. The reaction mixture was cooled down after 15 seconds by using water bath. Subsequently 20 mL of ethyl acetae and toluene mixture (with ratio of 6:1) was added into crude solution to destabilize the colloids and NCs were collected by centrifugation at 9000 rpm for 10 minutes. Finally the supernatant was discarded and precipitate was redispersed in toluene.

Computational Modelling. The simulations were performed in vacuum at the DFT level of theory using the CP2K quantum chemistry code[24] and employing the PBE exchange-correlation functional[25] and a double ζ basis set plus polarization functions[26]. Scalar relativistic effects have been accounted for by using effective core potential functions in the basis set. Spin-orbit coupling effects were not included in the calculations. For ground state relaxations the default force convergence threshold of $4.5*10^{-4}$ Ha/bohr was used. Molecular dynamics (MD) simulations included an equilibration phase of 1000 fs with thermostat and barostat annealing time constants of 150 fs, and a production stage of 500 fs with preceded by annealing time constants of 500 fs. At first, we performed structural optimizations at 0 K, allowing the relaxation of the supercell in all directions. For these preliminary calculations, we considered platelets with maximum surface ligand coverage, i.e. each surface Cs ion is replaced by ammonium, following our previous works[27,28]. We then computed the elongation of the supercell along the diagonal direction against the cell with only Cs ions at the surface, noticing an expansion of the lattice of about 32% for the secondary amines against the only 1% induced by primary amines. We then performed the ab-initio MD simulation abd computed the Pb-Pb and Cs-Cs (and N-N) pair distance distributions for the primary and secondary amine passivated cases.

Nuclear magnetic resonance experimental details:

All NMR spectra were acquired on a Bruker Avance III 400 MHz spectrometer, equipped with a Broad Band Inverse probe (BBI) at 300K. In the *quantitative* ^{1}H-NMR (*q*-NMR) experiment, after the ^{1}H 90° pulse was optimized, by an automatic pulse calculation routine,[29] 16 transients were acquired, using 64k data points, 30s of inter-pulses delay and no steady state scans, over a spectral width of 20.55 ppm (offset at 6.175 ppm), at a fixed receiver gain (64). ^{1}H-NMR spectra for the titration curves were performed using identical acquisition parameters except the receiver gain (1). *2D ^{1}H-^{1}H NOESY (Nuclear Overhauser Effect SpectroscopY)* experiment (*noesygpphpp*, Bruker library)[30] was performed using a mixing time of 300 ms, with 32 transients, 2048 data points and 256 increments. 2D ^{1}H-^{13}C HSQC (multiplicity edited Heteronuclear Single Quantum Coherence, hsqcedetgpsp.3, Bruker library)[31] spectrum was acquired using 12 transients, 2048 data points and 400 increments, with an automatic spectral width and transmitter frequency offset optimization for ^{1}H. A line broadening of 0.3 Hz was applied to FIDs (Free Induction Decay) before Fourier Transform. The NMR chemicals shifts were referenced to the peak of residual non-deuterated toluene at 7.09 ppm (^{1}H) and 129.2 ppm (^{13}C).

Confocal photoluminescence microscopy of superlattices:

The photoluminescence imaging of $CsPbBr_3$ NC superlattices grown on Si wafer was performed using a Nikon confocal microscope system A1-plus-s [Nikon Instruments, Yokohama, Japan; equipped with the A1-DUS Spectral Detector Unit that allows the parallel acquisition of 32 channel spectral image at a maximum wavelength resolution of 2.5nm]. Depending on the level of details desired, we used a 10X air (Nikon CFI Plan Apo Lambda 10x 0.45NA) and a 60x oil (Nikon CFI Plan Apo Lambda 60X Oil 1.4NA) objective lens, the selected excitation wavelength was 488 nm. The spectrally-resolved images were recorded with the emission detection bandwidth of 2.5 nm over 498-578 nm wavelength range. The resulting stacks (32 spectral slices per stack) were processed using open source Fiji distribution of ImageJ ver. 1.52e. [32] The spectral profiles of individual superlattices were obtained by drawing polygonal regions of interest (ROIs) around selected superlattices and performing "Plot Z-stack Profile" operation in Fiji, that yields a plot of the brightness of ROI (mean grey value, proportional to the number of emitted photons) as a function of the slice number (emission wavelength bin with the width of the spectral resolution). The overall spectrum-colored images shown below were obtained by using "Temporal Color Code" hyperstacks function in Fiji with LUT setting "Spectrum."

5.3. Results and discussion

In this work, we used a modified version of our recently developed synthesis approach of $CsPbX_3$ NCs, in which lead acetate trihydrate ($PbAc_2 \cdot 3H_2O$) and a benzoyl halide are separately used as precursors for Pb and X (Cl, Br, I) respectively,[9] instead of the more common approach in which PbX_2 is introduced as the combined source of Pb and X. In our revised scheme, a benzoyl bromide is injected into a solution containing cesium and lead oleates only or in the presence of secondary amines. After the synthesis, the NCs were separated and cleaned by adding a 1:6 volume ratio mixture containing toluene and ethyl acetate (or acetone) to the crude solution, followed by centrifugation and are redispersed in toluene. A major finding is that no basic (amines/ammonium) ligands are in reality needed for this type of synthesis: first, the Pb and Cs salts are perfectly soluble in a mixture of ODE and OA alone, as they form the corresponding metal oleates. Then, once the bromide precursor is injected, $CsPbBr_3$ NCs are immediately formed. These NCs have cube shapes, as seen by transmission electron microscopy (TEM) (Figure 1a) and overall good optical quality, as attested by UV-Vis optical absorption and photoluminescence (PL) spectra (Figure 1c). Their X-ray diffraction (XRD) pattern conforms to the orthorhombic phase (Figure 1b). These NCs are clearly passivated only with oleate or oleic acid, as no other surfactants are used in the synthesis.

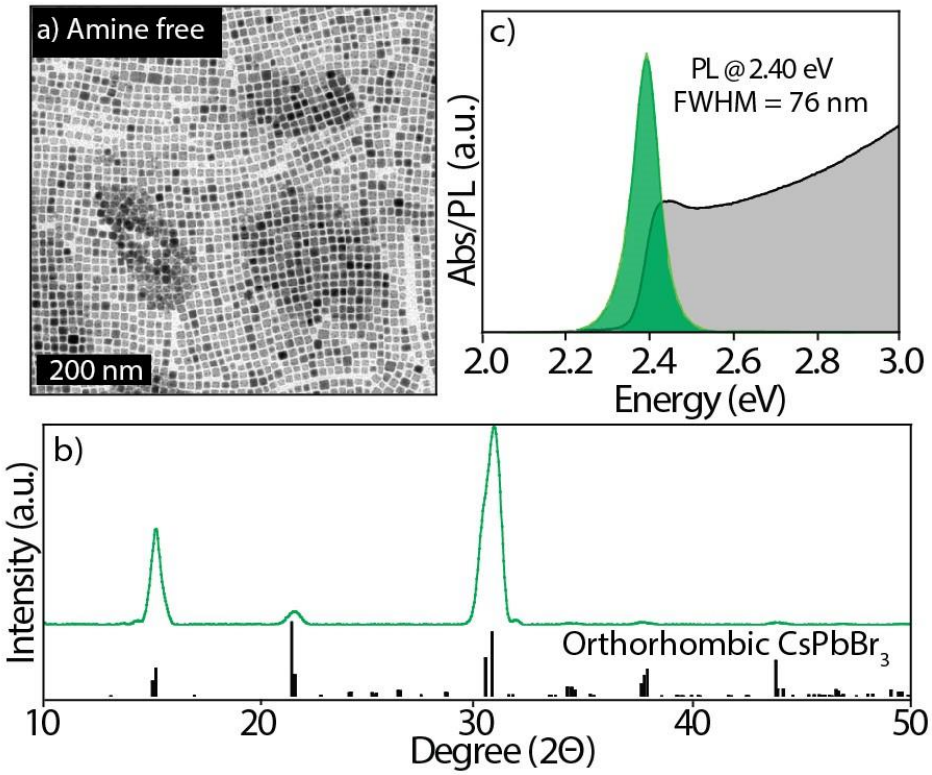

Figure 1. Amine free synthesis of $CsPbBr_3$ NCs; a) TEM image b) XRD pattern and c) UV-Vis absorption and PL spectra.

This conforms with other studies reporting the same type of surface passivation for the NCs, although they were grown in mixtures containing alkyl-ammonium ions in addition to OA.[33] In our "minimal" reaction scheme, the list of chemicals needed for the synthesis is stripped to the minimum requirement and that exclusive surface passivation by oleate species is a direct consequence of this choice. Further attempts to improve the size and size distribution of OA capped NCs, for example by performing syntheses at different concentrations of OA (see figure 2), were unsuccessful, as the NCs remained polydisperse, and their size could not be tuned. It appears therefore that this over-simplified scheme, despite providing some basic understanding of the growth and surface chemistry of the NCs, does not afford optimal samples.

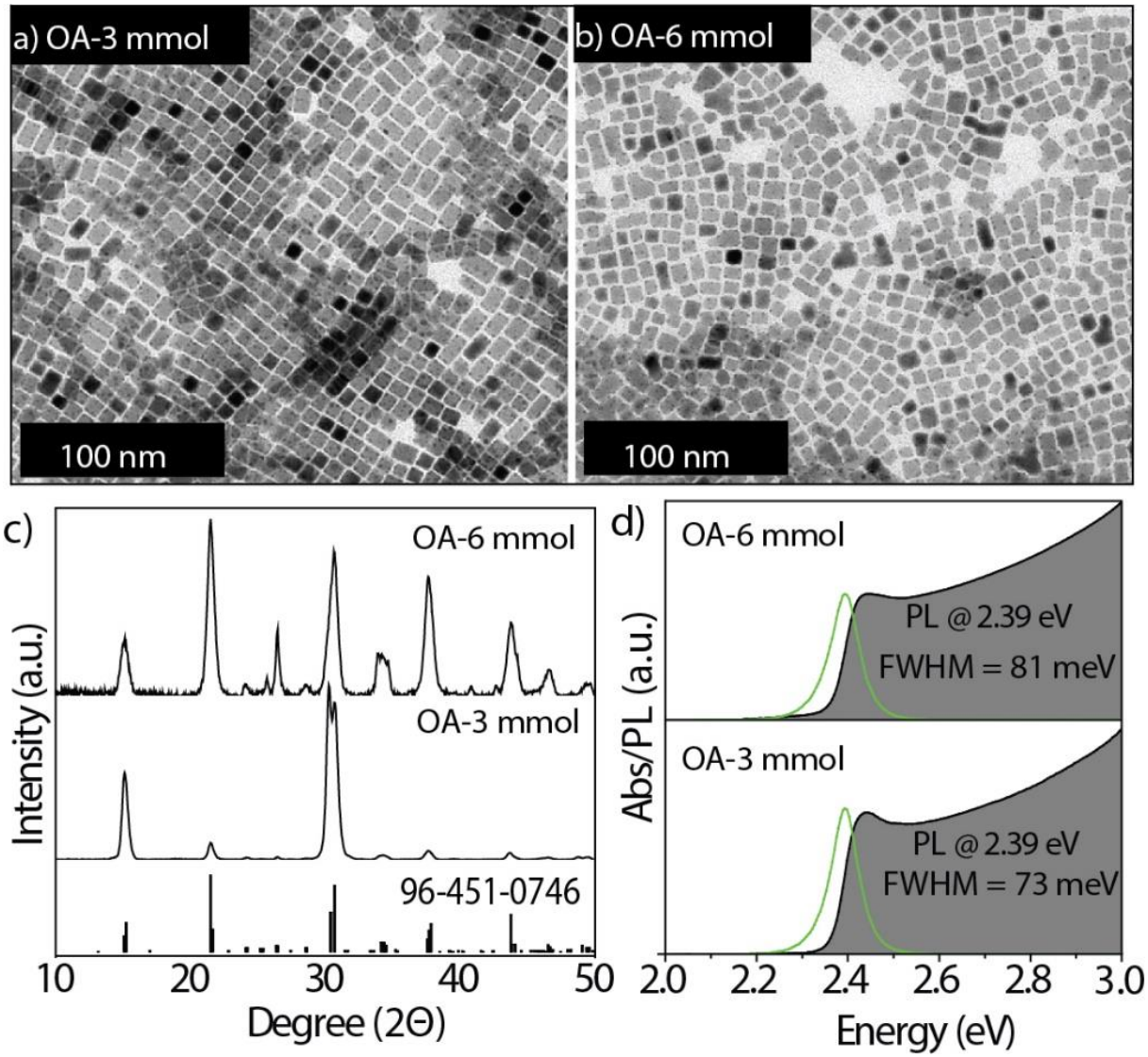

Figure 2. a) TEM image, b) XRD patterns, c) absorption and PL spectra of $CsPbBr_3$ NCs synthesized without any amine. Syntheses were as carried out as follows. Amount of precursors: 0.2mmol of $PbAc_2 \cdot 3H_2O$, 0.05mmol of Cs_2CO_3, 4.75mmol of OA, 1.25mmol of dialkylamine; reaction temperature: 80 °C; 50 µl of Benzoyl bromide diluted in 0.5ml of octadecene; reaction time: 15 seconds

To overcome these issues, but at the same time avoiding use of primary amines, we tested the effect of introducing secondary aliphatic amines in our synthesis, under similar reaction conditions. In a first series of experiments, we systematically varied the hydrocarbons chain length of the secondary amine, starting from dihexylamine and going to dioctadecylamine, while keeping all the other reaction conditions fixed (see Figure 3). We observed the formation of nearly monodisperse nanocubes in all cases, regardless of the type the dialkylamine used, as shown in the TEM images of Figure 1a-e. By increasing the chain length of the secondary amine, the size of the NCs decreased from 17 nm, in the case of dihexylamine, to 7.5 nm in case of dioctadecylamine. The XRD patterns evidence the crystalline nature of the nanocubes, matching well with the orthorhombic perovskite phase (Figure 3f).

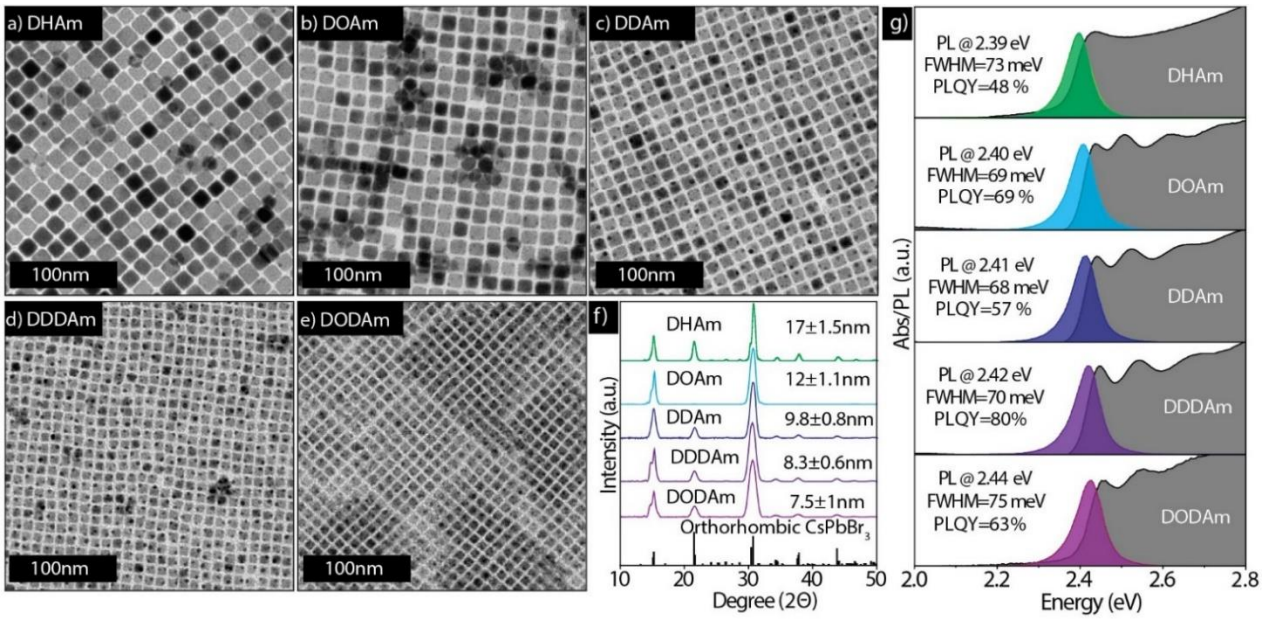

Figure 3. a-e) TEM images of $CsPbBr_3$ nanocubes synthesized by varying the hydrocarbon chain length of secondary amines. a) dihexylamine (DHAm); b) dioctylamine (DOAm), c) didecylamine (DDAm), d) didodecylamine (DDDAm) and e) dioctadecylamine (DODAm), f) Corresponding XRD patterns with reference ($CsPbBr_3$, ICSD code 96-451-0746) and g) absorbance and PL spectra. Average sizes of the nanocubes are written in panel f). The reactions conditions used in all these syntheses were as follows. Amount of precursors: 0.2mmol of $PbAc_2{\cdot}3H_2O$, 0.05 mmol of Cs_2CO_3, 4.75 mmol of OA, 1.25 mmol of dialkylamine; reaction temperature: 80 °C; 50 µl of benzoyl bromide diluted in 0.5 ml of octadecene; reaction time: 15 seconds.

The size uniformity in all the samples is also evident from the optical absorption spectra (Figure 3g, grey shadowed spectra), with distinctive excitonic features, and from the PL spectra characterized by narrow emission lines with linewidths in the 68-75 meV range. The PL quantum yield (PLQY) of the various washed $CsPbBr_3$ samples was in the 48-80% range, with average life times around 5-10 ns

(see Figure 4 and Table 1). Such PLQYs are comparable to the previous reports employing similar washing protocols using ethyl acetate or acetone.[27,33]

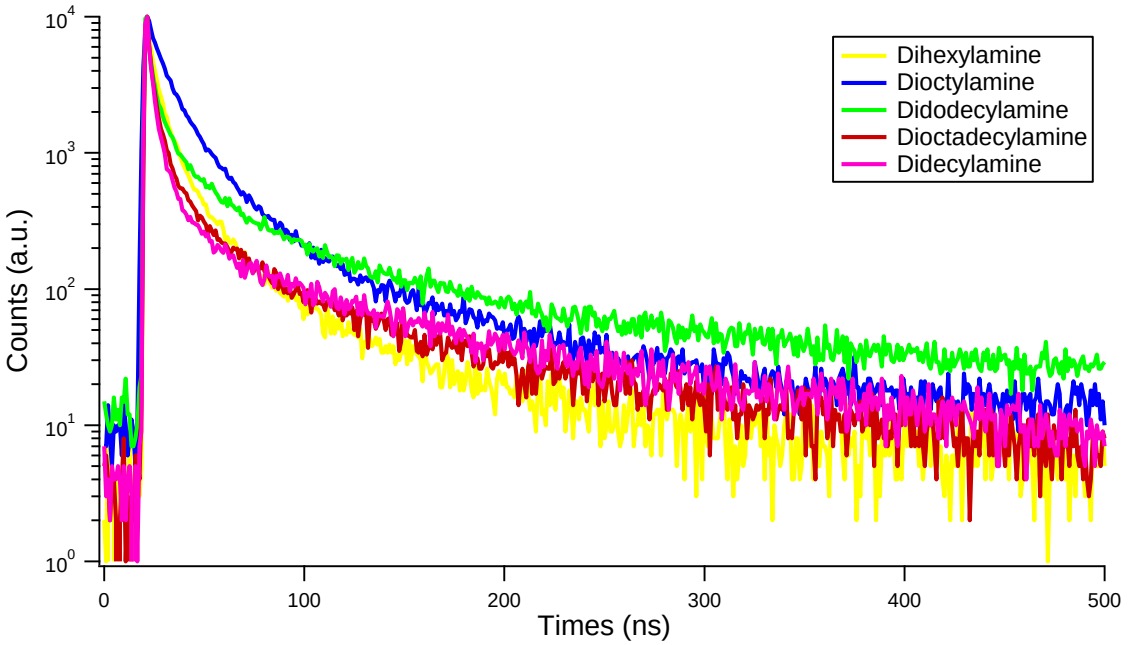

Figure 4. Decay lifetimes of $CsPbBr_3$ nanocubes prepared by using various secondary amines.

Table 1. The summary of PL, PLQY and life time measurements of $CsPbBr_3$ nanocubes prepared by using secondary amines with varying chain lengths.

Sample Name	PL max (nm)	A_1	τ_1 (ns)	A_2	τ_2 (ns)	A_3	τ_3 (ns)	τ_{AVG} (ns)	QY (%)
Dioctadecylamine	502	9220.28	3.77475	602.585	33.0702	57.0491	175.272	6.55	63
Didodecylamine	509	8829.71	3.11997	1501.01	22.8472	239.645	146.727	9.18	80
Didecylamine	513	11408.5	3.44428	363.521	38.1308	85.3936	167.707	5.69	57
Dioctylamine	515	8149.19	3.32575	4140.72	10	265.491	51.6817	6.55	69
Dihexylamine	516	8805.44	5.2776	1039.79	26.375	37.2879	166.154	8.10	48

The fact that secondary amines with longer alkyl chains promote the formation of smaller NCs is most likely due to the reduced diffusivity of the various species in the presence of bulkier molecules[34] (hence growth rates should be reduced). Also, our reaction scheme is quite flexible in terms of the parameters that can be tuned to modify the size of the NCs, yet it is quite robust, as nanocubes are always formed. For example, using didodecylamine and varying the reaction temperature (from 50 °C to 140 °C) enables the synthesis of monodisperse nanocubes with sizes ranging from 6.2 nm to 19 nm (Figure 5a-d).

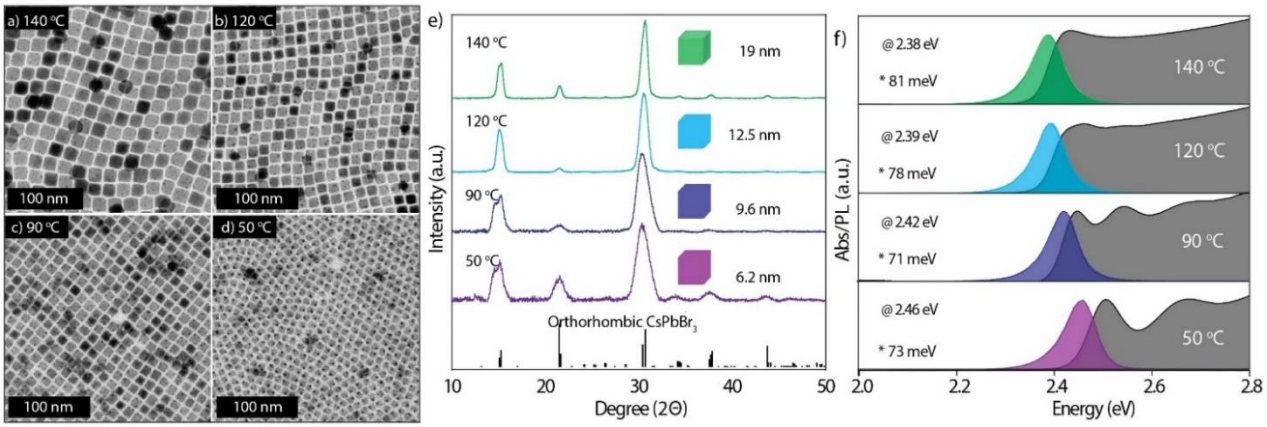

Figure 5. $CsPbBr_3$ NCs were synthesized by using didodecylamine at various temperatures while keeping rest of the reaction conditions unchanged as illustrated in Figure 1. a-d) TEM images of $CsPbBr_3$ nanocubes, e) XRD patterns of $CsPbBr_3$ NCs matching with the orthorhombic perovskite crystal structure ($CsPbBr_3$, ICSD code 96-451-0746); f) absorption, PL spectra, PL max (@) and FWHM (*) of corresponding samples.

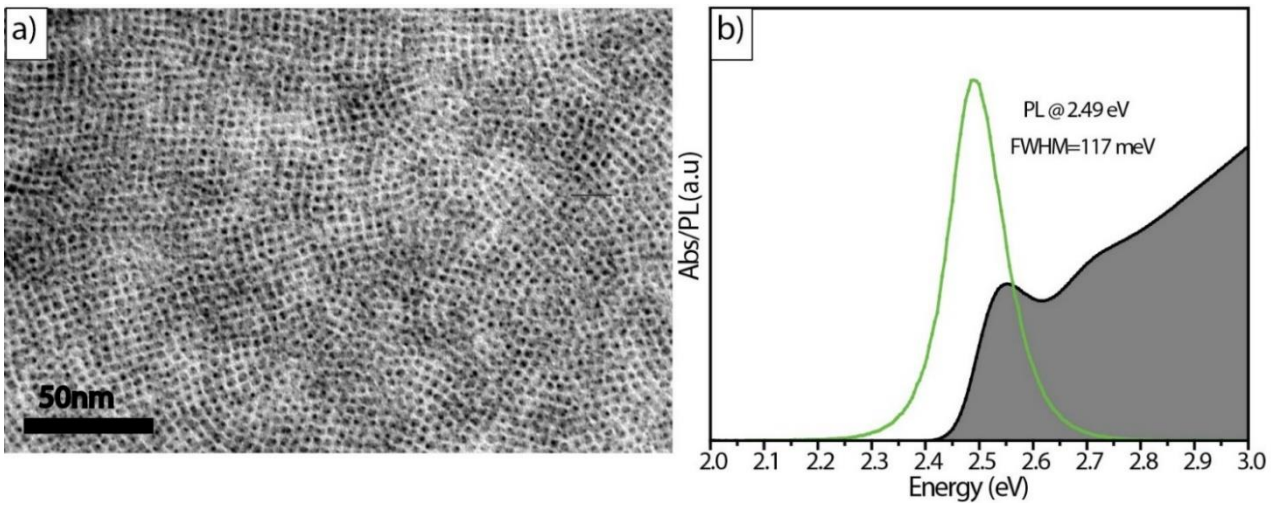

Figure 6. The synthesis was carried out by using 0.2 mmol $PbAc_2{\cdot}3H_2O$, 0.05 mmol Cs_2CO_3, 4.75 mmol

of oleic acid, 1.25 mmol of dioctadecylamine at the injection temperature of 50 °C. a) TEM image of $CsPbBr_3$ nanocubes and b) absorbance and PL spectra.

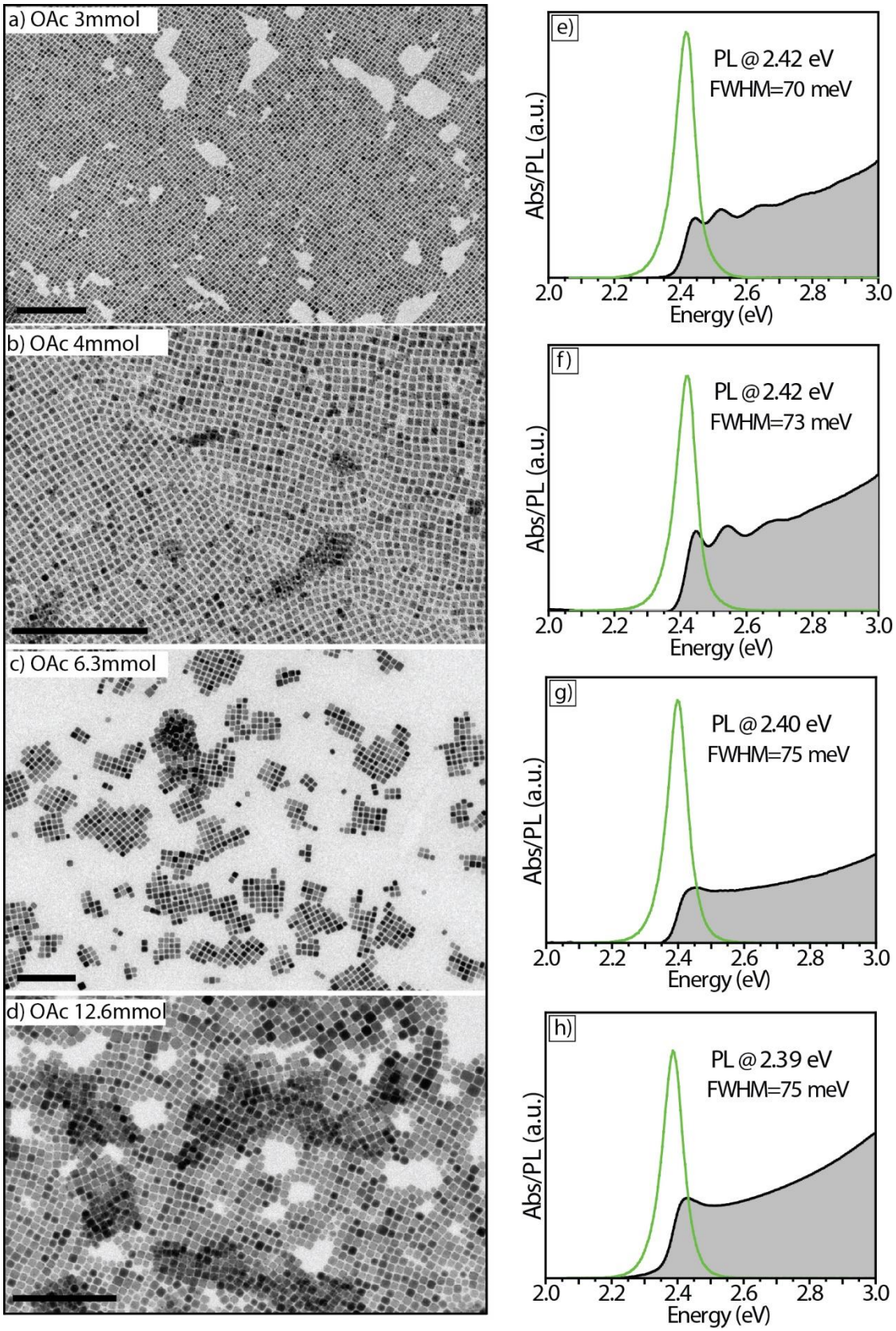

Figure 7. Synthesis of $CsPbBr_3$ nano cubes by using 1.25 mmol of didodecylamine and various concentrations of oleic acid at the injection temperature of 80 °C.

XRD diffractogram further evidence their crystalline nature conforming the orthorhombic perovskite phase, (Figure 5e). The degree of size monodispersity in the samples characterized by smaller sizes is evident by the multiple excitonic peaks, with increasing energy separation between the peaks as the size decreases, in accordance with what observed in ensemble optical spectra of classical quantum dots. The size of the nanocubes could be further decreased to 5.1 nm by replacing didodecylamine with dioctadecylamine and working at 50 °C (Figure 6). Instead, by using didecylamine, the size of the nanocubes could be further tuned from 9 nm to 25 nm by varying the reaction temperature from 80 °C to 140 °C. Another parameter that we tested in our syntheses is the concentration of OA. Even when the concentration of OA was increased by four times (from 3 mmol to up 12.6 mmol), which strongly promotes the formation of NPLs in case of primary amines[19], no NPLs were observed for example with didodecylamine (see figure 7). To compare the primary and secondary amines, several control syntheses were carried out, by separately using primary and secondary amines under fully protonated conditions as verified by NMR spectroscopy see later. In two series of experiments, we directly compared two pairs of amines: oleylamine *versus* dioctadecylamine, and dodecylamine *versus* didodecylamine. OA was used as the carboxylic acid in all the syntheses, and all other reaction conditions were kept the same, with an reaction temperature of 100 °C, which is known to promote the synthesis of NSs and NPLs in the case of primary amines.[21] Indeed, when primary amines were used, we observed the formation of NSs or NPLs, as evidenced by TEM, optical absorbance and PL spectroscopy (Figures 8 a-d) and XRD analysis (Figure 9).

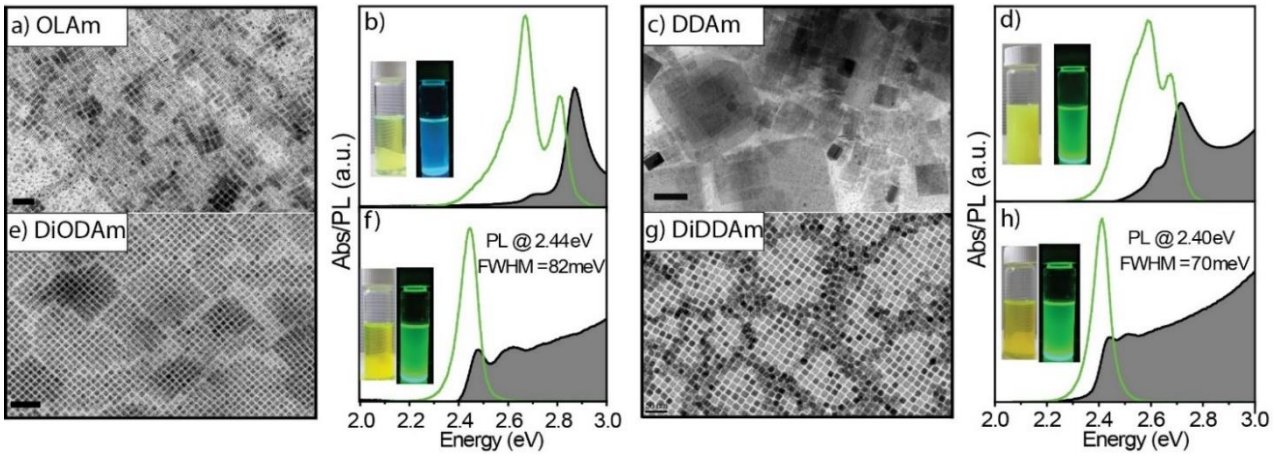

Figure 8. a-d and e-h) are TEM images and absorption PL spectra of $CsPbBr_3$ NCs synthesized by using primary and secondary amine, respectively. Synthesis was carried out under standard reaction condition (described earlier in Figure 1) except reaction temperature of 100 °C. Insets in Figure b and d) are the photographs of corresponding NCs solution under ambient and UV light.

Instead, monodisperse nanocubes were formed in the case of secondary amines (Figures 9e-h). To further study the effect of the dialkylamine, and its inability to form 2D perovskites, we performed

the synthesis of $CsPbBr_3$ in absence of the Cs^+ precursor, as these conditions are known to form a 2D hybrid layered phase when using primary amines.[35-37] Here, we indeed observed the formation of a white precipitate immediately after the injection of benzoyl bromide in case of dodecylamine. Combined TEM, XRD, UV-Vis absorption and PL analysis confirmed that the white precipitate corresponds to the 2D $(dodecylammonium)_2PbBr_4$ phase (Figure 10). Under the same reaction conditions, but working with didodecylamine, no precipitate was collected and the reaction mixture remained clear and colorless.

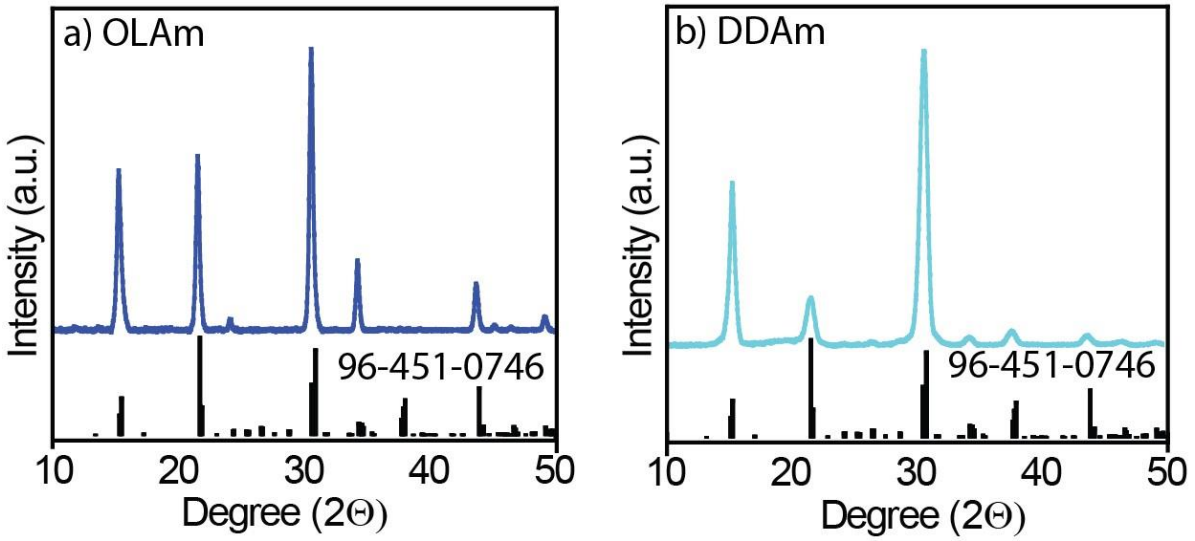

Figure 9. XRD patterns of $CsPbBr_3$ NPLs synthesized by using primary amines; oleylamine a), and dodecylamine b).

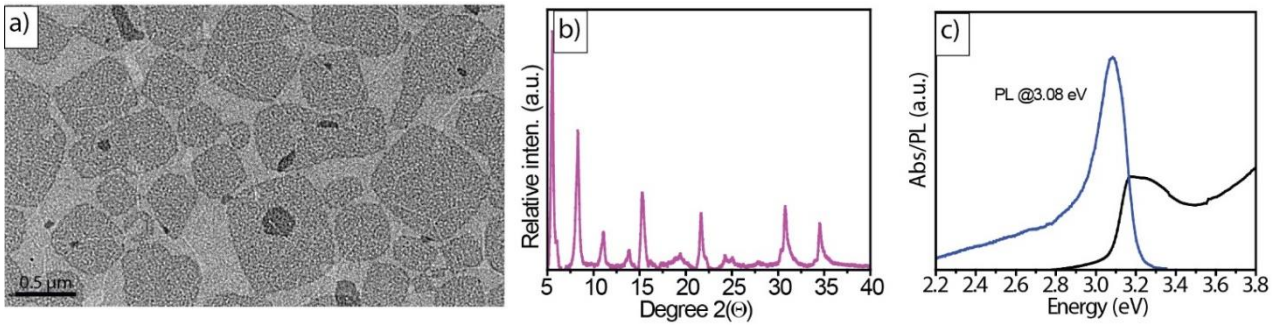

Figure 10. a) TEM image of layered lead bromide perovskite, b) XRD pattern, and c) absorbance and PL spectra.

We also ran syntheses under conditions that promote the formation of the Pb-depleted Cs_4PbBr_6 phase in the case of primary aliphatic amines (that is, in the presence of a large excess of the amine). Note additional peaks other than orthorhombic $CsPbBr_3$ perovskite phase in XRD patterns are due to excess of unreacted DDDAm in the sample and it can be indexed by accordingly.

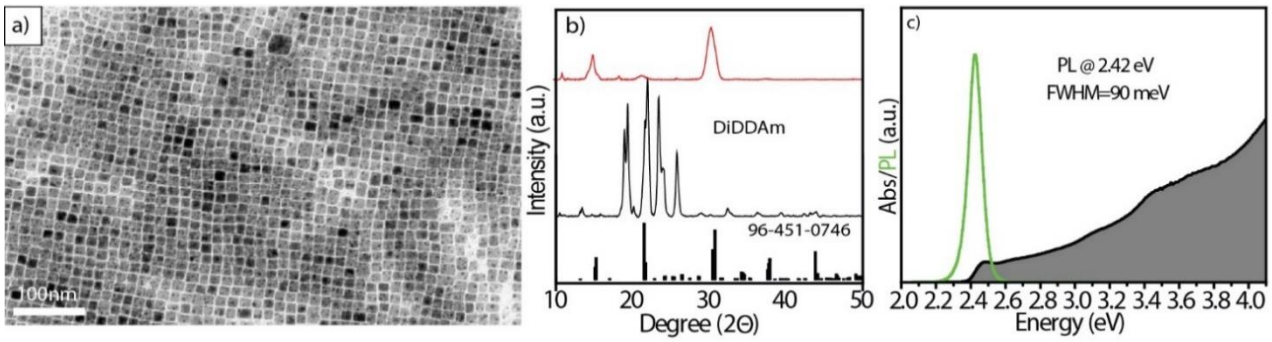

Figure 11. The synthesis was carried out by using 0.2 mmol $PbAc_2 \cdot 3H_2O$, 0.05 mmol Cs_2CO_3, 3 mmol of oleic acid, 5 mmol (a four-fold excess compared to the standard procedure) of didodecylamine (DDDAm) and injection temperature of 80 °C. a) TEM image of the resulting $CsPbBr_3$ nanocubes, b) XRD pattern showing the absence of other cesium lead bromides, and c) absorbance and PL spectra.

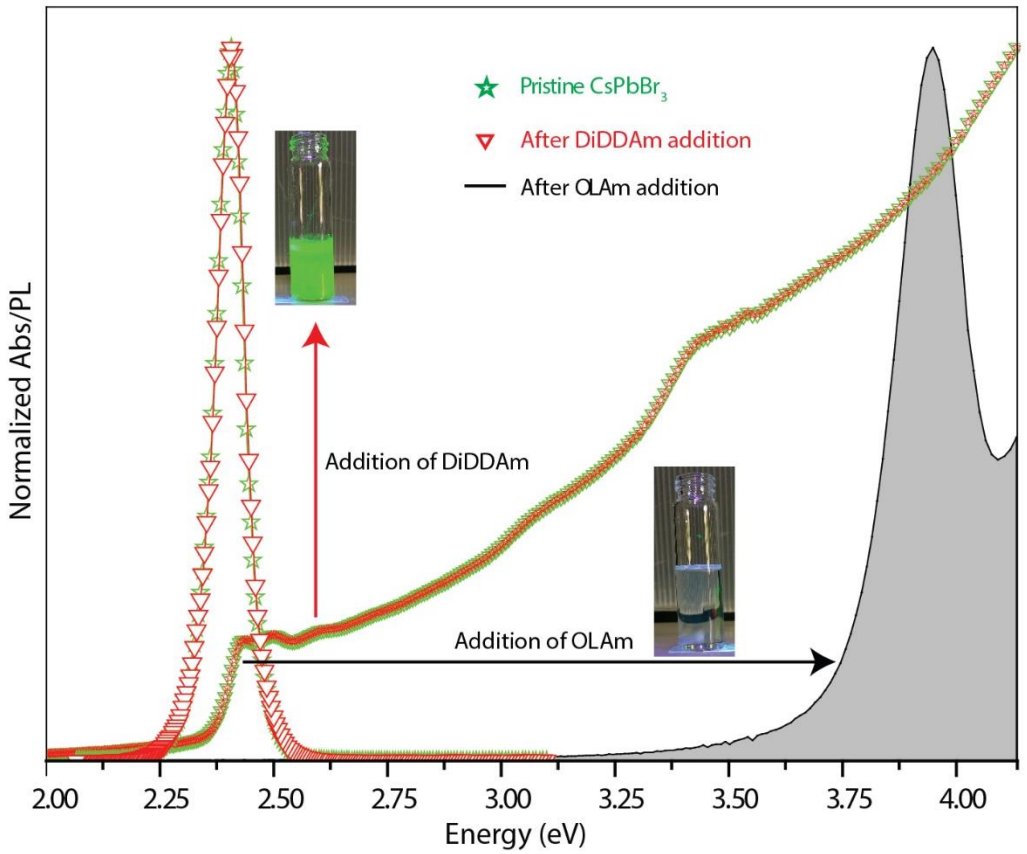

Figure 12. Absorption and PL spectra of the $CsPbBr_3$ nanocubes synthesized in the presence of didodecylamine (DDDAm) are shown in green. The overlaid red absorption and PL spectra were measured after an excess of DDDAm was added to the toluene dispersion of the nanocubes. The black shaded absorption spectrum was measured after an identical toluene dispersion of initially $CsPbBr_3$ nanocubes was mixed with an excess of oleylamine. The photographs in the insets show resulting mixtures under UV light. The excess of oleylamine triggers complete conversion of emissive $CsPbBr_3$ nanocubes to non-emissive Cs_4PbBr_6 phase, while DDDAm is inactive for that transformation.

Primary aliphatic amines can stabilize $PbBr_2$, therefore depriving the reaction environment of Pb^{2+} species and promoting the formation of the Cs_4PbBr_6 phase over the $CsPbBr_3$ one. With our secondary amines, again only $CsPbBr_3$ nanocubes were obtained (Figure 11). We ascribe this behavior to the inability of secondary amines to stabilize $PbBr_2$. This was also proven in a control experiment in which $CsPbBr_3$ NCs were mixed with a large excess of a secondary amine (didodecylamine). Notably, the NCs remained stable and UV-Vis absorption spectra did not show any signature of the Cs_4PbBr_6 phase. **The same experiment, carried out with oleylamine, produced the Cs_4PbBr_6 phase (Figure 12), as already reported previously.**[38-40]

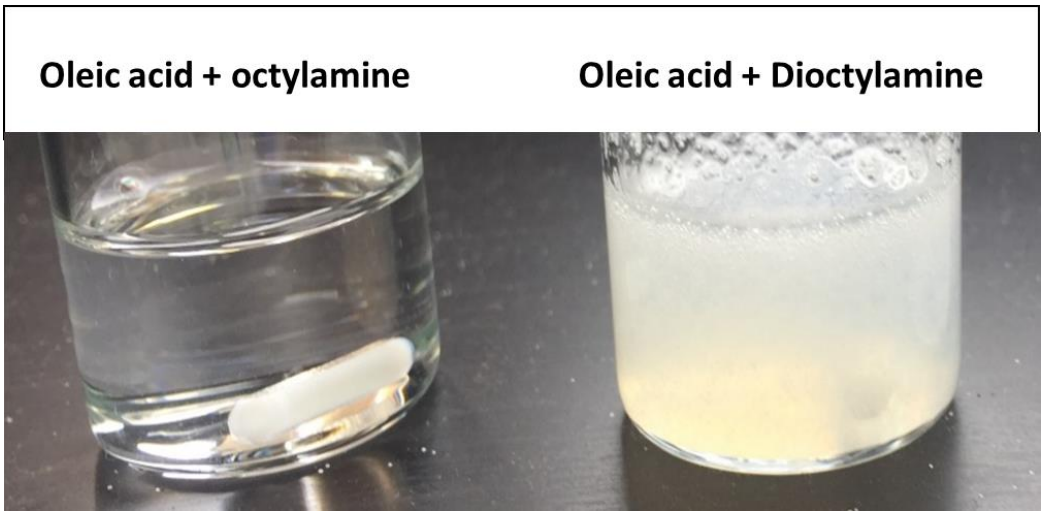

Figure 13. Solubility of lead bromide in primary (left vial) and secondary (right vial) amine with the same hydrocarbon chain length. Experimental details: 72 mg of $PbBr_2$ were mixed with 3 mmol of amine (octylamine or dioctylamine), 3 mmol of oleic acid, 5 ml of octadecene were combined in 20 mL vial and heated up to 130 ^oC on a hotplate and kept at that temperature for 30 minutes.

We note that the solubility of PbX_2 salts in the mixture of both acid (oleic acid) and a primary amine (oleylamine) that is typically used for the synthesis of $CsPbX_3$ NCs is highly limited by the formation of the ammonium carboxylate salt.[19] Figure 13 shows how for example $PbBr_2$ is easily dissolved in an oleic acid-octylamine mixture, but not in oleic acid-dioctylamine mixture or an oleic acid alone.[19] For primary amines, in the presence of excess amine, this salt can undergo dissociation by homoassociation (i.e. hydrogen bonding between a base and its conjugate acid),[41] which can be described as:

$$\mathrm{BH^+ \cdots A^-} + \mathrm{B} \leftrightharpoons (\mathrm{BH^+ \cdots B})\mathrm{A^-}$$

Where $\mathrm{BH^+ \cdots A^-}$ is the ammonium carboxylate salt, formed by the acid AH (oleic acid in this case) and the base B (the primary amine in this case). Homoassociation (the formation of $\mathrm{BH^+ \cdots B}$) in turn

promotes the solvation of PbX_2. Homoassociation cannot take place with secondary aliphatic amines when substituents are bulkier than the methyl groups.[41]

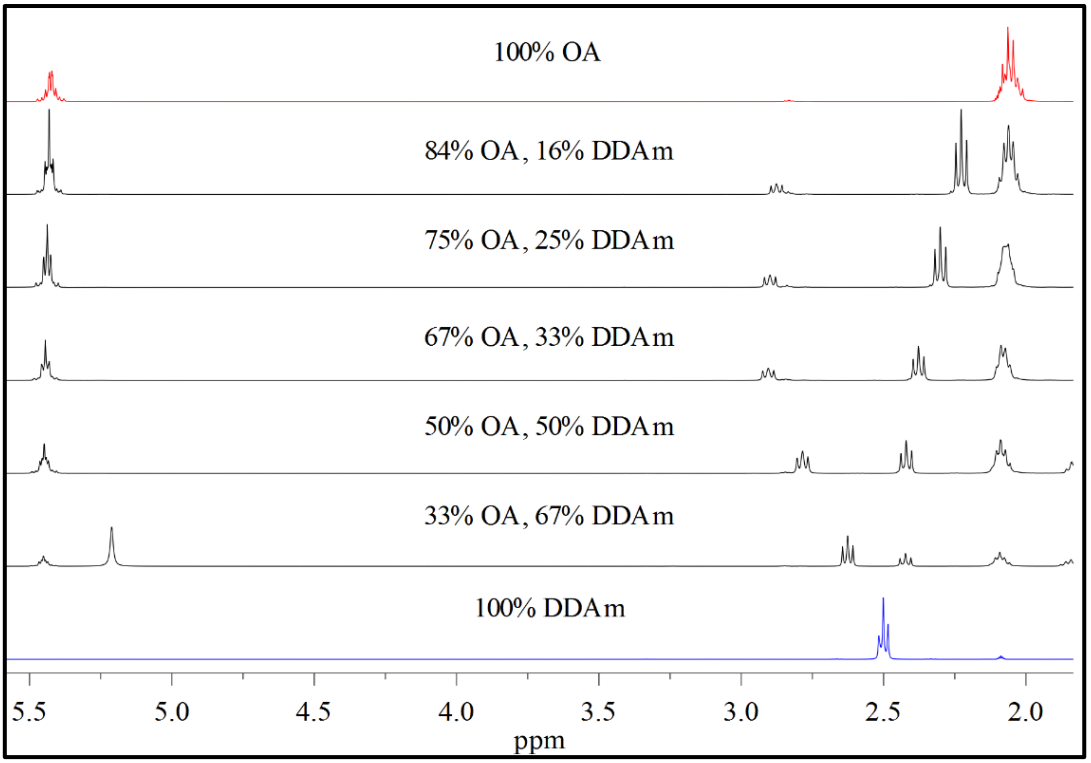

Figure 14. Selected regions of the ^{1}H NMR spectra of dodecylamine (DDAm), oleic acid (OA) and their at various molar %various mixtures in toluene-d8

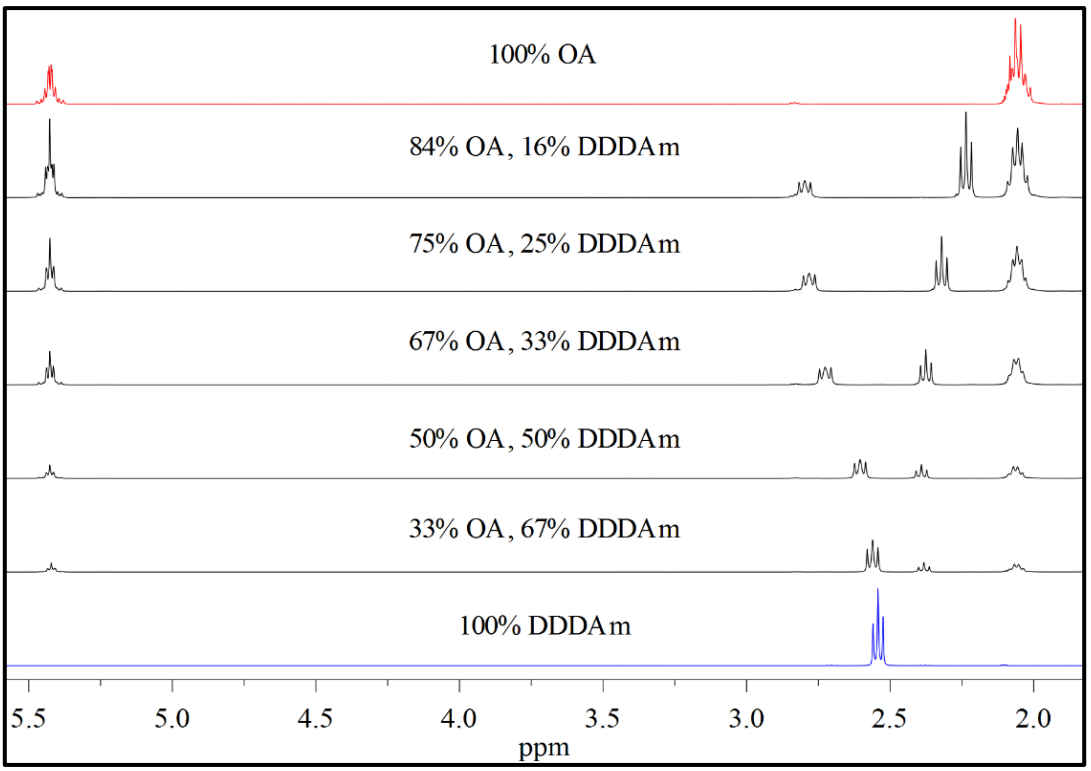

Figure 15. Selected regions of the ^{1}H NMR spectra of didodecylamine (DDDAm), oleic acid (OA) and their various mixtures in toluene-d8 at various molar %

To better explain the way primary and secondary amines interact with oleic acid, we resorted to nuclear magnetic resonance (NMR) spectroscopy. ^{1}H NMR was used to investigate the protonation of dodecylamine and didodecylamine in the presence of OA. Details of this study are reported in the Figure 14-18. According to the ^{1}H NMR data, at an acid:amine (primary or secondary) ratio of 3:1 or higher, as mostly employed in our syntheses, the amine is fully protonated (Figure 14-16).

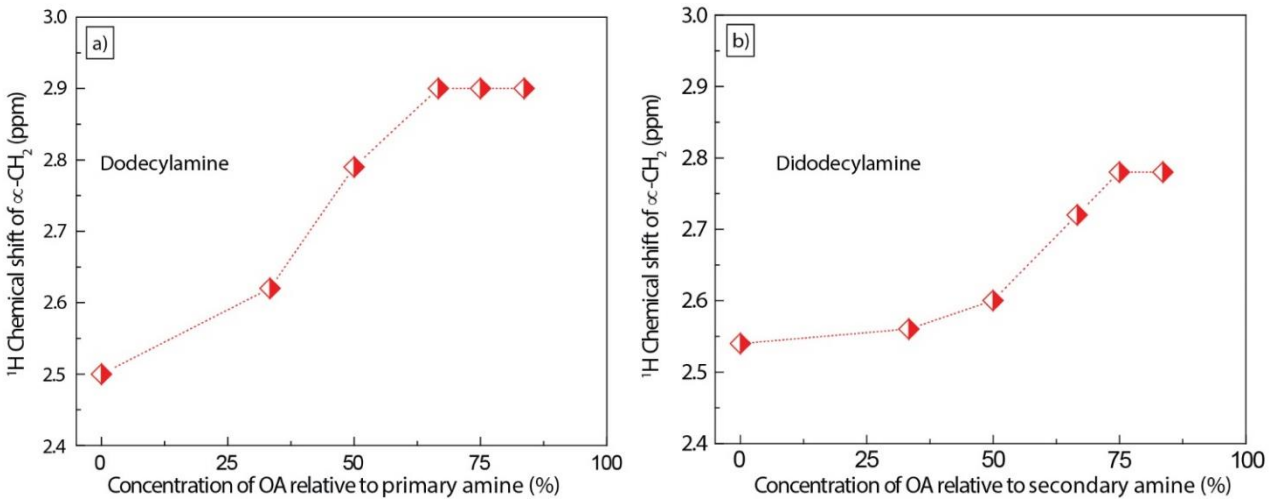

Figure 16. Comparison of ^{1}H chemical shifts of α-CH_2 for primary and secondary amines as a function of the relative amount of oleic acid.

However, while an environment rich of fully protonated amines is ideal for the synthesis of NCs with two-dimensional shapes or layered phases,[19] for secondary amines this seems to have no influence on the shape control (only cubes are formed). We also performed Nuclear Overhauser Effect Spectroscopy (NOESY) on washed $CsPbBr_3$ nanocubes synthesized using didodecylamine, dispersed in deuterated toluene, to investigate the nature of the surface ligands.

The NOESY spectrum (Figure 17a) indicates that both the acid and the secondary amine interact with the NCs surface, suggesting that both ligands are, at least to some extent, bound species. Heteronuclear Single Quantum Coherence (^{1}H-^{13}C HSQC) was also performed to confirm that the signals of interest observed in NOESY belong to the acid and amine ligands (Figure 17b). The ^{1}H NMR spectrum of this sample (Figure 17c) shows broadening of signals of both ligands, suggesting that both species are in active dynamic processes with the NCs surface (with longest correlation times (τ_c), compared to free ligands). In order to estimate the ratio between the two ligands (OA and didodecylamine) present on the surface of the NCs, we ran quantitative ^{1}H NMR on a washed $CsPbBr_3$ nanocubes sample dissolved in deuterated DMSO. Quantitative analysis of alkene protons of OA and α-CH_2 protons of the amine indicated that the majority of the ligands present in the sample belong to OA species (92-94%), while the amine species represent only 6-8% (Figure 17d). Similar values

were obtained from quantitative analysis (by X-Ray photoelectron spectroscopy, XPS) of the signals due to N (here chosen as "marker" for the presence of didodecylamine molecules) and C, focusing on the spectral component due to the acidic COOH moiety of OA (Figure 18). It is important to notice that the position of this C component is at (288.1±0.2) eV, corresponding to carbon atoms in COO^- groups.[42] No signal due to carbons in COOH groups could be detected at approx. 289 eV, suggesting that the signal considered for XPS quantitative analysis is only coming from bound molecules in the form of oleates.

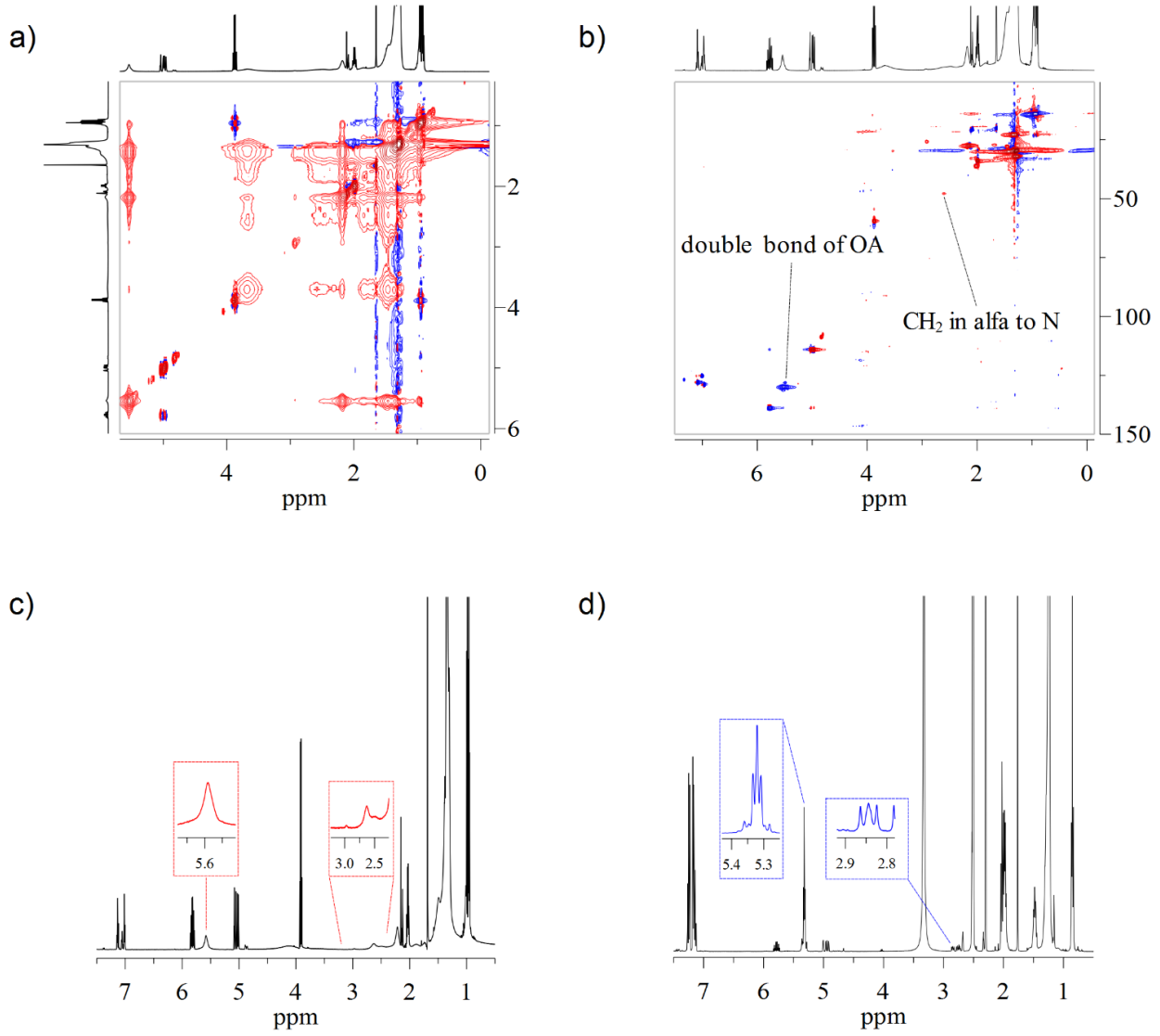

Figure 17. a) ^1H-^1H NOESY and b) ^1H-^{13}C HSQC and c) ^1H- NMR spectrum on washed $CsPbBr_3$ nanocubes synthesized using didodecylamine, in toluene-d8; d) ^1H NMR on a washed NC sample dissolved in deuterated DMSO.

We also investigated, by XPS, the surface ligands ratios of $CsPbBr_3$ nanocubes prepared by using primary amine.[9] Remarkably, no signal of COOH moiety of OA was detected whereas a strong signal of N was observed, suggesting that these NCs are mainly capped with ammonium species (Figure 18).

This is fully in line with previously reported NMR studies on $CsPbBr_3$ NCs synthesized using oleic acid and primary amines, which indicate that only ammonium species are bound, and no oleate is present on the surface.[20,43] The high excess of oleate species in the NCs prepared in the presence of secondary amines indicate that we are dealing with cations-rich NCs: in particular, as suggested by elemental composition obtained *via* XPS, the as-prepared NCs most likely have a Pb-rich surface, being the Cs:Pb:Br ratio close to 1:1.1:2.4.

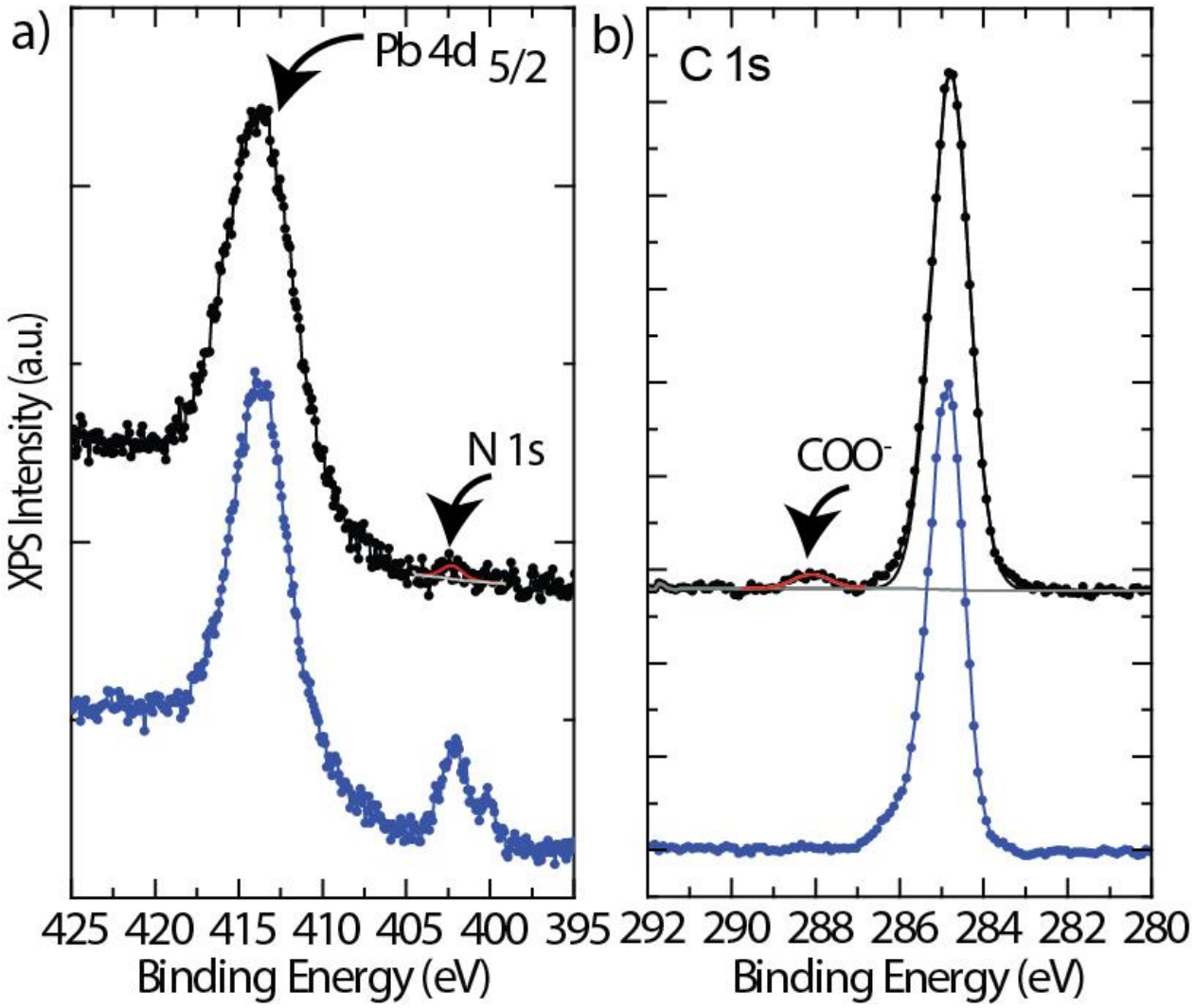

Figure 18. XPS quantitative analysis of ligand composition on the surface of $CsPbBr_3$ nanocubes synthesized by using didodecylamine(black) and OLAm (Blue).

Bromine content could be quite underestimated here, due to X-ray radiation induced Br desorption. To further gain mechanistic insights into how secondary amines can be bound to the surface of $CsPbBr_3$ NCs, and how this differs from the primary amine case, we carried out DFT calculations. We modelled a $CsPbBr_3$ slab employing 4x4 unit cells in the *x, y* periodic directions and 2 unit cells in the *z* finite direction, which was cut along the (100) direction, ensuring CsBr termination on both sides. The passivation of primary and secondary amines was reproduced by replacing surface Cs^+ ions with

methylammonium and dietyhlammonium ions for primary and secondary ammonium ions, respectively. Due to the small size of the alkyl chain, these calculations take into account mostly the effect of the anchoring group to the surface, while neglecting most of the chain-to-chain interactions. Further details on the calculations are provided in the experimental part.

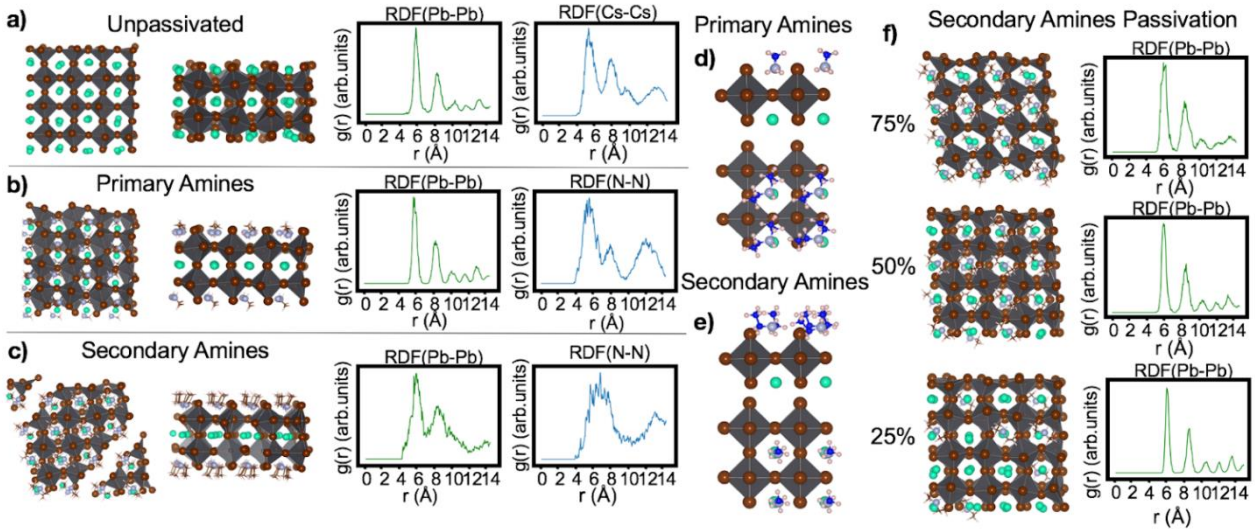

Figure 19. (a-c), planar and side views of the slabs optimized at 0 K, with Cs^+, primary (methylammonium) and secondary (di-ethylammonium) amines passivated structures given from top to bottom. On the right of each structure, their corresponding pair radial distribution functions for the Pb-Pb and Cs-Cs (or N-N) atomic distances, calculated by ab-initio MD simulations at the DFT/PBE level of theory with the NPT ensemble (T=300 K, P=1atm). (d-e) side and planar view of the binding of primary (top) and secondary amines (bottom). (f) Structures and radial distribution functions for the nanoplatelets where the ligand surface coverage of secondary amines has been reduced to 75-50-25%.

Taking a slab passivated with Cs^+ ions as reference, we could calculate the effect of the lattice strain induced by the ammonium ions bound to the surface by analyzing the pair radial distribution functions (*rdf*) for the Pb-Pb atomic distance. We quantified the changes in the lattice by performing ab-initio molecular dynamics simulations for 2 ps and 2.5 fs time steps in an isothermal-isobaric ensemble at constant pressure (1 atm) and temperature (300 K). We chose the Pb-Pb distance because this is associated to the lattice vector of the cubic perovskite unit cell, and, although the lattice distorts to an orthorhombic conformation, it still represents a good reference parameter when we compare the passivation with ammonium ions against the unpassivated crystal structure, Figure 19a. As it is illustrated in Figure 19b, the passivation with methylammonium provides *rdf*(Pb-Pb) with well-resolved and narrow peaks. On the other hand, the dietyhlammonium passivated surface presents much broader and unresolved peaks (Figure 19c), a signal for a more deformed lattice. This

deformation is mostly attributed to the binding of the ion's anchoring group to the surface. The dietyhlammonium ion indeed places one of its two hydrogen atoms almost perpendicular to the surface, whereas the two ethyl groups (i.e. emulating the long alkyl chains in the experiments) and the remaining hydrogen atom rearranges to minimize steric interactions between nearby ammonium ligands (Figure 4d-e). In our computational model, dietyhlammonium ions attempt to reduce the strain by heavily distorting the lattice. In a more realistic environment as in the experiments, these ligands, rather than stretching the lattice, would likely detach from the surface. We also analyzed the *rdf*(N-N), i.e. the distance between the nitrogen atoms of the ammonium anchoring groups.

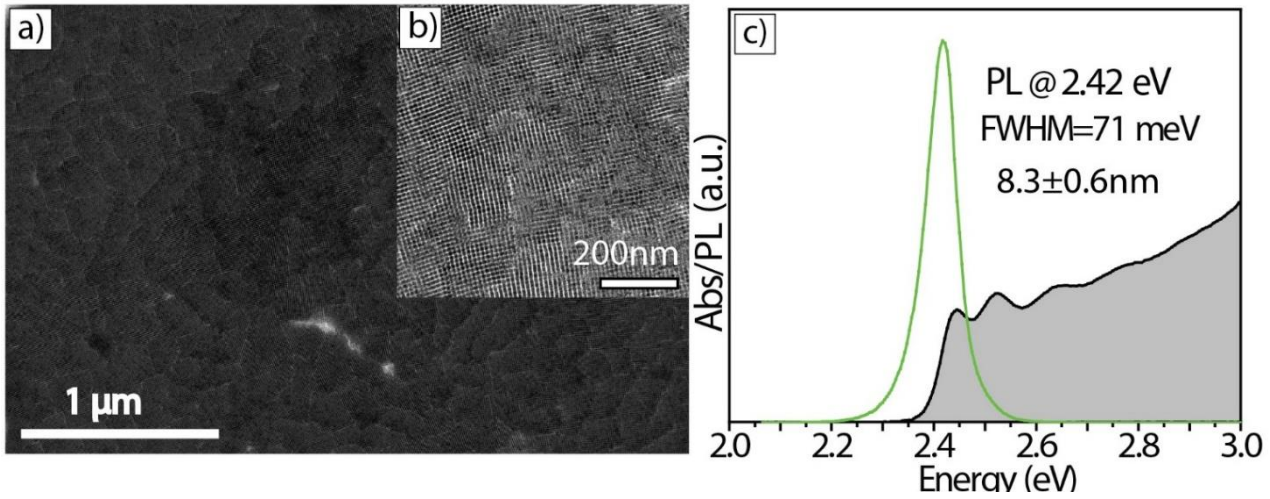

Figure 20. TEM images of the $CsPbBr_3$ nanocubes synthesized by using didodecylamine under standard synthesis conditions (Figure a, b) and their optical properties c).

On average, this *rdf* present less resolved and broader peaks due to the higher mobility of the amine ligands. However, in the case of the methylammonium ions, the closest distance between N atoms peaks at 5.8 Å, whereas for dietyhlammonium ions it peaks at significantly longer distances, 7.1 Å, supporting the presence of large steric repulsions between the ammonium groups. Such view is also confirmed in Figure 4f where we analyzed the effect of reducing the surface concentration of secondary amines up to 25% of the cation sites passivated. It is noticeable how the lattice diminish strain and recover the cubic shape when secondary amines are detached. These results, together with the experimental data, thus indicate that the dialkylammonium molecules cannot stabilize lamellar 2D perovskites, and thus do not promote the anisotropic growth of NPLs.

5.4. Superlattices

Colloidal NCs with high size and shape uniformity tends to self-assemble into ordered super structure upon solvent evaporation. The absence of contamination from other shapes and the narrow size distribution of cubic $CsPbBr_3$ NCs synthesized by using secondary aliphatic amines gives us access to high quality samples, suitable for self-assembly. Previously, the Kovalenko group reported 1-10 µm

square-shaped superlattices of size-selected $CsPbBr_3$ and $CsPbBr_2Cl$ NCs obtained by slow solvent evaporation on substrates,[7,44,45] Feldmann and co-workers reported the formation of sub-1 µm $CsPbBr_3$ NCs SLs *in situ* during the NC synthesis,[46] and Vanmaekelbergh and co-workers reported the preparation of ~1 µm SLs by antisolvent precipitation from NC solutions.[47]

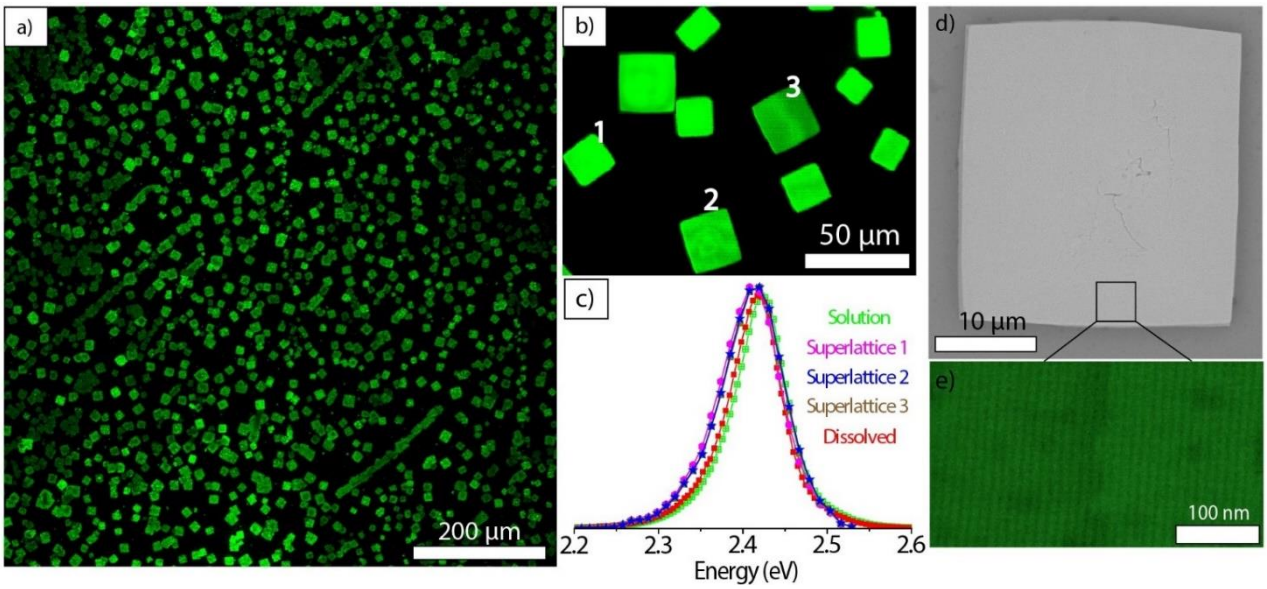

Figure 21. a) A low magnification confocal PL microscope image (under 488 nm excitation) of superlattices made from 8.3±0.6 nm $CsPbBr_3$ nanocubes (see text for description); b) confocal PL image of several square-shaped superlattices; c) PL spectra of $CsPbBr_3$ nanocubes before and after self-assembly overlaid with PL spectra from three individual superlattices labelled in panel b). PL of the superlattices is broadened and ~2.5 meV red-shifted compared to the PL of NCs in solution. d) SEM image of individual superlattice and e) high-resolution SEM inset showing close-packing of individual nanocubes.

The $CsPbBr_3$ NCs used for our self-assembly experiments were synthesized with didodecylamine under standard reaction condition without any size-selective precipitation and washings steps beyond the NCs isolation after synthesis. The average nanocube edge length estimated from TEM was 8.3 ± 0.6 nm with PL centered at 2.42 eV (Figure 20). The self-assembly of NCs was accomplished by a controlled solvent evaporation on top of a tilted Si wafer inside the glovebox. Cubic or rectangular shaped SLs with lateral dimensions ranging from 12 to 40 microns (Figure 21) were formed upon drying of ~6 µM NC solution in toluene overnight. To the best of our knowledge these are the largest reported NCs SLs for lead halide perovskites. The formation of SLs was also possible under ambient conditions on the lab bench instead of the glovebox. For that experiment, we used ~4 µM toluene solution of similar sized nanocubes (edge length of 8.5 ± 0.4 nm, Figure 22). In some parts of the Si wafer less regular polygonal SLs with long edges reaching up to 50 microns were observed (Figure 23). Confocal PL microscopy was used to obtain PL images (Figure 5a) and acquire

spectra of individual SLs (Figure 21c) under 488 nm excitation. The inspection of PL images (Figure 21b) revealed that the SLs show spatially uniform PL on a micron length scale and incorporate virtually all of the emissive material with no noticeable amorphous NC aggregates outside, which further highlights the shape purity and narrow size distribution of NCs synthesized using secondary aliphatic amines.

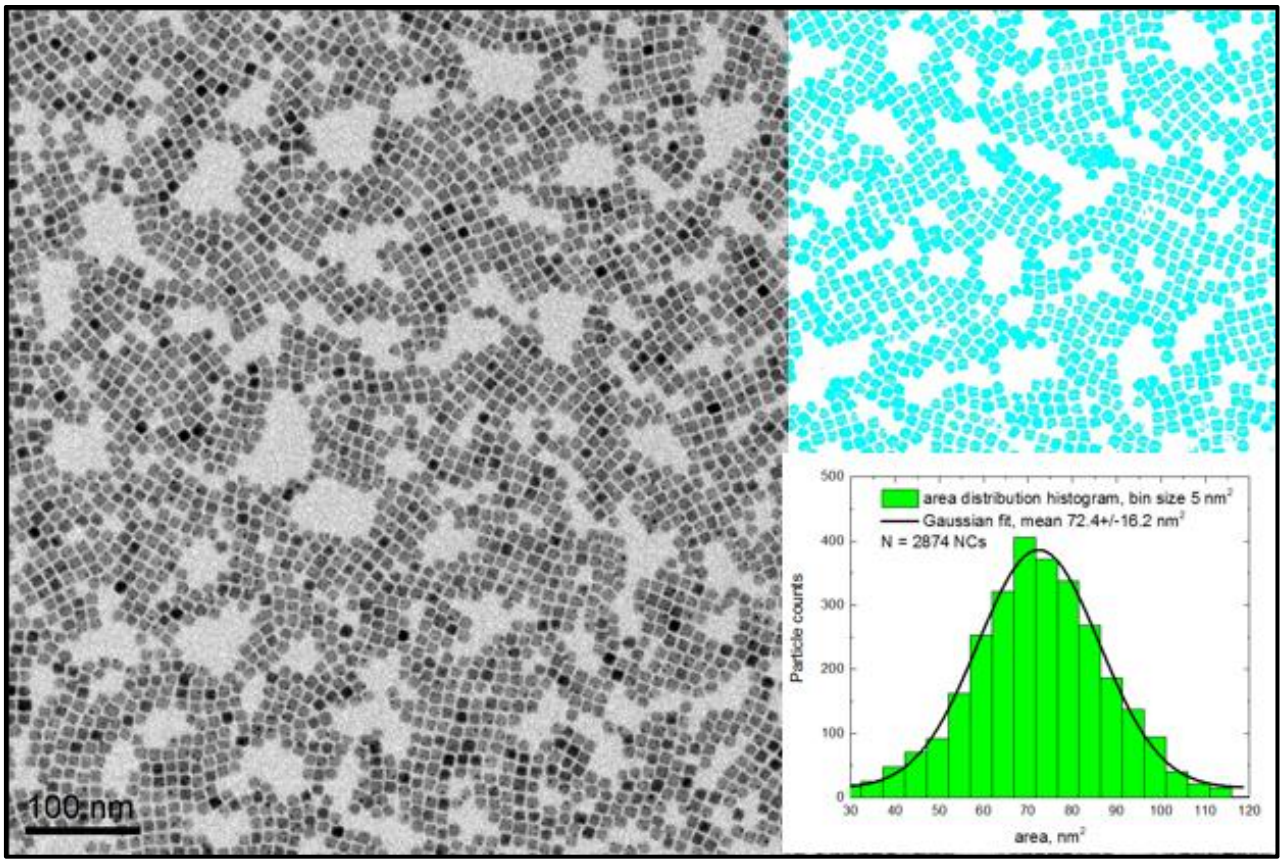

Figure 22. TEM image with results of the thresholding size analysis in ImageJ.[48,49] (top right) overlay of the cyan outlines of the NCs identified in the image, (bottom right) the histogram of the nanocrystal areas from the entire image (N = 2874 nanocrystals). Assuming square NC outline, the average NC area of 72.4+/-16.2 nm^2 corresponds to 8.5+/-0.9 nm edge length.

The PL spectra from individual SLs are practically indistinguishable from each other within the spectral resolution of the microscope detector (~3 nm) and show a 2.5 meV red shift compared to the starting NC solution or to a solution of NCs obtained by dissolving a small area of the self-assembled sample (Figure 21c). The latter indicates that the red shift is specific to the SLs and not due to any transformation occurred to the NCs. The red-shifted PL from the $CsPbBr_3$ NC SLs has been observed previously also, [7,44-47] but its exact origins are unclear and remain a subject of further investigation. High resolution SEM imaging of the individual SLs indicate that they have remarkably flat surfaces (aside of the obvious defects), and images acquired at higher magnifications evidence that the SLs consist of tightly packed nanocubes (Figure 21d,e). In summary, the record dimensions

of the SLs obtained by slow solvent evaporation without extensive post-synthetic manipulations of NCs highlight the advantages of the synthesis developed in this work compared to other approaches.

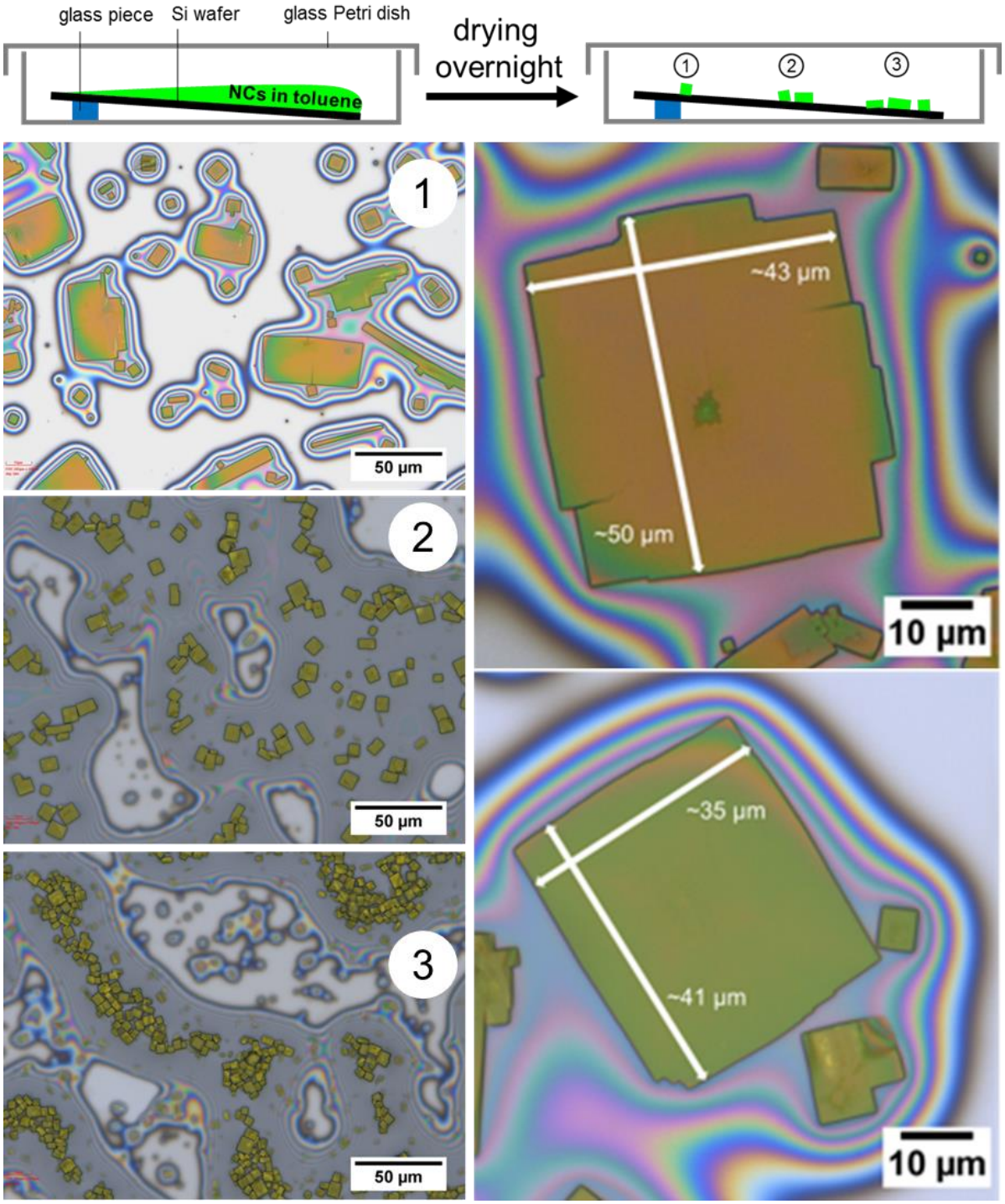

Figure 23. (top panel) Sketch of the self-assembly experiment; (right panels) optical microscopy images of the regions (1, 2, and 3, as illustrated in the top panel) showing three major populations of nanocrystal superlattices formed upon toluene evaporation; (left panels) images of two large superlattices with dimensions indicated.

5.5. Conclusions

A key finding of this work consists of substituting primary amine with secondary amine in the benzoyl halide-based hot-injection synthesis of $CsPbBr_3$ nanocubes. That substitution eliminates formation of nanocrystal shapes other than cubic, resulting in samples with remarkable uniformity of $CsPbBr_3$ nanocrystals. The shape uniformity and size tunability of the resulting nanocubes is demonstrated to persist independently on the temperature of the bromide precursor injection (50 °C to 140 °C range) or hydrocarbon chain length of secondary amines (from dihexyl to dioctadecyl). The resulting nanocubes demonstrate narrow PL linewidths (full width at half maxima 68-81 meV) and high PLQYs (48-80%) in solution. The DFT calculations revealed that the dialkylammonium molecules cannot stabilize lamellar 2D perovskites, and thus do not promote the anisotropic growth of NPLs, but rather promote the isotropic growth of nanocubes. The high uniformity of the obtained samples was utilized to obtain nanocrystal superlattices with lateral dimensions reaching up to 50 microns – the largest reported so far in lead halide perovskite family. We further believe that secondary amines will not only expand the ligands library of lead halide perovskite nanocrsytals but also paved a way to better elucidate photophysicscal properties of shape pure material.

5.5. References

(1) Park, N.-G.; Grätzel, M.; Miyasaka, T.; Zhu, K.; Emery, K. *Nature Energy* **2016**, *1*, 16152.

(2) Yang, W. S.; Park, B.-W.; Jung, E. H.; Jeon, N. J.; Kim, Y. C.; Lee, D. U.; Shin, S. S.; Seo, J.; Kim, E. K.; Noh, J. H. *Science* **2017**, *356*, 1376.

(3) Etgar, L.; Gao, P.; Xue, Z.; Peng, Q.; Chandiran, A. K.; Liu, B.; Nazeeruddin, M. K.; Grätzel, M. *Journal of the American Chemical Society* **2012**, *134*, 17396.

(4) Schmidt, L. C.; Pertegas, A.; Gonzalez-Carrero, S.; Malinkiewicz, O.; Agouram, S.; Minguez Espallargas, G.; Bolink, H. J.; Galian, R. E.; Perez-Prieto, J. *J Am Chem Soc* **2014**, *136*, 850.

(5) Protesescu, L.; Yakunin, S.; Bodnarchuk, M. I.; Krieg, F.; Caputo, R.; Hendon, C. H.; Yang, R. X.; Walsh, A.; Kovalenko, M. V. *Nano Lett* **2015**, *15*, 3692.

(6) Akkerman, Q. A.; Rainò, G.; Kovalenko, M. V.; Manna, L. *Nature materials* **2018**, 1.

(7) Kovalenko, M. V.; Protesescu, L.; Bodnarchuk, M. I. *Science* **2017**, *358*, 745.

(8) Protesescu, L.; Yakunin, S.; Bodnarchuk, M. I.; Krieg, F.; Caputo, R.; Hendon, C. H.; Yang, R. X.; Walsh, A.; Kovalenko, M. V. *Nano letters* **2015**, *15*, 3692.

(9) Imran, M.; Caligiuri, V.; Wang, M.; Goldoni, L.; Prato, M.; Krahne, R.; De Trizio, L.; Manna, L. *Journal of the American Chemical Society* **2018**, *140*, 2656.

(10) Ning, C.-Z.; Dou, L.; Yang, P. *Nature Reviews Materials* **2017**, *2*, 17070.

(11) Bekenstein, Y.; Koscher, B. A.; Eaton, S. W.; Yang, P.; Alivisatos, A. P. *Journal of the American Chemical Society* **2015**, *137*, 16008.

(12) Akkerman, Q. A.; Motti, S. G.; Srimath Kandada, A. R.; Mosconi, E.; D'Innocenzo, V.; Bertoni, G.; Marras, S.; Kamino, B. A.; Miranda, L.; De Angelis, F. *Journal of the American Chemical Society* **2016**, *138*, 1010.

(13) Zhang, D.; Eaton, S. W.; Yu, Y.; Dou, L.; Yang, P. *Journal of the American Chemical Society* **2015**, *137*, 9230.

(14) Imran, M.; Di Stasio, F.; Dang, Z.; Canale, C.; Khan, A. H.; Shamsi, J.; Brescia, R.; Prato, M.; Manna, L. *Chemistry of Materials* **2016**, *28*, 6450.

(15) Song, J.; Xu, L.; Li, J.; Xue, J.; Dong, Y.; Li, X.; Zeng, H. *Advanced materials* **2016**, *28*, 4861.

(16) Shamsi, J.; Dang, Z.; Bianchini, P.; Canale, C.; Di Stasio, F.; Brescia, R.; Prato, M.; Manna, L. *Journal of the American Chemical Society* **2016**, *138*, 7240.

(17) Sun, S.; Yuan, D.; Xu, Y.; Wang, A.; Deng, Z. *ACS nano* **2016**, *10*, 3648.

(18) Zhang, D.; Yu, Y.; Bekenstein, Y.; Wong, A. B.; Alivisatos, A. P.; Yang, P. *Journal of the American Chemical Society* **2016**, *138*, 13155.

(19) Almeida, G.; Goldoni, L.; Akkerman, Q.; Dang, Z.; Khan, A. H.; Marras, S.; Moreels, I.; Manna, L. *ACS nano* **2018**, *12*, 1704.

(20) Ravi, V. K.; Santra, P. K.; Joshi, N.; Chugh, J.; Singh, S. K.; Rensmo, H.; Ghosh, P.; Nag, A. *The journal of physical chemistry letters* **2017**, *8*, 4988.

(21) Pan, A.; He, B.; Fan, X.; Liu, Z.; Urban, J. J.; Alivisatos, A. P.; He, L.; Liu, Y. *ACS nano* **2016**, *10*, 7943.

(22) Akkerman, Q. A.; Park, S.; Radicchi, E.; Nunzi, F.; Mosconi, E.; De Angelis, F.; Brescia, R.; Rastogi, P.; Prato, M.; Manna, L. *Nano Lett* **2017**, *17*, 1924.

(23) Saidaminov, M. I.; Almutlaq, J.; Sarmah, S.; Dursun, I.; Zhumekenov, A. A.; Begum, R.; Pan, J.; Cho, N.; Mohammed, O. F.; Bakr, O. M. *ACS Energy Letters* **2016**, *1*, 840.

(24) Hutter, J.; Iannuzzi, M.; Schiffmann, F.; VandeVondele, J. *Wiley Interdisciplinary Reviews: Computational Molecular Science* **2014**, *4*, 15.

(25) Perdew, J. P.; Burke, K.; Ernzerhof, M. *Physical review letters* **1996**, *77*, 3865.

(26) VandeVondele, J.; Hutter, J. *The Journal of chemical physics* **2007**, *127*, 114105.

(27) Krieg, F.; Ochsenbein, S. T.; Yakunin, S.; Ten Brinck, S.; Aellen, P.; Süess, A.; Clerc, B.; Guggisberg, D.; Nazarenko, O.; Shynkarenko, Y. *ACS energy letters* **2018**, *3*, 641.

(28) ten Brinck, S.; Infante, I. *ACS Energy Letters* **2016**, *1*, 1266.

(29) Wu, P. S. C.; Otting, G. *Journal of Magnetic Resonance* **2005**, *176*, 115.

(30) Wagner, R.; Berger, S. *Journal of Magnetic Resonance, Series A* **1996**, *123*, 119.

(31) Boyer, R. D.; Johnson, R.; Krishnamurthy, K. *Journal of Magnetic Resonance* **2003**, *165*, 253.

(32) Schneider, C. A.; Rasband, W. S.; Eliceiri, K. W. *Nature methods* **2012**, *9*, 671.

(33) Yassitepe, E.; Yang, Z.; Voznyy, O.; Kim, Y.; Walters, G.; Castañeda, J. A.; Kanjanaboos, P.; Yuan, M.; Gong, X.; Fan, F. *Advanced Functional Materials* **2016**, *26*, 8757.

(34) De Nolf, K.; Capek, R. K.; Abe, S.; Sluydts, M.; Jang, Y.; Martins, J. C.; Cottenier, S.; Lifshitz, E.; Hens, Z. *Journal of the American Chemical Society* **2015**, *137*, 2495.

(35) Weidman, M. C.; Goodman, A. J.; Tisdale, W. A. *Chemistry of Materials* **2017**, *29*, 5019.

(36) Dohner, E. R.; Hoke, E. T.; Karunadasa, H. I. *Journal of the American Chemical Society* **2014**, *136*, 1718.

(37) Dou, L. *Journal of Materials Chemistry C* **2017**, *5*, 11165.

(38) Liu, Z.; Bekenstein, Y.; Ye, X.; Nguyen, S. C.; Swabeck, J.; Zhang, D.; Lee, S.-T.; Yang, P.; Ma, W.; Alivisatos, A. P. *Journal of the American Chemical Society* **2017**, *139*, 5309.

(39) Palazon, F.; Almeida, G.; Akkerman, Q. A.; De Trizio, L.; Dang, Z.; Prato, M.; Manna, L. *Chemistry of Materials* **2017**, *29*, 4167.

(40) Udayabhaskararao, T.; Houben, L.; Cohen, H.; Menahem, M.; Pinkas, I.; Avram, L.; Wolf, T.; Teitelboim, A.; Leskes, M.; Yaffe, O. *Chemistry of Materials* **2017**, *30*, 84.

(41) Davis, M. M. *Acid-base behavior in aprotic organic solvents*; US National Bureau of Standards, 1968.

(42) Thirunavukkarasu, K.; Thirumoorthy, K.; Libuda, J.; Gopinath, C. S. *The Journal of Physical Chemistry B* **2005**, *109*, 13272.

(43) De Roo, J.; Ibáñez, M.; Geiregat, P.; Nedelcu, G.; Walravens, W.; Maes, J.; Martins, J. C.; Van Driessche, I.; Kovalenko, M. V.; Hens, Z. *ACS nano* **2016**, *10*, 2071.

(44) Kovalenko, M. V.; Bodnarchuk, M. I. *CHIMIA International Journal for Chemistry* **2017**, *71*, 461.

(45) Rainò, G.; Becker, M. A.; Bodnarchuk, M. I.; Mahrt, R. F.; Kovalenko, M. V.; Stöferle, T. *arXiv preprint arXiv:1804.01873* **2018**.

(46) Yu, T.; En-Ping, Y.; Aurora, M.; Eva, B.; Kun, W.; Markus, D.; Sara, B.; Peter, M.-B.; S., U. A.; Lakshminarayana, P.; Jochen, F. *Advanced Materials* **2018**, *30*, 1801117.

(47) van der Burgt, J. S.; Geuchies, J. J.; van der Meer, B.; Vanrompay, H.; Zanaga, D.; Zhang, Y.; Albrecht, W.; Petukhov, A. V.; Filion, L.; Bals, S.; Swart, I.; Vanmaekelbergh, D. *The Journal of Physical Chemistry C* **2018**, *122*, 15706.

(48) Park, S. D.; Baranov, D.; Ryu, J.; Cho, B.; Halder, A.; Seifert, S.; Vajda, S.; Jonas, D. M. *Nano Letters* **2017**, *17*, 762.

(49) Segets, D.; Lucas, J. M.; Klupp Taylor, R. N.; Scheele, M.; Zheng, H.; Alivisatos, A. P.; Peukert, W. *ACS Nano* **2012**, *6*, 9021.

Chapter 6. Novel metastable CuAuS phase in colloidal nanodisks via partial cation exchange

Abstract: Cation exchange reactions have emerged as a powerful tool to design more complex structures which cannot be accessed through direct synthesis routes. Taking the advantage of this strategy, here in we reported a novel ternary chalcogenide phase, CuAuS, via post-synthesis chemical transformation on performed NCs. Albeit the large number of studies on the Cu chalcogenide and their combination with noble metals, including Au, no previous study reported this particular phase both in bulk and NCs so far. The reason for this may be its instability out of a very narrow window of conditions. Remarkably this new ternary alloyed semiconductor NCs exhibit an intense LSPR which can be interesting for bio-sensing and in-vivo imaging. Further study will be needed to understand the reason for energy instability of this phase, such that no previous report mentioned its formation.

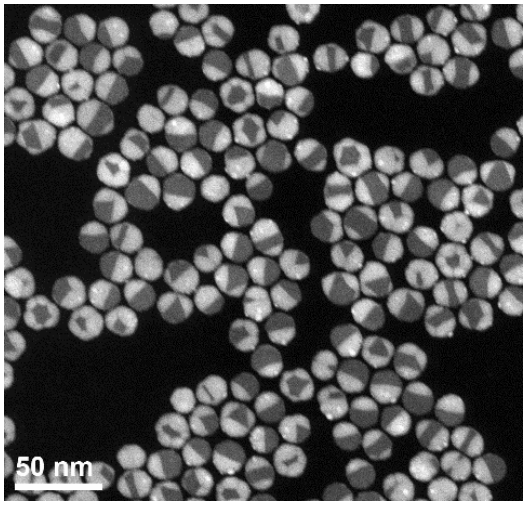

6.1. Introduction

During the last decades, nanometer-sized crystals of a wide variety of shapes and compositions were investigated, due to their enormous potential for many applications. Novel crystal phases were reported for these objects, which were never reported for the bulk, due to the high surface-to-volume ratio within these systems and the ensuing major role played by surface energy in the overall energy balance. In the realm of colloidal nanocrystals, one of the paths towards the creation of new phases is cation exchange,[1] i.e. the selective replacement of positive ions in a nanometer-sized object, the latter accessible via direct synthesis. In the cation exchange reaction, the anion framework is roughly preserved, while the initial cations, or part of them, are replaced. A metastable, hexagonal copper diselenide phase (Cu_2Se) was, for instance, reported by Li et al.,[2] obtained by replacing Cd^{2+} ions by Cu^{+} ions while keeping the anion lattice as well as the charge balance (i.e., each Cd^{2+} ion was replaced by two Cu^{+} ions), besides shape and size. In most cases, however, these new phases are not stable upon exposure to several conditions, ranging from photon irradiation to temperature variation to exposure to atmosphere. Among the sources of instability is beam irradiation within electron microscopes (EMs), precious tools needed for their same analysis. In particular, high energy electrons in a transmission EM (TEM), which are fundamental for the structural, morphological and compositional analysis of these nm-sized materials, are reported to induce transformations via radiolysis, knock-on, heating and other effects, the respective relevance depending on the electron energy and dose and on the material properties.[3] In some cases, electron beam irradiation is leading to an evolution to thermodynamically stable phases, thus particular care is required in the choice of experimental conditions in case metastable phases are investigated. For instance, the above-mentioned hexagonal Cu_2Se phase rapidly evolved into the higher stability cubic Cu_2Se phase upon 200 keV electron irradiation in the TEM, unless low-temperature conditions were used.[2]

Beside the Cd- and Pb-based II-VI and IV-VI semiconductors, in the last years several studies focused on Cu chalcogenide nanocrystals, due to their low cost, environmental-friendliness and low toxicity. Among them, Cu selenides and sulfides are promising due to their localized surface plasmon resonance (LSPR) exhibited in their Cu-deficient versions, with energy tunable with their composition and crystal structure.[4] An increasing number of studies, moreover, addressed the combination of Cu chalcogenide nanomaterials with noble metals,

with the aim of tuning their optical properties.[5-9] These materials indeed allow to combine the low cost and compositional tunability of Cu chalcogenides with the intense LSPR characteristic noble metals.

Within the context of cation-exchange mediated synthesis of new phases and Cu chalcogenide-based plasmonic nanomaterials, in the present work a novel phase is presented, synthesized within disk-shaped colloidal nanocrystals. This phase is obtained by replacement of half of the Cu^+ ions in a stoichiometric, low chalcocite Cu_2S phase by Au^+ ions. The result is a ternary alloy phase with the composition CuAuS, analogous to AgCuS orthorhombic phase (stromeyerite). This phase was never reported in ICDD nor in ICSD databases, nor in scientific literature, albeit the abundant literature on the $Cu_{2-x}S$-Au system. Our experiments, however, did never succeed in the complete transformation within our colloidal sample, and a maximum extent of about 50% of the pristine Cu_2S disks volume evolved into the CuAuS phase. The final product mainly consisted of Janus-type structures, with CuAuS and Cu_2S domains.

6.2. Experimental details

Synthesis of Cu_2S NCs

The synthesis of Cu_2S NCs was carried out by modifying a previously reported procedure.[10] Briefly, 1.0 mmol of $Cu(acac)_2$, 0.5 mmol of sulfur and 20 mL of oleylamine (OLA) were added into a 50 mL 3-neck round-bottom flask. The reaction mixture was degassed for 10 minutes under N_2 flux at room temperature, followed by heating up to 120°C and degassed for 20 minutes. Subsequently the reaction mixture was heated up to 200°C under N_2 and kept there for one hour and was finally cooled down to room temperature. 10 mL of isopropanol were added to the as-synthesized crude solution and NCs were collected by centrifugation at 5000 rpm for 10 min. The aforementioned washing step was repeated once more and finally the NCs were dispersed in 10 mL toluene for further use.

Reaction of Cu_2S NCs with Au(III)

6 mg of $AuBr_3$, 6 mg of dodecylamine (DDA) and 6 mL of toluene were combined in a 20 mL vial and sonicated at room temperature until the Au precursor completely dissolved. The resulting Au-DDA precursor was dropwise added to the NCs solution under inert atmosphere (N_2 glove box).

Reaction of CuAuS-Cu_2S NCs with Cd(II):

Briefly 1 mmol of Cadmium acetate, pre dried 5 mL ODE, 5 mL OLA and 5mL OA were combine in 20 mL vial in glove box and mixture was kept at 100 ^oC on hotplate until all the precursors dissolved. This cadmium precursor was stored inside glove box for further use. In a separate vial 300 ul of Cu_2S NCs solution was further diluted by adding 2 mL of anhydrous toluene. Then 50 uL TOP was added to the NCs solution and kept at hot already set at 60 ^oC. After 15 minutes, 200 uL of Cd precursor was added drop wise under continuous stirring and solution was left to react for 5 minutes further. Subsequently solution was cool down to room temperature and NCs were collected by 2mL of isopropanol.

6.3. Results and discussion

The initial Cu_2S colloidal nanoparticles, synthesized by slightly modifying the protocol reported by Lotfipour et al.[10] (see the experimental section), are displayed in Figure 1 and 2(a). The NPs exhibit a hexagonal platelet habit, with a diameter of 18 nm and 5.5 nm thickness. The highly improved shape and size monodispersity of these NCs, compared to the reference paper, are mainly due to the lower temperature kept throughout our synthesis (200°C, to be compared to 260°C).

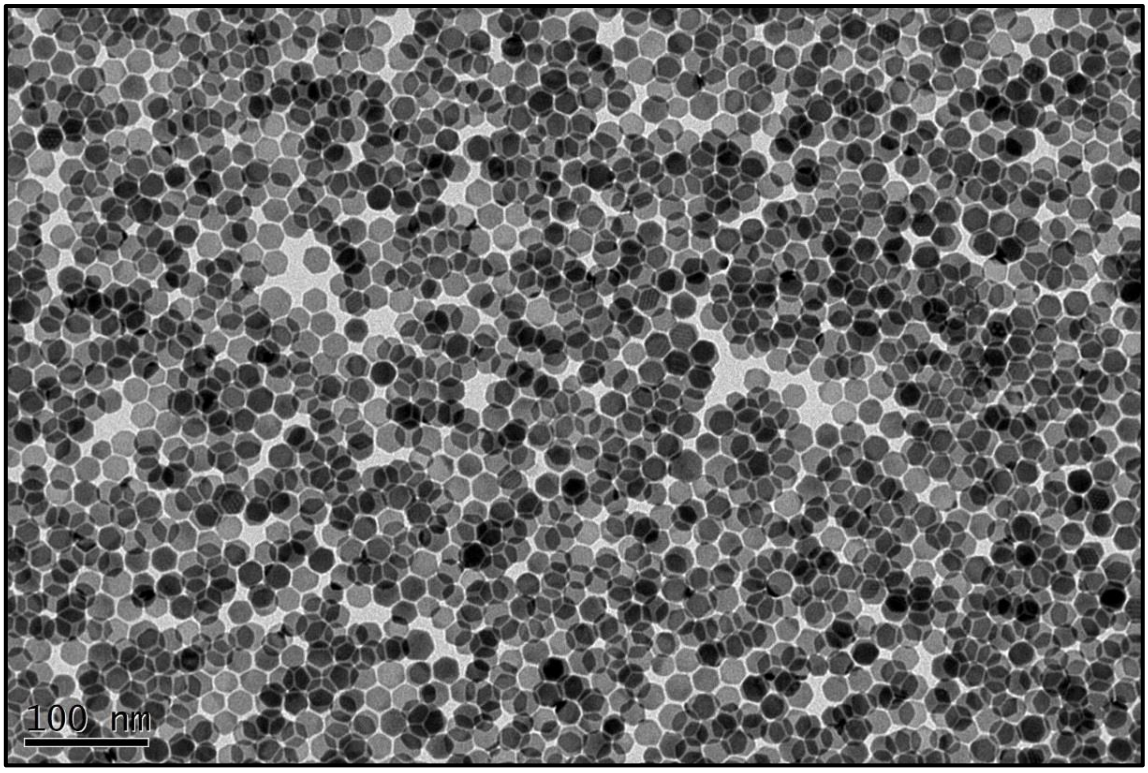

Figure 1. BF-TEM image of Cu_2S NCs, exhibiting their monodispersity

In analogy to the paper reporting the synthesis protocol, these NCs exhibit a monoclinic, low chalcocite structure (ICSD 100333), as proven by overview SAED patterns and HRTEM analyses on individual NCs (Figure 2(b-e)). It is worth noticing that the low chalcocite phase, also termed α-chalcocite, can be viewed as a slight distortion of the higher symmetry, hexagonal chalcocite phase, also termed β-chalcocite (ICSD 20560). The NCs stoichiometric composition (atomic ratio Cu:S = 2) was verified by STEM-EDS analyses over a large number of NCs. The exact stoichiometry and the lack of copper vacancies are indirectly demonstrated by the absence of LSPR signal, as shown in the absorption spectrum reported in Figure 3.[11] As widely reported in literature, ageing of the initially stoichiometric Cu_2S sample leads to oxidation, with the subsequent LSPR arising, with the maximum frequency depending on the degree of oxidation.

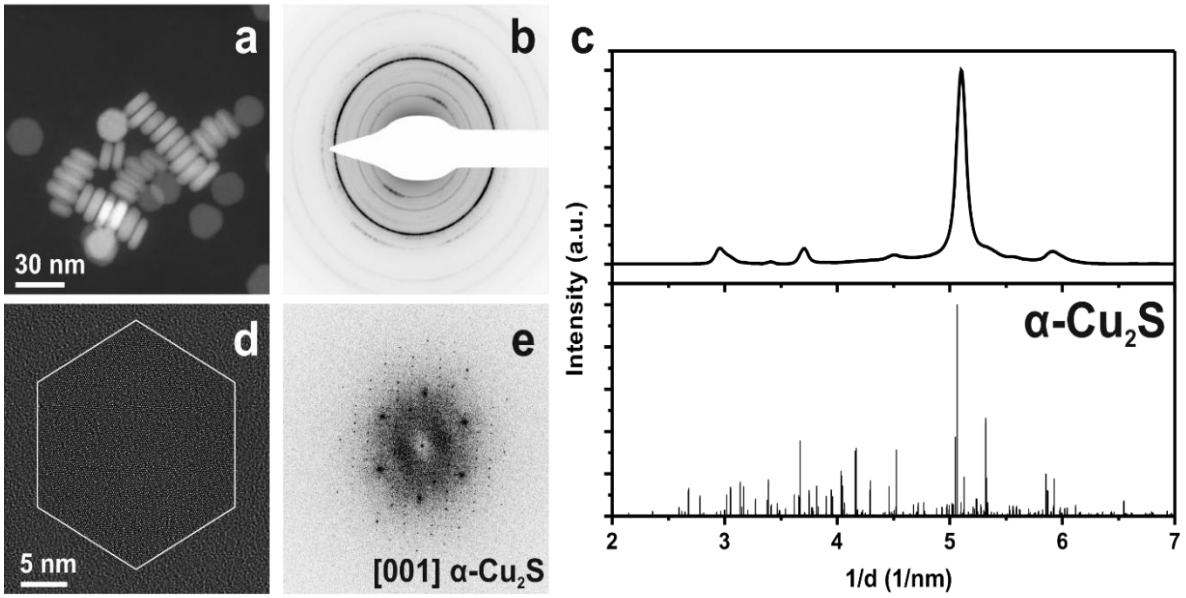

Figure 2. (a) HAADF-STEM overview image of the Cu_2S NCs in the initial sample. (b) SAED pattern obtained from a large number of NCs and (c) corresponding profile obtained by azimuthal integration,[12] compared to the X-ray powder diffraction files calculated for α-Cu_2S (ICSD 100333). (d) HRTEM image of a nanodisk in the sample and (d) corresponding fast Fourier transform (FFT), matching with the [001] zone-axis of α-Cu_2S.

The exposure of these NCs to Au(III) precursor (under the conditions described in the experimental section) results in the diffusion of Au^+ ions into the α-Cu_2S NCs and the replacement of half of the Cu^+ ions by Au^+ ions. As a result, a ternary alloy is formed, with

higher mean atomic number than Cu_2S, as clearly proven by HAADF-STEM imaging, an imaging technique enhancing the atomic number (Z) dependent contrast (see Figure 4a).

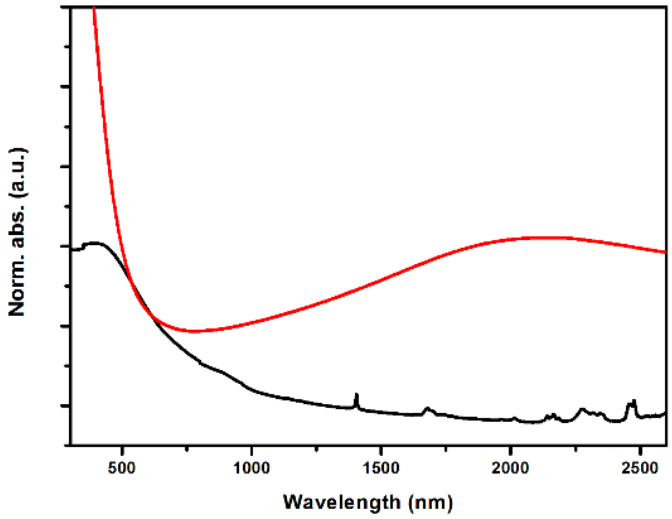

Figure 3. UV-visible-NIR absorption spectra collected on sample (Figure1) shortly after synthesis (black line) and after three weeks storage at room temperature and under N_2 atmopshere (red line): a broad band centered at about 2100 nm appears upon ageing of the sample, due to oxidation.

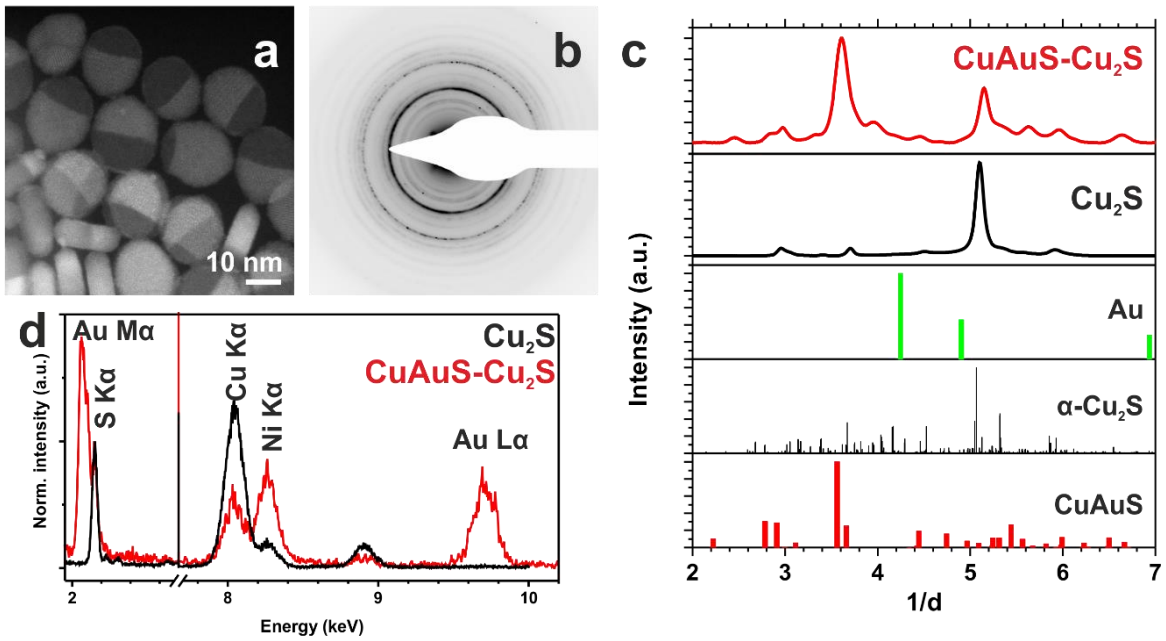

Figure 4. (a) HAADF-STEM overview image of the CuAuS-Cu_2S Janus-type NCs and (b) SAED pattern obtained on a large number of NCs. (c) The azimuthally integrated SAED pattern is compared to that of the pristine Cu_2S NCs and with the X-ray powder diffraction files calculated for Au (ICSD 52700), α-Cu_2S (ICSD 100333) and the novel CuAuS phase. In (d) the

comparison between EDS patterns obtained from only the CuAuS domains within the CuAuS-Cu_2S Janus-type and pristine Cu_2S NCs (spectra normalized to the maximum of S Kα peak).

The elemental composition of these higher-Z domains is assessed by EDS, and results in the atomic composition Au:Cu:S = 1:1:1 (see Figure 4d). However, while some of the NCs entirely evolve into CuAuS, most of them are only partially involved in the transformation.

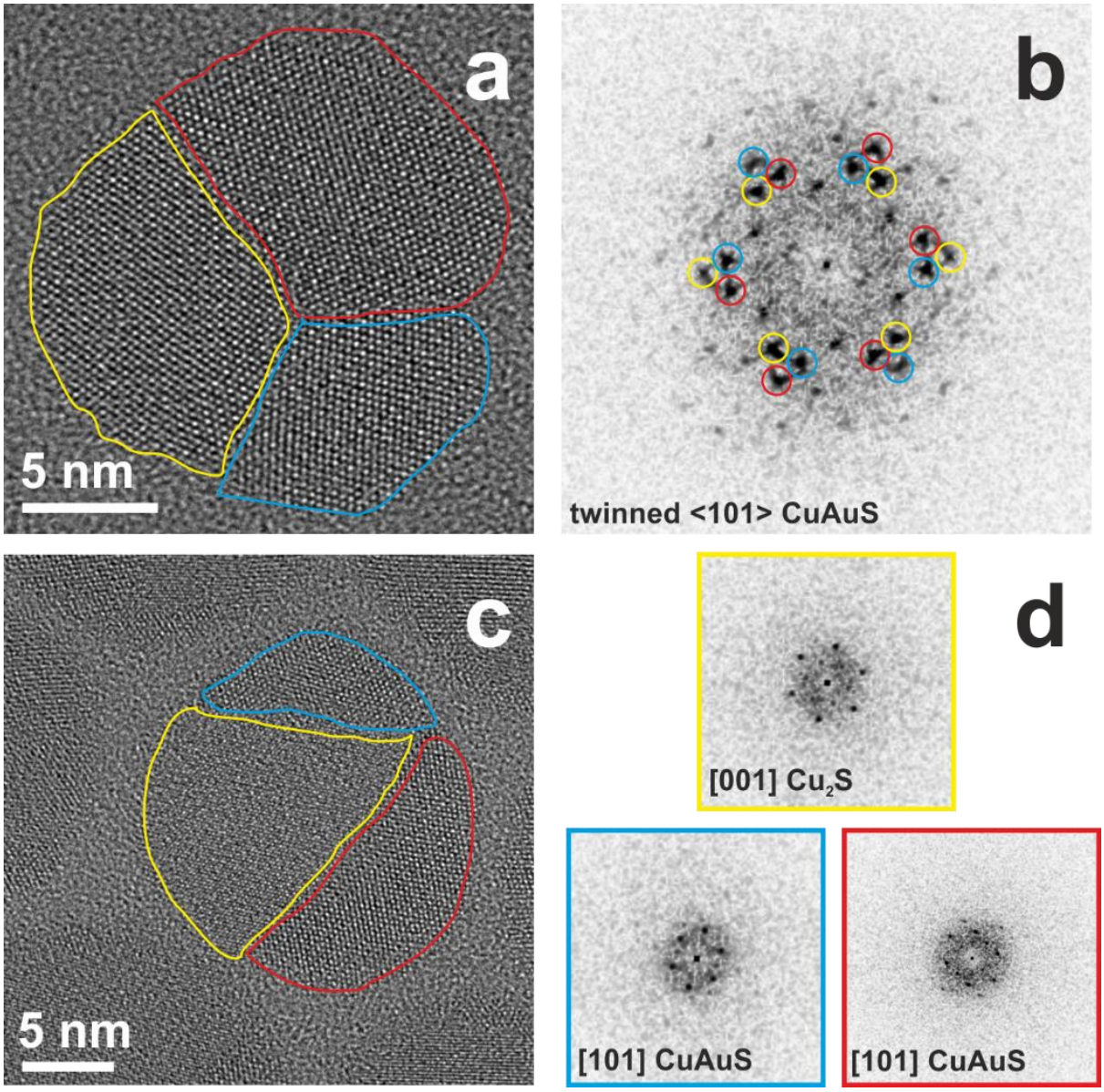

Figure 5. (a) HRTEM image of a CuAuS NC and (b) corresponding FFT. The NC is clearly formed by three twinned domains, each one exhibiting [101] orientation of the novel CuAuS phase. The partially converted NC in (c) allows to identify the corner of the pristine chalcocite disks as the entering points for Au ions, which diffuse into the structure along [110], [100], [010]

Additionally, the completely transformed NCs are composed of more than one crystalline domain, as shown by HRTEM analyses (Figure 5). As no crystal structure is reported with the composition CuAuS, neither in ICDD nor in ICSD databases, the best match with our experimental results was obtained by applying a ~7% expansion to the cell of the orthorhombic AgCuS phase (stromeyerite, ICSD 66580), reported by Baker et. al. to occur at ambient conditions.[13] The stromeyerite phase is based on distorted hexagonal close packing of S atoms, with the Cu atoms lying in trigonal coordination with the S layers, bridged by two-coordinate Ag atoms. The similarity between the stromeyerite and the chalcocite structures, based on their hexagonal close-packed framework of S atoms, is well reported in literature,[14-15] proving the presumption for this new ternary phase is a good starting point. directions, forming 120° with each other. The SAED patterns collected on a region including a large number of CuAuS-Cu_2S Janus-type particles, as well as the HRTEM images of the CuAuS domains, show a good match with the expanded CuAgS phase (see Figures 4(b-c) and Figure 5), with a = 4.216 Å, b = 6.8740 Å, c = 9.0 Å (for CuAgS: a=4.059 Å, b=6.617 Å, c=8.525 Å). However, albeit a platelet-shape is kept, the lower in-plane symmetry of the new phase manifests itself in an elongation of the CuAuS domains compared to the initial nanodisks.

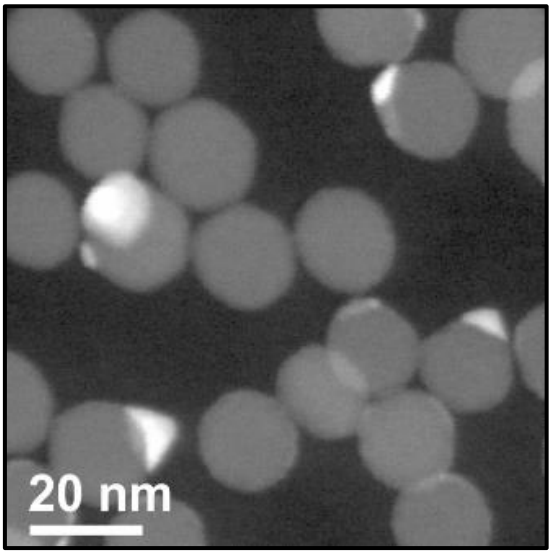

Figure 6. Effect of heating the CuAuS-Cu_2S NCs up to 150°C within the TEM: the brighter domains within the HAADF-STEM images are metallic Au NCs decorating the subsequently Cu-deficient $Cu_{2-x}S$ NCs.

Partially converted CuAuS-Cu_2S NCs allow for insights into the occurring transformation: the Au^+ ions enter the α-chalcocite structure from the corners of the hexagonal disks, and diffuse

along the [110], [100], [010] directions of α- Cu_2S, forming ternary domains with a 60° mutual rotation (see Figure 3(c-d)). These crystallographic directions are the elongation directions in the Janus-type NCs. The lack of three-fold symmetry in the [110] planes of the CuAuS phase explains the observed multi-domain structure: while the entering directions in α-Cu_2S are equivalent for the entering ions, when the evolution into the new phase has started, the three (or more) CuAuS phase cannot merge into a unique crystal domain. Exposure of the obtained CuAuS-Cu_2S Janus-type NCs to the electron beam, both in STEM (convergent beam) and TEM (parallel beam) irradiation conditions, with 100 keV and 200 keV of the primary electron beam, induced outwards diffusion of the Au atoms and decoration of the resulting Cu-deficient NCs with metallic Au NCs.

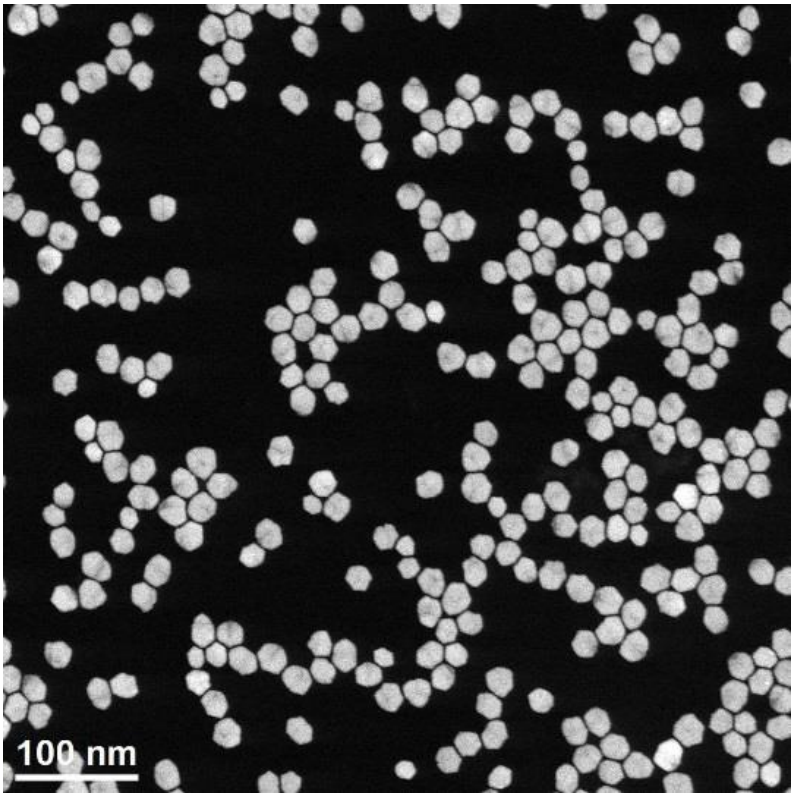

Figure 7. Multi-domain Au_2S NCs obtained after overnight exposure of initial Cu_2S NCs to the Au(III) precursor.

This effect is equivalent to heating the NCs up, as shown in Figure 6. The outwards diffusion of Au upon electron-beam irradiation and/or heating up is well-documented in literature for nanocrystals.[7, 16] Moreover, several attempts were done to obtain full conversion of the initial Cu_2S NCs into AuCuS. Firstly, they were exposed to the Au(III) precursor for a longer time (about 12 hours), with the complete replacement of Cu^+ ions from the Cu_2S lattice by Au^+ ions

leads to the formation of Au_2S NCs as a final result (see Figure 7). A similar result is obtained by addition of oleylamine (OLA) along with DDA in Au precursor and its susequrnt addition the NCs solution, as previously reported by Wang et al.[7] Most likely, OLA extracts the Cu^+ ions from pristine NCs and favors their complete replacement by Au^+ ions.

All these experiments are direct and indirect proofs of the instability of the CuAuS phase in ambient conditions, even within nm-sized objects. The impossibility to reach complete conversion into CuAuS one-domain NCs is a strong indication that this phase is unfavoured due to energetic reasons. Density-functional theory calculations are ongoing with the aim of substantiating this argument. The difficulty in obtaining the full conversion of the initial α-Cu_2S into a homogeneous colloidal sample composed of CuAuS NCs limited the possibility to test its properties. However, absorption spectra acquired in the UV-visible-NIR range strongly indicate the plasmonic properties of the novel ternary phase. In Figure 8, a clear absorption band centered at about 1480 nm is exhibited by the CuAuS-Cu_2S NC sample. Its attribution to possibly Cu-deficient phase in the binary domain can be excluded, given the stoichiometric composition of the phase in the domains, as carefully assessed by EDS analyses. This plasmonic resonance was reproducibly obtained over several samples proving that, albeit the precise extent of the Au reaction cannot be controlled, the optical properties of the resulting material, as well as its crystal structure, are reproducible.

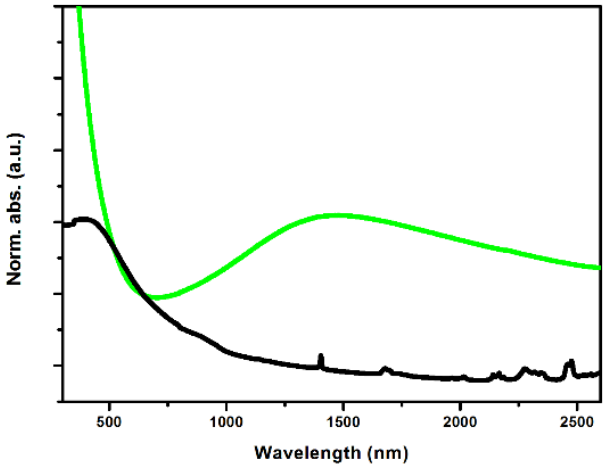

Figure 8. UV-visible-NIR absorption spectra collected on the CuAuS-Cu_2S sample (green line), compared to the Cu_2S NC sample shortly after synthesis (black line): a broad band centered at about 1480 nm appears after Au^+ ions enter the α-Cu_2S structure.

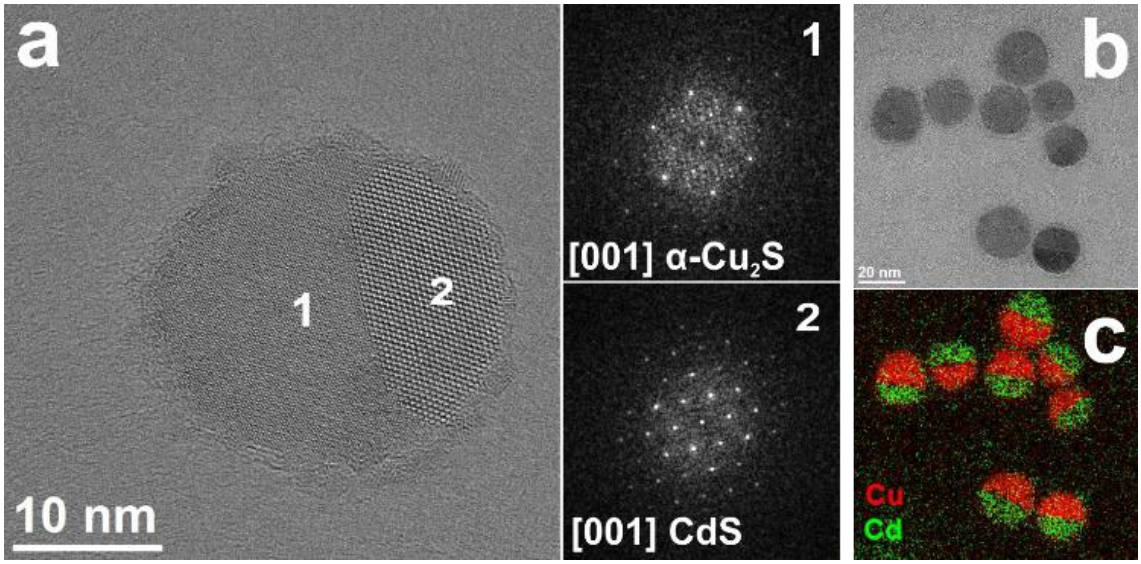

Figure 9. (a) HRTEM images of CdS-Cu2S heterostructures. The CdS domain is epitaxially oriented to Cu_2S and exhibits a hexagonal structure (ICSD 81925). (b) Zero-loss filtered BF-TEM image and (c) corresponding elemental EFTEM map for Cu and Cd, confirming the partial Cd-exchange occurred after exposing the pristine Cu_2S NCs to Cd(II) precursors.

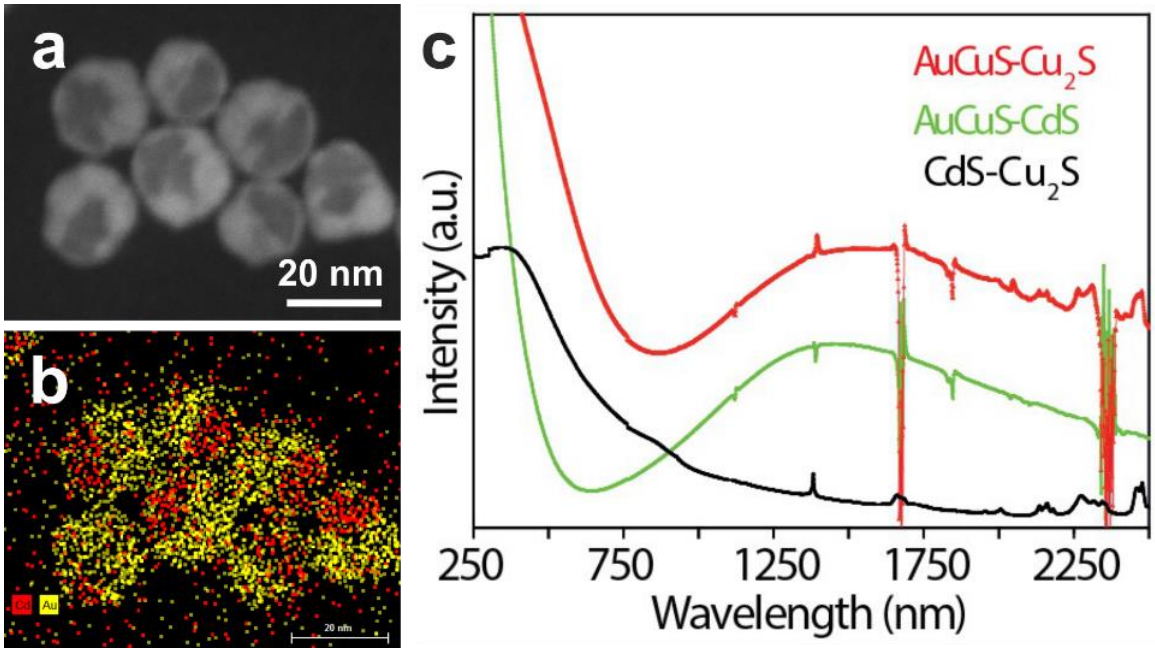

Figure 10. (a) HAADF-STEM overview image of CuAuS-CdS sample and (b) STEM-EDS map for Au (yellow) and Cd (red) showing the two well-separate domains. (c) The absorption spectrum of this sample, mainly consisting of CuAuS and CdS, demonstrate that the plasmonic properties are characteristic of the novel ternary phase.

The exposure to Au(III) was tested also for partially Cd^{2+}-exchanged Cu_2S disks, with the aim of creating new plasmonic-semiconductor heterostructure. To this end, we first exposed the initial α-chalcocite nanodisks to the correct amount of Cd(II) (see experimental section) so as to obtain a CdS-Cu_2S heterostructure (see Figure 9), following a "standard" Cu^{+}- to - Cd^{2+} cation exchange scheme. At a following step, the obtained Janus-type structures were exposed to the Au(III) precursor, and the outcome was a sample formed by CuAuS-CdS heterostructures (see Figure 5). The absorption spectrum shows a similar LSPR as the CuAuS-Cu_2S NC sample, confirming the desired plasmonic nature of the final product of this two-step reaction. With this last experiment, we proved the possibility of using the tunability of the cation-exchange strategy to obtain nanometer-sized structures with well-connected domains with different and complementary optical and electronic properties.

6.5. Conclusion

A novel ternary chalcogenide phase, CuAuS, was obtained via post-synthesis chemical reaction within colloidal NCs. Albeit the large number of studies on the Cu chalcogenide and their combination with noble metals, including Au, no previous study mentioned this phase before. The reason for this may be its instability out of a very narrow window of conditions. However, it proves to exhibit an intense LSPR which can be interesting for bio-sensing and in-vivo imaging. Further study will be needed to understand the reason for energy instability of this phase, such that no previous report mentioned its formation.

6.6. References

1. Son, D. H.; Hughes, S. M.; Yin, Y.; Paul Alivisatos, A., Cation Exchange Reactions in Ionic Nanocrystals. *Science* **2004,** *306* (5698), 1009.

2. Li, H.; Zanella, M.; Genovese, A.; Povia, M.; Falqui, A.; Giannini, C.; Manna, L., Sequential Cation Exchange in Nanocrystals: Preservation of Crystal Phase and Formation of Metastable Phases. *Nano Letters* **2011,** *11* (11), 4964-4970.

3. Egerton, R. F., Control of radiation damage in the TEM. *Ultramicroscopy* **2013,** *127*, 100-108.

4. Liu, Y.; Liu, M.; Swihart, M. T., Plasmonic Copper Sulfide-Based Materials: A Brief Introduction to Their Synthesis, Doping, Alloying, and Applications. *The Journal of Physical Chemistry C* **2017,** *121* (25), 13435-13447.

5. Deng, X.; Li, K.; Cai, X.; Liu, B.; Wei, Y.; Deng, K.; Xie, Z.; Wu, Z.; Ma, P. a.; Hou, Z.; Cheng, Z.; Lin, J., A Hollow-Structured CuS@Cu2S@Au Nanohybrid: Synergistically Enhanced Photothermal Efficiency and Photoswitchable Targeting Effect for Cancer Theranostics. *Advanced Materials* **2017,** *29* (36), 1701266.

6. Hu, C.; Chen, W.; Xie, Y.; Verma, S. K.; Destro, P.; Zhan, G.; Chen, X.; Zhao, X.; Schuck, P. J.; Kriegel, I.; Manna, L., Generating plasmonic heterostructures by cation exchange and redox reactions of covellite CuS nanocrystals with Au3+ ions. *Nanoscale* **2018,** *10* (6), 2781-2789.

7. Wang, X.; Liu, X.; Zhu, D.; Swihart, M. T., Controllable conversion of plasmonic Cu2-xS nanoparticles to Au2S by cation exchange and electron beam induced transformation of Cu2-xS-Au2S core/shell nanostructures. *Nanoscale* **2014,** *6* (15), 8852-8857.

8. Wolf, A.; Kodanek, T.; Dorfs, D., Tuning the LSPR in copper chalcogenide nanoparticles by cation intercalation, cation exchange and metal growth. *Nanoscale* **2015,** *7* (46), 19519-19527.

9. Dalmases, M.; Ibáñez, M.; Torruella, P.; Fernàndez-Altable, V.; López-Conesa, L.; Cadavid, D.; Piveteau, L.; Nachtegaal, M.; Llorca, J.; Ruiz-González, M. L.; Estradé, S.; Peiró, F.; Kovalenko, M. V.; Cabot, A.; Figuerola, A., Synthesis and Thermoelectric Properties of Noble Metal Ternary Chalcogenide Systems of Ag–Au–Se in the Forms of Alloyed Nanoparticles and Colloidal Nanoheterostructures. *Chemistry of Materials* **2016,** *28* (19), 7017-7028.

10. Lotfipour, M.; Machani, T.; Rossi, D. P.; Plass, K. E., α-Chalcocite Nanoparticle Synthesis and Stability. *Chemistry of Materials* **2011,** *23* (12), 3032-3038.

11. Xie, Y.; Riedinger, A.; Prato, M.; Casu, A.; Genovese, A.; Guardia, P.; Sottini, S.; Sangregorio, C.; Miszta, K.; Ghosh, S.; Pellegrino, T.; Manna, L., Copper Sulfide Nanocrystals with Tunable Composition by Reduction of Covellite Nanocrystals with Cu+ Ions. *Journal of the American Chemical Society* **2013,** *135* (46), 17630-17637.

12. Gammer, C.; Mangler, C.; Rentenberger, C.; Karnthaler, H. P., Quantitative local profile analysis of nanomaterials by electron diffraction. *Scripta Materialia* **2010,** *63* (3), 312-315.

13. Baker, C. L.; Lincoln, F. J.; Johnson, A. W. S., A low-temperature structural phase transformation in CuAgS. *Acta Crystallographica Section B* **1991,** *47* (6), 891-899.

14. Wuensch, B. J.; Buerger, M. J., The crystal structure of chalcocite, Cu2S. *Mineralogical Society of America* **1963,** *Special Paper 1*, 164-170.

15. Evans Howard, T., The crystal structures of low chalcocite and djurleite. In *Zeitschrift für Kristallographie - Crystalline Materials*, 1979; Vol. 150, p 299.

16. van Huis, M. A.; Figuerola, A.; Fang, C.; Béché, A.; Zandbergen, H. W.; Manna, L., Chemical Transformation of Au-Tipped CdS Nanorods into AuS/Cd Core/Shell Particles by Electron Beam Irradiation. *Nano Letters* **2011,** *11* (11), 4555-4561.

Chapter 7. Metal-semiconductor heterostructures by thermally induced transformations in Cu-chalcogenide NCs

Abstract: Thermal stability of the Cu chalcogenide nanocrystals is extremely important prior to their integration in devices, due to their phase-dependent properties. Herein we first investigated heating-up of Cu_2S NCs in high vacuum, in-situ and ex-situ. Interestingly, we observed that heated-up $Cu_{2+x}S$ nanorods (NRs)/nanowires (NWs) evolved into stoichiometric Cu_2S NRs/NWs with the formation of metallic copper domains on the surface of the NCs. In presence of additional metallic NCs, such as Au and Pt NCs, this transformation not only improves their thermal stability but also leads to the formation of Cu_2S NRs/NWs decorated with bi-metallic NCs. The underlying mechanism of this transformation is volume/surface diffusion, either of individual metal atoms or of clusters of atoms, to a location for which a metal-semiconductor junction is more thermodynamically favoured. This process is probably combined with sulfur oxidation and sublimation. The so-formed heteroepitaxial metal-semiconductor systems will allow for a more controllable and reproducible behaviour in electronic devices than in non-epitaxial structures (ensuring efficient charge separation/collection at the nanoscale).

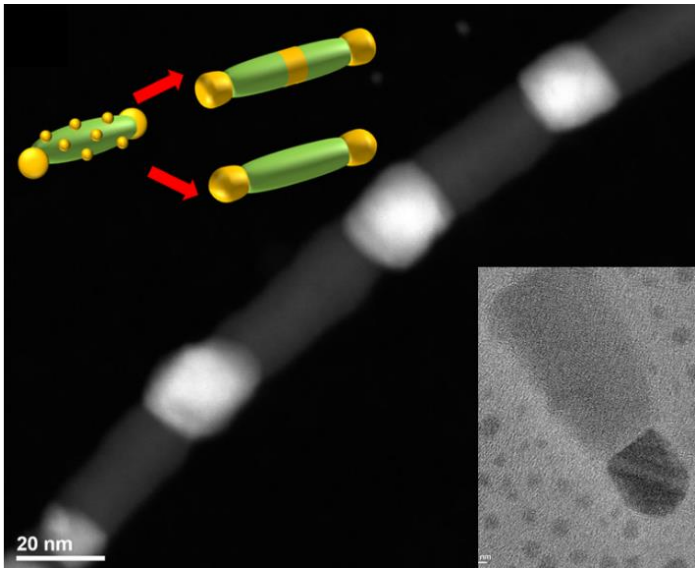

7.1. Introduction

Owing to their tuneable optical and optoelectronic properties, metal chalcogenide NCs have been extensively investigated during the past few years. In particular, considerable attention has been paid to the copper chalcogenide NCs as functional materials for photovoltaics and photothermal applications due to the high electrical conductivity, low cost, environmental friendliness and abundance in nature. In addition to this, these NCs specifically have versatile properties, for instance tuneable plasmon resonance frequency, due to the tendency to exhibit cation vacancies and subsequent variable composition and phase. Engineering of cation-vacancy in copper chalcogenides gives rise to distinct crystal phases that have similar crystal structures but different material properties. For example, low chalcocite, djurleite, and roxbyite are $Cu_{2-x}S$ phases having similar hexagonal close packing sulfur sublattices but significantly different material properties [1-8]. Due to the highly tuneable composition, the evolution of one phase into another is easy and needs to be controlled. In particular, for some applications the thermal stability in a certain range is desirable. Phase transformations of Cu chalcogenides nanometer-sized systems, in particular $Cu_{2-x}S$, have been extensively studied from the thermodynamics and kinetics point of view, but their thermally-induced transformations have been rarely reported so far. Recently, in-situ transmission electron microscopy (TEM) has proven to be useful in monitoring of such dynamic processes. Transformations induced by in-situ heating-up in conjunction with electron beam irradiation in some cases leads to formation of new nano-heterostructures [9-10]. In the first part of this chapter, ex-situ and in-situ studies of thermal stability of copper di-chalcogenide ($Cu_{2-x}S$, $Cu_{2-x}Se$) on homogeneous NCs of various aspect ratios will be presented. Following the results of these analyses, identical treatments have been applied in presence of nanoparticles of noble metals (Au, Pd, Pt) decorating the Cu chalcogenide NCs. As a subsequent step, the thermal stability of heterostructured NCs based on the same materials ($Cu_{2-x}Se$(core)/$Cu_{2-x}Se$(shell)) has been studied. When these core-shell nanocrystals were exposed to a Pd^{2+} precursor, with the aim of colloidal metal nanoparticle growth, a side reaction was found to prevail over the desired one, i.e. cation exchange of Cu^{+} ions. This behavior was not observed in case of Pt^{2+}.

7.2. Experimental details

Chemicals

Palladium acetylacetonate (99%), Platinum acetylacetonate, Trioctylphosphine oxide (TOPO, 99%), Trioctylphosphine (TOP, 97%), Sulfur powder (S, 99%), Selenium powder (Se, 99.99%), Copper(I) chloride (CuCl, 99.999%), Mercury(II) bromide (HgBr2, ACS) were purchased from Strem Chemicals. Octadecylphosphonic acid (ODPA, 99%) and Hexylphosphonic acid (HPA, 99%) were purchased from Polycarbon Industries. Cadmium oxide (CdO, 99.5%), Cadmium chloride (CdCl2, 99.99%), Tetrakis(acetonitrile)copper(I) hexafluorophosphate ([Cu(CH3CN)4]PF6, 99.99%), Oleylamine (Olam, 70%), 1-octadecene (ODE 90%), Gold(III) chloride ($AuCl_3$, 99%), dodecylamine (DDA, 98%), were purchased from Sigma-Aldrich. Anhydrous methanol and toluene were purchased from Carlo Erba reagents.

Synthesis experiment for CdS NRs, CdSe NRs, CdSe/CdS core shell RIRs and CdS NWs by following already reported methods [21-24] with slight modifications except partial cation exchange reaction with divalent metals.

Synthesis of CdS nanorods

TOPO (3.0 g), ODPA (0.280 g), HPA (0.110 g), CdO (0.050 g) and CuCl2 (0.006 g) were mixed in a 50 mL flask and degassed under vacuum at 130 °C for one hour. After that the solution was heated up to 300 °C under nitrogen and 1.5 g of TOP was injected into the flask. The temperature was then set to 350 °C and a S:TOP solution (prepared by dissolving 0.06 g of sulfur powder in 1.5 g of TOP) was injected into the flask to start the nucleation of the NCs. The NCs were allowed to grow for 10 minutes, after which the flask was rapidly cooled down to room temperature. After the synthesis, the NCs were washed by repeated precipitation with the addition of methanol and re-dissolution in toluene.

Synthesis of CdSe NRs

CdO (0.060 g) was mixed with TOPO (3.0 g), ODPA (0.280 g) and HPA (0.110 g) in a 50 mL flask, heated up to 130°C and exposed to vacuum for one hour. Then, under nitrogen, the solution was heated up to 300°C to dissolve the CdO. When the reaction mixture became optically clear and colourless, 1.5 g of TOP was injected into the flask. The temperature was then set to 350 °C and a Se:TOP solution (obtained by dissolving 0.15 g of selenium powder in 1.5 g of TOP) was injected into the flask to start the nucleation of the NCs. The NCs were allowed to grow for 8 minutes, after which the flask was rapidly cooled down to room temperature. The NCs were repeatedly precipitated with methanol and were eventually dissolved in toluene.

Synthesis of CdSe/CdS core/shell RIRs

CdSe/CdS core/shell RIRs was done via a seeded growth approach by following the procedures previously reported by our group. In particular CdO (0.060 g) and $CdCl_2$ (0.006 g) were mixed in a flask together with TOPO (3 g), ODPA (0.280 g) and HPA (0.080 g) and degassed under vacuum for about one hour at 130°C. The resulting solution was heated up to 300 °C under nitrogen and, after the complete dissolution of the CdO precursor, 1.5 g of TOP was injected into the flask. The temperature was allowed to reach 350 °C and a solution containing both the sulfur precursor and the CdSe seeds was quickly injected. Such solution was previously prepared by dissolving 0.060 g of sulfur powder in 1.5 g of TOP and adding 200 µL of a 400 µM solution of CdSe rods in TOP. The NCs were allowed to grow for 7 minutes, then the synthesis was quenched by removing the heating mantle and leaving the solution to cool down to room temperature. After a first precipitation with methanol, the NCs were redispersed in toluene.

Synthesis of CdS Nanowires

A mixture of CdO (64 mg, 0.5 mmol), oleic acid (0.40 mL, 1.27 mmol), HDA (0.024 g, 0.1 mmol) and ODE (5 mL, 15.59 mmol) was heated and degassed at 100 °C for 1 hour. The reaction vessel was then backfilled with nitrogen and the temperature was raised to 315 °C. When the reaction mixture turned clear, an injection solution consisting of 1M TOPS (0.08 mL, 80 µmol) and 0.02 M $BiCl_3$ in acetone (50 µL, 1.0 µmol) was introduced into the reaction mixture. The color of the solution immediately turned orange whereupon the reaction was kept at this temperature for 2 minutes. Afterwards, it was slowly cooled to 80°C. The reaction mixture was then diluted with toluene (3 mL) whereupon NWs were extracted from solution by adding a large excess of Methanol (~20 mL). At least 3 subsequent washings of the NWs were conducted using a mixture of toluene/methanol (80/20) to remove any excess surfactant.

Cation exchange (Cu^+) on Cd-based NCs & NWs

$Cu_{2-x}Se$ NRs, $Cu_{2-x}S$ NR, $Cu_{2-x}Se/Cu_{2-x}S$ core/shell RIRs and $Cu_{2-x}S$ nanowires were prepared through a complete cation exchange from Cd^{2+} to Cu^+ performed in a nitrogen-filled glovebox. In each experiment a Cu^+ solution in methanol was prepared by dissolving 0.03 mmol of tetrakis(acetonitrile)copper(I) hexafluorophosphate in 5 mL of methanol. 0.01 mmol of Cd-based NCs were dispersed in 5 mL of toluene and then mixed with the Cu^+ solution, under stirring for 5 minutes, at room temperature. The Cu/Cd atomic ratio all the experiment was 5. The exchanged NCs were precipitated through centrifugation and redispersed in toluene.

Ex-situ heating-up experiment details

Heating-up experiments were performed in a vacuum furnace under high vacuum conditions (P ~1 x 10^{-6} to 1 x 10^{-7} mbar), comparable to the vacuum conditions in the TEM column. Samples were prepared by depositing NCs on ultrathin carbon-coated Ni/Au/Al grids in order to obtain fast and homogeneous heat diffusion across the sample. All the samples were heated from room temperature to the desired temperature at a controlled heating rate and kept there for one to two hours.

In-situ heating-up experiments details

The in-situ thermal heating experiments were performed within the JEM-2200FS TEM column, i.e. under high vacuum conditions (pressure P ~1.5 x 10^{-7} mbar), using a dedicated single tilt heating holder capable to reach a maximum temperature of 800°C. Samples were prepared by depositing NCs/nanowires on ultrathin carbon-coated Ni/Al/Au grids in order to obtain fast and homogeneous heat diffusion and no interference in the EDS quantification of the desired elements. In-situ TEM thermal treatment of all samples was carried out in same way: the system was initially heated from room temperature (RT) to 300 °C at a heating rate of 15 °C/min and afterwards slowly heated up to 450 °C. The slow heating rate at later stage allows to minimize thermal drift and enable in-situ monitoring of transformations over time.

7.3. Results and discussion

As a starting experiment, the thermal stability of $Cu_{2-x}S$ rod-shaped nanocrystals (nanorods, NRs) was studied. These nanocrystals (NCs) were obtained by cation exchange (Cd^{2+} to Cu^{+}) on initial CdS NCs, as described in the experimental section. It is known that, for bulk material of roughly stoichiometric composition (Cu:S~2), several phases occur, all of them stable in the solid state up to temperatures higher than 800°C [11]. Instead, these $Cu_{2-x}S$ NRs, characterized by a relatively small aspect ratio, 1.9 (length/width=50±5nm/26±2nm), exhibited interesting features after a thermal treatment at 350°C (heating rate 7°C/min, sample kept 2 hours at max. temperature), as shown in Figure 1. From the comparison of pre- and post-thermal treatment, a small domain is clearly formed upon thermal treatment almost uniformly in all the NCs, mostly close to the central region. Besides this, $Cu_{2-x}S$ NRs did not undergo clear morphological changes. The composition of pristine $Cu_{2-x}S$ NCs was analysed by STEM-EDS analysis (Fig.2), showing a Cu:S atomic ratio 2.2:1 ($Cu_{2.2}S$) . Figure 2 also shows elemental maps, indicating the homogeneous distribution of Cu and S.

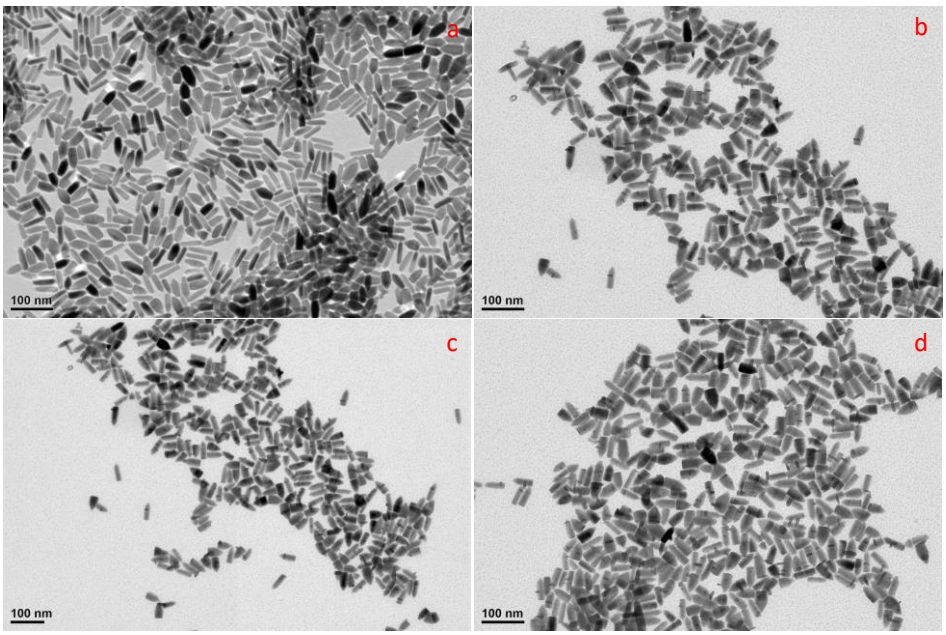

Figure 5. Bright field TEM images of as synthesized $Cu_{2-x}S$ NCs (a) and after thermal treatment up to 350°C in HV furnace (b, c, d).

The elemental analysis of thermally treated $Cu_{2-x}S$ NCs clearly shows that the domain formed upon heating-up is made of copper, while the remaining nanorod composition keeps close to stoichiometric (Cu:S~2). This suggests that, at high temperature, a partial sublimation of sulfur in the NRs takes place, and as a consequence the excess Cu in the NCs diffuses out of the NCs, forming a metallic Cu "attachment".

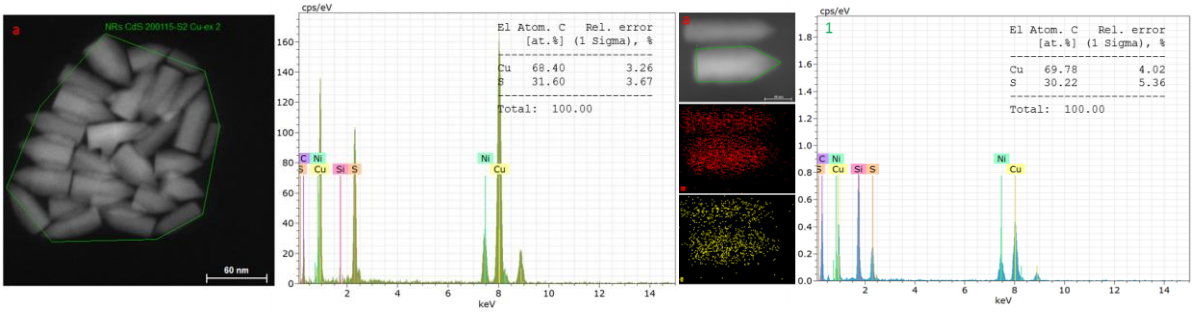

Figure 6. Left: HAADF-STEM image of a group of Cu-exchanged CdS NRs and corresponding overall EDS spectrum. Right: HAADF-STEM images and corresponding STEM-EDS maps showing the Cu and S distribution along with spectrum of elemental quantification across individual NR.

In-situ heating-up experiments were then carried out, aimed at real time monitoring of the metallic Cu domain formation taking place in the pristine $Cu_{2-x}S$ NRs as observed in ex-situ

thermal treatments. Morphological and structural analysis of the $Cu_{2-x}S$ NCs were performed before and after in-situ heating experiments. The in-situ TEM heating-up experiment confirms the formation of the metallic Cu domain. In particular, high resolution TEM (HRTEM) analysis of individual NCs at room temperature reveals that crystal structure of the nanocrystals belongs to high chalcocite Cu_2S (ICSD reference 20560,Fig. 3a).

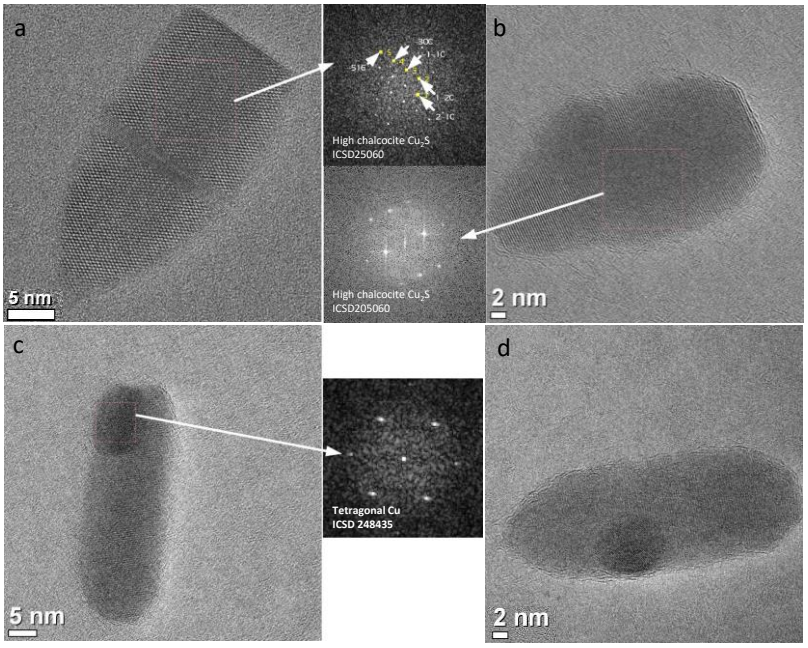

Figure 7. HRTEM images acquired before and during in-situ heating experiments, room temperature (a) 400°C (b) and at 370°C (c,d) along with and FFT patterns.

After in-situ heating up to 400°C crystal structure does not change while the d spacing values decreased, probably due to Cu deficiency in the lattice, known to induce cell contraction. HRTEM analysis of the extruded Cu domain at 370°C shows that its structure is ascribable to tetragonal Cu (ICSD reference 248435, Fig. 3c). We can still presume that this process is due to release of elastic strain building up in the central region of the $Cu_{2-x}S$ NR, where stacking faults are typically observed. A further interesting result of the in-situ heating-up experiment is related to the effect of electron beam irradiation, in particular on the extruded Cu domain, at 400°C and room temperature. When the Cu domain was exposed to electron beam at 370°C, without changing the temperature, for 100-300 seconds it sublimated, leaving behind intact, homogeneous and perfectly crystalline nanocrystals (compare Fig. 4 a and e, b and f, c and g). The same treatment, carried out after cooling down the same sample to room temperature, led not only to sublimation of the Cu domain but also to disgregation of the entire NRs (compare Fig.4 d and h). The sublimation of the Cu domain

in both temperature conditions might be due to a beam-induced heating, which might lead to sublimation of Cu in such nano-sized domain. On the other hand, the dismantling of the entire NC at room temperature, not occuring at 370°C, can be attributed to the inability of the crystal to anneal the structural defects formed due to the Cu NC gradual disappearing.

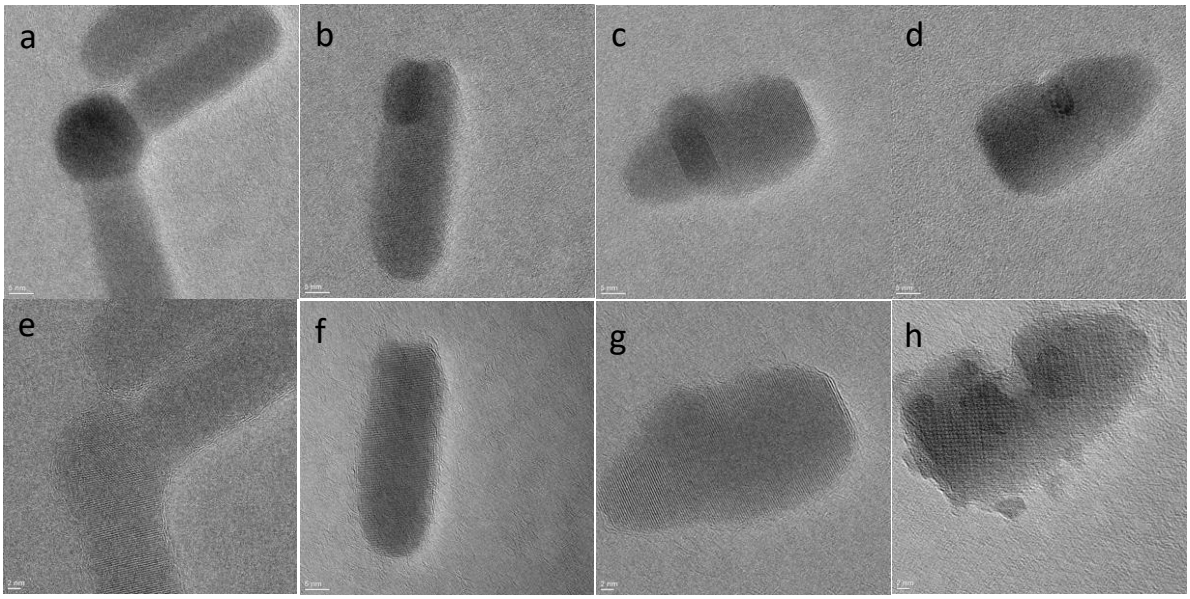

Figure 8. HRTEM images acquired at 370°C before (a-c) and after exposure to electron beam (e-g) and at room temperature, (d) before and (h) after electron beam exposure**.**

Given the observed formation of the extruded Cu domain in $Cu_{2-x}S$ NRs upon heating-up, we were interested to verify how this can combine with the presence of a pre-existing metal domain on the NC surface. In particular, for the first experiments, Au was chosen as a metal, due to the interesting system consisting in the combination of the two materials in the nanoscale, and their potential interest in device applications. For the sake of simplicity, Au was deposited by physical methods (i.e., sputter coating) on top of the TEM support on which the $Cu_{2-x}S$ NRs were located. Two identical samples, one with and one without sputtered Au on top, were heated up to 350°C (7°C/min, 2 hours at maximum temperature) The comparison between BF-TEM images of the two samples shows the reproducible formation of the Cu domain in simple $Cu_{2-x}S$ NCs, while in presence of Au a single, large, darker domain (i.e., higher atomic number) is formed on each NR, clearly acting as a sink for neighbouring Au NCs deposited on the carbon support film on the grid (Fig.5a-d), as the surrounding support is depleted of sputtered Au. Moreover, no sign of a distinct extruded Cu domain is visible on the Au-sputter-coated, thermally-treated, NRs.

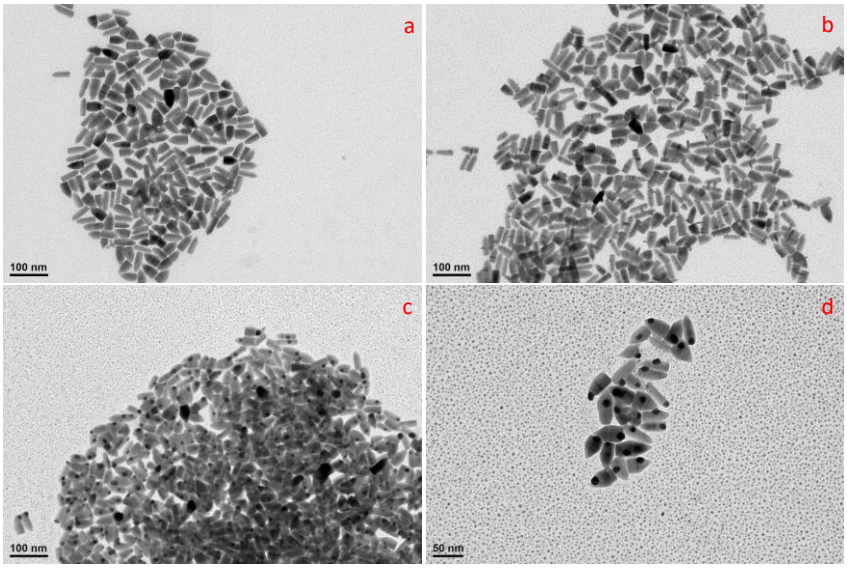

Figure 9. BF-TEM images of (a) pristine $Cu_{2-x}S$ NCs, (b) after heating up in HV furnace up to 350°C in absence of Au. (c,d) Result of $Cu_{2-x}S$ NCs heating-up in HV furnace up to 350°C in presence of sputtered Au.

HAADF-STEM images and STEM-EDS analysis of such a thermally treated sample (Au-sputter-coated $Cu_{2-x}S$ NRs) shows the distribution of Cu, S and Au across the NCs (Fig. 6). From the STEM-EDS maps it is clear that all the Au available on the NC surface and on the support around the NCs migrated via collective cluster/atomic diffusion and resulted in formation of a single domain.

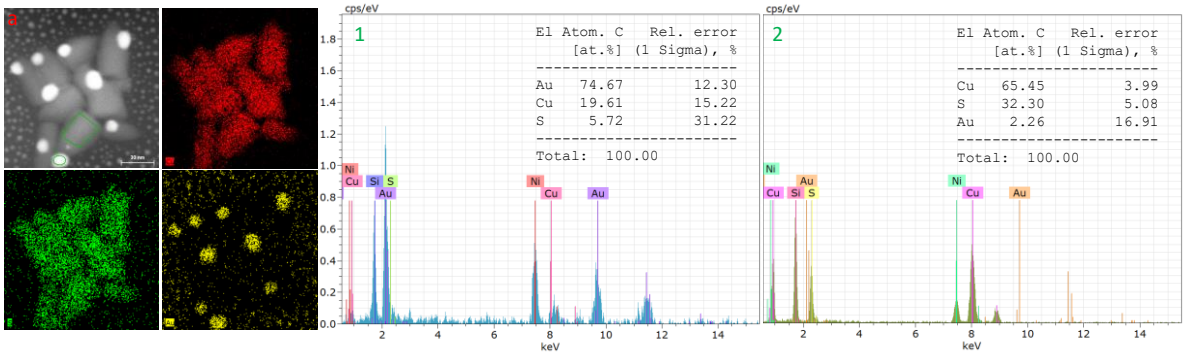

Figure 10. STEM-EDS images and corresponding STEM-EDS maps of thermally treated $Cu_{2-x}S$ NCs in presence of Au showing the distribution of Cu, S and Au along with spectrum of elemental quantification over individual nanorod only at the tip (1) and across NR (2).

Furthermore, STEM-EDS elemental analysis (Fig.6-1) reveals that the metallic domain mainly consists of an alloy of gold and copper with Au:Cu atomic ratios 3.81:1. Instead, the composition of the remaining NC (Fig.6-2) is Cu:S = 2.03:1 This result demonstrates that,

besides acting as a sink for the neighboring Au atoms/clusters, the large Au domain, mainly forming in proximity of the NR sharp tip, probably collects all extruded Cu atoms which would otherwise form a separate metallic Cu domain. In-situ heating experiment of NCs in presence of Au also leads to same results (Fig. 7).

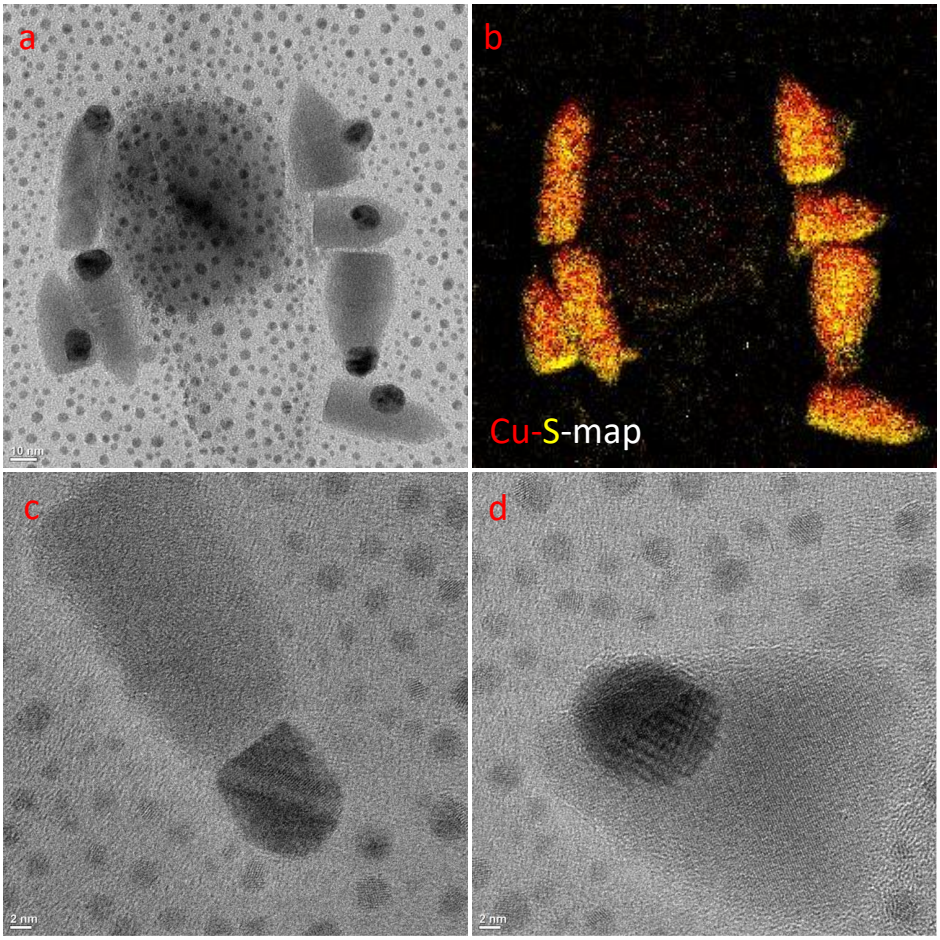

Figure 11. HRTEM images and EFTEM elemental maps for Cu and S acquired during in-situ heating-up of $Cu_{2-x}S$ NCs 400°C.

The above-mentioned results were compared to the ones obtained on $Cu_{2-x}S$ NRs with different aspect ratio, 2.26, namely larger NRs (not shown here). It was interesting to notice that no Cu domain formation occurred in that case. This might support the elastic-strain-release driven mechanism for Cu extrusion, as soon as the NR lattice is given enough thermal energy. A totally different aspect ratio system was afterwards tested in similar experiments, namely $Cu_{2-x}S$ nanowires (NWs) with 18(±2) nm diamter and length up to few tens of µm. These NWs were also obtained via cation-exchange (Cd^{2+} to Cu^{+}), (see experimental details). SAED patterns show hexagonal phase of the starting CdS NWs remain preserved [13] after cation exchange (Fig.8).

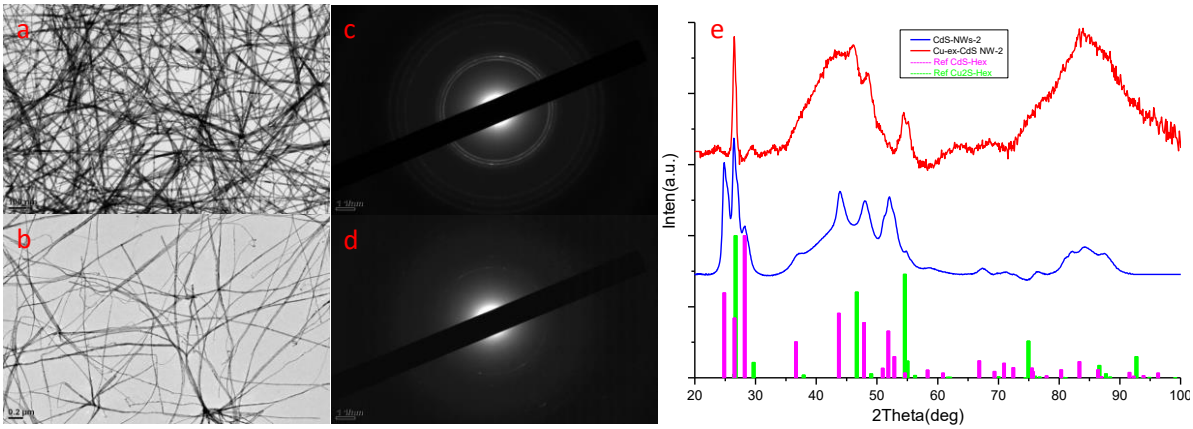

Figure 12. TEM Images of as synthesized CdS nanowires (a), after Cu exchange (b), their SAED patterns (c, d) respectively and 2-theta values (converted from SAED k values) compared with references (CdS-ICSD-154186 and Cu_2S-ICSD-20560).

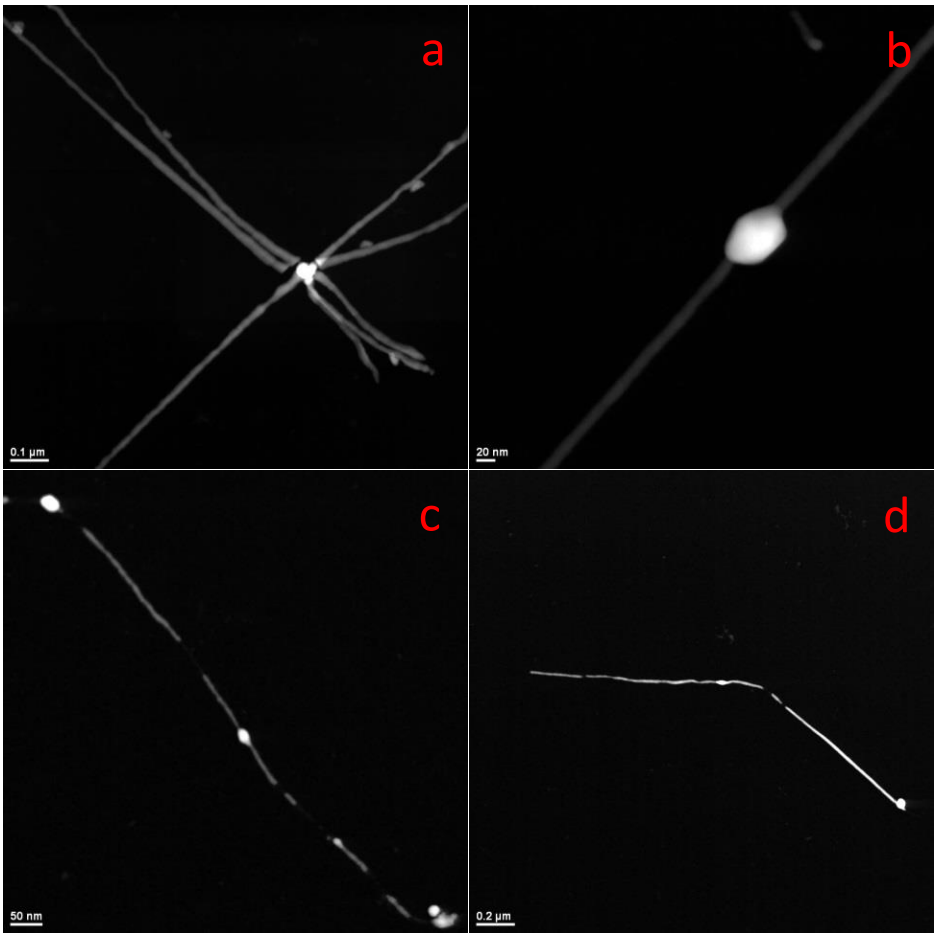

Figure 13. HAADF-STEM images of Cu-ex-CdS NWs at RT (a) and in-situ heating up to 450°C (b, c and d).

For these samples, preliminary results were obtained only via in-situ heating experiments. In-situ heating experiment study was carried out in STEM mode in order to minimize the effect

of electron beam irradiation. Morphological and compositional analysis of the NWs was performed at room temperature (RT), before and after in-situ heating. During in-situ heating experiments we observe the outer diffusion of copper and formation of metallic copper domains in certain regions while leaving the remaining nanowires unstable (Fig.9 c, d). STEM-EDS analysis of pristine and in-situ thermally treated $Cu_{2-x}S$ NWs indicated a slight decrease in the Cu:S atomic ratio from 2.50:1 to 2.07:1 respectively (Fig.10a, b). Furthermore STEM-EDS maps before and after in-situ heating shows the distribution of Cu and S across the nanowires. It is confirmed from the maps of in-situ heated NWs that domains appearing brighter in HAADF-STEM images (higher mean atomic number and/or thickness) correspond to metallic copper. This result is promising in that it elucidates how a simple thermal treatment, if suitably controlled, can give rise to a semiconductor-metal segmented structure which might show interesting hybrid properties.

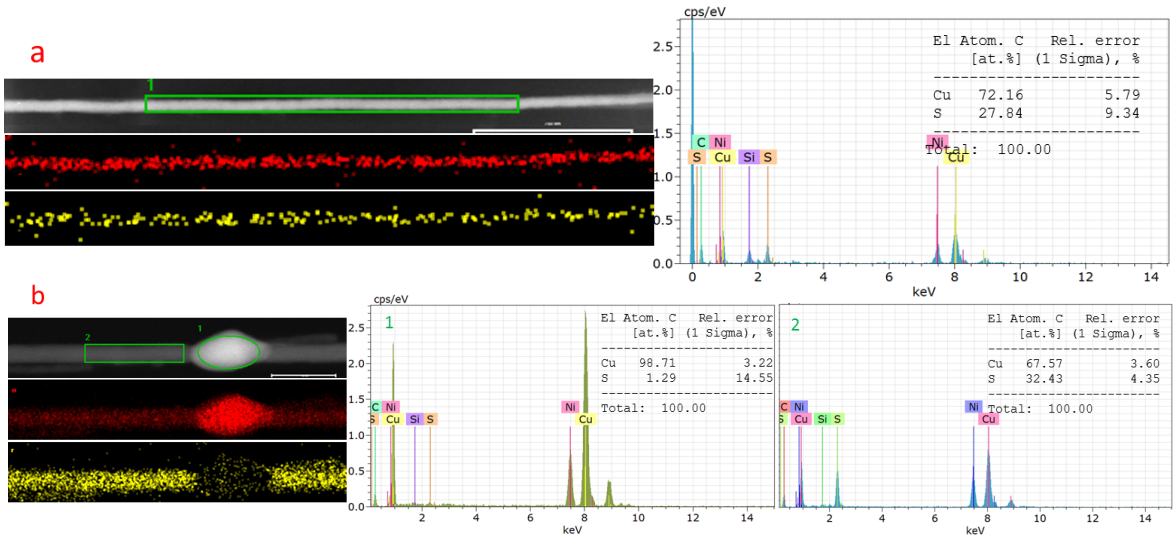

Figure 14. HAADF-STEM image and corresponding STEM-EDS maps of before (a) and after in-situ thermally treated (b) $Cu_{2-x}S$ NWs showing the distribution of Cu and S along with spectrum of elemental quantification in ROI (1) and NR (2).

Similarly, Au-sputter-coated $Cu_{2-x}S$ NWs were heated in-situ heated up to 350°C (25°C/min heating rate). HAADF-STEM images at room temperature, before the heating treatment, shows the nanostructured Au layer homogeneously deposited onto the NWs (Fig.11 a-c). Interestingly, heating-up of the NWs leads to the formation of segmented nanowires, with an almost periodic arrangement of metal domains on the semiconductor NWs (Fig.11 d-f).

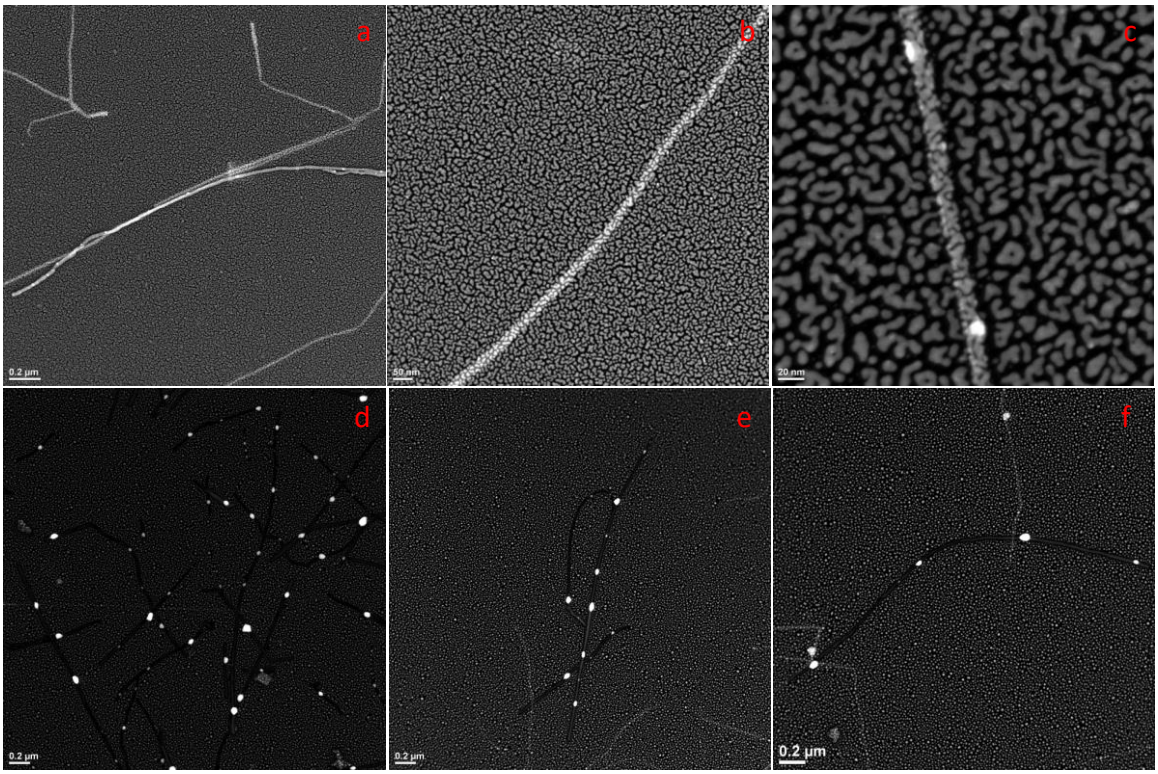

Figure 15. HAADF-STEM images of Au deposited $Cu_{2-x}S$ NWs at RT (a-c) and after in-situ heating upto 450^{o}C (d-f)

Presence of Au around nanowires makes them very stable as no sublimation/deformation of the nanowires was observed in any region during/post in-situ heating experiment analysis (Fig-11 d-f) while the same nanowires under same conditions in absence of Au were not stable (Fig-9 c,d). HAADF-STEM images and STEM-EDS analysis of the nanowires were done at room temperature before and after in-situ heating experiment. STEM-EDS elemental maps shows the uniform distribution of Au across nanowires before in-situ heating experiment (Fig.12) while after thermal treatment nanowires are segmented and entire Au is diffused into the segments while leaving the nanowires clean between segments (Fig.13). Elemental quantification of the segments indicated that Au:Cu atomic ratios are 2.55:1. The formation of segments across the nanowires making system much more stable. Ripening processes have been extensively investigated for various materials such as metals and semiconductors. Controlled formation of metallic domains on the surface of Cu chalcogenide nanocrystals and the quality of the interface between the metallic domain and parent nanocrystals are an important aspect of NCs processing by considering their possible use in electronic devices [14-18].

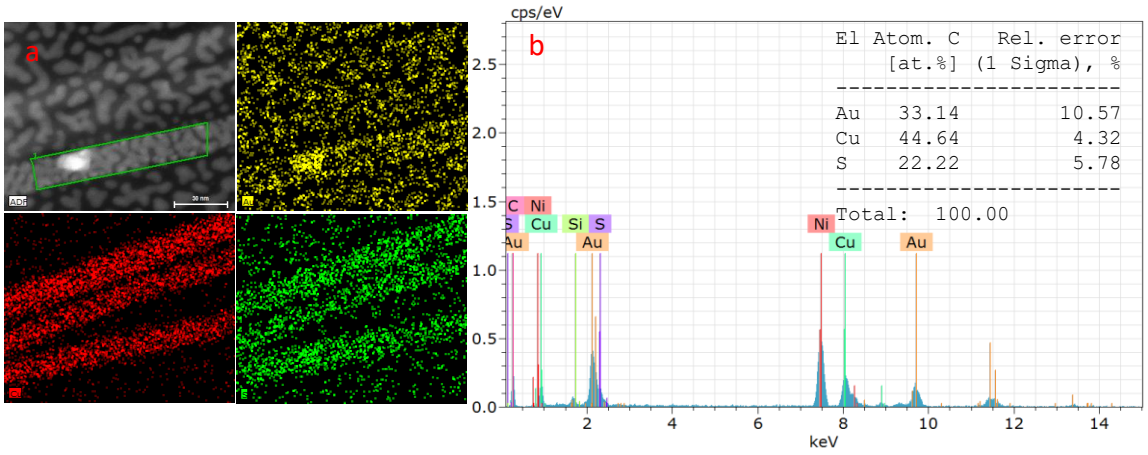

Figure 16. HAADF-STEM image and STEM-EDS maps of Au deposited Cu-ex-CdS NWs (RT) showing the distribution of Cu, S and Au along with spectrum of elemental quantification in ROI.

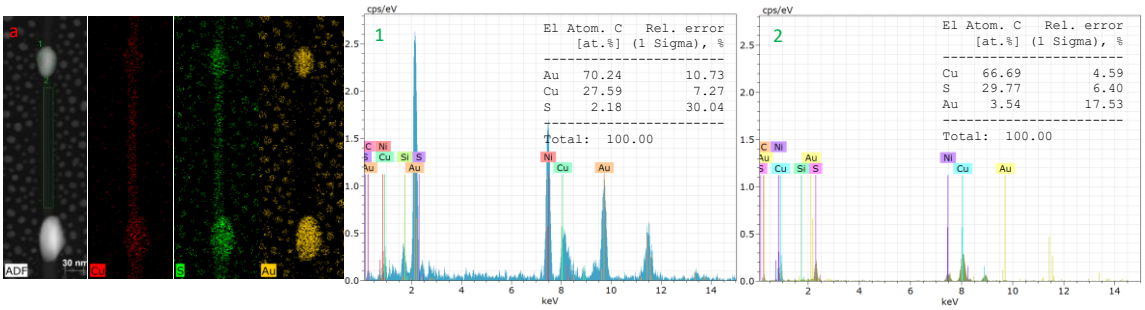

Figure 17. HAADF-STEM images of representative section of NWs and corresponding STEM-EDS elemental maps along with spectrum of elemental quantification in ROI (1) and (2) respectively.

During in-situ heating-up experiments from 350°C to 450°C we observe thermally induced collective migration of a multi atomic/cluster diffusion with in the larger domains (Fig.14a, b). Attempt to grow colloidal Au nanocrystals directly on Cu_2S NWs does not work due to the fact that Au efficiently replacing Cu forming Au_2S or CuAuS through cation exchange reaction (see chapter 6). In order to overcome this issue we developed an alternate strategy by growing Au NCs on CdS nanowires and subsequently transforming the CdS nanowires in to Cu_2S again through cation exchange reaction in solution as shown in figure 15 a). Interestingly thermal annealing of Au decorated Cu_2S NWs leads again to the formation of AuCu-Cu_2S metal heterostructure similar to the previous experimental findings (Figure 15b). Compositional analysis by STEM-EDS along with elemental maps in the desired regions further confirm the elemental ratios.

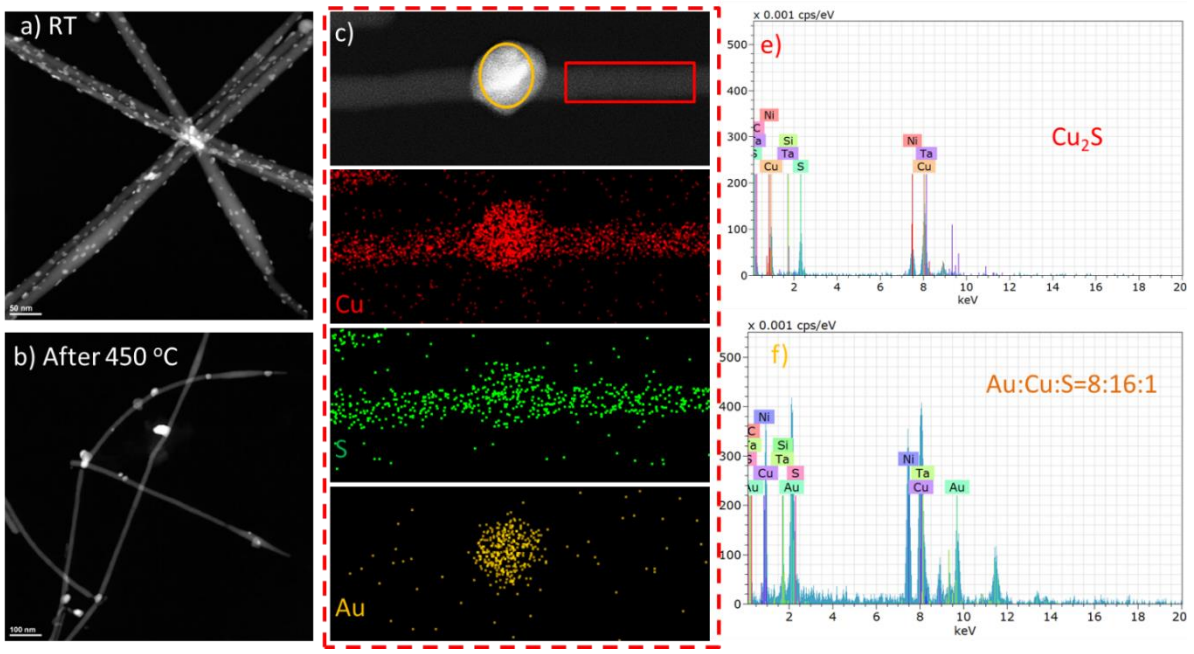

Figure 15. HAADF-STEM image and corresponding STEM-EDS maps of (a) Au decorated Cu2S NWs at room temperature, b) after thermal treatment up to 450 °C. Corresponding STEM-EDS elemental maps along with spectrum of elemental quantification in highlighted regions of the NWs respectively.

We further extended same strategy to another noble metal, namely Pt. Following our above mentioned procedure, we prepared first the Pt decorated CdS NWs and then through cation exchange reaction transformed them to Pt-Cu_2S nanowires as shown in figure 16 (a). Thermal annealing on these nanowires leads to the formation of similar higher contrast domains as observed in the case of Au. In order to gain further insight into this transformation, HAADF-STEM images and STEM-EDS analysis of the nanowires was systematically done at room temperature before and after in-situ heating experiment. STEM-EDS elemental maps shows the uniform distribution of Pt across nanowires before in-situ heating experiment (Figure 16 b) while after thermal treatment nanowires are segmented and entire Pt is diffused into the segments while leaving the nanowires clean between segments (Figure 16 e). Compositional analysis together with elemental maps revealed that high contrast are mainly an alloy of PtCu while notably in-between these segments nanowire still maintain the stoichiometric Cu_2S phase (Figure 16 e, f).

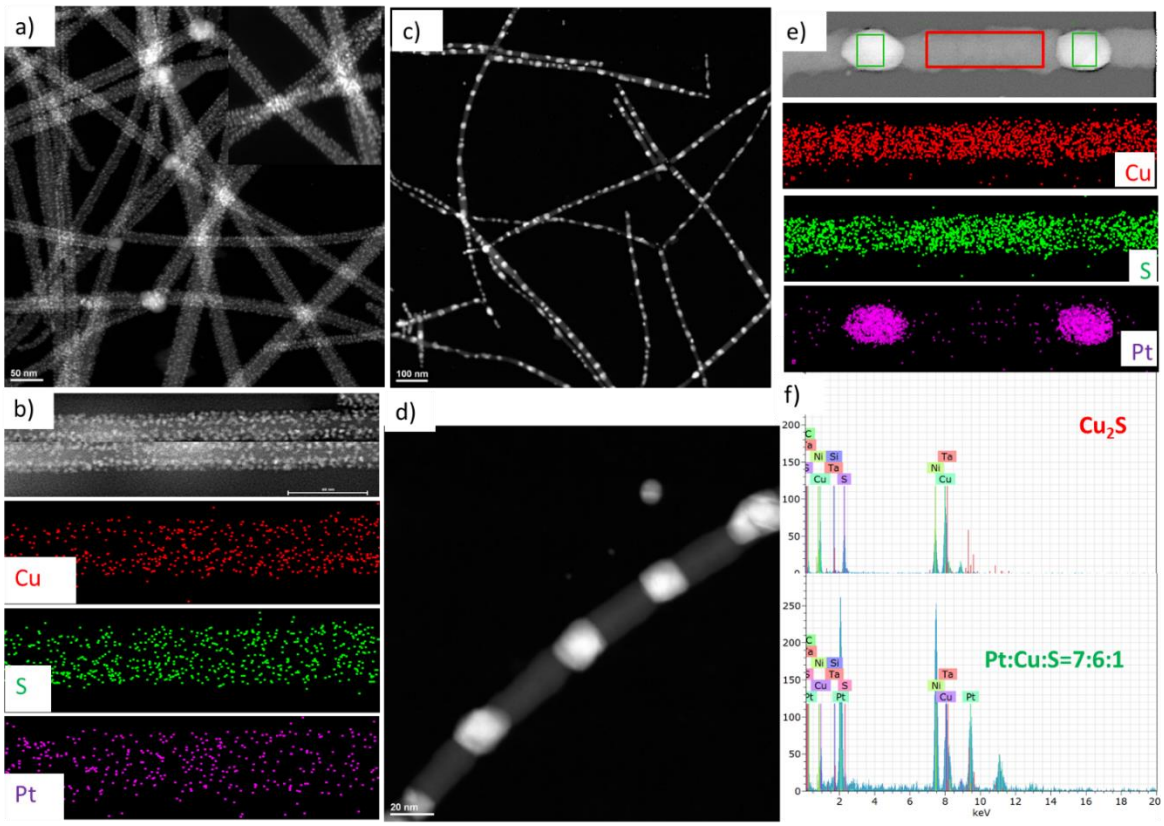

Figure 16. HAADF-STEM image and corresponding STEM-EDS maps of (a) Au decorated Cu2S NWs at room temperature, b) after thermal treatment upto 450 ^{o}C. Corresponding STEM-EDS elemental maps along with spectrum of elemental quantification in highlighted regions of the NWs respectively.

The behaviour of Cu sulfide NCs of different aspect ratios under heating-up in high-vacuum, especially in presence of noble metals, appears potentially interesting for the design of semiconductor-metal junctions which may find applications in devices.

7.4. Conclusion

We investigated systematically the thermal stability of Cu_2S NCs in-situ by using HRTEM and ex-situ in high vacuum furnace. Interestingly it was observed that upon heating up to 400^{o}C, Cu rich NRs/NWs transformed to stoichiometric Cu_2S NCs/NWs with the formation of metallic cupper domain on the surface of the NCs. Additional this transformation in presence of additional metallic NCs such as Au, Pt not only increases their thermal stability but also leads to the formation of Pt/AuCu-$Cu_{2-X}S$ metallic alloys semiconductor heterostructure NRs/NWs. The formation of epitaxial metal semiconductor will behave more reproducibly in electronic devices than their corresponding non-epitaxial structures (ensuring efficient charge

separation/collection at the nanoscale). The basic mechanism of this transformation is surface diffusion, either of individual metal atoms or of clusters of atoms, to a location for which a metal-semiconductor junction is more thermodynamically favoured. The results presented in this chapter are preliminary, and will be further investigated in particular in view of the applications in devices.

7.5. References

1. A. Comin, L. Manna, New materials for tuneable plasmonic colloidal nanocrystals. Chem. Soc. Rev. 2014, 43, 3957.
2. R. D. Robinson, B. Sadtler, D. O. Demchenko, C. K. Erdonmez, L. W. Wang, A. P. Alivisatos, Spontaneous superlattice formation in nanorods through partial cation exchange. Science 2007, 317, 355.
3. V. Lesnyak, R. Brescia, G. C. Messina, L. Manna, Cu vacancies boost cation exchange reactions in copper selenide nanocrystals J. Am. Chem. Soc. 2015, 137, 9315−9323.
4. D. H. Son, S. M. Hughes, Y. D. Yin, A. P. Alivisatos, Cation exchange reactions in Ionic nanocrystals. Science 2004, 306, 1009.
5. J. Beberwyck, A. P. Alivisatos, Ion exchange synthesis of III–V nanocrystals J. Am. Chem. Soc. 2012, 134, 19977.
6. N. R. Rao, K. P. R. Pisharody, Progress in Solid State Chemistry. 1976, 10 (Part4), 207.
7. D. C. Reynolds, G. Leies, L. L. Antes, R. E. Marburger, Photovoltaic effect in cadmium sulfide. Phys. Rev. 1954, 96, 533.
8. J. A. Bragagnolo, A. M. Barnett, J.E. Phillips, R. B Hall, A. Rothwarf, J. D. Meakin, The design and fabrication of thin-film CdS/Cu_2S cells of 9.15-percent conversion efficiency. IEEE Trans. Electron Devices 1980, 27, 645.
9. M. A. V. Huis, A. Figuerola, C. Fang, A. Béché, H. W. Zandbergen, L. Manna, Chemical transformation of Au-Tipped CdS nanorods into AuS/Cd Core/Shell Particles by Electron Beam Irradiation. Nano Lett. 2011, 11, 4555.
10. L. De Trizio, F. De Donato, A. Casu, A. Genovese, A. Falqui, M. Povia and L. Manna, Colloidal CdSe/Cu_3P/CdSe nanocrystal heterostructures and their evolution upon thermal annealing. ACS Nano, 2013, 7, 3997.
11. D. J. Chakrabarti, D. E. Laughlin, The Cu-S (Copper-Sulfur) system. Bulletin of alloy phase diagrams, 1988, 4, 3.
12. K. Miszta, G. Gariano, R. Brescia, S. Marras, F. D. Donato, S. Ghosh, L. D. Trizio, L. Manna, Selective cation exchange in the core region of $Cu_{2-x}Se$/$Cu_{2-x}S$ Core/Shell nanocrystals. J. Am. Chem. Soc. 2015,137, 38.
13. H. Li, M. Zanella, A. Genovese, M. Povia, A. Falqui, C. Giannini, L. Manna, Sequential cation exchange in nanocrystals: preservation of crystal phase and formation of metastable phases. Nano Lett. 2011, 11, 4964.

14. B. L. V. Prasad, S. I. Stoeva, C. M. Sorensen, K. J. Klabunde, Digestive-Ripening agents for gold nanoparticles: alternatives to Thiols. Chem. Mat. 2003, 15, 935.
15. Y. G. Sun, B. Mayers, Y. N. Xia, Transformation of silver nanospheres into nanobelts and triangular nanoplates through a thermal process. Nano Lett. 2003, 3, 675.
16. D. V. Talapin, A. L. Rogach, M. Haase, H. Weller, Evolution of an ensemble of nanoparticles in a colloidal solution, theoretical study. J. Phys. Chem. B 2001, 105, 12278.
17. M. A. V. Huis, , C. Fang, A. Béché, H. W. Zandbergen, L. Manna, Chemical transformation of Au-tipped CdS Nanorods into AuS/Cd Core/Shell particles by Electron Beam Irradiation. Nano Lett. 2011, 11, 4555.
18. A. Figuerola, M. V. Huis, M. Zanella, A. Genovese, S. Marras, A. Falqui, H. W. Zandbergen, R. Cingolani, L. Manna, Epitaxial CdSe-Au nanocrystal heterostructures by thermal annealing. Nano Lett. 2010, 10, 3028.
19. G. D. Moon, S. Ko, Y. Xia, U. Jeong, Chemical transformations in ultrathin chalcogenide nanowires. ACS Nano 2010, 4, 2307.
20. G. D. Moon, S. Ko, Y. Min, J. Zeng, Y. Xia, U. Jeong, Chemical transformations of nanostructured materials. Nano Today 2011, 6, 186.

21. L. Carbone, C. Nobile, M. D. Giorgi, F. D. Sala, G. Morello, P. Pompa, M. Hytch, E. Snoeck, A. Fiore, I. R. Franchini, M. Nadasan, A.F. Silvestre, L. Chiodo, S. Kudera, R. Cingolani, R. Krahne, L. Manna, Synthesis and micrometer-Scale assembly of colloidal CdSe/CdS nanorods prepared by a seeded growth approach. Nano Letters 2007, 7, 2942.
22. K. Miszta, R. Brescia, M. Prato, G. Bertoni, S. Marras, Y. Xie, S. Ghosh, M. R. Kim, L. Manna, Hollow and concave nanoparticles via preferential oxidation of the core in colloidal Core/Shell nanocrystals J. Am. Chem. Soc, 2014. 136, 9061.
23. B. Sadtler, D.O. Demchenko, H. Zheng, S. M. Hughes, M. G. Merkle, U. Dahmen, L. W. Wang, A. P. Alivisatos, Selective facet reactivity during cation exchange in cadmium sulfide nanorods. J. Am. Chem. Soc. Society 2009, 131, 5285.
24. L. Puthussery, T. H Kosel, M. Kuno, Facile synthesis and size control of II–VI nanowires using Bismuth Salts. Small 2009, 5, 1112.

Chapter 8.

8.1. Conclusions

This dissertation encompasses five projects, each of them achieving the proposed target. The first three chapters are related to the synthesis advances in lead halide perovskite nanocrystals (NCs) whereas the last two are mainly about the post synthesis transformation of Cu chalcogenide NCs.

The specific scientific findings of all these projects can be summarized as follows:

1. As described in Chapter 3, we have developed a colloidal synthesis strategy for tuning the width of $CsPbBr_3$ perovskite nanowires (NWs) from the non-confined regime (green emission) to the strong quantum-confinement regime (blue emission), by introducing carboxylic acids with short aliphatic chains (octanoic acid or hexanoic acid). Notably such a size tunability down to the quantum confinement regime in $CsPbBr_3$ nanowires was demonstrated for the first time. The NWs had photoluminescence quantum yield that could be as high as 77%, with PL spectral position that could be varied from green to blue. NWs with a width below ~5 nm show a reduced stability with the appearance of additional PL and absorption peaks and a reduction in PL quantum yield (PLQY). Future progress in this direction will require the stabilization of the thinnest wires. Another challenge will reside in understanding and modeling the growth kinetics and thermodynamics of these nanostructures.
2. The main limitation of protocols that are currently in use, such as the hot-injection and the ligand assisted reprecipitation routes, is that they employ PbX_2 (X= Cl, Br, or I) salts as both lead and halide precursors. This imposes restrictions on being able to precisely tune the amount of reaction species and, consequently, on being able to regulate the composition of the final NCs. In order to overcome this issue, we have demonstrated a new colloidal synthesis approach for the preparation of both all-inorganic and hybrid organic-inorganic $APbX_3$ NCs (A= Cs, MA, FA and X= Cl, Br, I). Our approach is based on the injection of benzoyl halides (as halide precursors) into a solution of desired cations and proper ligands (oleylamine and oleic acid) at a desired temperature. After the injection, a fast release of halide ions occurs, which is followed by the nucleation and growth of metal halide NCs.

In all the cases, the resulting $APbX_3$ NCs show a high phase stability, a very good size distribution and excellent optical properties. They exhibit a narrow PL emission and high PLQYs, which are around 90% in the case of $APbBr_3$ systems, 55% in the case of $APbI_3$ materials, and a record value of 65% in the case if $CsPbCl_3$ NCs. The optical quality of our materials was also reflected by the low values of their amplified spontaneous emission thresholds. The origin of such improvements with regards to the stability and optical properties of $CsPbX_3$ NCs was tentatively ascribed to the formation of lead-halide terminated surfaces in which Cs ions are partially replaced by oleylammonium ions. Indeed, the formation of such surfaces are promoted under our synthetic conditions and this is the first ever generalized synthesis approach that is broadly applicable to entire family of lead halide perovskite NCs. To conclude, we believe that the versatility of our synthetic approach could allow for the future new development of inorganic and organic metal halide NC systems.

3. Most strategies for synthesizing $CsPbX_3$ NCs so far are highly sensitive to the processing conditions and ligands combination. For example, in the synthesis of nanocubes of different sizes, it is not uncommon to have samples containing various other shapes, such as nanoplatelets and nanosheets. Ideally, one would need a robust synthesis scheme to prepare nanocubes that is not limited by all these reaction parameters, so that cubes of various sizes can be reproducibly prepared by sampling a broad set of reaction conditions, with no contamination of NCs with other shapes and/or crystal phases. To overcome this issue we devised a strategy by substituting primary amine with secondary amine in the benzoyl halide-based hot-injection synthesis of $CsPbBr_3$ nanocubes. That substitution eliminates formation of nanocrystal shapes other than cubic, resulting in samples with remarkable uniformity of $CsPbBr_3$ nanocrystals. The shape uniformity and size tunability of the resulting nanocubes is demonstrated to persist independently on the temperature of the bromide precursor injection (50 °C to 140 °C range) or hydrocarbon chain length of secondary amines (from dihexyl to dioctadecyl). The resulting nanocubes demonstrate narrow PL linewidths (full width at half maxima 68-81 meV) and high PLQYs (48-80%) in solution. The DFT calculations revealed

that the dialkylammonium molecules cannot stabilize lamellar 2D perovskites, and thus do not promote the anisotropic growth of NPLs, but rather promote the isotropic growth of nanocubes. The high uniformity of the obtained samples was utilized to obtain nanocrystal superlattices with lateral dimensions reaching up to 50 microns – the largest reported so far in lead halide perovskite family. We further believe that secondary amines will not only expand the ligands library of lead halide perovskite nanocrsytals but also paved a way to better elucidate photophysicscal properties of shape pure material.

4. Cation exchange reactions have emerged as a powerful tool to design more complex structures which cannot be accessed through direct synthesis routes. Taking the advantage of this strategy, here in we devloped a novel ternary chalcogenide phase, CuAuS, via post-synthesis chemical transformation on performed Cu_2S NCs. Albeit the large number of studies on the Cu chalcogenide and their combination with noble metals, including Au, no previous study reported this particular phase both in bulk and NCs so far. The reason for this may be its instability out of a very narrow window of conditions. Remarkably this new ternary alloyed semiconductor NCs exhibit a localized surface plasmon resonance (LSPR) which can be interesting for bio-sensing and in-vivo imaging. Further study will be needed to understand the reason for energy instability of this phase, such that no previous report mentioned its formation.
5. Thermal stability of Cu_2S NCs with different aspect ratios was systematically investigated upon annealing in-situ and ex-situ. Interestingly it was observed that upon thermal annealing extrusion of Cu took place from NRs/NWs most likely due to the partial sublimation of S and subsequently transforming the NCs to stoichiometric Cu_2S with the formation of metallic cupper domain on the surface of the NCs. Remarkably this transformation in presence of additional metallic NCs such as Au or Pt leads to the formation of metal-semiconductor heterojunction (for example Au_xCu-Cu_2S NCs). This formation of epitaxial metal semiconductor will behave more reproducibly in electronic devices than their corresponding non-epitaxial structures (ensuring efficient charge separation/collection at the nanoscale). The basic mechanism of later transformation is surface diffusion,

either of individual metal atoms or of clusters of atoms, to a location for which a metal-semiconductor junction is more thermodynamically favored.

8.2. List of publication

Most recent first,

- **Imran M, et**.al. Novel metastable CuAuS phase in colloidal nanodisks via partial cation exchange, a new plasmonic material (in preparation).
- **Imran M**, Ijaz P, Goldoni L, Maggioni D, Petralanda U, Prato M, Almeida G, Infante I, Manna L. Quaternary Ammonium Ligands for Colloidally Stable $CsPbBr_3$ Nanocrystals with Near-Unity Photoluminescence Quantum Yield, November **2018 (**Submitted).
- Baranov D, Toso S, **Imran M**, Manna L. An Investigation into the Photoluminescence Red Shift in Cesium Lead Bromide Nanocrystal Superlattices. November **2018 (**Submitted).
- Shamsi J, Urban A, **Imran M,** De Trizio L, Manna L. Metal Halide Perovskite Nanocrystals: Synthesis, PostSynthesis Modifications and Their Optical Properties. ***Chemical Reviews***, **2018**.
- **Imran M**, Ijaz P, Baranov D, Goldoni L, Petralanda U, Akkerman QA, Abdelhady AL, Prato M, Bianchini P, Infante I, Manna L. Shape Pure, Nearly Monodisperse $CsPbBr_3$ Nanocubes Prepared using Secondary Aliphatic Amines. ***Nano letters***. **2018**, *18* (12), pp 7822–7831.
- Palazon F, Chen F, Akkerman QA, **Imran M**, Krahne R, Manna L. Effects of Oxygen Plasma on the Chemical, Light-Emitting, and Electrical-Transport Properties of Inorganic and Hybrid Lead Bromide Perovskite Nanocrystal Films. ***ACS Applied Nano Materials***. 2018, 1(10), 5396-400.
- Akkerman QA, Martínez-Sarti L, Goldoni L, **Imran M**, Baranov D, Bolink HJ, Palazon F, Manna L. Molecular Iodine for a General Synthesis of Binary and Ternary Inorganic and Hybrid Organic–Inorganic Iodide Nanocrystals. ***Chemistry of Materials***. 2018, 30 (19), 6915-21.
- Caligiuri V, Palei M, **Imran M**, Manna L, Krahne R. Planar Double-Epsilon-Near-Zero Cavities for Spontaneous Emission and Purcell Effect Enhancement. ***ACS Photonics***, 2018, *5* (6), 2287–2294
- **Imran M,** Caligiuri V, Wang M, Goldoni L, Prato M, Krahne R, De Trizio L, Manna L. Benzoyl Halides as Alternative Precursors for the Colloidal Synthesis of Lead-Based Halide

Perovskite Nanocrystals. ***Journal of the American Chemical Society***. **2018**, 29 (140), 2656-64.

- Dang Z, Shamsi J, Akkerman QA, **Imran M**, Bertoni G, Brescia R, Manna L. Low-Temperature Electron Beam-Induced Transformations of Cesium Lead Halide Perovskite Nanocrystals. **ACS Omega**. 2017, 2(9), 5660-5.
- Di Stasio F, **Imran M**, Akkerman QA, Prato M, Manna L, Krahne R. Reversible Concentration Dependent Photoluminescence Quenching and Change of Emission Color in $CsPbBr_3$ Nanowires and Nanoplatelets. ***Journal of Physical Chemistry Letters,*** **2017**, *8* (12), 2725–2729.
- Dang Z, Shamsi J, Palazon F, **Imran M**, Akkerman QA, Park S, Bertoni G, Prato M, Brescia R, Manna L. In Situ Transmission Electron Microscopy Study of Electron Beam-Induced Transformations in Colloidal Cesium Lead Halide Perovskite Nanocrystals. ***ACS Nano***, 2017, *11* (2), 2124–2.
- **Imran M**, Di Stasio F, Dang Z, Canale C, Khan AH, Shamsi J, Brescia R, Prato M, Manna L. Colloidal synthesis of strongly fluorescent $CsPbBr_3$ nanowires with width tunable down to the quantum confinement regime. ***Chemistry of Materials***. 2016, *28* (18), 6450–6454.

8.3. Abbreviations

Full name	Abbreviation
Atomic force microscopy	AFM
Conduction band	CB
Density functional theory	DFT
Dihexylamine	DHAm
Dioctylamine	DOAm
Didecylamine	DDAm
Didodecylamine	DDDAm
Dioctadecylamine	DODAm
Dimethylsulfoxide	DMSO
Energy-disperse X-Ray spectroscopy	EDX
Electron energy loss spectroscopy	EELS
Full width at half maximum	FWHM
High-angle annular dark -field	HAADF
High resolution transmission electron microscopy	HRTEM
Lead halide perovskite	LHP

Nanocubes	NCs
Nanowires	NWs
Nanoplatelets	NPLs
Nanosheet	NSs
Nuclear magnetic resonance	NMR
Oleic acid	OA
Octadecene	ODE
Oleylamine	OLAm
Photoluminescence	PL
Photoluminescence quantum yield	PLQY
Quantum dots	QDs
Superlattices	SLs
Transmission electron microscopy	TEM
X-ray diffraction	XRD
X-ray Photoelectron Spectroscopy	XPS